University of Oxford
Department of Engineering Science

Nanomechanical Behaviour of the Monolithic Framework Solids: An Experimental and Modelling Study

Michele Tricarico
Balliol College

A thesis submitted for the degree of
Doctor of Philosophy

Hilary 2023

A mamma, papà, Francesco e Alessandro,
che ci sono sempre stati e ci saranno sempre.

“You have power over your mind — not outside events. Realise this, and you will find strength.”

— Marcus Aurelius

Acknowledgments

Three and a half years have gone by in a wink and yet many beautiful people have crossed my path since that rainy night when I first arrived in Oxford, loaded with suitcases and hope, and excited for the start of a new, fascinating adventure.

I would like to start by thanking my supervisor, Prof. Jin-Chong Tan, who gave me the opportunity to pursue my doctoral studies in one of the best universities in the world and funded my research with the ERC Consolidator Grant 771575 (PROMOFS). I will always be grateful to Prof. Tan for his continuous guidance, support, and inspiration throughout these years.

I am grateful to all the collaborators, particularly Dr Gianfelice Cinque, Dr Cyril Besnard and Dr Igor Dyson, whose help and advice strongly contributed to the outcomes of this thesis.

I would also like to thank all my colleagues and friends of the Multifunctional Materials & Composites (MMC) Lab: Samraj, Annika, Yang, Jiahao, Tianhuai, Dylan, Vishal, Ben, Arun, Abhijeet, Bárbara, Mario, Yueting, Sujeet and Tao. Thanks for the countless coffee breaks with scientific and non-scientific discussions, the support and company in the lab, the squash sessions, the punting, all the lunches and dinners and beyond.

Outside the lab, I was blessed with many other friends, that made my time in Oxford unforgettable. Firstly, a big thank you to the Italian friends, Marino, Patanè, Salvati, Laurenti and Piccione, that warmly welcomed me in their group since my very first days in Oxford and have always been there, especially during the tough times of Covid-19. I will never forget all the friendship dinners, the culturally elevated movie nights (*cineforum*), the long lockdown strolls in the parks and the memorable nights in Oxford and London. Furthermore, thanks to my Balliol friends Manos (for your genuine companionship, topped with a lot of non-sense), Quentin (for the tennis, squash and padel matches and the French lessons over lunch) and Angelo (actually, you should thank me for being your mentor). Thanks

also to my St Clement's housemates, Ed, Emile, Emily, Lilian and Lucrezia, whose company kept me going during these last hectic months.

Finally, I want to thank all my family and friends back home for the continuous (remote) support. Most importantly, I would like to thank my parents, Isa and Leo, and my brothers, Francesco and Alessandro, to whom this thesis is dedicated. Without your unconditional love and support I would not have achieved half the things that I have now.

Preface

This thesis is submitted for the degree of Doctor of Philosophy in the University of Oxford, United Kingdom. The research presented in this work was carried out by the author between October 2019 and March 2023 in the Department of Engineering Science, under the supervision of Professor Jin-Chong Tan.

To the best of my knowledge, the work described in this dissertation is original, except where due reference has been made, acknowledging the work of others. Nothing has been included that is the outcome of work done in collaboration with others, except where explicitly noted. No part of this dissertation, or any similar to it, has been, or is currently being submitted for any degree at this, or any other university. This thesis is less than 250 pages in length.

The work presented herein has been partially published in the following journal papers:

- **M. Tricarico**, J.-C. Tan, Mechanical properties and nanostructure of monolithic zeolitic imidazolate frameworks: a nanoindentation, nanospectroscopy, and finite element study, Mater Today Nano 17 (2022) 100166.
- **M. Tricarico**, J.-C. Tan, Nanostructure-dependent indentation fracture toughness of metal-organic framework monoliths, Next Materials (2023).

- **M. Tricarico**, C. Besnard, G. Cinque, A. M. Korsunsky, J.-C. Tan, Stress-strain relationships and yielding of MOF monoliths, Manuscript under preparation (2023)

Other manuscripts were published/submitted during my DPhil but are not directly related to the work developed in this thesis:

- M.E. Carrington, N. Rampal, D.G. Madden, D. O'Nolan, N.P.M. Casati, G. Divitini, J.Á. Martín-Illán, **M. Tricarico**, R. Cepitis, C. Çamur, T. Curtin, J. Silvestre-Albero, J.-C. Tan, F. Zamora, S. Taraskin, K.W. Chapman, D. Fairen-Jimenez, Sol-gel processing of a covalent organic framework for the generation of hierarchically porous monolithic adsorbents, Chem 8(11) (2022) 2961-2977.
- Y. Zhang, S. Mollick, **M. Tricarico**, J. Ye, D.A. Sherman, J.-C. Tan, Turn-On Fluorescence Chemical Sensing through Transformation of Self-Trapped Exciton States at Room Temperature, ACS Sensors 7(8) (2022) 2338-2344.
- S. Mollick, Y. Zhang, W. Kamal, **M. Tricarico**, A.F. Möslein, V. Kachwal, N. Amin, A.A. Castrejón-Pita, S.M. Morris, J.-C. Tan, Surface modulation of metal-organic frameworks for on-demand photochromism in the solid state, Submitted (2022).
- Y.D. More, S. Mollick, S. Saurabh, S. Fajal, **M. Tricarico**, S. Dutta, M.M. Shirolkar, W. Mandal, J.C. Tan, and S.K. Ghosh, "Trap Grafting in Anionic MOF for Superior Uranium Extraction from Seawater", Submitted (2023).

- McLuskie, C.N. Brodie, **M. Tricarico**, C. Gao, G. Peters, A.B. Naden, C.L. Mackay, J.C. Tan, A. Kumar, "Manganese Catalysed Dehydrogenative Synthesis of Polyureas from Diformamide and Diamines", Submitted (2023).

Michele Tricarico
Oxford
March 2023

Abstract

Metal-organic frameworks (MOFs) have established themselves as a versatile material platform for a wide variety of applications such as gas adsorption, energy conversion and storage, luminescence and chemical sensing. Over the past two decades, scientists have designed numerous MOF systems and composites that are specifically tailored for different applications, thanks to their extraordinarily large internal surface area and high tuneability. However, the integration of MOFs into real-world sensors and devices still represents a challenge. The majority of MOFs reported to date is in fact synthesised in the form of polydisperse powders, characterised by some intrinsic limitations. The aim of this thesis is to gain understanding of the mechanical behaviour of robust monolithic sol-gel MOFs, identified as a promising candidate for the transition of this class of materials from the academia to industrial deployment. The advantages and potential applications of MOF monoliths are described in Chapter 1. An overview of nanoindentation, the most used technique for the mechanical characterisation of MOFs, is provided in Chapter 2, along with a literature review of the field of MOF mechanics. Chapter 3 summarises the synthesis protocols and the material characterisation techniques utilised throughout the thesis. In Chapters 4, 5 and 6, different aspects of the mechanical response of the prototypical MOF monoliths were systematically studied by means of nanoindentation, spectroscopy, and finite element simulations. In particular, plasticity, fracture toughness and stress-strain relationships underpinning the mechanical performance of MOF monoliths are investigated, and their connections to the nanostructure and the framework architecture are established. Finally, the reported findings are critically summarised in Chapter 7, along with a personal perspective on the future development of the field.

Table of Contents

List of Abbreviations

AFM	Atomic Force Microscopy
ATR-FTIR	Attenuated total reflection fourier transform infrared spectroscopy
BDC	1,4-benzenedicarboxylate
BIF	Boron Imidazolate Framework
bImH	2-benzimidazole
BTC	benzene-1,3,5-tricarboxylate
C	Carbon
C3D8	8-node linear brick element (Abaqus)
CAX4	4-node bilinear elements (Abaqus)
CCDC	Cambridge Crystallographic Data Centre
COF	Covalent Organic Frameworks
CSM	Continuous Stiffness Measurements
Cu	Copper
dcImH	4,5-dichloroimidazole
DFT	Density functional theory
DMF	dimethylformamide
FEM	Finite Elements method
FIB	Focused Ion Beam
GBS	Grain Boundary Sliding

H	Hydrogen
HCR	High Concentration Reaction
HKUST	Hong Kong University of Science and Technology
IIT	Instrumented Indentation Testing
Im	Imidazolate
ImH	Imidazole
LEFM	Linear Elastic Fracture Mechanics
LEM	Lawn-Evan-Marshall
microRaman	Confocal Raman microscopy
MIL	Matériaux de l′Institut Lavoisier
mImH	2-methylimidazole
MOF	Metal-Organic Framework
N	Nitrogen
nanoFTIR	nanoscale Fourier transform infrared spectroscopy
Ni	Nickel
SAXS	Small-Angle X-ray Scattering
SEM	Scanning Electron Microscopy
Si	Silicon
TEM	Transmission Electron Microscopy
TFM	Tip Force Microscopy
UiO	Universitetet i Oslo
UTSA	University of Texas at San Antonio
VOC	Volatile organic compound

XRD	X-Ray Diffraction
ZIF	Zeolitic Imidazolate Framework
Zn	Zinc
Zr	Zirconium

1 Introduction

1.1 Motivation

Nanoporous materials are particularly attractive for a wide range of applications, such as miniaturized and portable devices. Their unique nanoscale structure, which confers several beneficial attributes (i.e., porosity, conductivity), can easily be adjusted at the fabrication stage. This exceptional tuneabilty extends their use to several applications, making this research field very promising (1).

Nanoporous materials have been used in several commercial applications as well (2), such as medical diagnostics, drug delivery and anti-cancer treatment (3), food analysis, chemical decontamination and catalysis (4) and gas storage (5). Examples of nanoporous materials are activated carbons, zeolites, alumina, mesoporous silicas, and metal-organic frameworks.

Metal-organic frameworks (MOFs) are hybrid nanoporous compounds, consisting of metal nodes and organic ligands that self-assemble to form lattice structures (6). This results in an extraordinary large internal surface area, which makes these materials of interest for carbon sequestration (7), water purification (8, 9), catalysis (10), and gas storage (e.g., hydrogen and carbon dioxide) (11, 12). However, many MOFs are currently synthesised as powders, which limits the range of engineering applications.

The focus of this DPhil thesis is on the fabrication and mechanical characterisation of mechanically robust MOF monoliths (Figure 1.1), which represent a promising solution for the future industrialisation of MOFs.

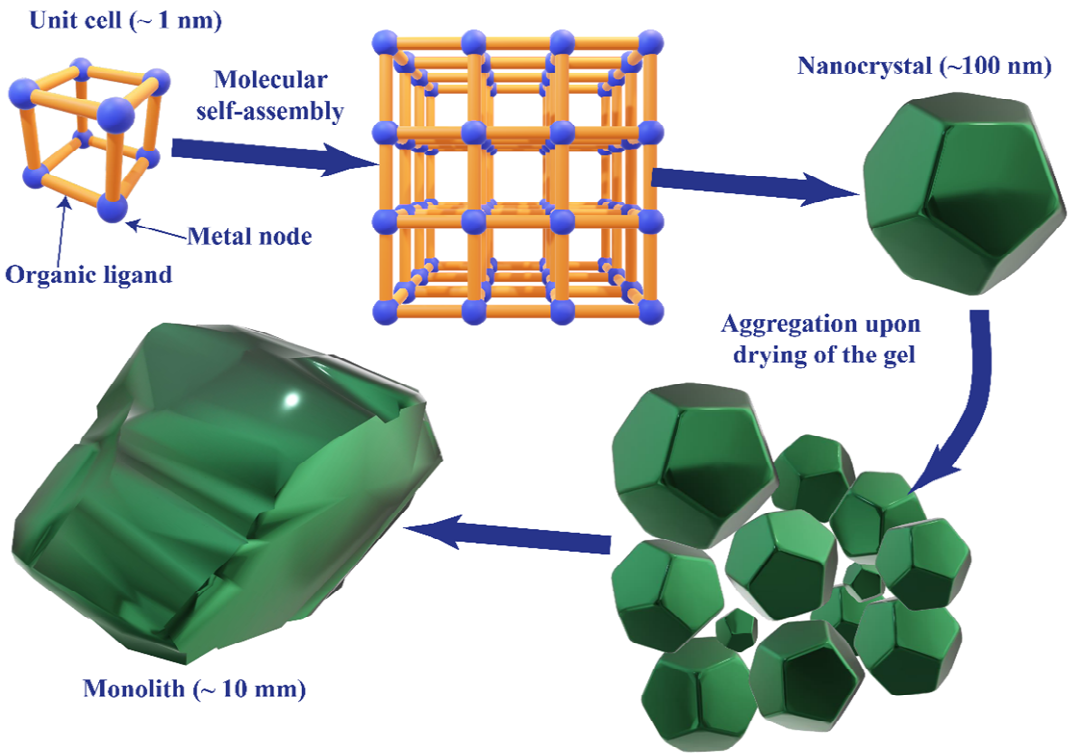

Figure 1.1 Graphical representation of MOF crystals and MOF monoliths. Lattice structures at the sub-nanometric scale are formed upon self-assembly of metal nodes and organic linkers. Monoliths are formed as a result of nanoparticles aggregation. Adapted with permission from (13).

1.1.1 Overview of MOFs and applications

Extensive research into the design and synthesis of MOFs over the last 25 years (14) has resulted in a large class of crystalline and amorphous (i.e., MOF glasses, obtained by melt quenching the crystalline framework (15)) materials with high stability, tuneable metrics, organic functionality, and porosity (6, 16). Particularly, the porosity observed in MOFs can be either “intrinsic” (within the framework),

when resulting from the shape of the molecular building blocks themselves, in the form of pores and channels, or “extrinsic” (between the frameworks), as a consequence of the packing of the molecules (17).

The availability of such a large number of versatile structures has led to a very wide literature in terms of possible applications (18-20), as summarised in Figure 1.2. Some examples include solvents (21) and VOCs sensing (22-24), drug delivery (25, 26), CO_2 capture (27-29), gas separation (30, 31), micromotors (32), semiconductors and low-*k* materials (33), luminescent materials (34, 35), and catalysis (36).

Another important capability of MOFs, coming from their exceptional internal surface area, is the so called “guest@host” concept: the MOF can act as a host to confine guest molecular species inside its voids (37). This unveils a new class of functional composite materials, suitable for applications in many fields like optics, electronics, and drug delivery to name a few (38).

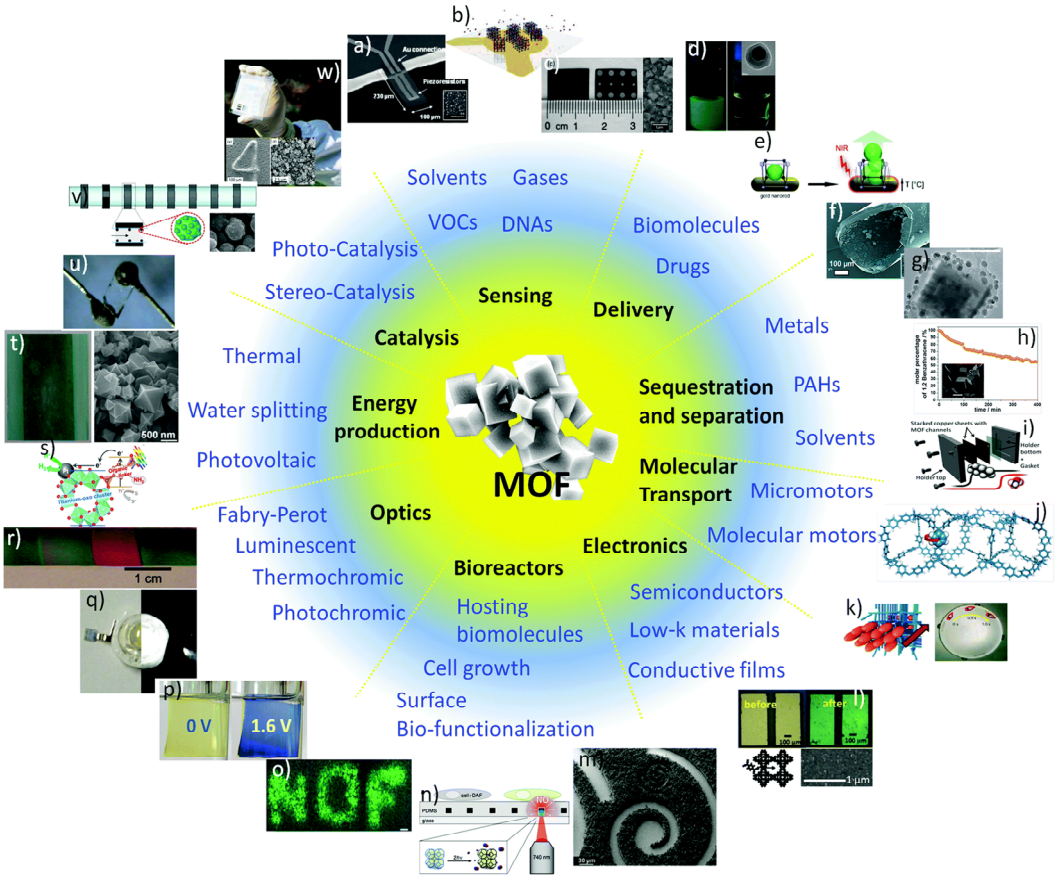

Figure 1.2. Overview of potential MOFs applications, adapted with permission from (18).

1.1.2 Advantages of MOF monoliths

The majority of MOFs are synthesised as polydisperse microcrystalline powders. These may present intrinsic limitations such as poor handling properties, mass transfer limitations, and mechanical instability, which could reduce the range of applications.

In order to broaden the use of MOFs, the realisation of structurally robust and continuous morphologies, known as monoliths, is needed (17). There are many advantages of monoliths over powders, such as:

- Easier handling associated with higher structural rigidity.
- Low mass transfer resistance (for example, in adsorption columns, the packing of MOF "loose" powder can lead to a significant pressure drop over time, caused by the gradual compaction of the powder with pressure, resulting in higher mass resistance within the column) (39).
- Higher volumetric adsorption capacities and higher surface areas (large quantities of void space between individual crystallites in powders reduces the packing density and compromises the volumetric adsorption capacities).
- Hierarchical porosity (40).

Monoliths present also many advantages over MOF-polymer composites (41), which represents the easier solution for improving the mechanical stability of these materials:

- High effective volumetric loadings. In MOF-polymer composites effective loadings are limited due to reduced colloidal stabilities during the fabrication process. This means that aggregates and sediments of MOF powders will form as the loading increases.
- Full accessibility of nanopores. The polymer can block the internal porosity. This is not the case in pure MOF monoliths.

In the literature, several methods for the fabrication of MOF monolithic architectures have been explored. We can divide them into two classes:

- formation of composites using binders (i.e., extra materials added to hold particles together) and scaffolds
- formation of “pure monoliths”

Composite monoliths have been fabricated by employing both inorganic (silica) (42) and organic (porous carbon) (29) scaffolds. Küsgens *et al.* (43) manufactured monoliths using an industrially available extrusion technique, by initially mixing the MOF powders with a binder and a plasticiser.

Some attempts of 3D printed MOF monoliths are also available in the literature. For example, Thakkar *et al.* (44) fabricated MOF-74 (Ni) and UTSA-16 (Co) 3D-printed monoliths (with a concentration of MOF higher than 80 wt.%, using PVA as a plasticiser, i.e., a substance added to make the material softer and more flexible, in order to improve its workability) exhibiting CO_2 capture capacities comparable to those of the respective powders. Chaudhari *et al.* (45) 3D-printed a photoluminescent composite material, by combining a novel dual-guest@MOF system, obtained by confining fluorescein and rhodamine B in the cages of ZIF-8, with an acrylic-based photopolymer resin.

Within the “pure monoliths” class, we can list techniques such as mechanical densification (40, 46, 47) and morphological replacement of a shaped sacrificial metal oxide mesoscopic template (48). Mechanical densification is a very easy process: the powders are filled into a die, which is then pressed by a punch, in order to obtain a tablet. The resulting monoliths usually show an improved gas adsorption capacity when compared to powdered counterparts (46, 47). The morphological replacement of a shaped sacrificial metal oxide mesoscopic

template, also known as pseudomorph mineral replacement, consists in the dissolution of the metastable metal oxide product at the solid/liquid interface, and its prompt recrystallisation as a more thermodynamically stable crystalline phase at the same site in the presence of organic ligands. As an example, Moitra *et al.* (48) converted a hierarchically porous $Cu(OH)_2$-based monolith to $Cu_3(btc)_2$ [btc = benzene-1,3,5-tricarboxylate] (HKUST-1) monolith by coordination replication in the presence of H_3btc as a ligand with complete preservation of the macroporous structure.

Another approach to the formation of pure MOF monoliths is *via* the sol-gel state: by removing the solvent from a MOF gel, a monolithic state is achieved (17, 49). Several works concerning the synthesis of sol-gel MOF monoliths have been published in the recent years, for a wide range of MOFs, such as HKUST-1 (50, 51), ZIFs (13, 52, 53), UiO-66 (54) and MIL-68 (51). The structures of the most common MOFs reported to form monoliths are illustrated in Figure 1.3.

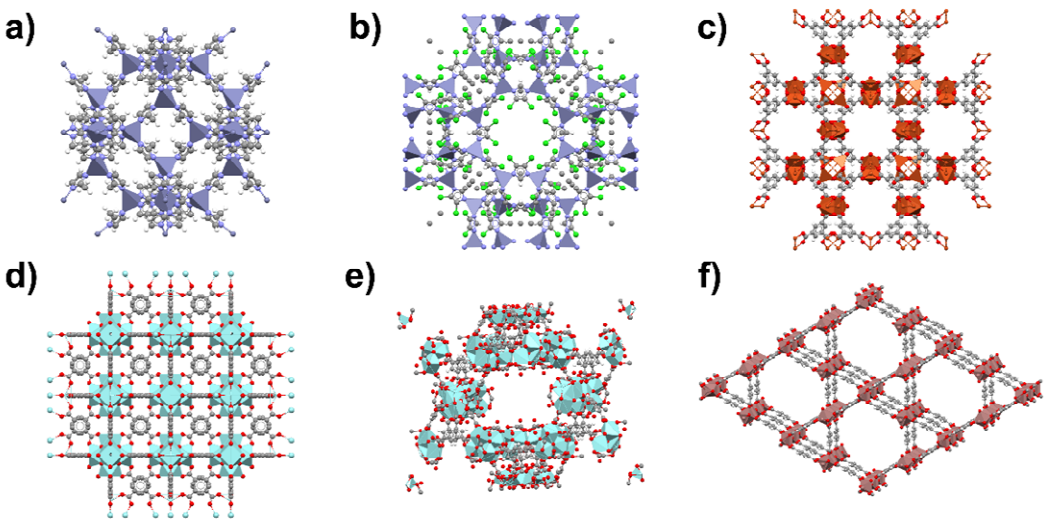

Figure 1.3 Schematic of the framework architectures of a) ZIF-8, b) ZIF-71, c) HKUST-1, d) UiO-66, e) MOF-808, f) MIL-68.

Compared to mechanical densification, this method allows for a better control. Moreover, it is possible to obtain different pore sizes within the same material, leading to increased capabilities of gas uptake (50, 52, 54, 55). However, the structures of both MOF gels and derived monoliths and the processes at the basis of their synthesis are still not very clear.

The sol-gel process consists in the production of a network (gel) from molecular precursor *via* the formation of colloidal particles (sol). The nanoparticles in the colloid aggregates *via* weak non-covalent interactions (mainly van der Waals forces), forming a viscous material: the gel. The formation of gel rather than precipitates is favoured by small size of the nanoparticles size (less than 100 nm). In order to get nanoparticles of the desired dimension, the crystallisation (self-assembly) process of MOFs must be understood. It basically consists of two stages: nucleation and crystal growth. As the solutions containing metal and linker are combined, nucleation sites are formed, and subsequently crystal growth occurs. These two processes are in competition with each other: the more the nucleation sites the less the crystal growth. This means that a fast nucleation rate (with respect to crystal growth) will result in finer nanocrystals (56, 57).

To promote the formation of a MOF gel, several parameters involved in the synthesis process need to be tweaked. For example, the type of metal source, concentration of reactants, choice of solvent and deprotonation of ligands were found to play an important role. Bueken *et al.* (58) observed that for some Zr-based MOFs an increased reactant concentration favours the formation of the gel.

However, by using a different metal source, it is possible in some cases to promote the formation of metal-organic clusters with a reduced reactant concentration. Deprotonation of the linker prior to addition of metal solution has been shown to result in a gel product in several MOFs, such as HKUST-1 (51, 59-61), ZIF-8 and ZIF-71 (13), MIL-68 (51, 62), and guest@ZIF-8 (34). The deprotonation boosts the formation of clusters and hence increases the number of nucleation sites (63). The solvent choice is also a key parameter, since an appropriate solvent can facilitate the assembly of metal clusters (60).

The formation of gels in MOFs depends on many parameters and, thus far, we have only a limited knowledge on a case-by-case basis. The drying of the MOF gel has unquestionably a prominent role on the formation of mechanically stable and robust monoliths. During solvent drying, there exist a mechanical stress at the gas-liquid interface in the pores, due to surface tension. This phenomenon is often the cause of cracking or collapse of the gel body. A slow solvent removal (typically at room temperature) and small size of the particles can better accommodate this stress, favouring the formation of denser monoliths. However, this is not always possible, especially in big monoliths, where large shrinkages occur, leading to cracking. Several procedures to avoid this issue have been explored for conventional sol-gels (i.e., silica), for example drying with supercritical fluids, that circumvents the gas/liquid interface, or freeze drying (64). Supercritical CO_2 drying has been leveraged to produce MOF aerogels (58, 65, 66), characterised by extremely high porosity and low density. Freeze drying, that would result in denser

aerogels (i.e., cryogels), has been employed to form MOF-hydrogels composites (67, 68), but not for “pure” MOF gels.

1.2 Research aims

The field of MOF monoliths is still in its early stages, with only a few examples recorded to date. Apart from very basic measurements of Young's modulus and hardness using nanoindentation, their mechanical behaviour has not been substantially investigated. The goal of this thesis was to gain a better understanding of the plasticity and the fracture behaviour of these materials. To assess the nanoctrucural properties of the materials and correlate them to their mechanical response, a variety of experimental approaches and simulations, in addition to nanoindentation, were employed.

1.3 Structure of the thesis

This integrated thesis is composed of seven chapters. The main results of the chapters and their interconnection are summarised in Figure 1.4.

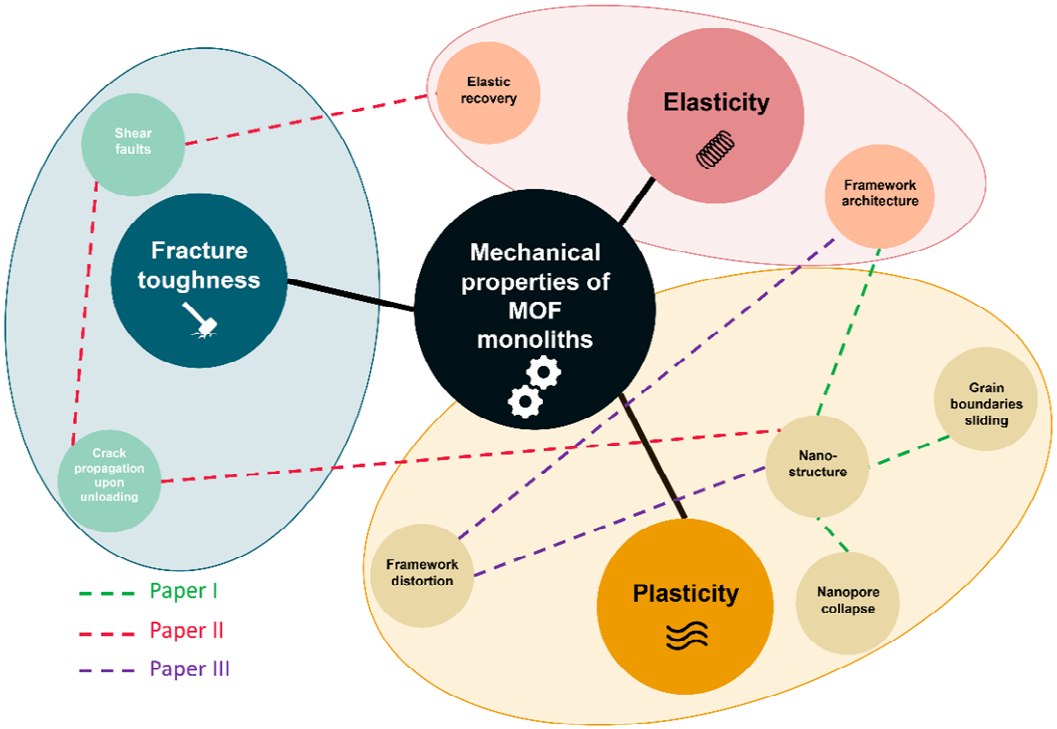

Figure 1.4 Mind map summarising the results and the interconnection of the chapters presented in this thesis.

The present Introduction (Chapter 1) sets out the motivation of the project, followed by a brief overview about MOF materials and their applications, with a special focus on the state of the art of MOF monoliths fabrication and processing.

Chapter 2 is a detailed literature review of the mechanical properties of MOFs. It begins with a brief overview of nanoindentation, the most employed technique for the mechanical characterisation of these materials. The second part of the chapter summarises the mechanical properties of different MOF single crystals,

monoliths, and glasses, measured by nanoindentation and other techniques. Young's modulus and hardness are the most reported properties, directly measured by instrumented indentation. Few attempts have been made to estimate the fracture toughness by combining nanoindentation and imaging techniques (i.e., optical microscopy, AFM, SEM).

Chapter 3 summarises all the techniques used to synthesise the materials and prepare the samples. Subsequently, the methods and instruments used to characterise the materials are described.

The following three chapters (Chapter 4, 5 and 6) consists of a stand-alone paper each. The papers were attached at the end of the respective chapters, preceded by a brief introduction and a summary of their content. Additional insights based on the Supplementary Information of each paper and the relevant literature were also provided.

Chapter 4 describes the mechanical behaviour of two prototypical ZIF monoliths, namely ZIF-8 and ZIF-71. A combination of nanoindentation, atomic force microscopy (AFM), tip force microscopy (TFM), nanoscale Fourier transform infrared spectroscopy (nanoFTIR) and finite element method (FEM) simulations was employed to identify the mechanical deformation mechanisms in monolithic ZIF materials: grain boundary sliding is dominating at low stresses, then breakage of chemical bonds and a partial failure of the framework occur, eventually leading to a densification of porous framework at the contact zone. Finally, the fracture toughness was measured using a cube corner indenter.

Chapter 5 explores the cracking behaviour of four different monoliths (ZIF-8, HKUST-1, MIL-68 and MOF-808) under nano- and micro-indentation and nanoscratching. A correlation was established with their nanostructure and framework architecture. MIL-68 and MOF-808, exhibited a remarkable resistance to radial cracking and the occurrence of shear faults as the principal failure mechanism. The cracks follow the low-energy grain boundaries separating the aggregated nanocrystals forming the monolith: this allows to confine the damage within the contact area and avoid, to some extent, catastrophic failure.

In Chapter 6, the yielding of MOF monoliths was further investigated. In particular, ZIF-8 and MIL-68, which, according to the results of Chapter 5, are characterised by different failure mechanisms, were studied and compared. Flat punch indentation and micropillar compression were employed to estimate the stress-strain relationships. Spectroscopy techniques (particularly confocal Raman microscopy) were used to carry out an analysis of the residual strains at the framework level after plastic flow.

The concluding chapter provides an overview of the results of the thesis, together with some perspectives and ideas on future developments in the field.

2 Mechanical Properties of Metal-Organic Frameworks

The inherent porosity of MOFs and their exceptional degree of structural and functional tuneability, results in many interesting and sometimes unexpected phenomena upon physical and chemical stimuli. An understanding of mechanical properties plays an essential role in the post-synthetic processing of MOFs, which is crucial in the efficacious transition of these materials from academic research to practical applications. However, in contrast with the large amount of work devoted to the chemical synthesis of novel framework structures and characterisation of their functional properties, the field of MOF mechanics is still at an early stage (69-72). At present, there is very limited use of MOF materials in the commercial sector.

2.1 Overview of nanoindentation

The mechanical characterisation of MOFs has mostly relied on nanoindentation measurements, which allow for the possibility of testing very small samples, such as single crystals (73-76) thin films (77) or small monoliths (50, 52, 54).

Nanoindentation tests have been widely used to measure the elastic and fracture behaviour of solids and to examine the adhesion between coatings and substrates. In a traditional nanoindentation test, a hard tip whose mechanical properties are known (frequently made of a very hard material, i.e., diamond) is pressed into a sample whose properties are unknown. By analysing the indentation load-depth data as exemplified in Figure 2.1 it is possible to derive important properties of the sample, such as hardness (defined as the maximum load divided by the residual contact area) and the Young's modulus (which is a function of the contact stiffness, i.e., the slope of the indentation load-depth curve upon unloading).

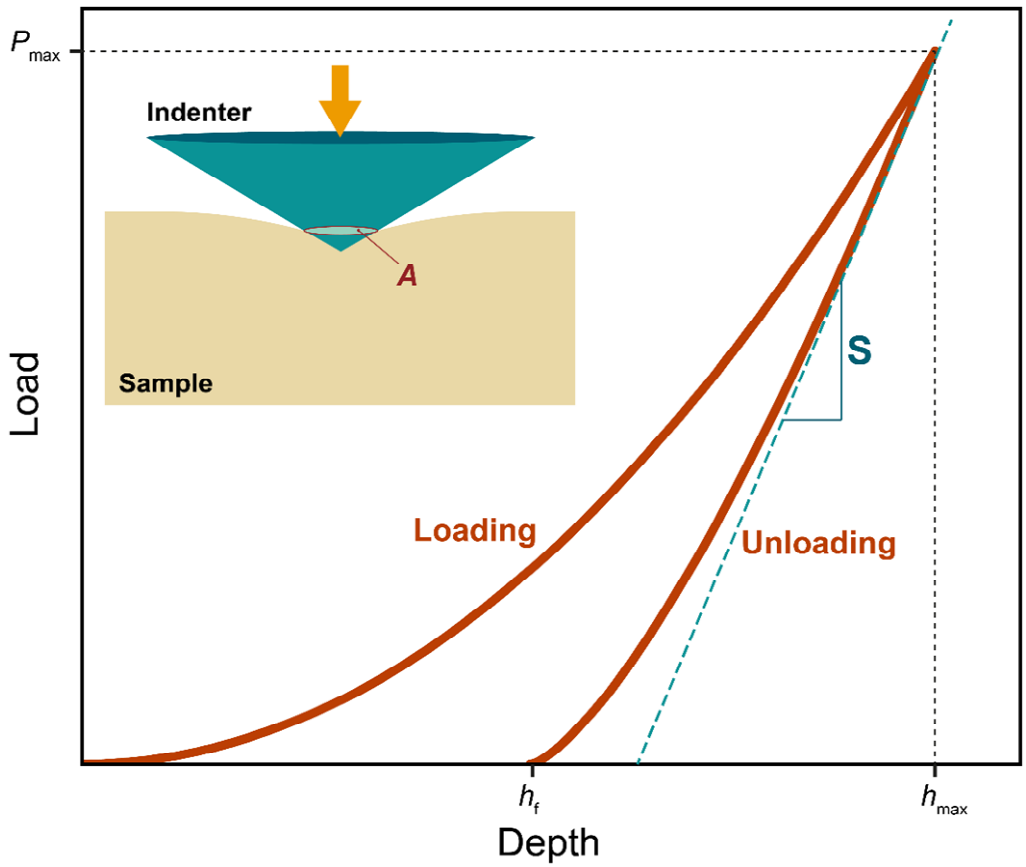

Figure 2.1 Schematic representation of load-depth (P–h) data for a nanoindentation experiment. The quantities shown are P_{max}, the peak indentation load; h_{max}, the indenter depth at peak load; h_f, the final depth of the contact impression after unloading and S, the initial unloading stiffness.

2.1.1 Indenter shapes

Nanoindentation tests can be performed with several indenter shapes. Hardness tests are usually made with spherical (Brinell), conical (Rockwell) and pyramidal (Vickers) indenters. The Berkovich indenter is used for small-scale indentations. The most common indenter types are the following:

- *Vickers*: a four-sided pyramid;
- *Berkovich*: a three-sided pyramid. This configuration allows the edges to meet more easily at a single point, rather than the inevitable line that occurs in the four-sided Vickers. This makes it the most suitable indenter for small-scale measurements. The tip radius is of the order of 50-100 nm;
- *Knoop*: a four-sided pyramidal indenter with two different face angles. Measurements of the unequal length of the diagonals of the residual impressions is useful for studying mechanical anisotropy;
- *Cube corner*: a three-sided pyramid with mutually perpendicular faces. The sharpness of the cube corner produces much higher stresses and strains in the area of the contact. This results in the formation of well-defined cracks around the indent in brittle materials, which can be used to measure fracture toughness at small scales;
- *Conical*: its main advantage is axial symmetry. Using specific values of semi-angle is possible to obtain contact areas equivalent to pyramidal indenters;
- *Spherical*: it provides a smooth transition from elastic to plastic contact. Particularly suitable for probing soft materials;

- *Flat punch*: can be used to determine viscoelastic properties.

2.1.2 Indentation load-depth data

The main goal of a nanoindentation test is to measure the Young's modulus and hardness of the specimen, by analysing the experimental load-depth data. A typical nanoindentation load-depth curve consists of two segments: elastic-plastic loading and elastic unloading (Figure 2.1). If no plastic deformation occurs, the two segments will overlap. The elastic modulus can be estimated by considering the unloading response, which is supposed to be fully elastic. Let us consider the simple case of a flat cylindrical punch, whose elastic load-depth relation is the following:

$$P = 2aE^*h \tag{2.1}$$

where a is the contact radius and E^* is the contact modulus. By taking the derivative one can arrive at an expression of the slope of the unloading segment, which corresponds to the stiffness (S):

$$S = \frac{dP}{dh} = 2aE^* = 2E^*\sqrt{\frac{A}{\pi}} \tag{2.2}$$

where A is the contact area. The same relation is valid for all axisymmetric indenters. In fact, as Doerner and Nix (78) observed, the initial part of the unloading curve is very well approximated by a straight line, since the contact area remains fairly constant. By measuring the initial unloading stiffness the modulus can thus be derived. Sneddon (79) studied the indentation problems of a homogeneous material by using Hankel's transforms. His results show that the load-depth

relationships for many simple punch geometries can conveniently be written as a generic power law:

$$P = kh^n \tag{2.3}$$

where k and n are constants. Values of the exponent n for some common punch geometries are $n = 1$ for flat cylinders, $n = 2$ for cones, $n = 1.5$ for spheres in the limit of small displacements, and $n = 1.5$ for paraboloids of revolution.

There are several factors affecting the nanondentation test data, such as thermal drift, instrument compliance, piling-up and sinking-in (i.e., deviations of actual contact area from the ideal one, as described in detail in Section 2.1.3.2) and surface roughness (80). Thermal drift may be due to creep of the sample or thermal contraction or expansion of the tip: both phenomena result in errors in the indentation depth readings. Instrument compliance can affect the contact stiffness; therefore, it needs to be measured and accounted for. These factors are usually automatically corrected for within most of the modern nanoindentation systems, without the need of further post-processing the raw data. Surface roughness is also a crucial issue, since it affects the contact area: this effect can be attenuated by increasing the indentation depth, resulting in a larger contact area.

2.1.3 Oliver and Pharr method

Instrumented Indentation Testing (IIT) (81) is a technique based on the method proposed by Oliver and Pharr (82), and can be considered a development of the classical hardness tests (Brinell, Vickers, *etc.*). The latter require only one measure of deformation (residual contact area) at one applied force, whereas during an IIT

test, force and indentation depth (i.e. P–h curves) are measured continuously as long as the indenter is in contact with the sample.

By analysing the load-depth curves recorded during the test, one can easily measure the contact modulus and hardness using the following relationships:

$$E^* = \frac{\sqrt{\pi}}{2}\frac{S}{\sqrt{A}} \tag{2.4}$$

$$H = \frac{P_{\max}}{A} \tag{2.5}$$

The projected contact area A is used in both equations 2.4 and 2.5. It is computed as a function of contact depth h_c (called "area function"):

$$A = f(h_c) \tag{2.6}$$

This function is determined by a process of calibration, consisting of the indentation of an isotropic material (such as fused silica) whose properties are known. In this way, by using equation 2.4 we can derive the area function by measuring the contact stiffness S. The contact depth h_c is given by:

$$h_c = h - \varepsilon\frac{P_{\max}}{S} \tag{2.7}$$

where ε is a constant depending on the indenter geometry (derived from Sneddon's elastic solution). For example, for a Berkovich indenter $\varepsilon = 0.72$.

In the appendix of their paper, Oliver and Pharr described an extension of their method, based on dynamic measurements, known as Continuous Stiffness Measurements (CSM) (83). This technique superimposes a small oscillation on the quasi-static force, using a frequency-specific amplifier to measure the response of the indenter. The benefits of CSM include:

- ability to measure mechanical properties as a continuous function of distance into the surface;
- ability to measure storage and loss modulus of polymers as a function of frequency;
- improved *in situ* surface detection;
- alternate imaging modes when the indentation system is used as a profilometer.

2.1.3.1 Corrections

In equation 2.4, crucial for nanoindentation analysis, a multiplicative correction factor is generally needed. In the literature, one can find different interpretations of such a correction factor: Hay *et al.* (84) refer to it as γ, which takes into account the elastic radial inward displacements; King (85) introduced the factor to correct for the fact that the indenter shape is not a perfect cone (β = 1.034 for a Berkovich indenter). These two effects can actually simultaneously coexist and thus, as proposed by Troyon *et al*. (86), this correction factor is $\alpha = \beta\gamma$. Therefore, equation 2.4 can be rewritten as:

$$E^* = \alpha \frac{\sqrt{\pi}}{2} \frac{S}{\sqrt{A}} \tag{2.8}$$

The correction factor has been demonstrated to depend on the tip rounding and also on the deformation of the indenter during indentation. It seems to increase with the tip radius and also with the elastic modulus of the measured materials.

2.1.3.2 Pile-up and sink-in

It is very important to stress that equations 2.2, 2.4, 2.7 were derived from a purely elastic solution, and how well they work for elastic/plastic indentation is not entirely clear. These equations turn out to be inadequate when pile-up or sink-in of material around the indenter is observed (Figure 2.2). When the indentation is purely elastic, the material always sinks in, while, if plasticity occurs, the material may either sink-in or pile-up. Since this has important effects on the contact area, it is not entirely surprising that the Oliver–Pharr method has been found to work well for hard ceramics, in which sink-in predominates, but significant errors can be encountered when the method is applied to soft metals that exhibit extensive pileup. The degree of pile-up and sink-in depends upon the Young's modulus to yield strength ratio ($\frac{E}{\sigma_Y}$) of the sample and the strain hardening exponent *n*:

- for materials with no strain hardening, a large $\frac{E}{\sigma_Y}$ generally translates into piling-up, while, when $\frac{E}{\sigma_Y}$ is low, sink-in is more likely to occur.
- for materials with an appreciable work-hardening sink-in is demonstrated to be predominant.

The finite element study of conical indentation of elastic-plastic materials carried out by Bolshakov *et al.* (87) have shown that the parameter $\frac{h_f}{h_{max}}$ (where h_{max} is the maximum indentation depth and h_f is the residual depth after unloading, as illustrated in Figure 2.1), which can be measured experimentally and correlates with the material parameters *E*, *n*, σ_Y, and *h*, which control indentation deformation, can be used as an indication of when pile-up is an important factor. Pile-up is significant

only when $\frac{h_f}{h_{max}} > 0.7$ and the material does not appreciably work harden. In such a case, disregarding the pileup can result in an error in the contact area of up to 60%. When $\frac{h_f}{h_{max}} < 0.7$, or in all materials that moderately work harden, pileup is not significant, and the Oliver–Pharr's data analysis method is supposed to give reliable results.

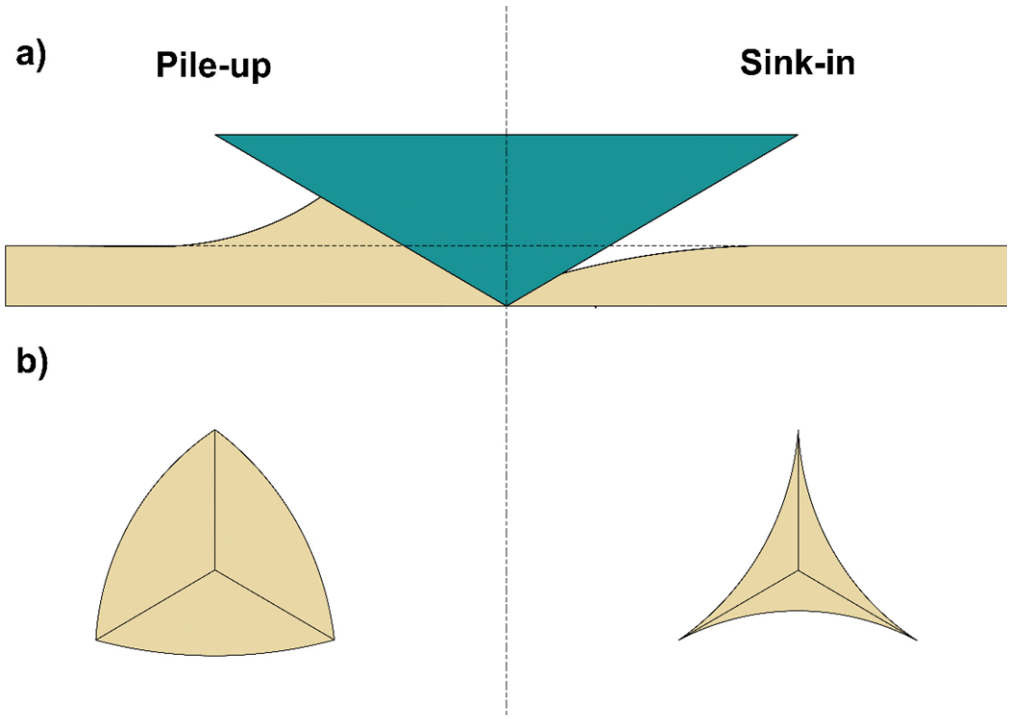

Figure 2.2 Effect of piling-up and sinking-in on the contact area. (a) Cross-sectional view; (b) plan view.

2.1.4 Detection of non-linear events

Nanoindentation is performed on a wide range of materials, from soft polymers to hard coatings. The shape of the load-depth curve, in addition to elastic modulus and hardness, can often give important insights about non-linear events such as plasticity, phase transition, cracking, creep, and delamination of films (Figure 2.3) (80). For example, a sudden depth excursion upon loading, known as "pop-in"

(Figure 2.3e), corresponds to the elastic–plastic transition, i.e., yielding and the onset of plasticity. If the sample is susceptible to stress-induced phase transition, a sudden depth jump at constant load occurs, this time upon unloading. This kind of event, called ”pop-out” (Figure 2.3d) occurs due to sudden changes in the volume of the material, associated with stress-induced phase transformation.

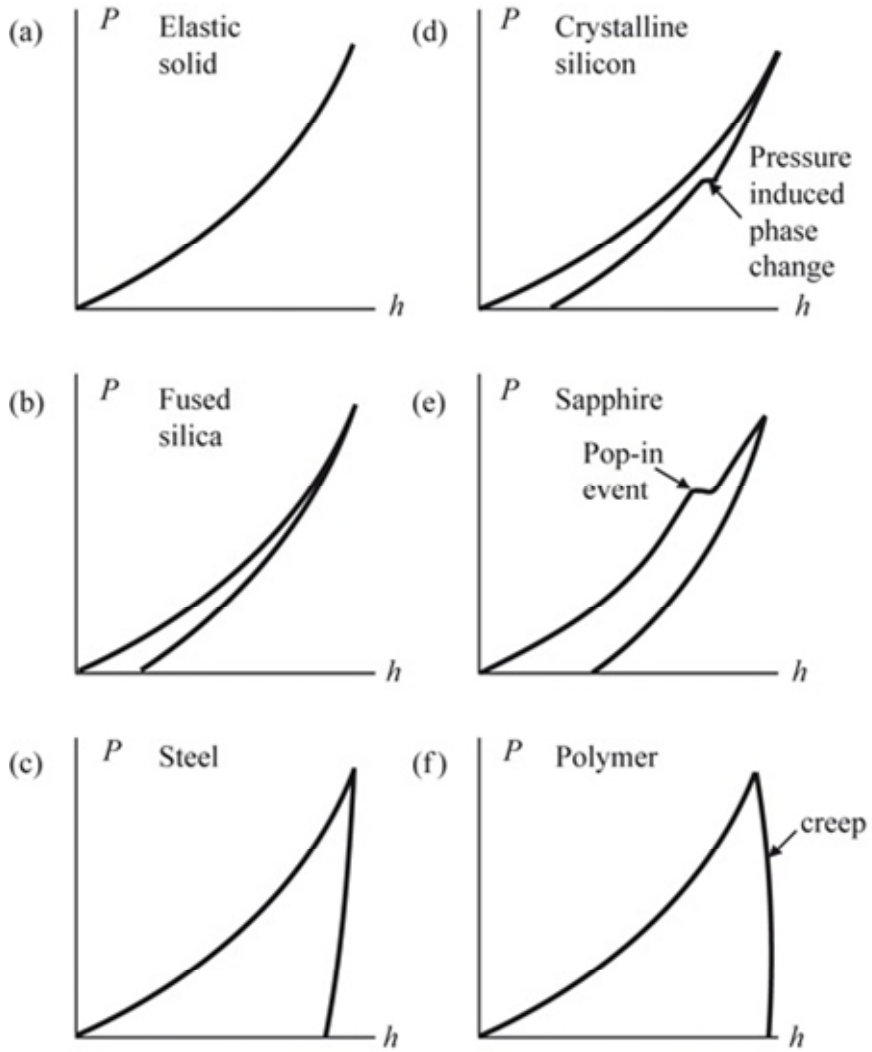

Figure 2.3: Schematic of some commonly observed phenomena in nanoindentation curves for different materials. (a) Fully elastic solid, (b) brittle solid, (c) ductile solid, (d) crystalline solid exhibiting stress-induced phase transition, causing a ”pop-out” on the curve, (e) brittle solid with cracking during loading, resulting in a ”pop-in” on the loading curve, and (f) polymer exhibiting creep, resulting in a negative slope of unloading test segment. Adapted with permission from (80).

2.1.5 Onset of plastic yield

Let us consider the simple case of the Hertzian contact between a sphere of radius *R* and the surface of a half-space (88):

$$P = \frac{4}{3} E^* R^{\frac{1}{2}} h^{\frac{3}{2}} \tag{2.9}$$

Dividing the load by the contact area ($A = \pi a^2 = \pi R h$) we obtain the expression of the mean contact pressure:

$$p_m = \frac{4}{3\pi} \frac{E^*}{R^{\frac{1}{2}}} h^{\frac{1}{2}} \tag{2.10}$$

which is basically the hardness in the case of a Hertzian contact (fully elastic). In order to define a condition for the onset of yielding, let us consider the Tresca criterion, which states that yielding ensues when the maximum shear stress approaches a critical shear stress $k = \frac{\sigma_Y}{2}$:

$$\tau_{max} = \frac{1}{2}(\sigma_1 - \sigma_3) \geq k \tag{2.11}$$

Where σ_1 and σ_3 represents the maximum and minimum principal stresses respectively. As demonstrated by Johnson (89), for the Hertzian contact:

$$\tau_{max} = 0.47 p_m \text{ at } z = 0.57a \tag{2.12}$$

(computed for $\nu = 0.3$) which means that yielding ensues initially below the surface and the plastic zone is surrounded by elastic material. Now we can write the Tresca criterion as follows:

$$\tau_{max} \approx \frac{p_m}{2} \geq \frac{\sigma_Y}{2} \tag{2.13}$$

By substituting equation 2.10 in equation 2.13 we get:

$$\frac{4}{3\pi}\frac{E^*}{R^{\frac{1}{2}}}h^{\frac{1}{2}} \geq \sigma_Y \tag{2.14}$$

which represents the condition to be satisfied in order to initiate plastic flow. When full plasticity is achieved, experiments shows that the mean pressure p_m is directly proportional to the yield strength σ_Y. Given that the hardness H measured by nanoindentation is nothing but the mean pressure itself, we can write (90):

$$H = C\sigma_Y \tag{2.15}$$

The constant C is called the "constraint factor" and it depends upon material, indenter shape and other experimental parameters. For metals and other materials with a large value of the ratio $\frac{E}{\sigma_Y}$, $C \approx 3$, while for low values of $\frac{E}{\sigma_Y}$ (*e.g.*, glasses), $C \approx 1.5$.

2.1.6 Indentation of elastically anisotropic materials

The Oliver and Pharr method is based on the hypothesis that the sample is elastically isotropic. This assumption allows to easily derive the contact modulus, by modelling the first part of the unloading curve as a contact problem for a flat punch (equation 2.1).

It goes without saying that, in some cases, this could represent a quite strong approximation, for example when dealing with single crystals. Several theoretical models have been developed to obtain the contact modulus of an anisotropic sample. Vlassak and Nix (91, 92) obtained simple expressions for the indentation modulus for a flat punch and for cases of indentation by a parabola of revolution

with material symmetries that produce circular contact area. Later, the same approach has been extended by Swadener and Pharr (93) to spherical and conical indenters. The model proposed by Vlassak *et al.* (94) can be considered the most general, valid for materials with any degree of anisotropy and for indenters of an arbitrary shape. This model provides an exact solution for the contact modulus, as a function of the elastic constants of the anisotropic materials.

2.2 Nanoindentation of MOFs

2.2.1 Young's modulus and hardness

The majority of the mechanical characterisation of MOFs to date is based on nanoindentation experiments, particularly of Young's modulus and hardness. To put these findings into perspective and contrast the mechanical performances of MOFs with those of more traditional engineering materials like metals, ceramics, and polymers, material properties charts, also known as Ashby plots, are particularly helpful. In terms of Young's modulus and hardness (Figure 2.4), MOFs place themselves at the intersection between polymers, which are purely organic, and ceramics that are purely inorganic.

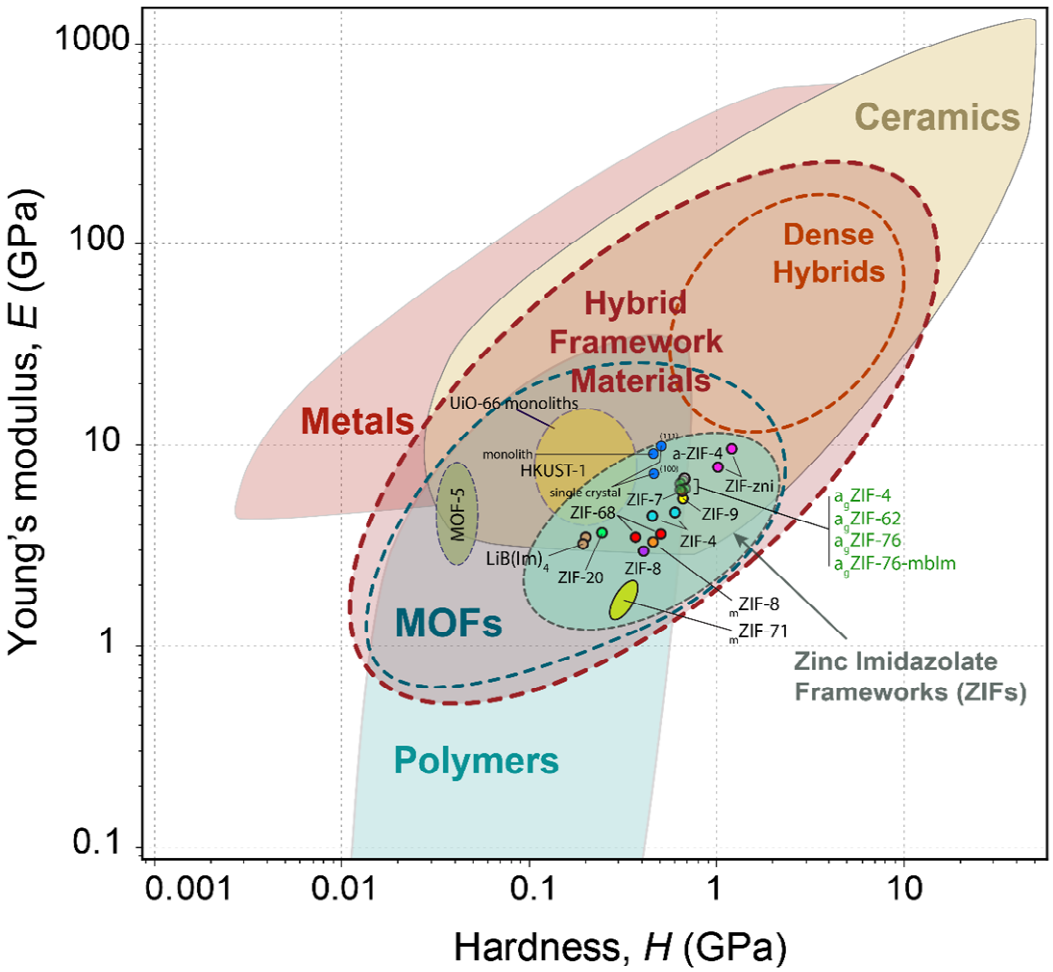

Figure 2.4 Young's modulus vs hardness (*E*-*H*) material properties chart of MOFs and other common classes of materials, adapted with permission from (72). Representative MOFs include ZIFs (single crystals (74), monoliths (13, 52) and glasses (95, 96)), HKUST-1 (single crystals (97) and monoliths (50)), UiO-66 monoliths (54), lithium-boron analogue of ZIF [$LiB(Im)_4$], melt-quenched MOF glasses (95), and MOF-5 (98).

One of the first studies reporting the mechanical properties of a MOF material were carried out by Bahr *et al.* (98). They characterised the MOF-5 crystal, a zinc-based framework, and determined a Young's modulus of 7.9 GPa for the (100)-oriented face. However, this value was about three times lower than the one predicted by density functional theory (DFT) calculations. This discrepancy between computations and experiments, is considered to be a consequence of

physical degradation of the crystal, resulting from the poor water stability of MOF-5. One of the classes of MOFs most suitable for nanoindentation is represented by zeolitic imidazolate frameworks (ZIFs), nanoporous materials comprised of tetrahedrally-coordinated single-ion nodes (i.e., Zn^{2+} or Co^{2+}) and imidazole (ImH) derived organic linkers (28). This is due to their ease of synthesis, stability under ambient conditions and commercial availability. Tan *et al.* (74) performed nanoindentation measurements on different types of ZIFs (Figure 2.5). They were able to correlate the mechanical responses with the different ZIF structures (given by the different combinations of organic and inorganic building blocks): for example, crystals with a higher porosity (Figure 2.5c), like ZIF-8, ZIF-20 and ZIF-68, can sustain lower loads and show a smaller elastic recovery, compared to the structure characterised by smaller pore sizes. In the same work, they further illustrate the effect of ligands on ZIFs stiffness. In fact, if frameworks of the same topology are considered, the ones incorporating bulky imidazole ligands will exhibit a greater stiffness. The aromatic linkers tend to fill up the pores, inducing steric hindrance and additional short-range dispersion interactions resulting in the stiffening of the structure. As an example, the elastic properties of ZIF-7, ZIF-8 and ZIF-9 were considered. They all show the same structural topology, but ZIF-7 and ZIF-9 exhibit a Young's modulus which is twice higher than that of ZIF-8. In fact, ZIF-7 and ZIF-9's linker, 2-benzimidazole (bImH), is bulkier compared to 2-methylimidazolate (mIm) of ZIF-8 (Figure 2.5d-e). Furthermore, it is worth noticing that ZIF-7 and ZIF-9 exhibit a very similar elastic behaviour despite having different metals (Zn and Co respectively). This means that

the metal sites serve only as compliant nodes for connecting linkages (confirmed to be the case in (75)).

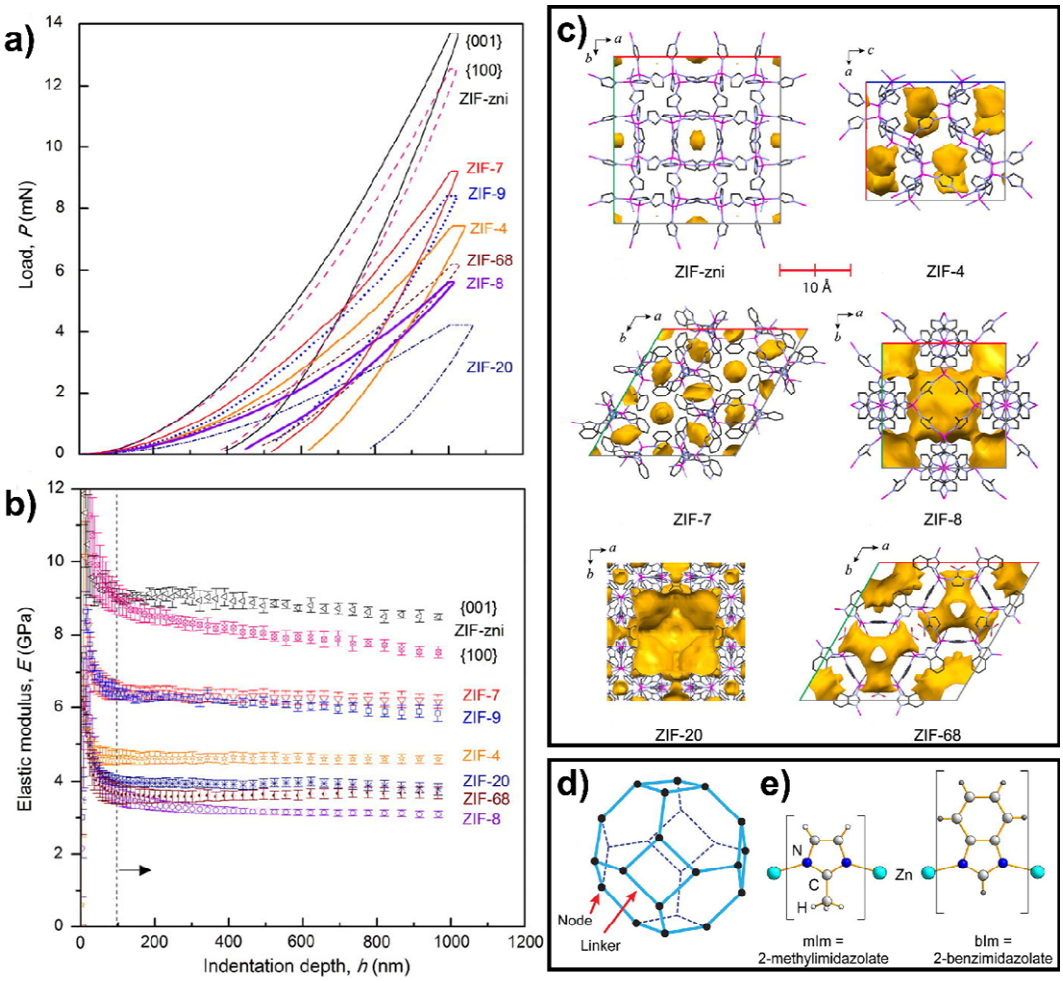

Figure 2.5 a) Load-depth curves from Berkovich nanoindentation of several ZIF single crystals. b) Young's modulus-depth curves resulting from CSM measurements. c) Porosity of some representative ZIF structures, calculated as solvent accessible volume (SAV). d) Schematic of the sodalite cage structure of ZIF-7, ZIF-8 and ZIF-9 (left), where the node are Zn(II) or Co(II) and the linkers are substituted imidazolates. e) Zn-mIm-Zn and Zn-bIm-Zn linkages of ZIF-8 and ZIF-7, respectively. Adapted with permission form (74), Copyright 2010 National Academy of Sciences.

The effect of linkers on the elastic properties was explored also by Bennett *et al.* (99), who observed that the Young's modulus of ZIF-zni is three times greater

than that of its Boron Imidazolate Framework (BIF) analogue (alternate Zn cations are replaced by Li^+ and B^+ respectively), $LiB(Im)_4$. Given that the two frameworks are isostructural, the difference in stiffness is explained by the fact that the Zn-Im-Zn bonds of ZIF-zni are considerably stiffer than the Li-Im-Li linkages of $LiB(Im)_4$. In a following study, Tan and co-workers (75) calculated the single crystal elastic constants of the cubic ZIF-8, estimating its degree of anisotropy. These constants were measured by Brillouin scattering and confirmed by nanoindentation tests and theoretical *ab initio* calculations. Tian *et al.* (52) synthesised mechanically and chemically robust ZIF-8 monoliths and measured their mechanical properties by nanoindentation, finding a slightly higher elastic modulus, with respect to their single crystal counterpart.

Nanoindentation is also very convenient tool for measuring hardness of single crystals, monoliths, or thin layers. The hardness of a material is strongly dependent on test parameters such as tip shape, applied load and indentation depth. However, by comparing the hardness values of different materials, it is possible to get insights about the inelastic behaviour. Amongst all the measured MOFs, MOF-5 is surely the softest, with hardness (measured *via* nanoindentation) of about 40 MPa (98), which is comparable to some soft polymers. Such a low hardness could be a result of the low shear modulus, which makes the framework very weak against the shear deformation induced by the indenter tip. At the same time, the low hardness could be a result of framework degradation, given the poor water stability of MOF-5. Hardness of ZIFs has also been widely studied (74): an inverse correlation with porosity/density is evident. The frameworks with a higher accessible void

space, such as ZIF-8, ZIF-20, and ZIF-68 exhibit a low hardness (200-500 MPa) if compared to denser framework like ZIF-zni ($H \approx 1.1$ GPa). It is noteworthy that the BIF analogue of ZIF-zni, $LiB(Im)_4$ is 10 times softer ($H \approx 100$ *MPa*). This, similarly to what is observed for stiffness, can be attributed to the higher flexibility of LiN_4 tetrahedra.

As described in section 2.1.1, the plastic behaviour of a material can be observed *via* spherical indentation. Plasticity in hybrid frameworks is often very limited, due to strong directional bonding (74). However, in polycrystalline structures, like monoliths, plastic deformations may arise, resulting from mechanisms such as grain boundary sliding (GBS). In one of the few works in literature exploring plastic deformation of hybrid framework material (73), the elastic-plastic transition of two copper phosphonoacetate polymorphs was studied. The yield strength was observed to vary with the crystal orientation, resulting also in different amount of pile-up in the residual indents associated with cracking.

Nanoindentation has also been used to investigate the mechanical properties of MOF polycrystalline thin films and surface coatings. Bundschuh *et al*. (77) prepared a (100)-oriented epitaxial film made of HKUST-1 crystals with a thickness of around 1 μm, grown on a gold-coated silicon substrate. The surface roughness of the epitaxial film was determined to be 10-15 nm, which made it suitable for nanoindentation without additional surface processing. It was observed that the indentation modulus increased significantly as a function of indentation depth, suggesting a substantial substrate influence. In order to reduce the substrate contribution, an average of the CSM measurements within 10% of the surface

penetration depth was considered, resulting in an indentation modulus of 11.4 ± 2 GPa. The Young's modulus of the coating was then found to be E = 9.3 GPa, assuming elastic isotropy and using a theoretical Poisson's ratio of ν = 0.433. This result is in contrast with theoretical DFT calculations (100), which predicted it to be three times smaller. Such a discrepancy could be explained by the contributions of grain boundaries in epitaxial films and the hard substrate effect. It is interesting to note that the Young's modulus of the epitaxial film has a magnitude that is similar to that of a monolithic HKUST-1 (9.3 ± 0.3 GPa (50)), composed of a random aggregation of nanocrystals.

Regarding monolithic MOFs, only a few nanoindentation studies have been reported to date, including HKUST-1, ZIF-8, and UiO-66. Their findings are plotted in Figure 2.4. Particularly noteworthy is the HKUST-1 monolith proposed by Tian *et al.* (101), obtained by using a sol-gel synthesis process (Figure 2.6), characterised by a record-breaking capacity for methane storage. This outstanding property results from the effective packing and densification of the nanosized HKUST-1 crystals that make up the monolith. Its Young's modulus, measured by Berkovich nanoindentation, was found to be 9.3 ± 0.3 GPa (Figure 2.6c), which resembles the stiffness value predicted by theoretical DFT (E = 8.1 GPa (100)). The monolith hardness (H = 460 MPa) is about 130% greater than the aforementioned HKUST-1 epitaxial film (H = 200 MPa), as illustrated in Figure 2.6d. The findings imply that the high bulk density of the HKUST-1 monolith ($P_{monolith}$ = 1.06 g cm^{-3} vs. $P_{crystal}$ = 0.883 g cm^{-3}) not only improves the volumetric adsorption capability but

also the mechanical resilience, as suggested by the absence of cracking in the vicinity of the indent's corners (Figure 2.6f).

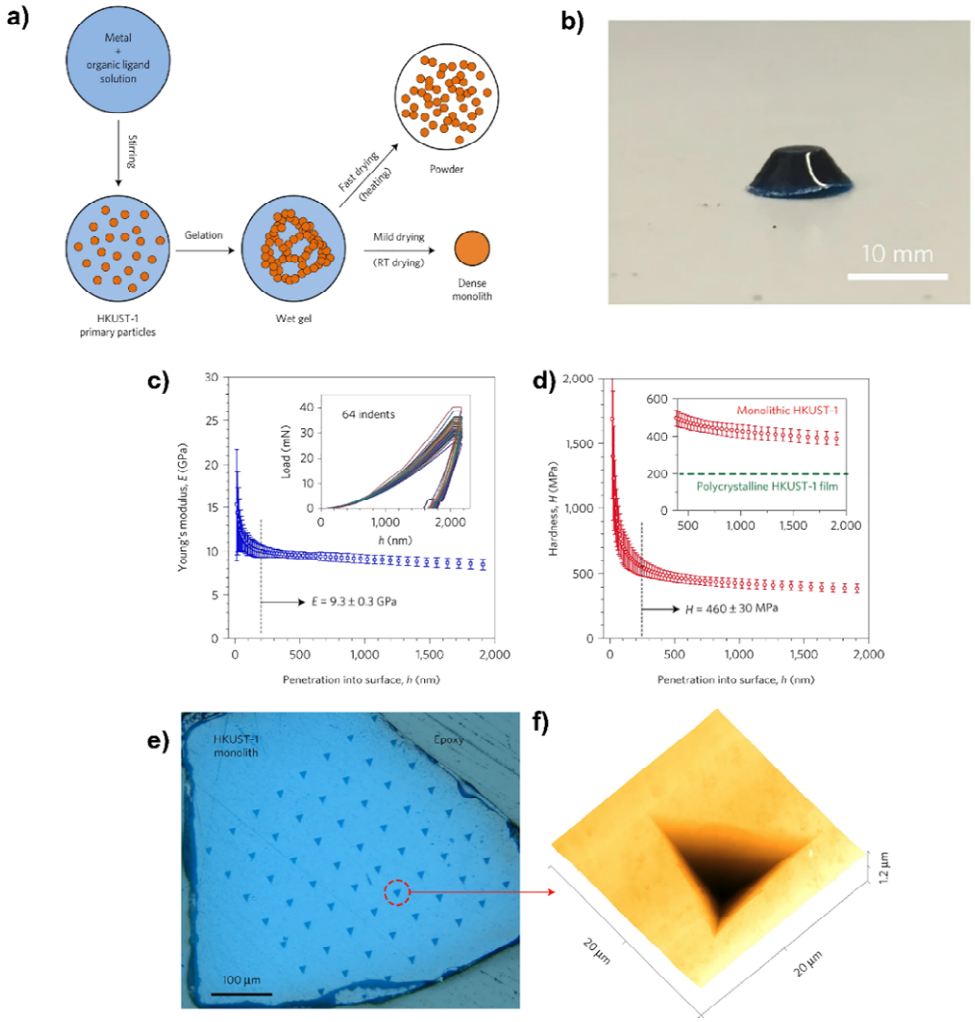

Figure 2.6 a) Schematic of the sol–gel process, leveraged to synthesise a dense monolith under mild drying conditions, whereas powders are obtained when the wet gel is dried at higher temperature or vacuum. b) Optical image of the monolithic HKUST-1. c) Young's modulus and b) hardness as a function of indentation depth, resulting from CSM during nanoindentation of the HKUST-1 monolith. e) Array of residual indents on the monolith, mounted in epoxy resin and polished. f) AFM height topography of a representative residual indent, no cracks are observed. Adapted with permission from (50).

2.2.2 Fracture toughness

Despite the fact that MOFs often show a brittle nature, to the best of my knowledge, before the work described in this thesis (13, 51), there has been only one attempt to

measure the indentation fracture toughness of hybrid materials by nanoindentation (73). In this work, nanoindentation was used to initiate cracks in CuPA dense frameworks, used to estimate the fracture toughness of different crystal facets, which was reported in the range of 0.08 - 0.33 MPa $m^{0.5}$. A more detailed overview of nanoindentation-based fracture toughness measurements is given in Chapter 5. However, alternative techniques have been explored. To *et al.* (102) recently measured the fracture toughness of a MOF glass (namely ZIF-62) using single-edge pre-cracked beam method. They determined a value of approximately 0.1 MPa $m^{0.5}$. The indentation fracture behaviour of ZIF-62 glass was further explored by Stepniewska *et al.* (103), who identified shear bands as the principal cracking mechanism. In a recent work of Zeng *et al.* (104) micropillar splitting technique was employed to estimate the fracture toughness of HKUST-1 single crystals on the [100]- and [111]-oriented faces.

In a fracture toughness vs. Young's modulus Ashby plot (Figure 2.7), hybrid framework materials and MOF can be seen to occupy the domain located between polymers and ceramics.

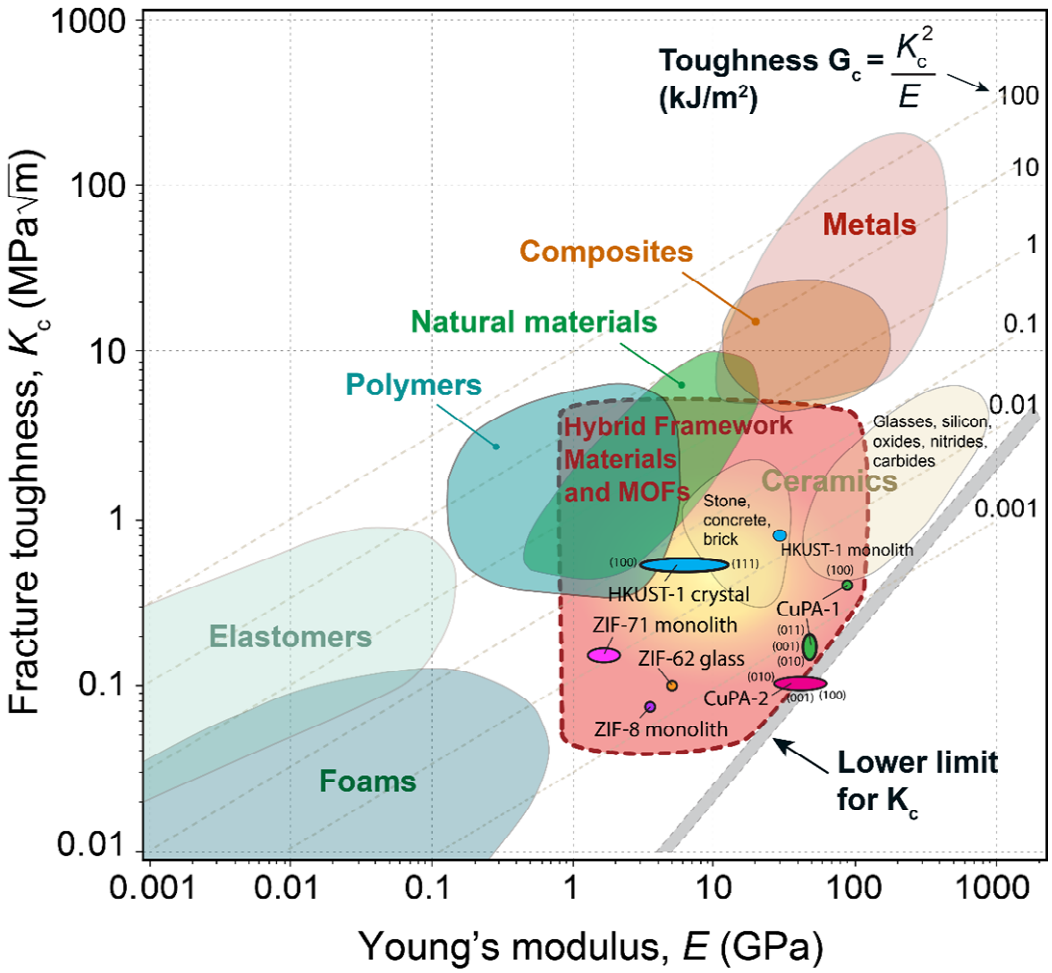

Figure 2.7 Fracture toughness vs Young's modulus (K_c-E) material properties chart of MOFs and other common classes of materials, adapted with permission from (72). Representative MOFs and hybrid framework materials include ZIF monoliths (13), HKUST-1 (single crystals (104) and monoliths (51)), melt-quenched ZIF-62 glass (102) and CuPA dense frameworks (73).

2.3 Other techniques

Besides nanoindentation, other techniques for measuring mechanical properties of MOFs, such as high-pressure crystallography, AFM and Brillouin spectroscopy have been explored in recent years.

High-pressure crystallography is suitable for single crystals or powder specimens. A hydrostatic pressure is applied to the specimen in a diamond anvil cell, inducing change in lattice volume. The latter, detected by high-pressure X-ray diffraction, allows to determine the bulk modulus (K) by using the Birch-Murnaghan equation of state (105). Exploiting this approach, Spencer *et al.* (106) measured the bulk modulus of ZIF-zni (which is the densest of the ZIFs family), finding a value of $K \approx 14$ *GPa*. Chapman *et al.* (107) estimated the bulk modulus of the lower-density ZIF-8 to be $K \approx 6.5$ *GPa*. Both the materials undergo phase transition at high pressures: ZIF-zni maintains its original tetragonal crystalline structure while ZIF-8, given its lower modulus, exhibits a larger volumetric change, to which follows structural amorphization.

Brillouin spectroscopy was used to explore elasticity of ZIF-8 (75). This technique, based on Brillouin scattering and subsequent solution of Christoffel's matrix (108) enables a complete measurement of the elastic tensor of the material. The main drawback of this method, is that it requires large single crystals as specimens, precluding the study of polycrystalline morphologies. To avoid this, bimodal amplitude modulated frequency modulated AFM was employed to measure the elastic properties of a series of MOF nanoparticles (100-500 nm) (109). AFM nanoindentation, which allows smaller force and displacement sensitivities with respect to conventional nanoindentation, have been employed to probe the local mechanical properties of small MOF crystal and thin films (110, 111).

Nanoindentation set-ups have been used also in lateral mode to perform nanoscratch experiments. This type of experiment enables to characterise the

abrasion resistance and the adhesion to different substrates, particularly important for thin films (112, 113).

2.4 Computer modelling

2.4.1 Finite element simulations of nanoindentation tests

The indentation of elastic materials is well known, and, for whatever indenter shape, relatively simple analytical solutions exist. When plasticity is considered, however, theoretical approaches are very difficult to derive, given the large number of parameters involved in the analysis (114, 115). In this case, finite element analysis represents a very valuable tool, allowing to get a good approximation of the stress field and contact area (84, 87).

Finite element modelling is very important in the study of complex samples such as thin films (116) or implanted layers (117), enabling the determination of mechanical properties for cases where the conventional analytical treatments fail. To the best of my knowledge, the only attempt to model a nanoindentation test of a MOF sample with the FEM has been made by Zeng *et al*. (110), who simulated the AFM nanoindentation of a stack of CuBDC nanosheets, in order to study the interfacial debonding.

2.4.2 Theoretical calculations

Atomistic modelling represents an important tool in the understanding of MOF structures and properties, which often could be challenging to observe experimentally (118). A lot of work has been done on the adsorption and diffusion

properties while the mechanical properties modelling is still at his infancy (70, 119). Most of the existing work is limited to elasticity, but initial efforts on plasticity have been recently reported (120). Density functional theory (DFT) calculations were employed to build the elastic tensor (C_{ij}) of some MOF single crystals. This approach allows to study the elastic anisotropy of such structures (75, 121). Flexible frameworks exhibit a very large anisotropy, with a ratio between the most rigid and weakest directions that can reach 400:1 (121). A low shear modulus is also observed (75, 121), implying a high probability of shear-induced structural failure. DFT calculations unveiled some anomalous elastic responses such as auxeticity (100). Recently, Banlusan *et al.* (122) have simulated the shock wave absorption of ZIF-8, by means of a molecular dynamics approach. The authors observed a linear decrease of the energy absorbed with the reduction of free volume fraction (i.e., increase of pore volume occupied by guest molecules). Simulations of defective frameworks have allowed to elucidate the effect of structural defects on the mechanical properties of MOF crystals. The elastic constants of an ideal framework can be compared with those obtained by introducing different types of defects in the simulation, as reported by Möslein *et al.* (123) and Thornton *et al.* (124) for ZIF-8 and UiO-66 frameworks, respectively.

3 Materials and Methods

3.1 Sample preparation

3.1.1 Synthesis of sol-gel MOF monoliths

The sol-gel monoliths studied in this thesis were synthesised by leveraging the high concentration reaction (HCR) approach (63). The organic linker is rapidly deprotonated, favouring the formation of metal-organic clusters (nucleation sites). This leads to gelation, given the small size of the resulting nanocrystals (17). The deprotonation was achieved by employing the base triethylamine (NEt_3), with the exception of MOF-808 monolith, for which formic acid was used as a modulator. All the gels were thoroughly washed before drying, to allow removal of excess reactants.

A schematic representation of the synthesis process (for the case of ZIF-8) is provided in Figure 3.1.

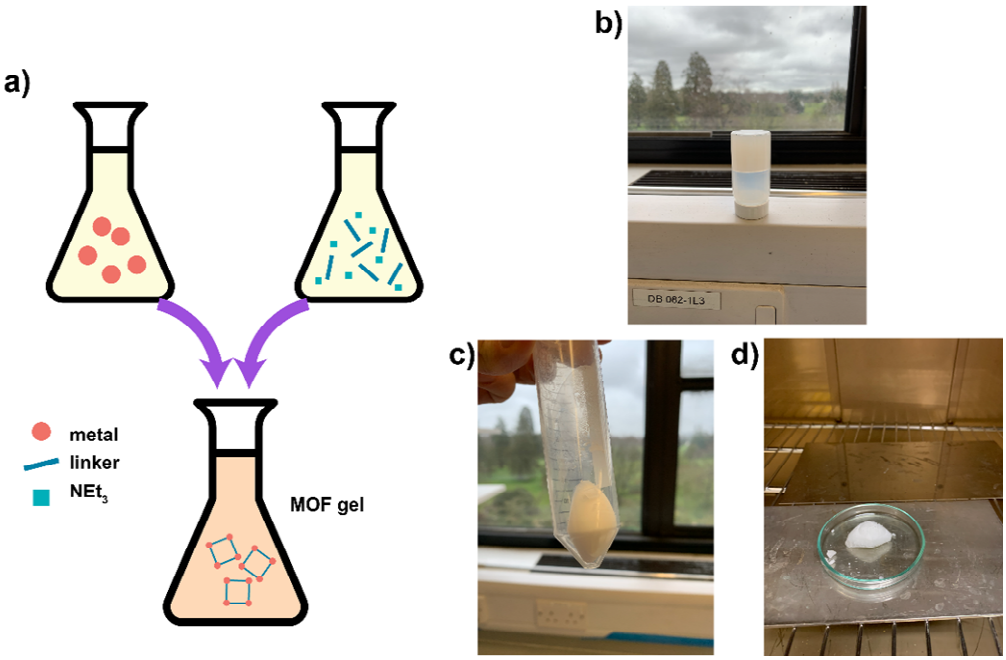

Figure 3.1 Synthesis of ZIF-8 monoliths. a) Schematic representation of the one-pot synthesis approach employed to construct the crystalline framework. b) Non-flowing gel obtained right after mixing the metal and linker solutions. c) Monolith obtained after 24 h slow drying under the fume cupboard. d) Monolith after additional 48 h drying at room temperature.

The synthesis routes used for each of the monoliths are listed below:

- ***ZIF-8 monoliths*** ($Zn(mIm)_2$): 0.595 g of zinc nitrate hexahydrate ($Zn(NO_3)_2 \cdot 6H_2O$) and 0.493 g of 2-methylimidazole (mImH) were dissolved in 9 mL of dimethylformamide (DMF) each and stirred for 5 minutes. Then, 0.837 mL of NEt_3 were added to the linker solution. Subsequently, the two solutions were combined in a 50 mL vial, where a gel was promptly formed. The molar ratio of $Zn(NO_3)_2 \cdot 6H_2O$: mIm : DMF : NEt_3 used was 1 : 3 : 116 : 3. The mixture was sonicated for 5 minutes and then washed three times, in 50 mL of DMF, methanol (MeOH) and acetonitrile (MeCN), respectively, followed by centrifugation at 8000 rpm.

The collected solid was dried slowly at room temperature (RT ~25 °C) for 3 days under the fume cupboard to yield monoliths.

- ***ZIF-71*** ($Zn(dcIm)_2$): the same procedure used for ZIF-8 monoliths was employed, starting from 0.439 g of zinc acetate dihydrate ($Zn(CH_3CO_2)_2 \cdot 2H2O$) and 0.822 g of 4,5-dichloroimidazole (dcImH). The compound was washed three times in MeOH.
- ***HKUST-1 (Cu_3BTC_2) monoliths:*** 300 mg of benzene-1,3,5-tricarboxylic acid (BTC) were dissolved in 10 mL of ethanol and subsequently 0.519 mL of Net_3 were added to the solution. 270 mg of copper nitrate were dissolved in 10 mL of EtOH and added to the linker solution. The resulting solution was stirred for 15 minutes and washed three times in ethanol (EtOH). A gel was collected and dried at RT for 2 days, yielding millimeter-sized "glassy" monoliths.
- ***MIL-68(In) monoliths:*** 9 mL DMF solution of 797 mg 1,4-benzenedicarboxylic acid (BDC) plus NEt_3 (9.6 mmol) were dissolved together. After that, 9 mL DMF solution of 1444 mg indium nitrate was immediately added into the mixture. Then the product was washed thoroughly 4 times (2 times with DMF, 2 times with MeOH). The nanocrystals of MIL-68(In) were separated from the suspension by centrifugation at 8,000 rpm for 10 mins and the excess solvent decanted. The obtained material was dried at room temperature for 3 days to yield monoliths.

- ***MOF-808 monoliths:*** 210 mg of benzene-1,3,5-tricarboxylic acid (BTC) and 970 mg of zirconyl chloride octahydrate were dissolved in a DMF/formic acid (30 mL + 30 mL) mixture, then transferred to a glass reagent bottle and heated at 130 °C for two days. The solution was centrifuged, and the collected material was washed four times with DMF. The resulting compound was then solvent exchanged by soaking in 100 mL of acetone for four days, with the solvent being replaced twice per day. The acetone-exchanged sample was finally evacuated at room temperature for 24 h and activated at 150 °C for 24 h to yield the monoliths.

The chemical reactions involved in the formation of each framework are illustrated in Scheme 1.

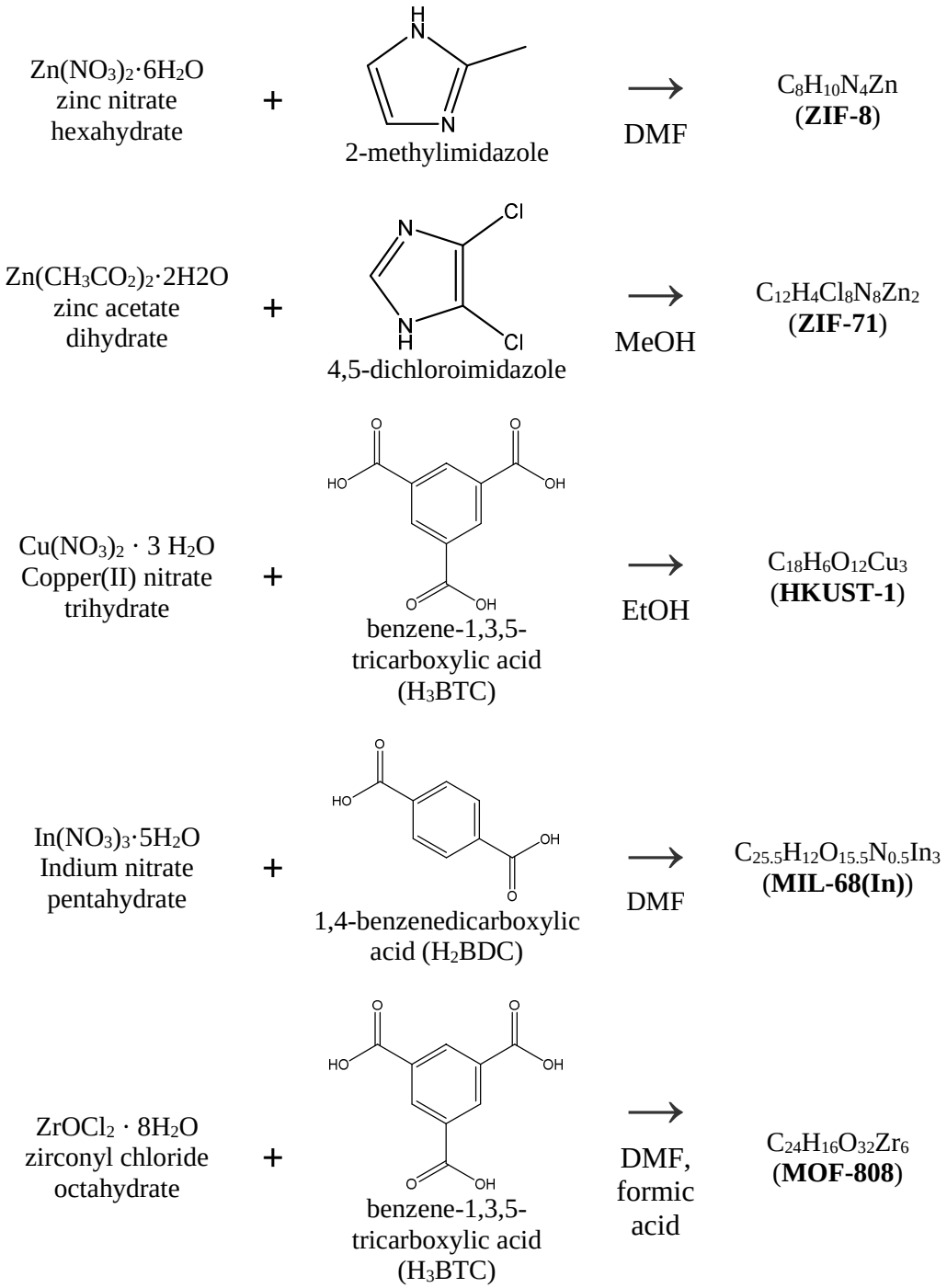

Scheme 1. Schematic of the chemical reactions taking place in the formation of the MOFs monoliths.

3.1.2 Preparation of drop-casted sample for AFM characterisation

A small quantity of gel (~ 1 mL) was pipetted out of the vial just before drying and diluted with copious amount of solvent (~20 mL), yielding a dispersion of nanocrystals. The dispersion was then drop casted on a silicon wafer (~ 1 cm × 1 cm), which was carefully wiped to remove dust and other surface impurities beforehand. Subsequently, the silicon chip was dried under a fume hood. This type of drop-casted samples was used to characterise the morphology and size of the single nanocrystals forming the gels under the AFM.

3.1.3 Preparation of nanoindentation sample

The dried monoliths were cold mounted in epoxy resin (Struers Epofix), using cylindrical moulds. The resulting samples are then carefully polished, with sandpapers and then diamond suspensions of decreasing grain size (namely 3 μm, 1 μm, and 0.1 μm) until the surface finishing was relatively smooth and scratch free. The thickness of the epoxy cylinders was limited to 5 mm *ca.*, to allow the characterisation of the indented samples with AFM, TFM and nanoFTIR. Nanoindentation tests required these thin discs to be fixed to aluminium cylindric stubs (matching the size of the nanoindenter sample holders) with thermoplastic wax.

3.2 Materials characterisation

3.2.1 X-ray diffraction (XRD)

X-ray diffraction allows to assess the crystallinity and molecular structure of solid samples and was used to confirm the crystallinity of the synthesised MOF samples. In a nutshell, the crystalline structure diffracts a beam of incident X-rays into many specific directions. The angles and intensities of these diffracted beams are measured and the spacing between the atomic planes is calculated using Bragg's law. For further details on XRD characterisation of nanomaterials, the readers may consult these references (125, 126).

Powder samples obtained by manually grinding the monoliths were analysed by XRD using a Rigaku MiniFlex diffractometer (Cu Kα source, 1.541 Å).

3.2.2 Attenuated total reflection fourier transform infrared spectroscopy (ATR-FTIR)

ATR-FTIR measurements on bulk materials allows to identify chemical substances or functional groups. It was used to verify the chemical fingerprint of the samples in the mid-infrared region.

The measurements were performed using a ThermoFisher Scientific Nicolet iS10 FTIR spectrometer with a spectral resolution of 4 cm^{-1}.

3.2.3 Atomic force microscopy (AFM)

The surface topography of the monoliths and the drop-casted nanocrystals and aggregates were measured by atomic force microscopy (AFM), implemented in a

neaSNOM instrument (neaspec GmbH) under the tapping-mode. A Scout350 (NuNano) probe was employed, with a nominal tip radius of 5 nm and a resonant frequency of 350 kHz.

3.2.4 Tip force microscopy (TFM)

TFM is an extension of AFM, which enables the characterisation of nanomechanical local properties of the sample along with the topography. The TFM mode extends the capabilities of AFM, allowing to image properties such as local stiffness and adhesion, resulting in high contrast images (127-129).

Figure 3.2 provides a representation of how TFM works. In Figure 3.2a, the dotted line represents the modulation voltage while the straight line is the force signal. At the starting point, the tip is well above the sample surface. Moving closer to the surface, the tip snaps into contact due to the attractive force acting between the tip and the sample surface. The piezo pushes the tip further towards the sample and the repulsive force reaches a maximum. As the piezo pulls back, the repulsive force gets smaller, and the force signal changes sign (from repulsive to attractive). Finally, the tip loses contact and the probe is free to oscillate. Once the oscillation is damped towards the baseline, the cycle starts again. The arrows indicate the points where the baseline, adhesion, stiffness, and max force are taken. From the signal in Figure 3.2a it is possible to extrapolate force-displacement curves (Figure 3.2b), from which material properties such as stiffness, adhesion and energy dissipation can be calculated pixel by pixel, obtaining maps like the ones shown in Figure 3.2c.

These types of maps were determined for ZIF-8 and ZIF-71 monoliths (13), using the s-SNOM instrument (Neaspec GmbH), operating under the contact mode. An Arrow-NCR probe (NanoWorld) was used, with a nominal tip radius of <10 nm and a resonance frequency of 285 kHz.

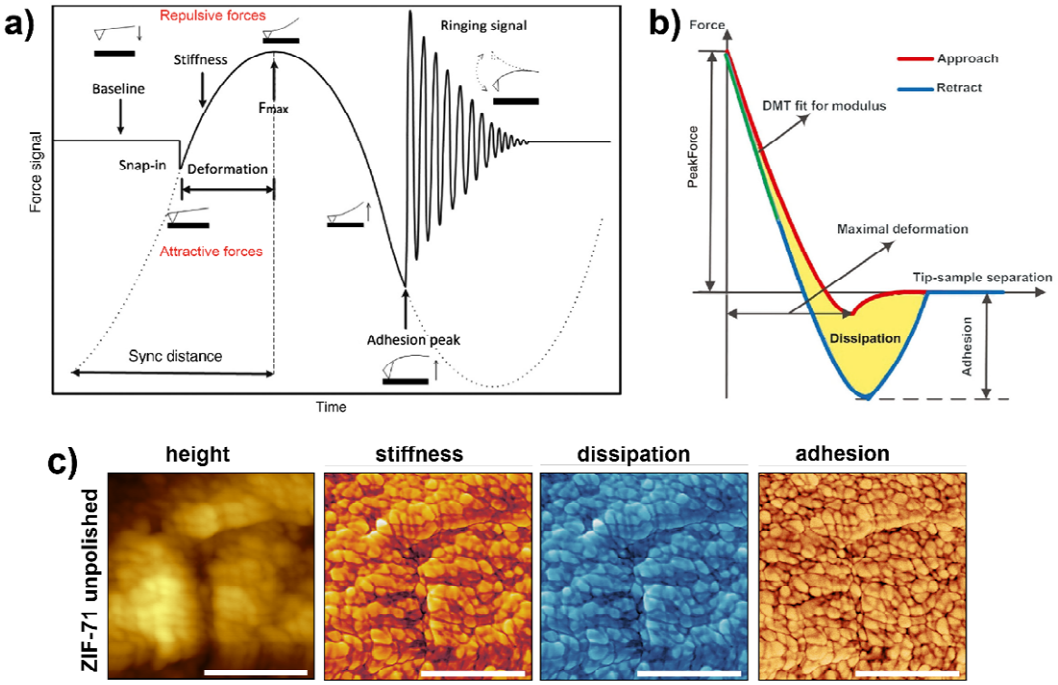

Figure 3.2 Typical a) force-time and b) force-displacement curves describing how the TFM mode operates, adapted with permission from (129). c) Examples of mechanical properties maps of a residual indent on a ZIF-71 monolith. The scale bar is 500 nm. Adapted with permission from (13).

3.2.5 Nanoscale fourier transform infrared spectroscopy (nanoFTIR)

Nearfield Fourier transform infrared nanospectroscopy (nanoFTIR) allows simultaneous imaging and FTIR spectroscopy with nanoscale spatial resolution (130).

NanoFTIR measurements were performed using the s-SNOM instrument (neaspec GmbH), where a platinum-coated AFM probe (Arrow-NCPt, tip radius < 25 nm, 285 kHz) under the tapping mode is illuminated by a broadband mid-infrared (IR) femtosecond laser (Toptica). Local nanoFTIR spectra of specific regions were measured under a spot size of *ca*. 20 nm. Each point spectrum was acquired as an average of 12 individual interferograms taken on the same spot, with 1024 pixels and an integration time of 14 ms per pixel, normalised by a reference spectrum taken on a silicon wafer.

3.2.6 Confocal Raman microscopy

Raman spectroscopy is a non-destructive chemical analysis technique which provides detailed information about chemical structure, phase, crystallinity and molecular interactions. It is based upon the interaction of light with the chemical bonds within a material and relies upon inelastic scattering of photons, termed Raman scattering.

Confocal Raman microscopy combines the spectral information from Raman spectroscopy with the spatial filtering of a confocal optical microscope for high-resolution chemical imaging of samples, with a spatial resolution of the order of 0.5-1 μm.

The Raman chemical maps shown in Chapter 6 were obtained using a Bruker Senterra confocal Raman microscope, located at Beamline B22 MIRIAM at the Diamond Light Source (Oxfordshire, UK). The measurements conditions were the following: objective 50×, laser 532 nm with grating 1200, resolution 3-5 cm^{-1},

laser power 12 mW, integration time 5000 ms, scan area 40 μm × 40 μm, (21 × 21 points).

3.2.7 Scanning electron microscopy (SEM)

The SEM images presented in this thesis were acquired with a Tescan Lyra 3 (Tescan, Czech Republic) field-emission scanning electron microscope, operating under a voltage of 10 keV. The nanoparticles samples analysed in Chapter 5 were prepared by drop-casting on a silicon wafer, following the same procedure employed for AFM samples (Section 3.1.2). Sputter-coating with conductive materials (i.e., gold or palladium) was not required, due to the conductivity of the silicon wafer used as a substrate.

3.2.8 Instrumented nanoindentation

All the nanoindentation tests reported in this thesis were carried out using a KLA iMicro nanoindenter. The machine is equipped with two interchangeable force actuators of maximum capacity of 50 mN and 1 N, used according to the test needs. Several tip geometries were employed, namely Berkovich, cube corner, spherical and flat punch. In particular, the Berkovich tip was used to measure Young's modulus and hardness (82), while the sharper cube corner tip was employed to induce radial cracks and measure fracture toughness.

Young's modulus and hardness values were obtained by averaging the data points obtained by continuous stiffness measurements (CSM, described in detail in Chapter 2) over a certain interval of surface penetration depth.

The maximum load was typically held for 1 s before unloading to quantify creep. Upon unloading, the load was held again at 10% of the maximum load for 3 min, in order to quantify thermal drift and correct the recorded value of load and depth accordingly. An example of test outputs is shown in Figure 3.3.

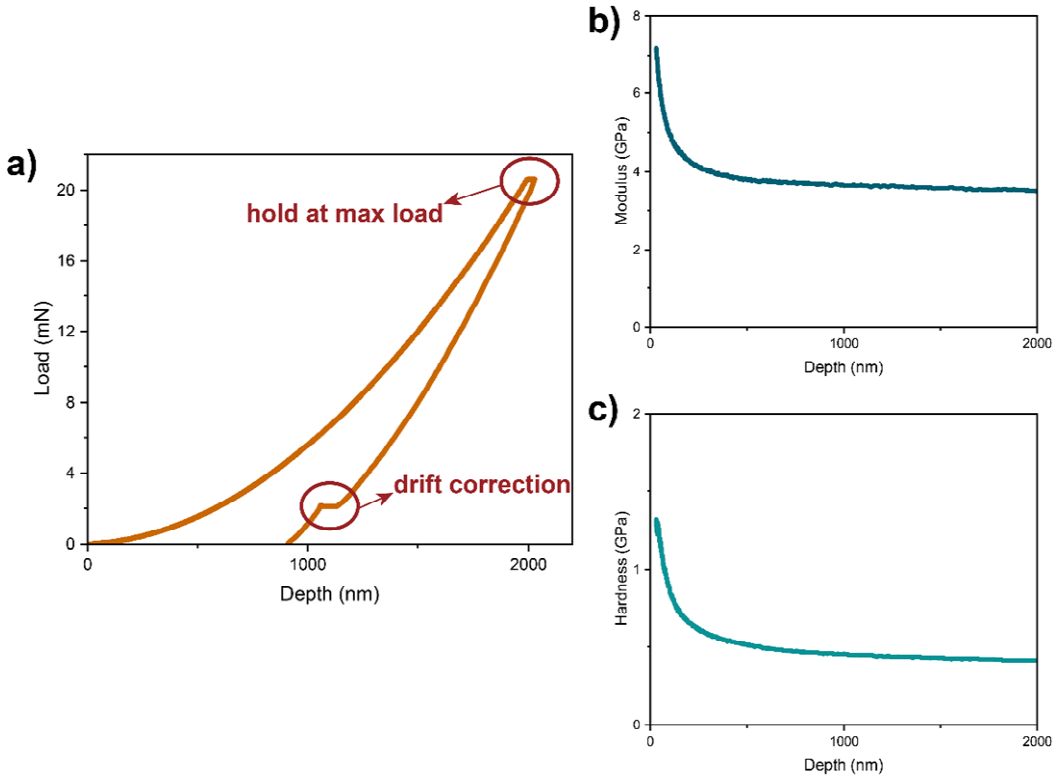

Figure 3.3 Results of a nanoindentation test on a ZIF-8 monolith. a) Load-depth curves. CSM data as a function of surface penetration depth for b) Young's modulus, and c) hardness.

3.2.9 Instrumented nanoscratch

Nanoscratch test is a well-established technique to characterise the wear resistance of materials such as thin films and coatings (131). In this thesis, such a test was used to get further insights on the fracture behaviour of MOF monoliths. The tests

were carried out on an iMicro nanoindenter (KLA-Tencor) equipped with a Berkovich tip. The maximum ramp load was set to 50 mN, the scratch length to 100 μm, and the scratch velocity to 10 μm s^{-1} for all the tests.

Each experiment consists of three test segments (Figure 3.4a):

1. a small normal load is applied allowing for the tip to work as a profilometer on the pre-scratch surface;
2. the same process is repeated during the actual scratch phase, with the prescribed ramp load;
3. the post-scratch profile and a cross-section profile (at half the length of the scratch) are recorded to measure the residual deformation of the surface after elastic recovery.

The scratches were performed using a Berkovich tip. This allows to define two different test modes, according to the end orientation of the tip which is cutting the material: ploughing (sharp end) or pushing (flat end). Other “angles of attack”, intermediate between plough and push, can also be used as illustrated in Figure 3.4b.

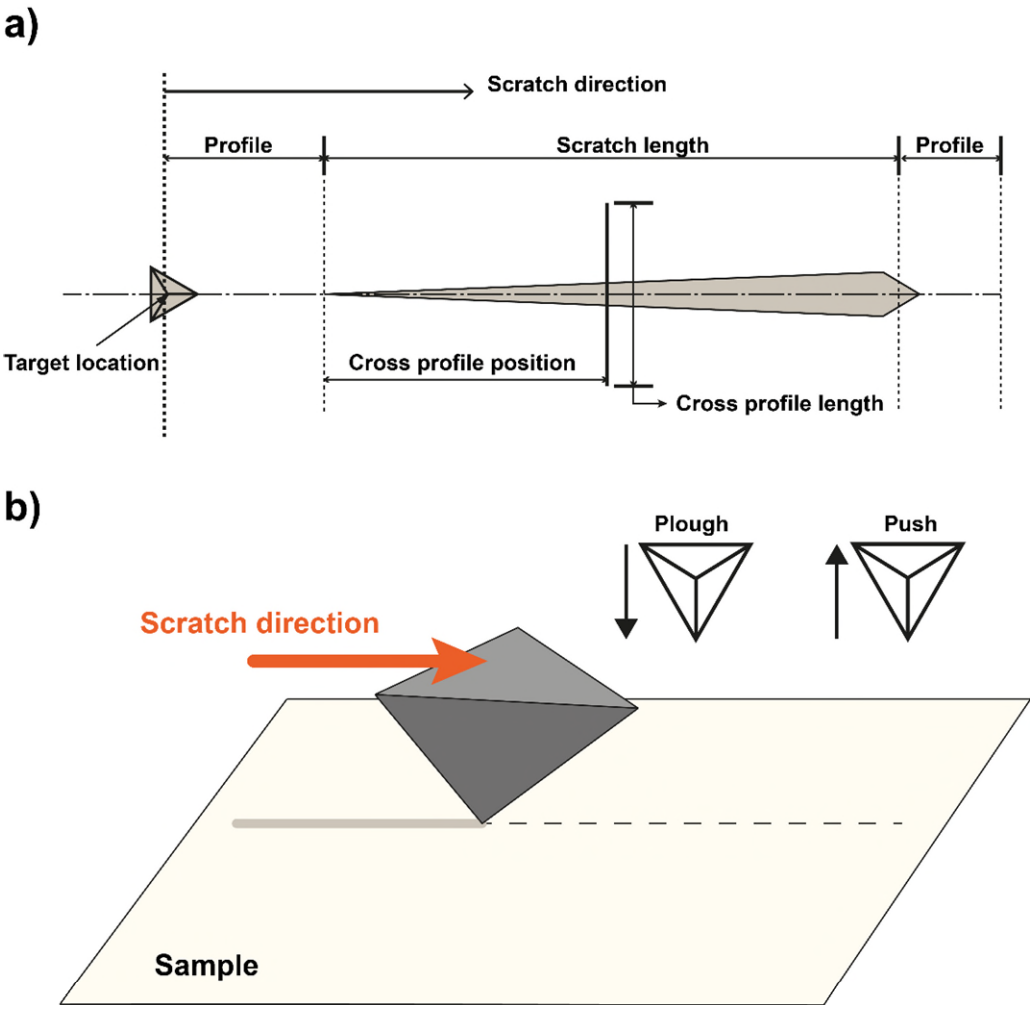

Figure 3.4 a) Key dimensions associated with the scratch[1]. b) Schematic illustration of the scratch test configuration.

3.2.10 Vickers microhardness

Vickers microindentation was performed using a Duramin-40 hardness tester (Struers), equipped with a Vickers tip. This test, compared to nanoindentation, is capable of higher loads, and was employed with the purpose of inducing radial cracks in the samples that did not exhibit this type of cracks under cube corner

[1] Adapted from Nanomechanics, Inc.® iMicro Indentation System operating instructions (OBID-1276-1)

nanoindentation (see Chapter 5). The maximum load (measured in gf) was held for 10 s before unloading.

3.3 Finite element method (FEM) simulations

Finite element method (FEM) simulations of the nanoindentation test were carried out alongside the experiments. The finite element software ABAQUS/Standard was employed.

The Berkovich, cube corner and spherical indenters were modelled as 3D and 2D parts (2D asymmetric cones with semi-apical angles of 70.3° and 42.3° for Berkovich and cube corner, respectively, and a circumference for the spherical indenter) and as rigid bodies. This latter approximation is justified by the fact that the real indenter, made of diamond, has a Young's modulus about 1000 times larger than the tested sample. This simplification allows to reduce the computational time. The 2D axisymmetric model was meshed with 12692 CAX4 type quadrilateral elements adapting the approach proposed in the Abapy package in Python (132). The mesh was refined in the proximity of the contact area, to maximise the reliability of the stress distribution under the indenter tip. A coarser mesh was used further away from the contact zone, to decrease number of elements in the model and thus reduce the computational time. The 3D model was modelled with 54688 linear hexahedral elements of type C3D8. However, as explained in Chapter 4, the difference between the 2D and 3D model, in terms of load-depth curve was demonstrated to be negligible.

The physics of the problem required some boundary conditions to be imposed to the 2D model. The nodes along the axis of revolution are free to move only along such an axis, whereas for the nodes at the bottom of the sample, all the degrees of freedom are set to zero ("*encastre*").

The indenter-sample interaction was modelled with a "surface-to-surface" contact discretisation. The contact constraint is imposed by defining the "master" (indenter) and "slave" (sample) surfaces. The slave surface cannot penetrate the master surface, and the direction of contact is perpendicular to the master surface. The slave surface is usually the softer of the two and needs to be meshed with finer elements.

The nanoindentation test was simulated by using two subsequent load steps, one for the loading part and the other for the unloading part. During the loading step, the indenter tip moves down along the axis of symmetry until the maximum depth is reached. The return of the tip to its original position takes place during the unloading step.

The elastic behaviour of the sample was modelled using the Young's modulus obtained from nanoindentation and the Poisson's ratio suggested in the literature. The plasticity of the sample was simulated by the elastic-perfectly plastic and Drucker-Prager models. The motivations are explained in detail in Chapter 4.

4 Mechanical Behaviour of Monolithic Zeolitic Imidazolate Frameworks (ZIFs)

4.1 Background and motivations

Zeolitic imidazolate frameworks (ZIFs) represent a particular class of MOFs, composed of tetrahedrally coordinated transition metal ions (*e.g.*, Fe, Co, Cu, Zn) coordinated to imidazolate linkers. ZIFs are topologically isomorphic to zeolites, as the metal-imidazolate-metal angle resembles the 145° Si-O-Si angle of zeolites. Since Huang *et al.* (133) first synthesised metal-organic sodalite cages constructed by tetrahedral building blocks (i.e., ZIF-7, ZIF-8 and ZIF-9), over one hundred ZIF topologies have been reported (28). Features like permanent porosity, flexibility, thermal and chemical stability have made them interesting candidates for a variety of applications such as gas separation and storage.

In this chapter, monolithic ZIF-8 ($Zn(mIm)_2$) and ZIF-71 ($Zn(dcIm)_2$) were shortlisted for a detailed study, given the simplicity of the synthesis, stability under ambient conditions and their mechanical stability when compared to other ZIFs.

The mechanical properties of several ZIFs single crystals have been extensively characterised by nanoindentation (74). Few works also report nanoindentation of ZIF-8 monoliths (52, 53). However, to the best of my knowledge, detailed studies going beyond simple measurements of Young's modulus and hardness have not been reported before Paper I. This work seeks to shed light on the deformation mechanism behind plastic deformation in ZIF-8 and ZIF-71 sol-gel monoliths by combining local imaging techniques (AFM and TFM), nanoindentation, finite element simulations and nearfield spectroscopy (nanoFTIR).

4.2 Summary of Paper I

4.2.1 Synthesis of sol-gel ZIFs monoliths

The two ZIF monoliths were synthesised following the synthesis route reported in Chapter 3.

The reproducibility of MOF sol-gel monoliths can be challenging, since even slight changes of the procedure can result in significant differences in terms of morphology and properties of the final product. As outlined in Chapter 1, the choice of solvent, its concentration, and the drying conditions play an important role. On top of these, quite surprisingly, the washing steps were found to be crucial for the formation of a robust, relatively uncracked monolith. This suggests that the washing process contributes significantly to the formation of the grain boundaries connecting the nanocrystals. During washing, the unreacted starting materials (particularly the linker, which is in excess to the stoichiometric ratio) are supposed

to be washed away, in order to vacate the pore sites. Such a process is not always entirely effective, meaning that a certain amount of reactants is retained and is likely to participate in the formation of grain boundaries. The parameters used to synthesise some representative batches are reported in Table 4.1. The resulting monoliths (Figure 4.1), although appear quite similar to each other, behaved in a different way during the polishing step, required to prepare suitable nanoindentation samples. ZIF-8 batch 3 and ZIF-71 batch 2, in fact, crumbled in contact with water. The samples investigated in Paper I correspond to ZIF-8 batch 1 and ZIF-71 batch 1.

Material	**Batch**	**Metal : linker ratio**	**Washing solvents**	**Drying time (days)**
ZIF-8	1	1 : 3	DMF, Methanol, Acetonitrile	3
	2	1 : 3	DMF, Methanol, Acetone	3
	3	1 : 4	DMF, Methanol, Acetone	3
ZIF-71	1	1 : 3	Methanol (x3)	3
	2	1 : 3	Methanol (x3)	1

Table 4.1 Synthesis parameters of ZIF-8 and ZIF-71 monoliths.

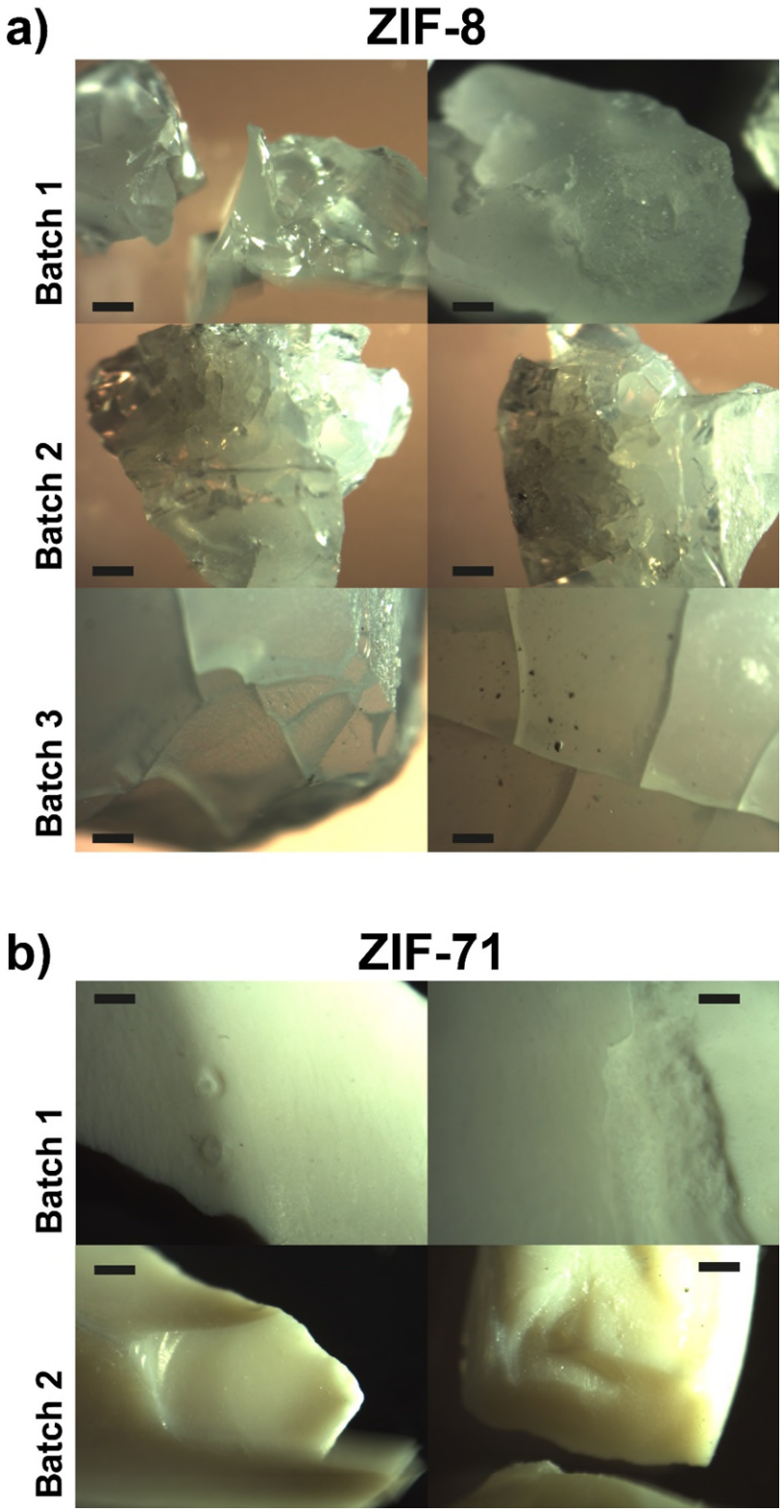

Figure 4.1 Optical micrographs of a) ZIF-8 and b) ZIF-71 monoliths, corresponding to the batches listed in Table 1. Scalebar 500 µm.

4.2.2 Nanoindentation experiments and finite-element method (FEM) simulations

The samples were probed with three different indenter shapes: Berkovich, cube corner and spherical. Young's modulus and hardness were measured with Berkovich indentation and found to be consistent with the values reported for single crystals (74) and monoliths (52).

The load-depth curves resulting from the tests were systematically compared to their finite element simulated counterparts. The simulations were performed using a 2D axisymmetric model, since the difference with the 3D model, in terms of load-depth curve was demonstrated to be negligible (Figure 3.2). The yield stress (σ_Y) used as input parameters for the material properties was reverse-engineered by iterating the simulation with different values of σ_Y (*i.e.*, different constraint factor C). The best fit was then selected as the actual σ_Y, as illustrated in Figure 4.3.

Two different material models were used for the FEM simulations: the elastic-perfectly plastic model and the Drucker-Prager model. The latter model is used for cohesive-frictional materials, whose yield stress increases with the hydrostatic pressure. The elastic-perfectly plastic model provides a good approximation of the Berkovich and spherical nanoindentation for both ZIF-8 and ZIF-71. However, this is not true in the case of cube corner nanoindentation. The greater sharpness of the cube corner (relatively to Berkovich) induces a densification effect, that makes the material stronger as the hydrostatic pressure increases. This effect is well modelled by the pressure-dependent Drucker-Prager

yield criterion. Other nanogranular materials, such as bones, have been reported to exhibit a similar behaviour (134).

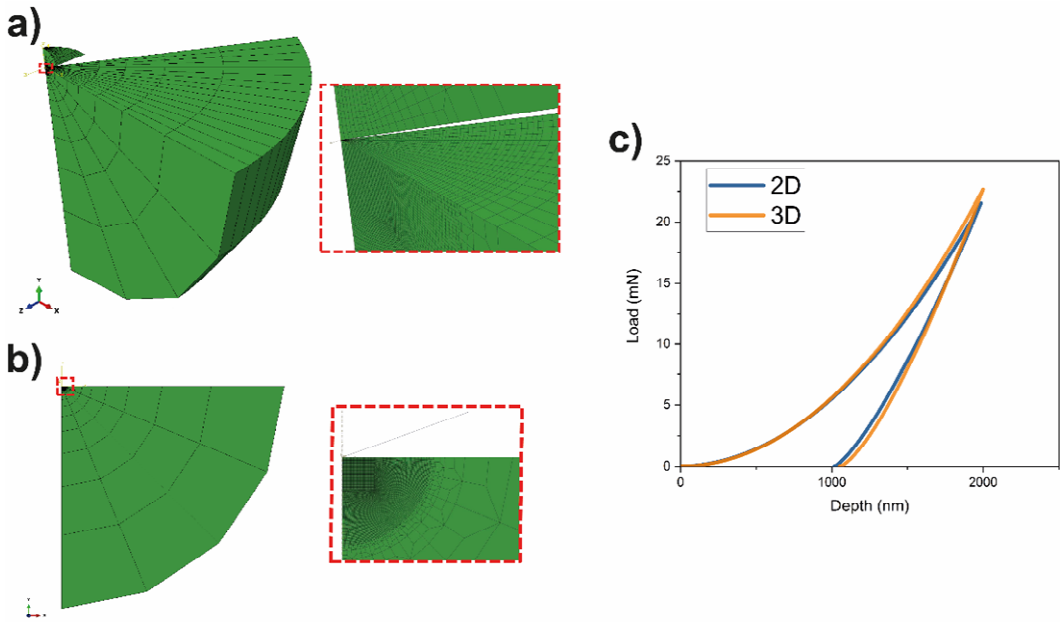

Figure 4.2 Comparison between 2D and 3D FEM indentation model (Berkovich indenter). a) 3D mesh of the sample, a zoomed in view of the contact region is highlighted in the red box. Note that only one sixth of the indenter and the sample were modelled, due to the symmetry of the Berkovich indenter. b) 2D mesh of the sample, a zoomed in view of the contact region is highlighted in the red box. c) Indentation load-depth curves obtained by using the 2D and 3D models.

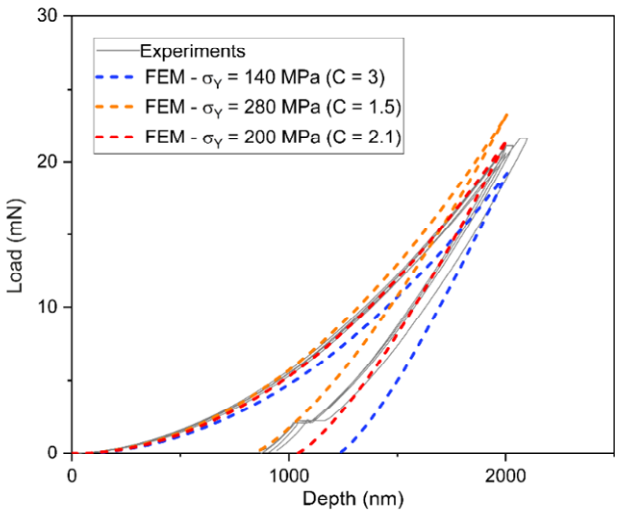

Figure 4.3 Finite element simulations of Berkovich indentation test of ZIF-8 monolith. The simulation was repeated with different values of the yield strength σ_Y (correspondingly different constraint factors). The best fit with the experiments was achieved with σ_Y = 200 MPa (C = 2.1).

4.2.3 Nanostructure characterisation and proposed deformation mechanism

The deformation mechanism proposed for ZIF-8 and ZIF-71 monoliths is grain boundary sliding (GBS), at the initial stage, followed by densification due to shear-induced structural amorphization at the framework level. GBS is justified by the nanograined structure of the monoliths, with each nanograin being a small (~ 100 nm in size) single crystal, revealed by TFM (Figure 4 in Paper I).

The subsequent densification, triggered by shear-induced collapse of the framework nanopores, was demonstrated by nanoFTIR spectroscopy (Figure 5 in Paper I). A sequence of IR spectra taken across a cube corner residual indent (where shear stress is the highest, according to Figure 3 in Paper I) with a resolution of 20 nm, shows that the intensity of the phonon band at 1311 cm^{-1}, attributable to defects of the ZIF-8 framework, increases as we approach the centre of the indent. In particular, the 1311 cm^{-1} band is related to the missing linker defect, as observed by Möslein *et al.* (123). This study combined nanoFTIR and DFT calculations to assign characteristic vibrational bands to different types of defects, occurring during the crystallisation process. Some of their results are summarised in Figure 4.4, showing that framework defects such as missing zinc and missing linker can give rise to new vibrational peaks in the IR fingerprint of ZIF-8 nanocrystals.

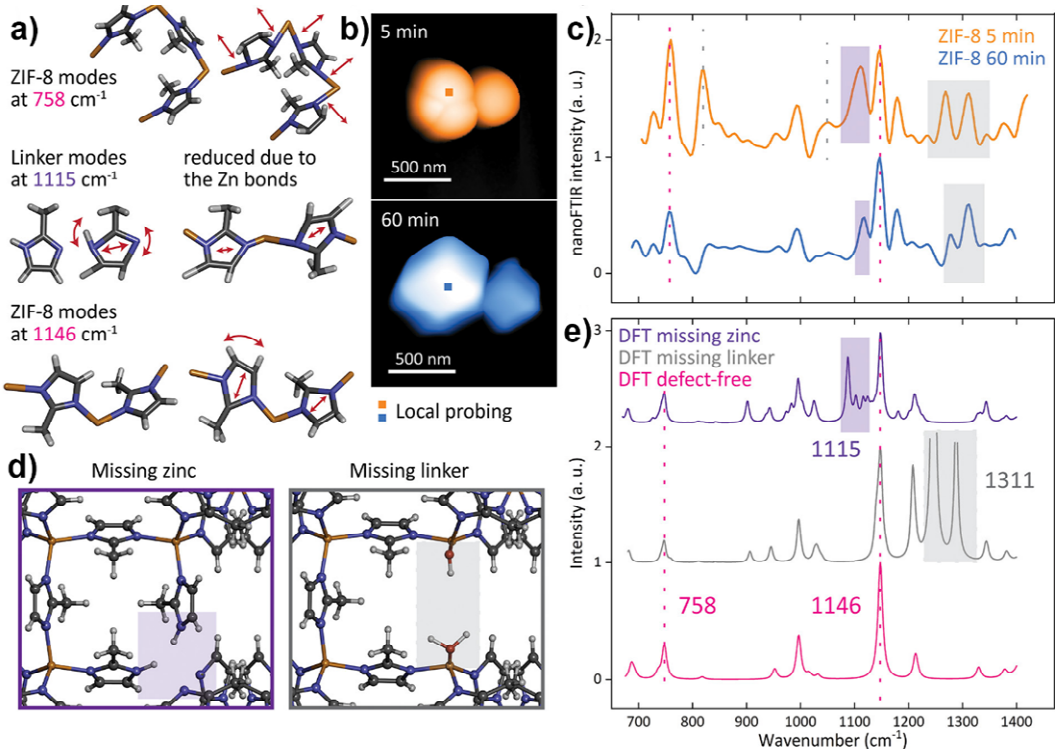

Figure 4.4 Defects identification in ZIF-8 nanocrystals. (a) Schematic representations of key vibrational modes. (b) AFM images of ZIF-8 crystals obtained after 5 and 60 min, indicating crystals selected for local probing. (c) Corresponding local nanoFTIR spectra. (d) Schematic representations of the simulated defects. (e) Corresponding simulated FTIR spectra compared with a perfect ZIF-8 crystal. Adapted with permission from (123).

4.2.4 Fracture toughness

In the last section of Paper I, the fracture toughness of the two monoliths was estimated by employing cube corner nanoindentation, combined with an empirical crack length method, namely Laugier's formula (equation 6 in Paper I) (135):

$$K_{\mathrm{IC}} = k\left(\frac{a}{l}\right)^{\frac{1}{2}}\left(\frac{E}{H}\right)^{\frac{2}{3}}\frac{P}{c^{\frac{3}{2}}} \tag{4.1}$$

where is k is an empirical constant of the indenter shape (k = 0.057 for cube corner (136)), a is the distance between the centre and the tip of the indent, l is the crack length starting from the corner of the indent, E is the Young's modulus, H is the

hardness, P is the maximum load, and $c = a + l$. This method relies on nanoindentation, which can probe within the μm-scale. At a larger length scale (i.e., mm-scale), the toughness will inevitably drop, due to the higher concentration of defects and porosity, inherent to the sol-gel processing.

Laugier's formula is not the only equation available in the literature for the measurement of fracture toughness *via* indentation. The choice depends on the crack system that emanates from the indentation corners (Figure 4.5). Laugier's expression is used when a "Palmqvist" crack configuration is assumed. If, instead, a "half-penny" crack is assumed, the following formula, proposed by Anstis *et al.* (137), would be more suitable:

$$K_{\mathrm{IC}} = \alpha \left(\frac{E}{H}\right)^{\frac{1}{3}} \frac{P}{c^{\frac{3}{2}}} \tag{4.2}$$

Where α depends on the crack length/indenter size (c/a) ratio:

$$\alpha = 0.0211 \left(\frac{c}{a}\right)^{0.3785}. \tag{4.3}$$

Since the crack system developing under the indenter in ZIF monoliths is unknown *a priori*, both the formulae could, in principle, be utilised. However, in this study the Laugier's formula was employed, since it was demonstrated to best describe crack propagating from a three-sided pyramidal indenter (138), like the cube corner.

The results (Table 2 in Paper I) show that ZIF-71 (0.145 MPa $m^{1/2}$) is tougher than ZIF-8 (0.074 MPa $m^{1/2}$). The values of fracture toughness are in the order of magnitude of 0.1 MPa $m^{1/2}$, resembling the ones reported for dense frameworks (73) and ZIF-62 glass (102).

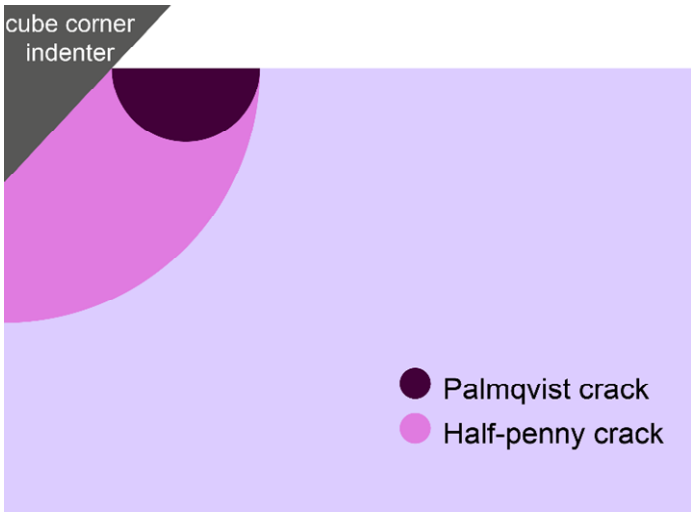

Figure 4.5 Schematic cross-section view of Palmqvist and half-penny crack systems induced by indentation with a cube corner tip.

4.3 Paper I: Mechanical properties and nanostructure of monolithic zeolitic imidazolate frameworks: a nanoindentation, nanospectroscopy, and finite element study

Online version: https://doi.org/10.1016/j.mtnano.2021.100166

Materials Today Nano 17 (2022) 100166

Contents lists available at ScienceDirect

Materials Today Nano

journal homepage: https://www.evise.com/profile/#/MTNANO/login

Mechanical properties and nanostructure of monolithic zeolitic imidazolate frameworks: a nanoindentation, nanospectroscopy, and finite element study

Michele Tricarico, Jin-Chong Tan*

Multifunctional Materials and Composites (MMC) Laboratory, Department of Engineering Science, University of Oxford, Parks Road, Oxford, OX1 3PJ, United Kingdom

ARTICLE INFO

Article history:
Received 1 October 2021
Received in revised form
24 November 2021
Accepted 2 December 2021
Available online 8 December 2021

Keywords:
MOF monolith
Sol-gel
MOF mechanics
Nano-FTIR
Finite element modeling (FEM)
Fracture toughness

ABSTRACT

The synthesis of metal-organic frameworks (MOFs) in a monolithic morphology is a promising way to achieve the transition of this class of materials from academia to industrial applications. The sol-gel process has been widely used to produce MOF monoliths. It is relatively cheap and simple compared with other techniques (e.g. mechanical densification), and moreover, it allows to produce 'pure' monoliths, that is, without the need of using binders or templates that could affect the functional properties of the MOF. Understanding the mechanical properties of these monoliths is crucial for their transit to practical applications. We studied the mechanical behavior of two zeolitic imidazolate frameworks (ZIF-8 and ZIF-71) by means of instrumented nanoindentation and atomic force microscopy (AFM). Tip force microscopy (TFM), an extension of AFM, was used to reveal the surface nanostructure of the monoliths. We used finite element (FE) simulations alongside the experiments, to establish a suitable constitutive model and determine an improved estimate of the yield stress (σ_Y) of ZIF monoliths. Nano-Fourier-transform infrared (nano-FTIR) spectroscopy was subsequently used to pinpoint local structural alteration of the framework in the contact area. The combination of TFM, FE simulations, and nano-FTIR enabled us to identify the mechanical deformation mechanisms in monolithic ZIF materials: grain boundary sliding is dominating at low stresses, then breakage of chemical bonds and a partial failure of the framework occur, eventually leading to a densification of porous framework at the contact zone. Finally, we measured the fracture toughness using a cube corner indenter to study the resistance of monoliths against cracking failure.

1. Introduction

Metal-organic frameworks (MOFs) are an emerging class of hybrid porous materials. They consist of metal clusters and organic ligands that self-assemble to form a lattice framework with a considerable internal surface area. Research over the last 25 years has led to a vast range of framework-type compounds with high chemical stability, tunable physical properties, organic functionality, and porosity [1,2], resulting in several possible technological applications [3–6].

The transition of these materials from academic research to industrial practical applications is however rather limited. One of the reasons for this deficiency is a limited understanding of the mechanical properties. Despite the large amount of work devoted to the chemical synthesis of novel framework structures and characterization of their functional properties, the field of MOF mechanics is still at an early stage [7–9].

The mechanical characterization of MOFs has mostly relied on nanoindentation measurements, which allow for the possibility of testing very small samples, such as single crystals [10–14], thin films [15], or small monoliths [16,17]. In particular, zeolitic imidazolate frameworks (ZIFs) [18] have been extensively studied by nanoindentation, owing to their ease of synthesis, stability under ambient conditions, and commercial availability of certain compounds [11,12,14].

Most MOFs are synthesized as polydisperse microcrystalline powders. These may present intrinsic limitations, such as poor handling properties, restricted mass transfer, and mechanical

* Corresponding author.
E-mail address: jin-chong.tan@eng.ox.ac.uk (J.-C. Tan).

https://doi.org/10.1016/j.mtnano.2021.100166
2588-8420/

instability, resulting in a further narrowing of the range of industrial applications. The realization of mechanically robust and bulk morphologies, known as 'monoliths', is therefore the preferred form factor for commercial applications [19,20]. The advantages of monolithic structures are multiple: easier handling associated with structural rigidity, low mass transfer resistance (for improved gas separation capabilities), and higher volumetric adsorption capacities [16]. MOF monoliths have been fabricated using different techniques, such as coating of organic [21] and inorganic [22] scaffolds, extrusion by means of binders and plasticizers [23], three-dimensional (3D) printing [24,25], mechanical densification [26–28], template morphological replacement [29], and sol-gel processes [19]. With this technique, it is possible to tune the hierarchical pore distribution within the monolith, leading to improved capabilities for gas uptake [16,17,20,30].

Several classes of MOFs have already been studied in their sol-gel monolithic form, including HKUST-1 [16], ZIFs [17,31], and UiO-66 [30]. The sol-gel process consists of the production of a network (gel) from molecular precursor via the formation of colloidal particles (sol). The nanoparticles in the colloid aggregate via weak non-covalent interactions (mainly van der Waals forces), forming a viscous material: the gel. On drying, the gel progressively transforms into a monolith, as illustrated in the scheme in Fig. 1a. The drying process plays undoubtedly a prominent role in the formation of mechanically stable monoliths. During solvent drying, there exists a mechanical stress at the gas-liquid interface in the pores, owing to surface tension. This phenomenon is often the cause of cracking or collapse of the gel body [32]. A slow solvent removal (typically at room temperature) and small particle size can better accommodate this stress, promoting the formation of dense monoliths. However, this is not always possible, especially with big monoliths, where large shrinkages occur, leading to cracking anyway. Another crucial requirement for the formation of a gel rather than a precipitate is the small size of the particles. This can be achieved during the crystallization phase, by increasing the number of nucleation sites. As a result, the crystal growth will be constrained, leading to the formation of fine particles (usually smaller than 100 nm) [19].

In this work, we aim to study the detailed mechanical behavior of the ZIF-8 and ZIF-71 sol-gel monoliths. To achieve the gel state, the high concentration reaction (HCR) synthetic approach, recently developed by our group [33,34], was leveraged. This HCR method consists of the accelerated deprotonation of the organic linker, which boosts the formation of metal-organic clusters and hence increases the number of nucleation sites, leading to the formation of fine nanoparticle size that promotes the formation of the gel. On drying of the gel, these particles aggregate and consolidate to form the monolith. Tip force microscopy (TFM) imaging of the surface of the monoliths revealed a fine-grained microstructure (grain size <100 nm) or 'nanostructure,' as shown in Fig. 1b and c, which gives us significant information to establish their structure-mechanical property relationships.

Moreover, we estimated the yield stress (σ_Y) of a monolithic MOF material, which underpins the elastic-plastic transition. To do so, we performed finite element (FE) simulations alongside the nanoindentation experiments to gain a better understanding of the underpinning mechanics. To the best of our knowledge, there is not yet any experimental/modeling study proposing a plasticity model for MOF monoliths and an estimate of the yield stress, which is a key material parameter in structural design of load-bearing applications. The nanostructure of the monoliths was mapped by TFM, which, together with the results of the FE simulations and the nano-Fourier-transform infrared (nano-FTIR) near-field spectroscopic measurement of the local regions of residual indents, allowed us to propose the deformation mechanisms of ZIF monoliths under stress.

2. Materials and methods

2.1. Materials

Zinc nitrate hexahydrate ($Zn(NO_3)_2{\cdot}6H_2O$), zinc acetate dihydrate ($Zn(CH_3CO_2)_2{\cdot}2H_2O$), 2-methylimidazole (mIm), 4,5-dichloroimidazole (dcIm), triethylamine (NEt_3), dimethylformamide (DMF), methanol (MeOH), and acetonitrile (MeCN) were purchased from Fisher Scientific and used as received.

2.2. Synthesis of monoliths

ZIF-8 (Zn $(mIm)_2$) monoliths were synthesized as per the following procedure: 0.595 g of $Zn(NO_3)_2{\cdot}6H_2O$ and 0.493 g of mIm were dissolved in 9 mL of DMF each and stirred for 5 min. Then, 0.837 mL of NEt_3 was added to the linker solution. Subsequently, the two solutions were mixed in a 50 mL vial, where a gel was promptly formed. The molar ratio $Zn(NO_3)_2{\cdot}6H_2O$: mIm: DMF: NEt_3 is 1 : 3: 116 : 3. The mixture was sonicated for 5 min and then washed three times, in 50 mL of solvent (DMF, MeOH, and MeCN, respectively), by centrifugation at 8,000 rpm. The collected solid was dried at room temperature (~25 °C) for three days under the fume cupboard.

ZIF-71 (Zn $(dcIm)_2$) monoliths were synthesized following the same procedures for ZIF-8 monoliths, starting from 0.439 g of $Zn(CH_3CO_2)_2{\cdot}2H_2O$ and 0.822 g of dcIm. The compound was washed three times in MeOH.

The powder X-ray diffraction (PXRD) patterns (Figs. S1 and S2) confirm the successful synthesis of the frameworks, because all the main characteristic Bragg diffraction peaks of both ZIF-8 and ZIF-71 are present.

2.3. Nanoindentation tests

In a nutshell, a nanoindentation test is conducted by pressing a hard tip whose mechanical properties are known (usually diamond) into a sample whose properties are unknown. The result of the test is a load-depth curve, from which the Young's modulus (E) and hardness (H) can be determined. A load-depth curve consists of two segments: elasto-plastic loading and elastic unloading. If no plastic deformation occurs, the two segments overlap. After the approach proposed by Oliver and Pharr [35], modulus and hardness can be calculated using the following equations:

$$E^* = \frac{\sqrt{\pi}}{2}\frac{S}{\sqrt{A(h_{max})}} \quad (1)$$

$$H = \frac{P_{max}}{A(h_{max})} \quad (2)$$

where E^* is the contact modulus, S is the contact stiffness (slope of the unloading curve at maximum load), $A(h)$ is the area function, and P_{max} and h_{max} are the maximum load and depth, respectively. The contact modulus (E^*) is a function of the Young's moduli and Poisson's ratios of the sample (E_s, ν_s) and the indenter (E_i, ν_i):

$$\frac{1}{E^*} = \frac{1-\nu_s^2}{E_s} + \frac{1-\nu_i^2}{E_i} \quad (3)$$

when the indenter is significantly stiffer than the sample, the second term on the right-hand side of Equation (3) can be neglected. The area function $A(h)$ is a third-order polynomial that relates the contact area to the contact depth, and it is determined through calibration using a fused silica sample.

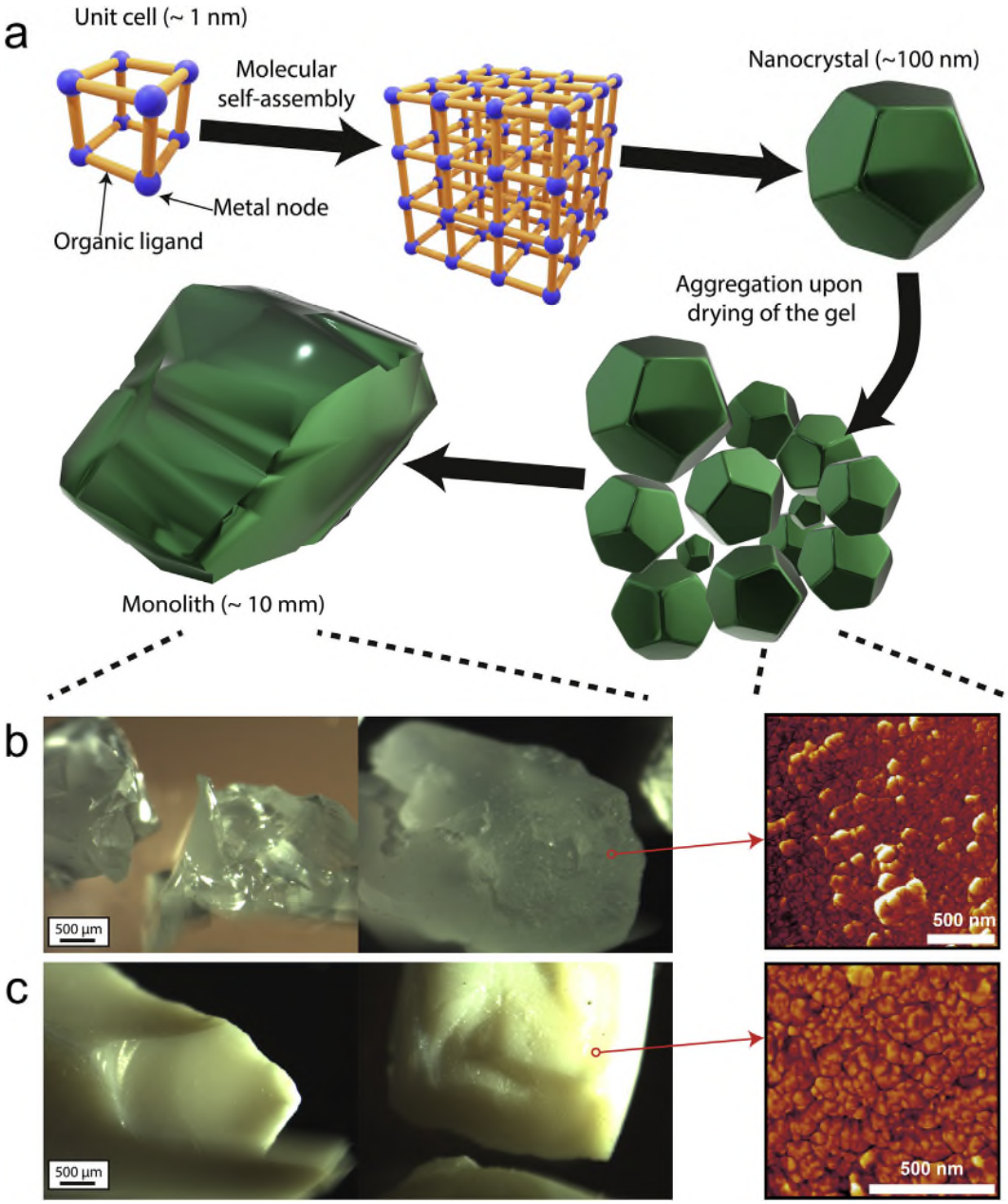

Fig. 1. (a) Schematics of the formation of the MOF monoliths. (b) and (c) Optical images of ZIF-8 and ZIF-71 monoliths, respectively. Right panels show the stiffness maps of the surface of the monoliths obtained by TFM, where the nanosized grain structure is prevalent.

The hardness is considered to be proportional to the yield stress (σ_Y) [36]:

$$H = C \cdot \sigma_Y \tag{4}$$

where C is called the 'constraint factor' and is material dependent. It usually lies between 1.5 (in glasses, characterized by a small E/σ_Y ratio) and 3 (in metals, large E/σ_Y ratio).

An extension of the Oliver and Pharr method is represented by the continuous stiffness measurements (CSM) [35,37]. This technique superimposes a 2-nm oscillation on the quasi-static force, using a frequency-specific amplifier to measure the response of the indenter. CSM enables the measurement of mechanical properties as a continuous function of the penetration depth into the surface.

The nanoindentation tests were conducted using an iMicro nanoindenter (KLA-Tencor). The as-synthetized monoliths were cold mounted in epoxy resin (Struers Epofix), resulting in a cylindrical sample, suitable for nanoindentation. To get reliable results from the indentation tests, the contact surface must be flat. Therefore, the specimen surface was thoroughly polished with sandpapers and diamond suspensions.

Berkovich, spherical, and cube corner diamond indenter tips were used. The Berkovich tip is a three-sided pyramid, generally used for small-scale measurements of Young's modulus and hardness. The spherical tip provides a smooth transition from elastic to plastic contact, which makes it particularly suitable for probing soft materials. The spherical tip used for this study has a radius of 4.53 µm. Cube corner is a three-sided pyramid with mutually perpendicular faces. The sharpness of the cube corner produces

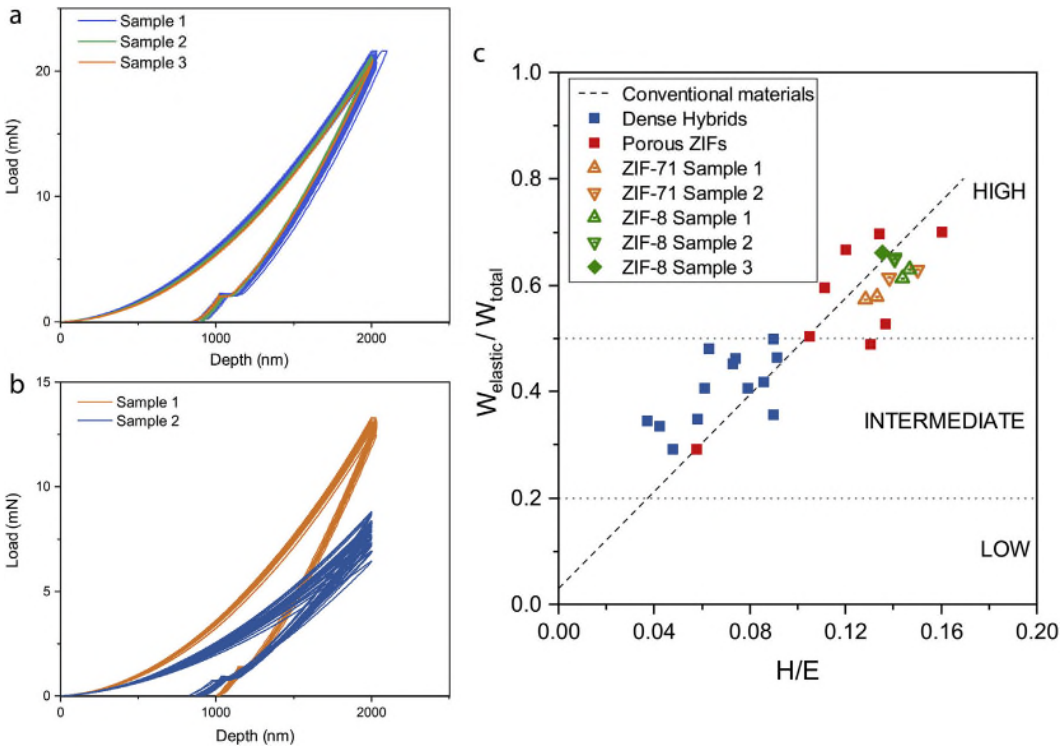

Fig. 2. Load-depth curves resulting from nanoindentation tests of (a) ZIF-8 and (b) ZIF-71 using a Berkovich indenter and a map of elastic recovery versus the ratio of hardness to Young's modulus (H/E) (c). The data for conventional materials, dense hybrids, and porous ZIFs were adapted from reference [13].

Table 1
Young's modulus and hardness measurements (CSM method) obtained via Berkovich nanoindentation. Mean values and standard deviations from this work were calculated from an indentation depth range of 500–2000 nm.

Sample	# of indents	Young's modulus, E (GPa)	Hardness, H (MPa)
ZIF-8 monolith	59	3.18 ± 0.04	452 ± 20
ZIF-8 single crystal, from the study reported by Tan et al. [12]	–	3.199 ± 0.092	531 ± 28
ZIF-71 monolith (total)	50	1.67 ± 0.38	227 ± 47
ZIF-71 sample #1	25	2.04 ± 0.06	273 ± 7
ZIF-71 sample #2	25	1.29 ± 0.07	180 ± 5

much higher stresses and strains in the region of contact. This results in the formation of well-defined cracks around the indent in brittle materials, which can be used to measure fracture toughness at small scales.

2.4. Density measurements

The density of the monoliths was measured using a Mettler Toledo laboratory balance equipped with a density kit. By exploiting Archimedes' principle, the density of the sample was derived by measuring its weight in air and in an auxiliary liquid (distilled water).

2.5. Atomic force microscopy imaging

The surface topography of indents was measured by AFM as implemented in a scattering-type scanning near-field optical microscopy (s-SNOM) instrument (Neaspec GmbH) under the tapping mode. A Scout350 (NuNano) probe was used, with a nominal tip radius of 5 nm and a resonant frequency of 350 kHz.

2.6. Tip force microscopy imaging

TFM is an extension of the AFM to enable characterization of nanomechanical properties of the sample along with the topography. The TFM mode extends the capabilities of AFM, allowing to image properties such as local stiffness and adhesion, resulting in high contrast images [38,39]. Height topography and stiffness, dissipation and adhesion maps were determined using the s-SNOM instrument (Neaspec GmbH), operating under the contact mode. An Arrow-NCR probe (NanoWorld) was used, with a nominal tip radius of <10 nm and a resonance frequency of 285 kHz.

2.7. nano-FTIR

Nano-FTIR spectroscopy was performed using the s-SNOM instrument (Neaspec GmbH), where a platinum-coated AFM probe (Arrow-NCPt, tip radius <25 nm, 285 kHz) under the tapping mode is illuminated by a broadband mid-infrared (IR) laser source (Toptica). A line scan of 15-point spectra was acquired along the residual indents of the Berkovich and cube corner indentations on the ZIF-8 monolith. Each point spectrum was acquired by Fourier-transform spectroscopy as an average of 11 individual interferograms taken on the same spot (spot size 20 nm), with 1024 pixels and an integration time of 12 ms per pixel, normalized by a reference spectrum taken on a silicon wafer.

2.8. Finite element modeling

For the FE simulation of the nanoindentation test, a two-dimensional (2D) axisymmetric model in ABAQUS/Standard [40] was used. The Berkovich and cube corner indenters can be modeled as conical indenters with semi-apical angles of 70.3° and 42.3° respectively, which result in the same area function of their

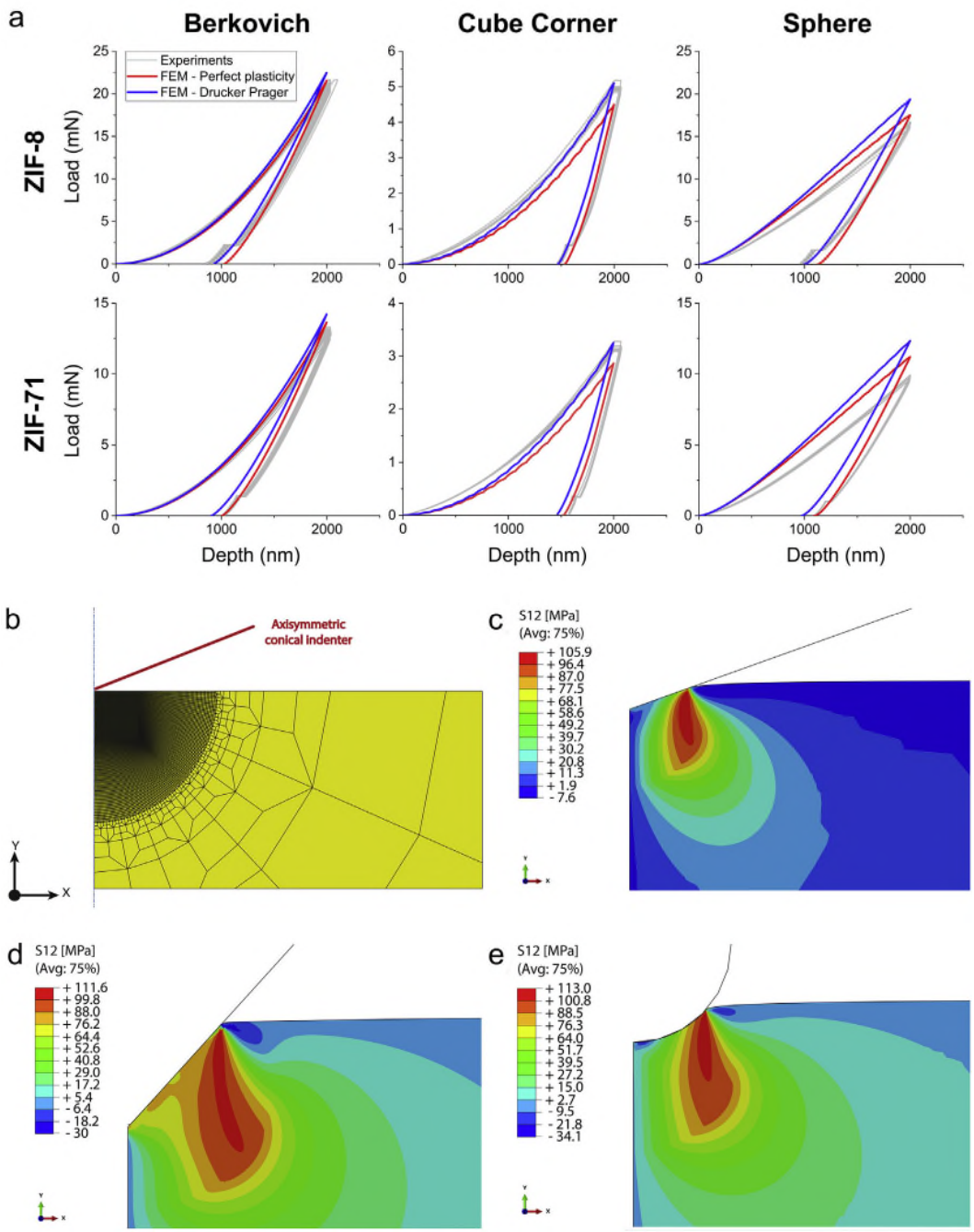

Fig. 3. Finite element modeling of the nanoindentation tests. (a) Predicted nanoindentation load-depth curves of the 2-D FEM model compared with the experimental data. The material behavior was simulated with two different material models (elastic-perfectly plastic and Drucker-Prager). (b) 2-D axisymmetric FE model: the Berkovich indenter was modeled as a semi-apical cone of 70.3° (red), the sample (yellow) was meshed using a finer element size in the proximity of the contact. (c–e) Shear stress contours of ZIF-8 monolith model at a maximum indentation depth (2000 nm) under the Berkovich, cube corner, and spherical indenters, respectively. For ZIF-8, the shear yield stress τ_{max} is estimated as $\sigma_Y/2$, such that the contour regions $\gtrsim$ 100 MPa are predicted to have yielded under shear. The Berkovich and cube corner indenters were modeled as equivalent 2-D cones with semi-apical angles of 70.3° and 42.3°, respectively. (For interpretation of the references to color in this figure legend, the reader is referred to the Web version of this article.)

pyramidal counterparts. As shown by Lichinchi et al. [41], the difference between the load-depth curves obtained from the 2D axisymmetric and the 3D Berkovich model is negligible. A comparison between the 2D and 3D load-depth curves resulting from a simulated Berkovich indentation of a ZIF-8 monolith is shown in Fig. S3. Considering that the 2D simulation is computationally less expensive, this is highly effective for simulating nanoindentation tests using a Berkovich indenter. All indenter geometries (including spherical) were modeled as rigid bodies. This approximation is justified because the real indenter, made of diamond, has Young's modulus about 1000 times larger than the tested material.

The sample was meshed with 12,692 CAX4-type quadrilateral elements, adapting the technique proposed in the Abapy package in Python [42]. A finer mesh was used in the contact area, to obtain an accurate representation of the stress distribution under the indenter tip. A coarser mesh was used further away from the contact zone to reduce the computational time (Fig. 3b).

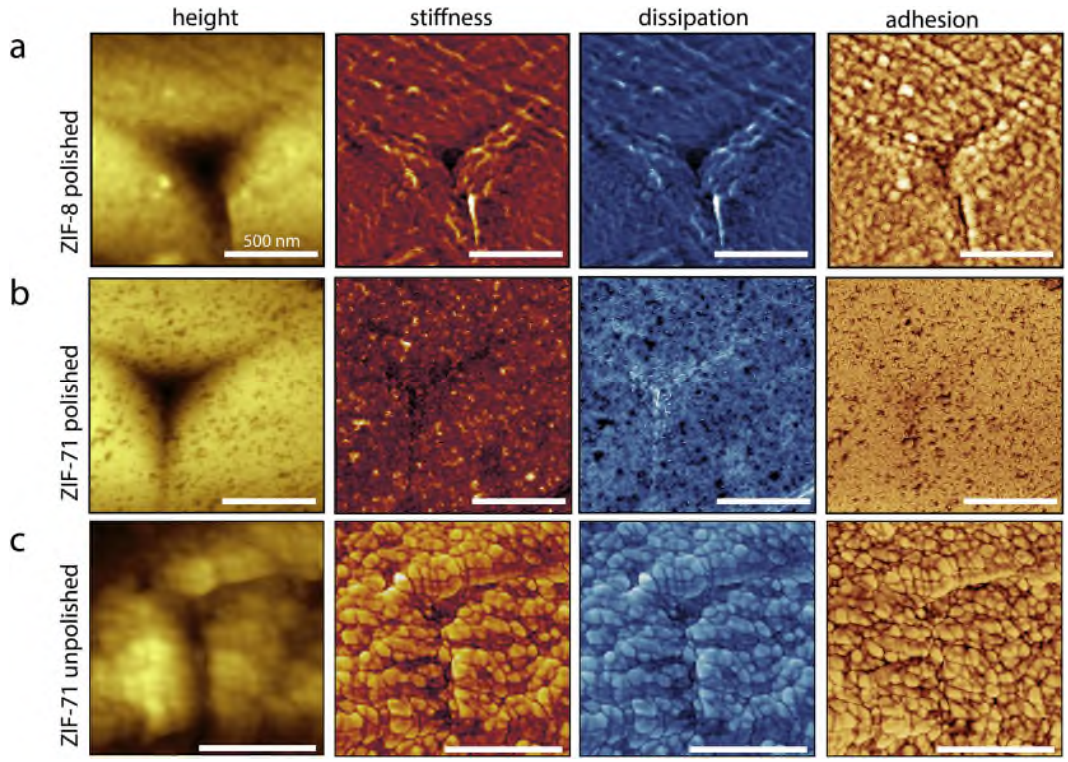

Fig. 4. AFM height topography (left panels) and TFM results show the stiffness, dissipation, and adhesion maps of residual indents on the surface of the ZIF-8 and ZIF-71 monoliths. The scale bar is 500 nm. The polished surface of ZIF-71 reveals prominent intergranular porosity.

The following boundary conditions were imposed: the nodes along the axis of revolution are free to move only along such an axis, whereas for the nodes at the bottom of the sample, all the degrees of freedom were set to zero ('encastre' boundary condition).

The indenter-sample interaction was modeled with a 'surface-to-surface' contact discretization. The contact constraint is imposed by defining the 'master' and 'slave' surfaces. The slave surface cannot penetrate the master surface, and the direction of contact is perpendicular to the master surface. The slave surface is usually the softer of the two and needs to be meshed with finer elements [40]. We chose the sample surface as the slave surface.

The nanoindentation test was simulated by using two subsequent load steps, one for the loading part and the other for the unloading part. During the loading step, the indenter tip moves down along the axis of symmetry until the maximum depth (2000 nm) is reached. The return of the tip to its original position takes place during the unloading step.

The mechanical behavior of the samples was simulated by two different models: elastic-perfectly plastic and Drucker-Prager (DP). The first one requires only three parameters to fully describe the elasto-plastic behavior of the material (Poisson's ratio, Young's modulus, and yield stress). The second one is used for pressure-dependent materials, whose yield behavior depends on the hydrostatic pressure. This model requires three more material parameters, namely, 'angle of friction,' 'flow stress ratio,' and 'dilation angle' [40], that were set to 10, 1, and 10, respectively.

3. Results and discussion

3.1. Nanoindentation experiments and finite element simulations

The results of a series of systematic nanoindentation measurements on the ZIF-8 monoliths are summarized in Fig. 2. The load-depth curves resulting from nanoindentation of ZIF-8 monoliths with the Berkovich tip are shown in Fig. 2a. A total of 59 tests on three different samples are considered. The load-depth curves show a very good repeatability, as well as the resultant values of Young's modulus (E) and hardness (H) with a relatively small standard deviation. Assuming a Poisson's ratio $\nu = 0.4$, [11] the CSM method gave the results listed in Table 1. The measured values of E and H are consistent with those observed before, for either single crystals [7,11] or monoliths [17]. To get some insights about the mechanical behavior of the monoliths, we compare the measurements with the literature available regarding the single crystal form of the same frameworks. Interestingly, we found that Young's modulus of the ZIF-8 monolith is reminiscent of the single crystal counterpart. This means that the nanocrystals forming the monoliths are efficiently packed, and intergranular porosity is limited. The reduced hardness of the monolith (declined by ~15% compared with single crystal) is justified by the presence of 'grain' boundaries between the adjacent nanocrystals forming the monolith, where the plastic deformation is more likely to initiate from a grain boundary 'defect.' The good repeatability of the tests obtained from the representative samples allows us to confidently classify the ZIF-8 monolith as mechanically isotropic.

In contrast, the nanoindentation of ZIF-71 monoliths resulted in a wider spread of load-depth curves (Fig. 2b) for each sample, indicating that this monolith is less homogeneous and non-isotropic. The resultant values of E and H (Table 1) are appreciably lower than those of ZIF-8 monoliths. To gain further insights, we measured the density of the two monoliths (via Archimedes' principle, see subsection 2.4). We found the ZIF-8 monolith to be denser than ZIF-71 (1.260 vs. 0.975 g/cm^3) as expected, because the density ρ of porous solids scales with its Young's modulus ($E \propto \rho^2$). As reported by Tian et al. [17], the density of ZIF-8 monolith is higher than the calculated theoretical density of the ideal framework structure (i.e. 0.95 g/cm^3) [12], owing to presence of unreacted species and impurities that can be trapped inside the

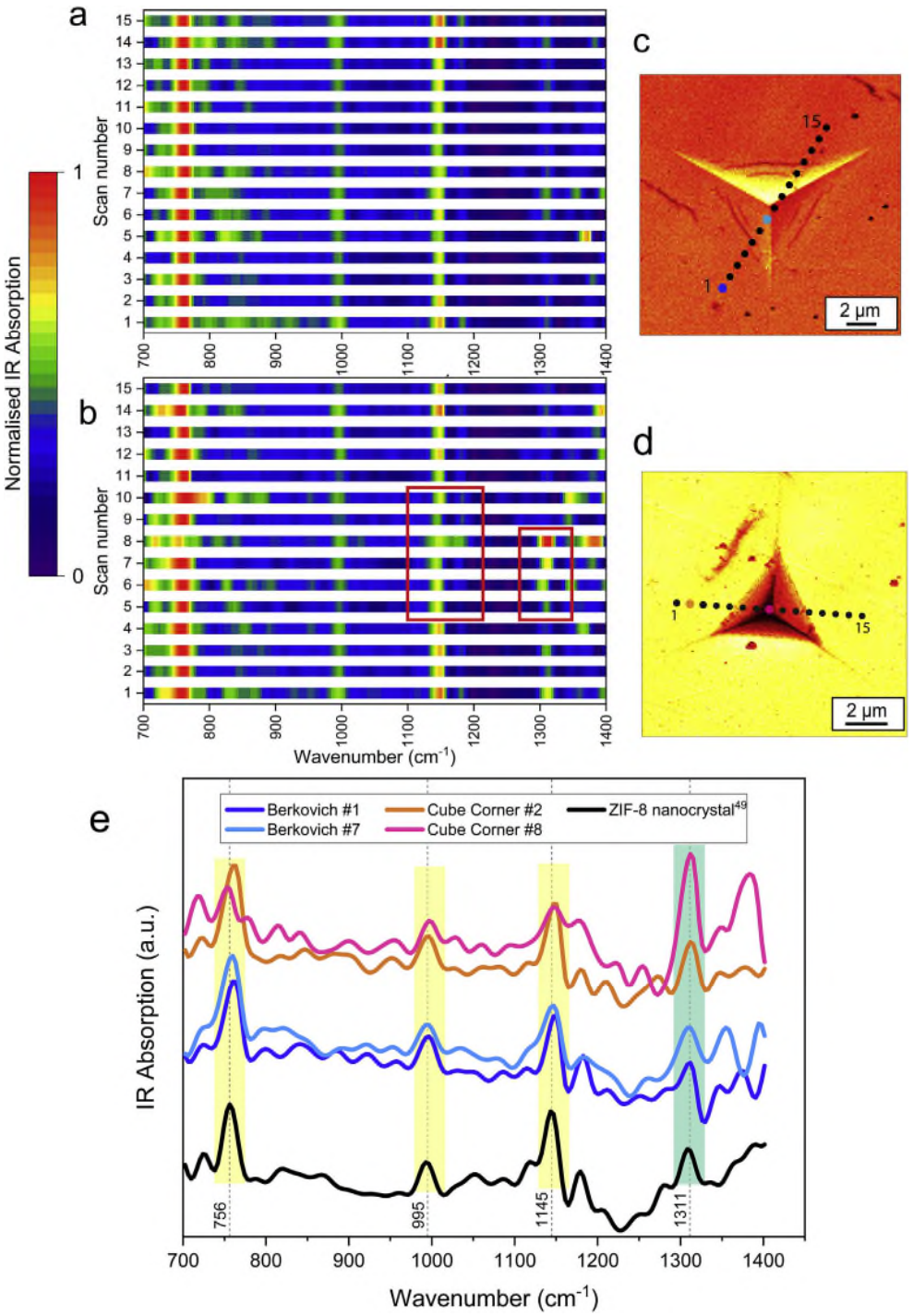

Fig. 5. Nano-FTIR absorption spectra of ZIF-8 monolith taken across (a) a Berkovich and (b) a cube corner residual indent, corresponding to the locations highlighted in (c) and (d), respectively. Note that (c) and (d) are the s-SNOM white light images. (e) Two spectra of each set, one measured outside and one inside the indent, were plotted and compared with the nano-FTIR spectra of an undeformed (pristine) ZIF-8 nanocrystal (adapted from the study reported by Moslein et al.[49]). The vibrational peaks at 756 cm^{-1}, 995 cm^{-1}, and 1145 cm^{-1} (highlighted in yellow) are related to the characteristic vibrational modes of ZIF-8, namely, out-of-plane deformation of mIm ring, in-plane stretching of the mIm ring and C–H rocking of mIm, respectively. The peak at 1311 cm^{-1} (in green) is related to pressure-induced defects in the framework, which developed as a result of indentation stress [45]. (For interpretation of the references to color in this figure legend, the reader is referred to the Web version of this article.)

pores or between the grains, increasing the bulk density of the monolith. Interestingly, the ZIF-71 monolith, as opposed to ZIF-8, shows a lower density compared with a theoretical value of 1.16 g/cm^3 (calculated from crystal structure, Cambridge Crystallographic Data Centre (CCDC) code GITVIP). This observation, consistently with the nanoindentation results, gives evidence of the more efficient packing of the ZIF-8 nanocrystals compared with the ZIF-71 counterpart. In fact, the poorer packing of ZIF-71 nanocrystals in monolith results in the formation of intergranular porosity (evident from TFM images presented in Section 3.2), which is more prevalent than that observed in ZIF-8 monolith. On this basis, we reasoned that for ZIF-71 monolith the impact of

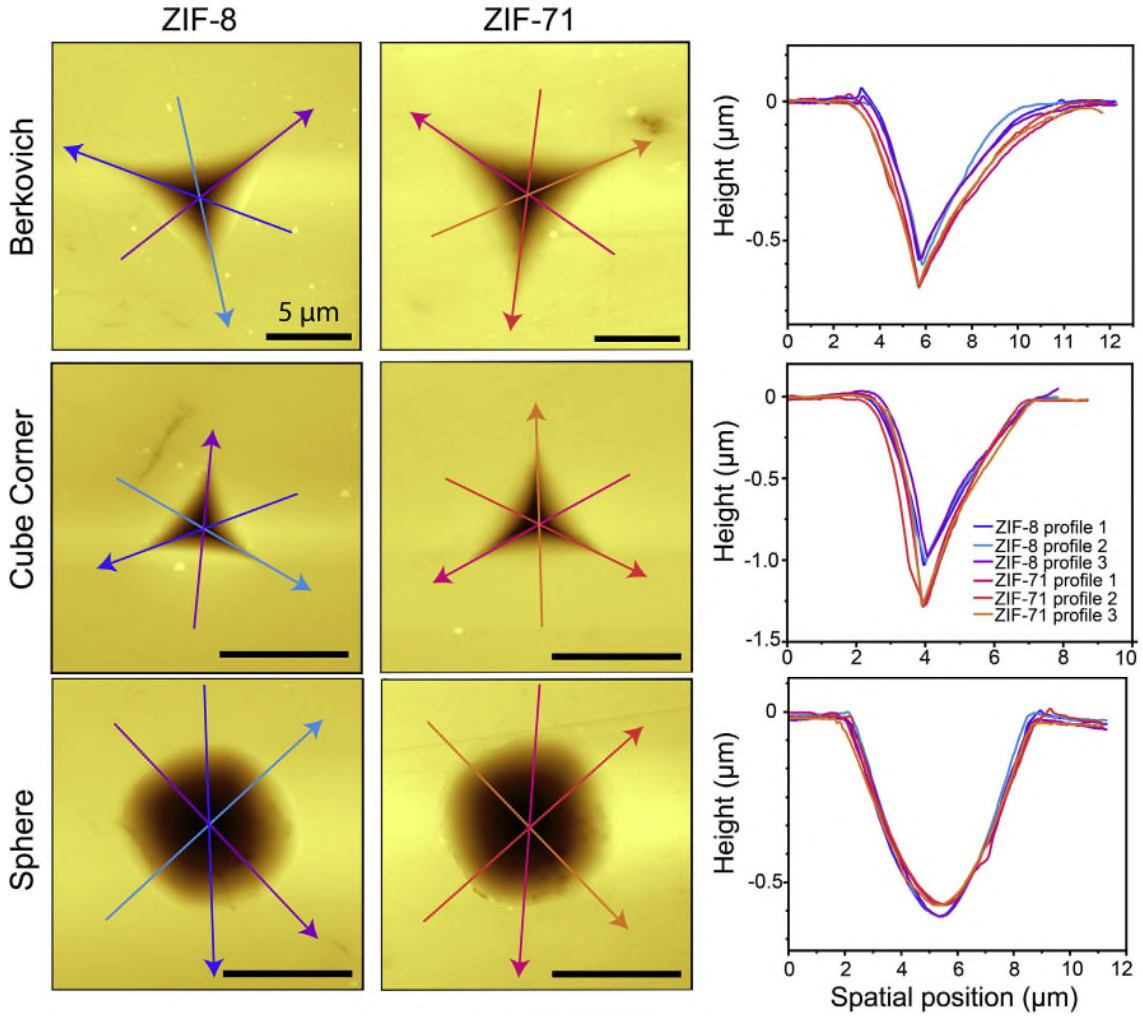

Fig. 6. AFM height topography of the residual indents of Berkovich, cube corner, and spherical indentations for ZIF-8 and ZIF-71 monoliths. The corresponding cross-sectional profiles along the designated paths are plotted on the right panels. The scale bar is 5 μm.

intergranular porosity supersedes that of impurities (dominant for ZIF-8 monolith) to yield a reduced bulk density.

From the load-depth curves, we also computed the elastic recovery, W_e, defined as the ratio between the area under the unloading and loading curves, respectively:

$$W_e = \frac{W_{elastic}}{W_{total}} = \frac{\int_{h_f}^{h_{max}} P_{unloading} dh}{\int_{0}^{h_{max}} P_{loading} dh} \quad (5)$$

where h_{max} is the maximum indentation depth, h_f is the residual depth after unloading, and $P_{unloading}$ and $P_{loading}$ are the loads applied on loading and unloading, respectively. We obtained the value $W_e = 64.1 \pm 1.8\%$ for ZIF-8 monoliths and $W_e = 59.9 \pm 2.4\%$ for ZIF-71 monoliths, which are consistent with values previously reported for porous ZIFs [13]. As per the classification proposed by Coates et al. [13], our monoliths follow the trend observed for other conventional materials [43] and fall into the category of materials with a high elastic recovery (Fig. 2c). This result, together with Young's modulus, suggests that the elastic response of the framework is not affected by the granular structure of the monoliths.

Finite element simulations of the indentation test of ZIF-8 monoliths were performed, by modeling the indenter as a rigid 2D axisymmetric cone (Fig. 3b). Because the monolithic sample was modeled as a homogeneous isotropic 'substrate', we calculated Young's modulus and hardness using the standard Oliver and Pharr method [35], instead of using the averaged value from CSM, which takes into account local effects. Equations (1) and (3) were used to calculate the modulus, where the contact stiffness (S) is the derivative of the unloading curve at maximum load. The Poisson's ratio (ν) was set to 0.4, consistent with the experiments. The hardness was computed by Equation (2). From FE modeling of nanoindentation, we determined that E = 2.87 GPa and H = 420 MPa for the ZIF-8 monolith and E = 1.80 GPa and H = 270 MPa for the ZIF-71 monolith.

As per Equation (4), the yield stress is directly related to the hardness via the constraint factor (C), which is not known *a priori* for our material; therefore, we need to make an assumption. We attempted different values of C and iterate to seek the best fit as the actual value of C, which usually lies in the range of 1.5–3 for conventional materials. We found the best fit to be C = 2.1 (Fig. S4), resulting in σ_Y = 200 MPa for ZIF-8 and σ_Y = 130 MPa for ZIF-71. Subsequently, the input material parameters for the simulations were set to be E = 2.87 GPa, ν = 0.4, and σ_Y = 200 MPa for ZIF-8. For

ZIF-71, the material parameters were set to be $E = 1.80$ GPa, $\nu = 0.4$, and $\sigma_Y = 130$ MPa.

The monolithic sample was modeled with two different material constitutive relations: the elastic-perfectly plastic model and the Drucker-Prager model. The latter model is suited for pressure-dependent materials, whose yield behavior depends on the hydrostatic pressure. The elastic-perfectly plastic model matches very well with the experimental data in the case of the Berkovich and spherical indenters for both ZIF-8 and ZIF-71. In the case of cube corner, which is sharper than the Berkovich indenter, it can be seen in Fig. 3a that such a model notably underestimates the maximum load. This can be explained by the effect of densification, which causes a reduction of the volume of material in the region immediately underneath the indenter under the effect of the hydrostatic pressure. Structural compression may occur owing to the collapse of nanopores in the framework. We established that this effect is significant only in the case of indentation with a cube corner indenter, which is characterized by a larger hydrostatic pressure generated under the indenter. According to Tan et al. [11], the amorphization of the ZIF-8 framework can be triggered by a shear stress, given its exceptionally low shear modulus, $G_{minimum} \lesssim 1$ GPa. We compared the shear stress fields at the maximum indentation depth (2000 nm) under the Berkovich, cube corner, and spherical indenters (Fig. 3c, d, e respectively). Similar contour plots were extracted for simulated ZIF-71 monoliths, showing the same trend, but values scaled down in proportion to σ_Y (Fig. S5). The shear stresses predicted immediately under the cube corner indenter are higher than the other two, meaning that ZIF-8 has the greater propensity to lose its crystallinity in this case. We propose that the framework densification is initiated by the shear stress that excessively distorts the porous framework (when shear yield stress, $\tau_{max} \gtrsim \sigma_Y/2$) triggering structural amorphization, which is then susceptible to undergo densification under the influence of a hydrostatic pressure.

3.2. Characterization of nanograined structures

TFM was used to image the surface of the monoliths. A nanograined microstructure, which we termed 'nanostructure,' was observed for the monoliths, see Fig. 4. Each nanograin is in fact a single crystal, and its size is below 100 nm. This reduced grain size suggests that the main deformation mechanism is grain boundary sliding (GBS), at least until a threshold value of stress, when, as per FE simulations, a certain amount of densification occurs. This mechanism is confirmed by nano-FTIR spectra taken across the residual indents. This near-field nanospectroscopic technique is capable of detecting pressure-induced structural amorphization of MOFs at the local scale (with a spatial resolution of ~20 nm), as previously elucidated by Babal et al. [44]. As it is visible from Fig. 5, the main ZIF-8 peaks remain unchanged in the Berkovich indent, but in the center, where the pressure is expected to be the highest, the infrared vibrational peaks at ~1311 cm^{-1} become more intense. As per a recent study [45], this particular peak can be associated with structural defects, namely, the missing imidazolate-type linker, induced by high stress or pressure. This phenomenon is even more pronounced inside the cube corner indent, where the stress level reached on loading is the highest, thereby resulting in bond breakage as evidenced by the local broadening of the nano-FTIR spectra shown in Fig. 5e.

AFM was used to observe the geometry of the residual pile-ups. As illustrated in Fig. 6, the residual indents left by each of the indenters in both ZIF-8 and ZIF-71 monoliths exhibit quite an insignificant pile-up. A small amount of pile-up is usually explained with a negligible work hardening, here facilitated by GBS mechanism, confirming that the elastic-perfectly plastic model represents a satisfactory approximation of the constitutive behavior of these monoliths. From a microstructural point of view, the absence of work hardening can be explained by the small size of the nanograins. Such a nanostructure also explains the absence of cracking in the vicinity of the indents. The reduced size of the grains facilitates the GBS mechanism. A similar behavior is observed for some conventional nanocrystalline material, for example, nanocrystalline ceramics, that exhibit ductility — perhaps even superplasticity — in compression, whereas their larger grained counterparts are extremely brittle [46]. The ductility may derive from the GBS and rotation, producing a flow of material [47]. For example, Karch et al. [48] indented (with a cube corner indenter) two samples of TiO_2, a conventional polycrystal and a nanocrystalline one: the first showed a brittle behavior, characterized by cracking and high hardness, whereas the latter exhibited a lower hardness and a ductile behavior, evidenced by the absence of cracking. We propose that this type of nanograined-induced phenomenon can be extended to our monolithic ZIFs.

Table 2
Values of the fracture toughness K_{IC} determined for the two monoliths using the residual indents generated by using a cube corner indenter in Fig. 7.

Monolith	Fracture toughness K_{IC} (MPa$\sqrt{m}$)
ZIF-8	0.074 ± 0.023
ZIF-71	0.145 ± 0.050

3.3. Fracture toughness

The fracture toughness (K_{IC}) of the ZIF-8 and ZIF-71 monoliths was evaluated by the indentation crack length method that relies on nanoindentation measurements obtained by using a cube corner indenter. Assuming a Palmqvist crack configuration, the Laugier's formula [50] was used:

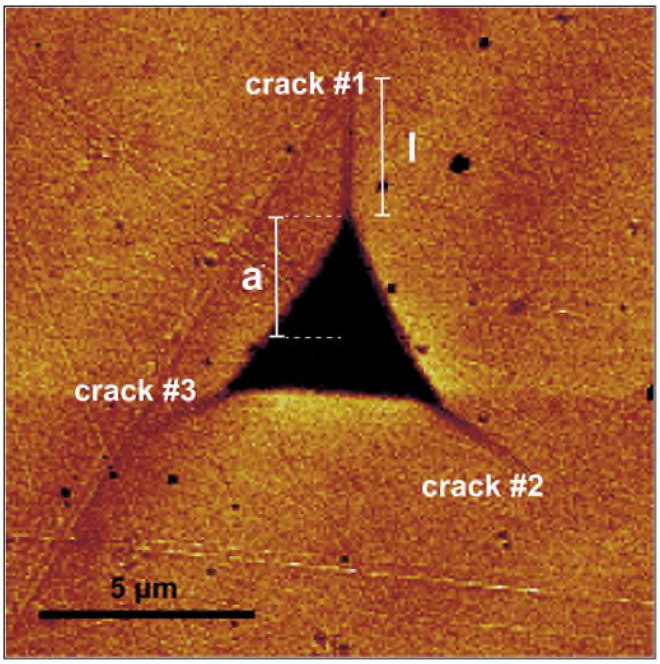

Fig. 7. Indentation-induced crack length measurement method for a cube corner residual indent on the surface of a ZIF-8 monolith. The radial cracks became clearly visible under the s-SNOM white light imaging mode.

$$K_{IC} = k\,(\frac{a}{l})^{\frac{1}{2}}(\frac{E}{H})^{\frac{2}{3}}\frac{P}{c^{\frac{3}{2}}} \quad (6)$$

where is k is an empirical constant of the indenter shape ($k = 0.057$ for cube corner [51]), a is the distance between the center and the tip of the indent, l is the crack length starting from the corner of the indent, E and H are Young's modulus and hardness, respectively, P is the maximum load, and $c = a + l$.

The obtained values of K_{IC} are shown in Table 2. Between the two monoliths being studied here, we show the ZIF-8 monolith is relatively easier to crack: the radial cracks propagating from the indent's corners are visible already with a maximum indentation depth of 2 μm (Fig. 7). ZIF-71 turned out to be twice as tough as ZIF-8, and a maximum indentation depth of 5 μm was required to detect any cracks. The fracture toughness obtained is consistent with the few values available in the literature, which reported the toughness of other classes of MOF materials, in the form of single crystals (0.08–0.33 MPa$\sqrt{m}$, for layered 2D to dense 3D frameworks) [10] and ZIF-62 glass by melting method (approximately 0.1 MPa$\sqrt{m}$) [52].

4. Conclusions

Two types of zeolitic MOF monoliths (ZIF-8 and ZIF-71) have been synthesized by a simple sol-gel process, a low-cost technique to produce MOF monoliths that do not require any support materials such as templates or binders and can be performed at room temperature and without the need of high compacting pressures. The mechanical properties were studied by means of Berkovich, cube corner, and spherical nanoindentation, AFM, and TFM imaging, where the experimental findings are further substantiated by FE simulations. The mechanical behavior of the material is well approximated by a simple elastic-perfectly plastic material, exhibiting a good ductility in compression. This result, together with the fine-grained nanostructure observed by TFM, suggests that the monoliths initially deform by GBS. When the stress increases, some densification occurs, owing to the failure of the framework, presumably triggered by shear, in the contact area, as demonstrated by nano-FTIR measurements of the local vibrational spectra. Our findings provide a starting point to gain new understanding of the mechanical behavior of sol-gel MOF monoliths, which is crucial for the transition of this class of materials from academia to practical applications.

Author contributions

Michele Tricarico: Conceptualization, Methodology, Software, Investigation, Data Curation, Writing – Original Draft, Visualization.

Jin-Chong Tan: Resources, Writing - Review & Editing, Supervision, Funding acquisition.

Declaration of competing interest

The authors declare that they have no known competing financial interests or personal relationships that could have appeared to influence the work reported in this paper.

Acknowledgments

The authors thank the ERC Consolidator Grant (PROMOFS grant agreement 771575) for funding this research.

Appendix A. Supplementary data

Supplementary data to this article can be found online at https://doi.org/10.1016/j.mtnano.2021.100166.

References

[1] H. Furukawa, K.E. Cordova, M. O'Keeffe, O.M. Yaghi, The chemistry and applications of metal-organic frameworks, Science 341 (2013) 1230444, https://doi.org/10.1126/science.1230444.
[2] R. Freund, et al., 25 Years of reticular chemistry, Angew. Chem. Int. Ed. (2021), https://doi.org/10.1002/anie.202101644.
[3] P. Falcaro, R. Ricco, C.M. Doherty, K. Liang, A.J. Hill, M.J. Styles, MOF positioning technology and device fabrication, Chem. Soc. Rev. 43 (2014) 5513–5560, https://doi.org/10.1039/c4cs00089g.
[4] I. Stassen, N. Burtch, A. Talin, P. Falcaro, M. Allendorf, R. Ameloot, An updated roadmap for the integration of metal-organic frameworks with electronic devices and chemical sensors, Chem. Soc. Rev. 46 (2017) 3185–3241, https://doi.org/10.1039/c7cs00122c.
[5] A. Bavykina, N. Kolobov, I.S. Khan, J.A. Bau, A. Ramirez, J. Gascon, Metal–organic frameworks in heterogeneous catalysis: recent progress, new trends, and future perspectives, Chem. Rev. 120 (2020) 8468–8535, https://doi.org/10.1021/acs.chemrev.9b00685.
[6] M.R. Ryder, J.-C. Tan, Nanoporous metal organic framework materials for smart applications, Mater. Sci. Technol. 30 (2014) 1598–1612, https://doi.org/10.1179/1743284714y.0000000550.
[7] J.C. Tan, A.K. Cheetham, Mechanical properties of hybrid inorganic-organic framework materials: establishing fundamental structure-property relationships, Chem. Soc. Rev. 40 (2011) 1059–1080, https://doi.org/10.1039/c0cs00163e.
[8] L.R. Redfern, O.K. Farha, Mechanical properties of metal–organic frameworks, Chem. Sci. 10 (2019) 10666–10679, https://doi.org/10.1039/c9sc04249k.
[9] N.C. Burtch, J. Heinen, T.D. Bennett, D. Dubbeldam, M.D. Allendorf, Mechanical properties in metal-organic frameworks: emerging opportunities and challenges for device functionality and technological applications, Adv. Mater. 30 (2018) 1704124, https://doi.org/10.1002/adma.201704124.
[10] J.C. Tan, C.A. Merrill, J.B. Orton, A.K. Cheetham, Anisotropic mechanical properties of polymorphic hybrid inorganic–organic framework materials with different dimensionalities, Acta Mater. 57 (2009) 3481–3496, https://doi.org/10.1016/j.actamat.2009.04.004.
[11] J.C. Tan, B. Civalleri, C.C. Lin, L. Valenzano, R. Galvelis, P.F. Chen, T.D. Bennett, C. Mellot-Draznieks, C.M. Zicovich-Wilson, A.K. Cheetham, Exceptionally low shear modulus in a prototypical imidazole-based metal-organic framework, Phys. Rev. Lett. 108 (2012), 095502, https://doi.org/10.1103/PhysRevLett.108.095502.
[12] J.C. Tan, T.D. Bennett, A.K. Cheetham, Chemical structure, network topology, and porosity effects on the mechanical properties of Zeolitic Imidazolate Frameworks, Proc. Natl. Acad. Sci. U.S.A. 107 (2010) 9938–9943, https://doi.org/10.1073/pnas.1003205107.
[13] C.S. Coates, M.R. Ryder, J.A. Hill, J.C. Tan, A.L. Goodwin, Large elastic recovery of zinc dicyanoaurate, Apl. Mater. 5 (2017), 066107, https://doi.org/10.1063/1.4990549.
[14] T.D. Bennett, D.A. Keen, J.C. Tan, E.R. Barney, A.L. Goodwin, A.K. Cheetham, Thermal amorphization of zeolitic imidazolate frameworks, Angew. Chem. Int. Ed. 50 (2011) 3067–3071, https://doi.org/10.1002/anie.201007303.
[15] S. Bundschuh, O. Kraft, H.K. Arslan, H. Gliemann, P.G. Weidler, C. Wöll, Mechanical properties of metal-organic frameworks: an indentation study on epitaxial thin films, Appl. Phys. Lett. 101 (2012) 101910, https://doi.org/10.1063/1.4751286.
[16] T. Tian, Z. Zeng, D. Vulpe, M.E. Casco, G. Divitini, P.A. Midgley, J. Silvestre-Albero, J.C. Tan, P.Z. Moghadam, D. Fairen-Jimenez, A sol-gel monolithic metal-organic framework with enhanced methane uptake, Nat. Mater. 17 (2018) 174–179, https://doi.org/10.1038/nmat5050.
[17] T. Tian, J. Velazquez-Garcia, T.D. Bennett, D. Fairen-Jimenez, Mechanically and chemically robust ZIF-8 monoliths with high volumetric adsorption capacity, J. Mater. Chem. 3 (2015) 2999–3005, https://doi.org/10.1039/c4ta05116e.
[18] A. Phan, C.J. Doonan, F.J. Uribe-Romo, C.B. Knobler, M. O'Keeffe, O.M. Yaghi, Synthesis, structure, and carbon dioxide capture properties of zeolitic imidazolate frameworks, Acc. Chem. Res. 43 (2010) 58–67, https://doi.org/10.1021/ar900116g.
[19] J. Hou, A.F. Sapnik, T.D. Bennett, Metal–organic framework gels and monoliths, Chem. Sci. 11 (2020) 310–323, https://doi.org/10.1039/c9sc04961d.
[20] B.M. Connolly, D.G. Madden, A.E.H. Wheatley, D. Fairen-Jimenez, Shaping the future of fuel: monolithic metal-organic frameworks for high-density gas storage, J. Am. Chem. Soc. 142 (2020) 8541–8549, https://doi.org/10.1021/jacs.0c00270.
[21] A. Sachse, R. Ameloot, B. Coq, F. Fajula, B. Coasne, D. De Vos, A. Galarneau, In situ synthesis of Cu-BTC (HKUST-1) in macro-/mesoporous silica monoliths for continuous flow catalysis, Chem. Commun. 48 (2012) 4749–4751, https://doi.org/10.1039/c2cc17190b.
[22] D. Qian, C. Lei, G.P. Hao, W.C. Li, A.H. Lu, Synthesis of hierarchical porous carbon monoliths with incorporated metal-organic frameworks for enhancing

volumetric based CO(2) capture capability, ACS Appl. Mater. Interf. 4 (2012) 6125–6132, https://doi.org/10.1021/am301772k.
[23] P. Küsgens, A. Zgaverdea, H.-G. Fritz, S. Siegle, S. Kaskel, Metal-organic frameworks in monolithic structures, J. Am. Ceram. Soc. 93 (2010) 2476–2479, https://doi.org/10.1111/j.1551-2916.2010.03824.x.
[24] H. Thakkar, S. Eastman, Q. Al-Naddaf, A.A. Rownaghi, F. Rezaei, 3D-Printed metal-organic framework monoliths for gas adsorption processes, ACS Appl. Mater. Interfaces 9 (2017) 35908–35916, https://doi.org/10.1021/acsami.7b11626.
[25] A.K. Chaudhari, J.C. Tan, Dual-guest functionalized zeolitic imidazolate framework-8 for 3D printing white light-emitting composites, Adv. Opt. Mater. 8 (2020) 1901912, https://doi.org/10.1002/adom.201901912.
[26] R.N. Widmer, G.I. Lampronti, B. Kunz, C. Battaglia, J.H. Shepherd, S.A.T. Redfern, T.D. Bennett, Manufacturing macroporous monoliths of microporous metal–organic frameworks, ACS Appl. Nano Mater. 1 (2018) 497–500, https://doi.org/10.1021/acsanm.7b00335.
[27] J. Dhainaut, C. Avci-Camur, J. Troyano, A. Legrand, J. Canivet, I. Imaz, D. Maspoch, H. Reinsch, D. Farrusseng, Systematic study of the impact of MOF densification into tablets on textural and mechanical properties, Cryst. Eng. Comm. 19 (2017) 4211–4218, https://doi.org/10.1039/c7ce00338b.
[28] A. Ahmed, M. Forster, R. Clowes, P. Myers, H. Zhang, Hierarchical porous metal-organic framework monoliths, Chem. Commun. 50 (2014) 14314–14316, https://doi.org/10.1039/c4cc06967f.
[29] N. Moitra, S. Fukumoto, J. Reboul, K. Sumida, Y. Zhu, K. Nakanishi, S. Furukawa, S. Kitagawa, K. Kanamori, Mechanically stable, hierarchically porous $Cu_3(btc)_2$ (HKUST-1) monoliths via direct conversion of copper(II) hydroxide-based monoliths, Chem. Commun. 51 (2015) 3511–3514, https://doi.org/10.1039/c4cc09694k.
[30] B.M. Connolly, M. Aragones-Anglada, J. Gandara-Loe, N.A. Danaf, D.C. Lamb, J.P. Mehta, D. Vulpe, S. Wuttke, J. Silvestre-Albero, P.Z. Moghadam, A.E.H. Wheatley, D. Fairen-Jimenez, Tuning porosity in macroscopic monolithic metal-organic frameworks for exceptional natural gas storage, Nat. Commun. 10 (2019) 2345, https://doi.org/10.1038/s41467-019-10185-1.
[31] E. Hunter-Sellars, P.A. Saenz-Cavazos, A.R. Houghton, S.R. McIntyre, I.P. Parkin, D.R. Williams, Sol–gel synthesis of high-density zeolitic imidazolate framework monoliths via ligand assisted methods: exceptional porosity, hydrophobicity, and applications in vapor adsorption, Adv. Funct. Mater. 31 (2020) 2008357, https://doi.org/10.1002/adfm.202008357.
[32] A. Feinle, M.S. Elsaesser, N. Husing, Sol-gel synthesis of monolithic materials with hierarchical porosity, Chem. Soc. Rev. 45 (2016) 3377–3399, https://doi.org/10.1039/c5cs00710k.
[33] A.K. Chaudhari, I. Han, J.C. Tan, Multifunctional supramolecular hybrid materials constructed from hierarchical self-ordering of in situ generated metal-organic framework (MOF) nanoparticles, Adv. Mater. 27 (2015) 4438–4446, https://doi.org/10.1002/adma.201501448.
[34] A.K. Chaudhari, H.J. Kim, I. Han, J.C. Tan, Optochemically responsive 2D nanosheets of a 3D metal-organic framework material, Adv. Mater. 29 (2017) 8491–8626, https://doi.org/10.1002/adma.201701463.
[35] W.C. Oliver, G.M. Pharr, An improved technique for determining hardness and elastic modulus using load and displacement sensing indentation experiments, J. Mater. Res. 7 (1992) 1564–1583, https://doi.org/10.1557/jmr.1992.1564.
[36] D. Tabor, Indentation hardness: fifty years on a personal view, Philos. Mag. A 74 (1996) 1207–1212, https://doi.org/10.1080/01418619608239720.
[37] J. Hay, P. Agee, E. Herbert, Continuous stiffness measurement during instrumented indentation testing, Exp. Tech. 34 (2010) 86–94, https://doi.org/10.1111/j.1747-1567.2010.00618.x.
[38] A. Rosa-Zeiser, E. Weilandt, S. Hild, O. Marti, The simultaneous measurement of elastic, electrostatic and adhesive properties by scanning force microscopy: pulsed-force mode operation, Meas. Sci. Technol. 8 (1997) 1333–1338, https://doi.org/10.1088/0957-0233/8/11/020.
[39] H.U. Krotil, T. Stifter, H. Waschipky, K. Weishaupt, S. Hild, O. Marti, Pulsed force mode: a new method for the investigation of surface properties, Surf. Interface Anal. 27 (1999) 336–340, https://doi.org/10.1002/(SICI)1096-9918(199905/06)27:5/6<336::AID-SIA512>3.0.CO;2-0.
[40] M. Smith, ABAQUS/Standard User's Manual, Simulia, Providence, RI, 2009. Version 6.9.
[41] M. Lichinchi, C. Lenardi, J. Haupt, R. Vitali, Simulation of Berkovich nanoindentation experiments on thin films using finite element method, Thin Solid Films 312 (1998) 240–248, https://doi.org/10.1016/s0040-6090(97)00739-6.
[42] L. Charleux, L. Bizet, Vkeryvin, Mousta, Abapy v1.0, Zenodo, 2015.
[43] Y.-T. Cheng, C.-M. Cheng, Relationships between hardness, elastic modulus, and the work of indentation, Appl. Phys. Lett. 73 (1998) 614–616, https://doi.org/10.1063/1.121873.
[44] A.S. Babal, B.E. Souza, A.F. Möslein, M. Gutiérrez, M.D. Frogley, J.-C. Tan, Broadband dielectric behavior of an MIL-100 metal–organic framework as a function of structural amorphization, ACS Appl. Electron. Mater. 3 (2021) 1191–1198, https://doi.org/10.1021/acsaelm.0c01045.
[45] A.F. Möslein, L. Donà, B. Civalleri, J.-C. Tan, Defects in ZIF-8 Crystallization and Their Impact on Mechanical Properties, arXiv preprint, 2021 arXiv: 2109.05557.
[46] C.C. Koch, Structural nanocrystalline materials: an overview, J. Mater. Sci. 42 (2007) 1403–1414, https://doi.org/10.1007/s10853-006-0609-3.
[47] H. Gleiter, Nanocrystalline materials, Prog. Mater. Sci. 33 (1989) 223–315, https://doi.org/10.1016/0079-6425(89)90001-7.
[48] J. Karch, R. Birringer, H. Gleiter, Ceramics ductile at low temperature, Nature 330 (1987) 556–558, https://doi.org/10.1038/330556a0.
[49] A.F. Moslein, M. Gutierrez, B. Cohen, J.C. Tan, Near-field infrared nanospectroscopy reveals guest confinement in metal-organic framework single crystals, Nano Lett. 20 (2020) 7446–7454, https://doi.org/10.1021/acs.nanolett.0c02839.
[50] M.T. Laugier, New formula for indentation toughness in ceramics, J. Mater. Sci. Lett. 6 (1987) 355–356, https://doi.org/10.1007/Bf01729352.
[51] N. Cuadrado, D. Casellas, M. Anglada, E. Jiménez-Piqué, Evaluation of fracture toughness of small volumes by means of cube-corner nanoindentation, Scripta Mater. 66 (2012) 670–673, https://doi.org/10.1016/j.scriptamat.2012.01.033.
[52] T. To, S.S. Sorensen, M. Stepniewska, A. Qiao, L.R. Jensen, M. Bauchy, Y. Yue, M.M. Smedskjaer, Fracture toughness of a metal-organic framework glass, Nat. Commun. 11 (2020) 2593, https://doi.org/10.1038/s41467-020-16382-7.

5 Indentation Fracture Toughness of MOF Monoliths

5.1 Background and motivations

Materials processing and manufacturing may often introduce flaws, defects, or porosity in a finished mechanical component. Such defects represent unwanted features that degrade the mechanical performances. Fracture mechanics consists of the analysis of flaws, allowing to differentiate the “safe” ones (i.e., cracks which do not grow, concept of “damage tolerance”) from those that catastrophically propagate leading to the fast fracture of the component.

Most practical engineering problems can be easily solved by using linear elastic fracture mechanics (LEFM), that models the propagation of cracks in linearly elastic isotropic materials. This theory was firstly developed by the English engineer A. A. Griffith during World War I. He used a thermodynamic approach, based on the energy release rate (G), i.e., the rate at which strain energy is dissipated as the crack propagates (139). It is defined as the loss of total potential energy U per unit crack growth area s:

$$G = -\frac{\partial U}{\partial s} \tag{5.1}$$

When a critical value G_C is reached ($G \geq G_C$), crack propagation will start.

This criterion can be expressed in term of stress (σ) by introducing the stress intensity factor K_I (140):

$$K_I = Y\sigma\sqrt{\pi a} \tag{5.2}$$

Where a is the crack length and Y a dimensionless factor dependent on the crack geometry. Crack propagation begins when $K_I \geq K_{IC}$.

The critical value K_{IC} is known as the fracture toughness, and it represents the mechanical property that describes the resistance of materials to crack propagation.

Fracture toughness of "bulk" engineering materials is normally measured using notched specimens in various configurations such as the Charpy impact test or three-point beam bending tests. However, for micro-sized materials like MOFs, the fabrication of these type of samples is not always possible (141, 142). In this instance, nanoindentation-based methods represent a valuable alternative. As already mentioned in Chapter 4, these methods allow to estimate K_{IC} from the length of indentation cracks, propagating from the indent's corner. The use of indentation to measure fracture toughness was introduced in the mid-1970s, with the classic Lawn-Evan-Marshall (LEM) (143, 144) approach for brittle bulk ceramics and it rapidly gained popularity (145, 146). Many other models have been proposed since then (135, 137, 147, 148), which consider various material property combinations and crack geometries. The latter are very important for the selection of most suitable model. We can discern different type of crack systems, such as median, radial, half-penny, cone, or lateral cracks (Figure 5.1).

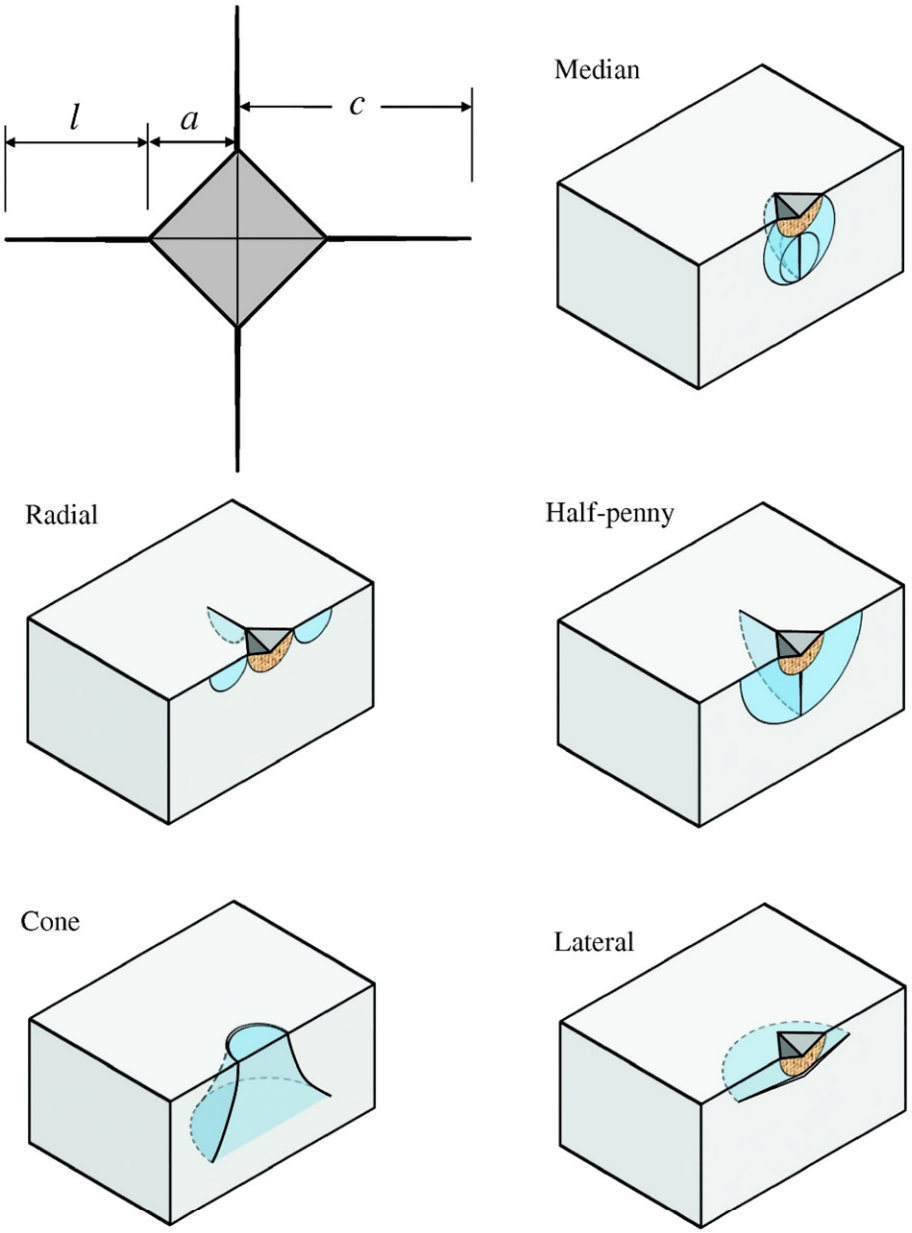

Figure 5.1 Example of possible crack geometries under sharp indentation loading. Reproduced with permission from (149).

As discussed in Chapter 4, the fracture toughness of ZIF-8 and ZIF-71 monoliths have been estimated by using a nanoindentation-based methods. Nevertheless, the origin of material failure, particularly in connection to the nature of crack initiation and propagation has not been investigated.

The goal of this chapter is to shed light on the fracture behaviour of four different MOF monoliths (ZIF-8, HKUST-1, MIL-68 and MOF-808) and the underpinning mechanisms behind it. A correlation between the fracture behaviour and the structure of the materials (both at the nanostructural and framework level) was found. This study was achieved by leveraging a combination of nanoindentation, microindentation and nanoscratching experiments.

To the best of my knowledge, this specific area of MOF monoliths mechanics has not been explored thus far. Only a few studies have touched on the field of MOF fracture, but these are limited to single crystals (73) and glasses (102, 103).

5.2 Summary of paper II

5.2.1 Nano and micro indentation-driven cracks

The mechanical properties, i.e., indentation modulus (E^*) and hardness (H), of the four as-synthesised monoliths were assessed by nanoindentation, using a Berkovich tip. The results are illustrated in Figure 5.2 and Table 5.1.

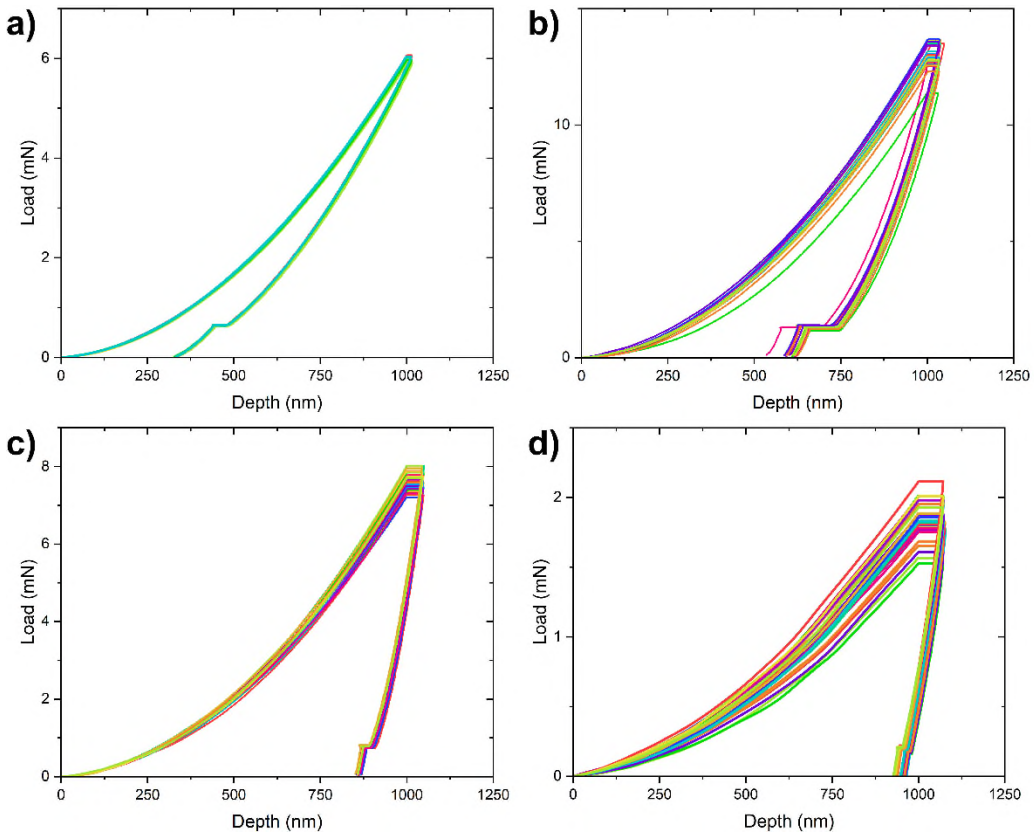

Figure 5.2 Nanoidentation load-depth curves with a Berkovich indenter to a maximum surface penetration depth of 1000 nm. a) ZIF-8, b) HKUST-1, c) MIL-68 and d) MOF-808. 32 indentations per sample were performed.

Monolith Sample	Density (g/cm^3)	Indentation Modulus E^* (GPa)	Poisson's Ratio ν	Young's Modulus E (GPa)	Hardness H (MPa)	Elastic energy $W_{elastic}/W_{total}$ (%)	Residual depth – load-depth curves (nm)	Residual depth – AFM (nm)
ZIF-8 ref. (13)	1.246 ± 0.010	3.78 ± 0.44	0.43 ref. (75)	3.18 ± 0.04	452 ± 20	64.1 ± 1.8	-	-
ZIF-8 This work	1.258 ± 0.022	4.03 ± 0.03	0.43 ref. (75)	3.28 ± 0.03	534 ± 6	65.3 ± 1.4	336 ± 5	246 ± 4
HKUST-1	1.529 ± 0.043	15.25 ± 0.61	0.45 ref. (100)	12.16 ± 0.48	761 ± 53	39.0 ± 1.8	602 ± 18	200 ± 1
MIL-68	1.475 ± 0.007	13.24 ± 0.52 ref. (62)	-	-	402 ± 13 ref. (62)	19.2 ± 1.0	861 ± 5	567 ± 20
MOF-808	1.522 ± 0.104	4.61 ± 0.32	-	-	122 ± 14	13.6 ± 1.1	948 ± 13	538 ± 5

Table 5.1 Mechanical properties of the monoliths obtained from nanoindentation with a Berkovich tip. The values for E^* (letting $\nu = 0$) and H were computed by averaging the CSM data between 500 and 1000 nm. For the materials whose Poisson's ratio (ν) is known from simulations study, also the Young's modulus was computed. The mean and standard deviations were calculated from 32 individual indents. The residual depth at the end of the indentation test was determined from the load-depth curves (Figure 5.2).

The four monoliths exhibit different values of elastic energy, $W_{elastic}/W_{total}$, computed as the ratio between the area under the unloading and loading curves respectively:

$$\frac{W_{\text{elastic}}}{W_{\text{total}}} = \frac{\int_{h_f}^{h_{\max}} P_{\text{unloading}}\, dh}{\int_{0}^{h_{\max}} P_{\text{loading}}\, dh} \tag{5.3}$$

where h_{max} is the maximum indentation depth, h_f the residual depth after unloading, and $P_{unloading}$ and $P_{loading}$ are the loads applied upon loading and unloading,

respectively. In particular, ZIF-8 shows high elastic recovery, HKUST-1 an intermediate one, while MIL-68 and MOF-808 exhibit a low elastic recovery (Figure 1b in Paper II). This mechanical response is ascribed to the different framework architectures.

AFM height topographies of the residual indents (Figure 5.3) indicate a reduction of residual depth compared to the load-depth curves in Figure 5.2, as reported in Table 5.1. This was attributed to viscoelastic recovery, associated with the organic component of MOFs.

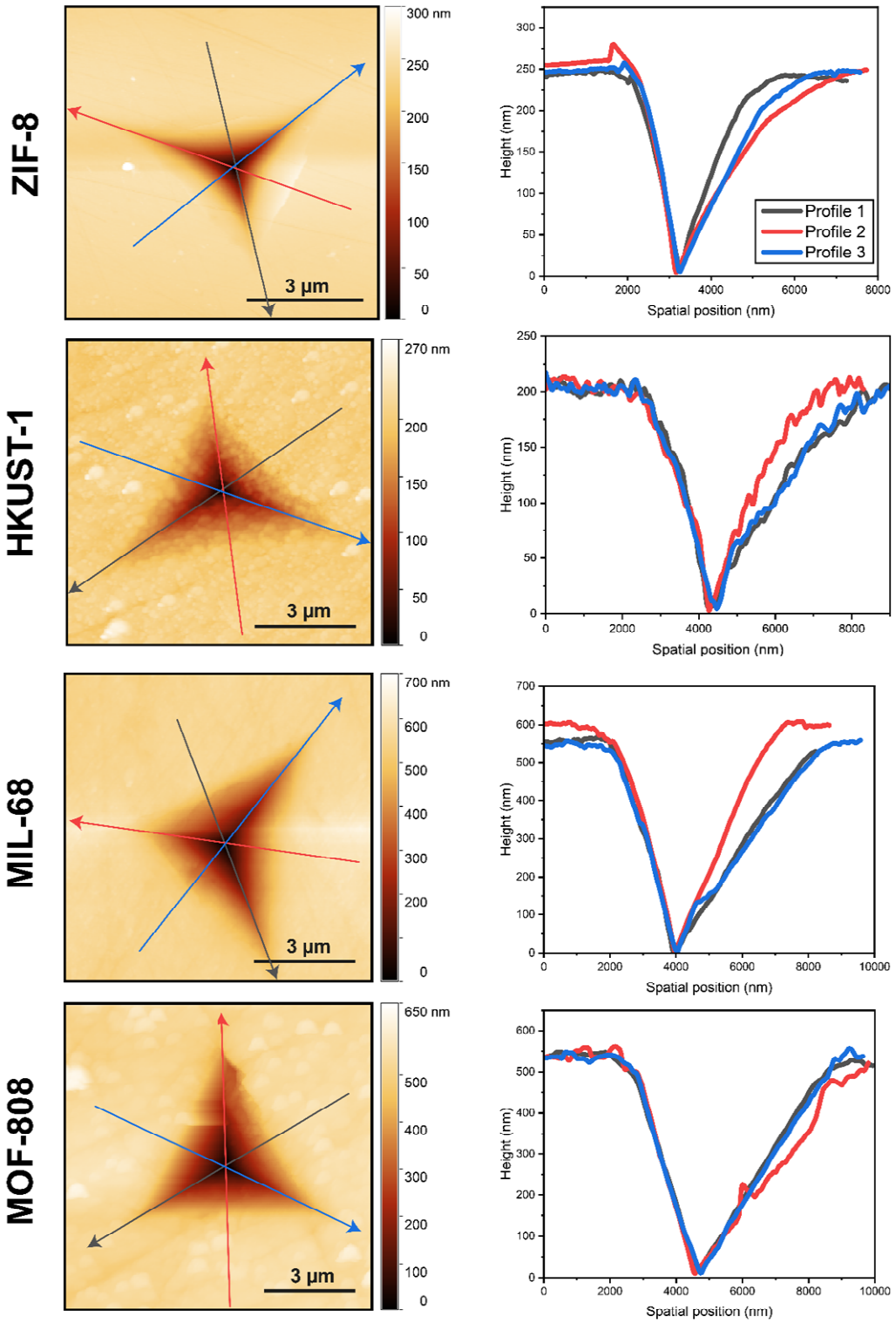

Figure 5.3 AFM height topographies of the residual indents on the four monoliths. The corresponding cross-sectional profiles along the specified paths are plotted on the right.

Following the same procedures described in section 2.4 of Chapter 4, a cube corner indenter was employed to induce and measure cracks. Surprisingly, only ZIF-8 and HKUST-1 show cracks propagating from the corner of the indents, while MIL-68 and MOF-808 monoliths are completely radial crack-free in the apparent vicinity of the residual indent (Figure 5.4). For HKUST-1, a fracture toughness of $K_c = 0.80 \pm 0.45$ MPa $m^{1/2}$ was estimated with Laugier's formula (equation. 4.1), making it the toughest MOF material reported so far (see Table 5.2). Notably, HKUST-1 is also the material exhibiting the lowest elastic recovery amongst the ones listed in Table 5.2. This, together with MIL-68 and MOF-808 (low elastic recovery) not showing any surface cracks, suggests that elastic recovery plays a prominent role in crack propagation. A correlation between elastic recovery and radial cracks propagation was proposed by Lawn *et al.* (147) for bulk ceramics. In a nutshell, the authors suggest that lateral and radial cracks initiate and propagate upon unloading, driven by residual stresses. These stresses result from the elastic-plastic mismatch existing at border of the plastic zone immediately underneath the indenter. This mechanism is described in detail in the discussion section of Paper II and illustrated in Figure 5.5.

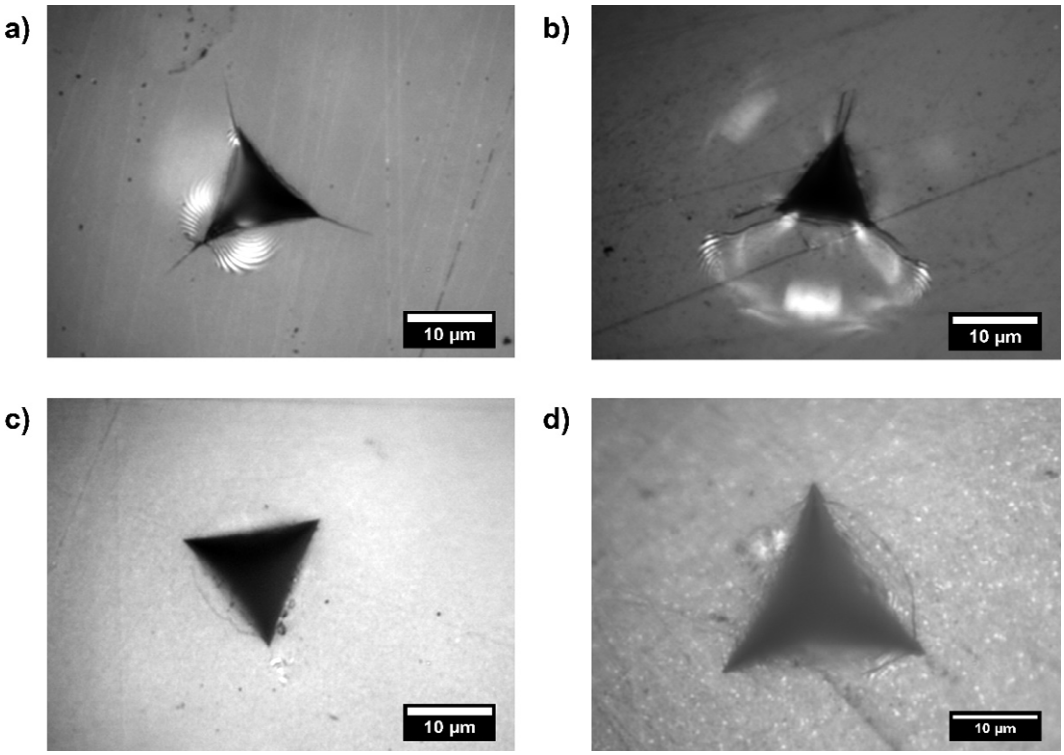

Figure 5.4 Cube corner residual indents on a) ZIF-8, b) HKUST-1, c) MIL-68, and d) MOF-808. A maximum load of 50 mN was applied in all tests.

Material	K_C (MPa m$^{1/2}$)	$W_{elastic}/W_{total}$ (%)	Reference
HKUST-1 monolith	0.80 ± 0.45	39.0 ± 1.8	This work
ZIF-8 monolith	0.074 ± 0.023	64.1 ± 1.8	(13) (Paper I)
ZIF-71 monolith	0.145 ± 0.050	59.9 ± 2.4	(13) (Paper I)
ZIF-62 glass	0.104 ± 0.020	53.8	(102)
Dense frameworks (CuPA1 and CuPA2)	0.1 – 0.3	39.9 ± 6.1	(73)

Table 5.2 Values of indentation fracture toughness and elastic energy of MOF materials reported in the literature so far.

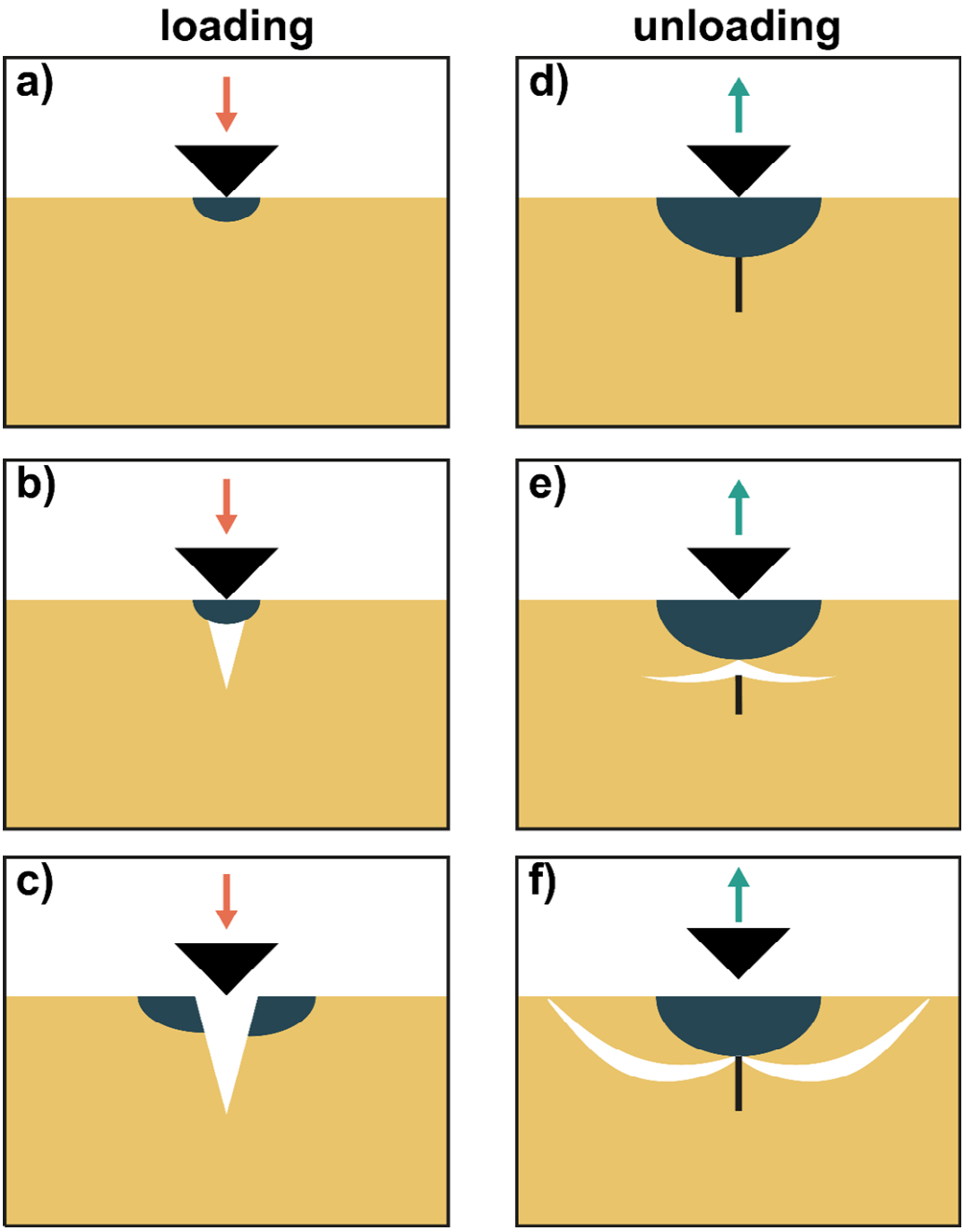

Figure 5.5 Evolution of cracks during sharp indentation: a) formation of plastic zone; b) sub-surface "penny-like" crack due to tensile stresses; c) downward and outward growth of the median crack that may lead the crack to break-through (however, if the sample is not heavily loaded, the crack remains sub-surface until unloading); d) upon unloading, the crack wants to close up, but this is precluded by residual stresses (elastic-plastic mismatch); e) the residual stress causes the formation of lateral cracks; f) extension of lateral crack upon unloading, driven by residual stress which may also drive partially developed sub-surface median cracks to completion.

With the aim of inducing radial cracks, a microhardness Vickers indenter, capable of applying much higher loads was employed (in the order of a few N, as opposed to the 50 mN maximum capacity of the nanoindentation system used). Nonetheless, using a load of 0.5 N, no cracks were induced from the indent's corner, not even in ZIF-8 and HKUST-1 that previously cracked under cube corner indentation.

However, shear faults were observed within the contact area (Figure 2 in Paper II). These features have been previously observed in soda lime glass (150) and notably in ZIF-62 glass (103).

Some cracks were observed on the surface of the monoliths when much higher loads were applied, namely 5 N for MIL-68 (Figure 5.6a) and 3 N (Figure 5.6b) for MOF-808, albeit propagating from the shear faults inside the contact area, rather than the indent's corners. However, when a 5 N indentation test was repeated on MIL-68, no cracks were observed (Figure 5.6c), suggesting that the cracks previously observed had nucleated from pre-existing defects within the monoliths (i.e., porosity and flaws resulting from gel drying), given the extended contact area.

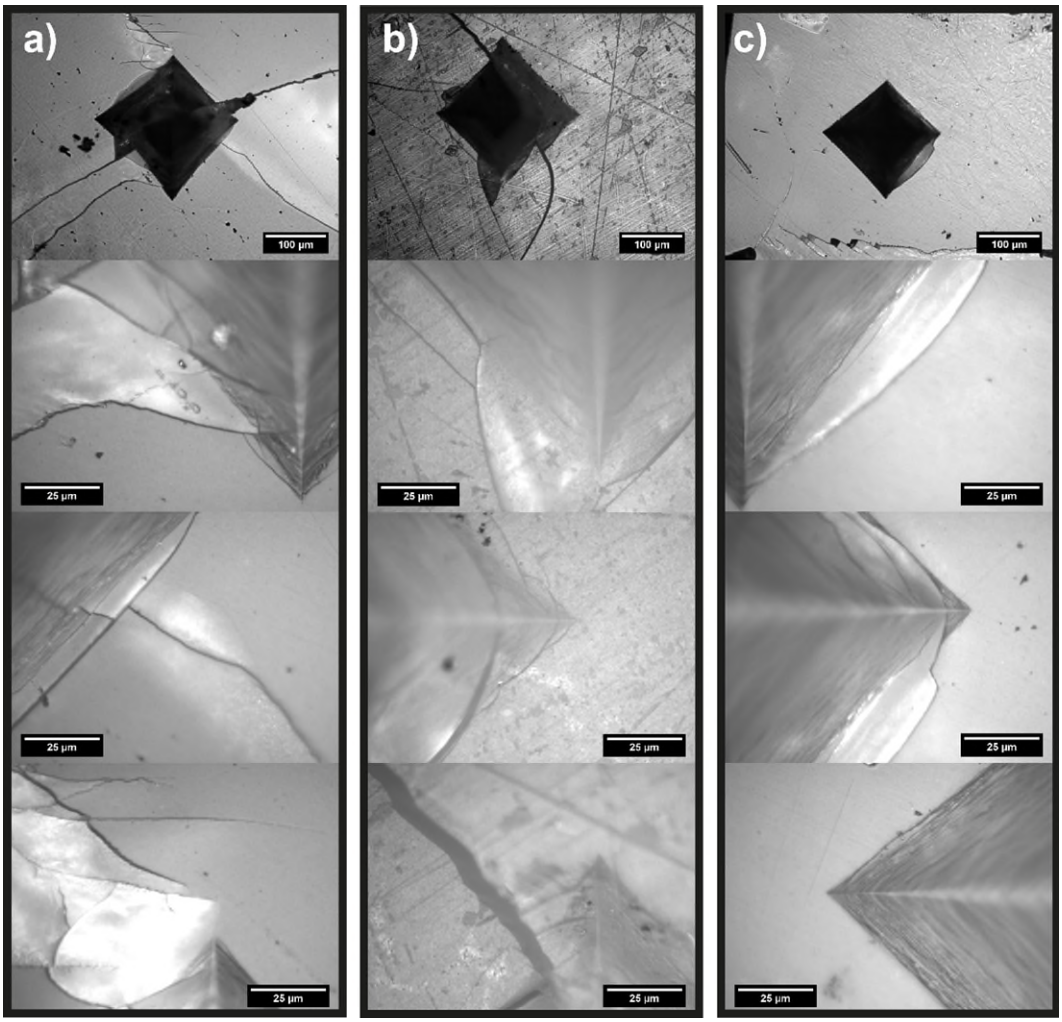

Figure 5.6 a) Vickers HV0.5 (~4.9 N) indent on MIL-68 monolith. Radial cracks propagate from shear faults inside the indent and deflect following low energy paths. b) Vickers HV0.3 (~2.9 N) indent on MOF-808 monolith. Radial cracks propagate from shear faults inside the indent and deflect following low energy paths outside the indent. c) Vickers HV0.5 (~4.9 N) indent on MIL-68 monolith. In this case no radial cracks are induced.

5.2.2 Nanoscratch tests

Nanoscratch tests were also carried out on the four monoliths, using a Berkovich tip and following the procedures described in Section 2.9 of Chapter 3. The maximum ramp load was set to 50 mN and the scratch length to 100 µm, the scratch velocity applied was 10 µm s^{-1}. The results of the tests, performed in both ploughing

and pushing modes, are listed in Table 5.3. A higher scratch critical depth was systematically observed in pushing mode, since the flat end of the indenter can sweep a larger amount of material than the sharp end. No pile-up was detected (Figure 5.7) and cracks propagating outward from the scratch direction were observed only for ZIF-8 (Figure 5.8).

Sample	**Scratch Critical Depth (nm)**	**Cross Profile Max Depth (nm)**
ZIF-8 plough	3088 ± 94	580 ± 72
HKUST-1 plough	1764 ± 60	671 ± 441
MIL-68 plough	4149 ± 339	1187 ± 209
MOF-808 plough	9255 ± 573	3266 ± 452
ZIF-8 push	3002 ± 170	911 ± 288
HKUST-1 push	2379 ± 138	502 ± 106
MIL-68 push	4895 ± 49	2050 ± 152
MOF-808 push	10549 ± 467	3762 ± 581

Table 5.3 Results of nanoscratch tests on the monoliths in the ploughing and pushing modes.

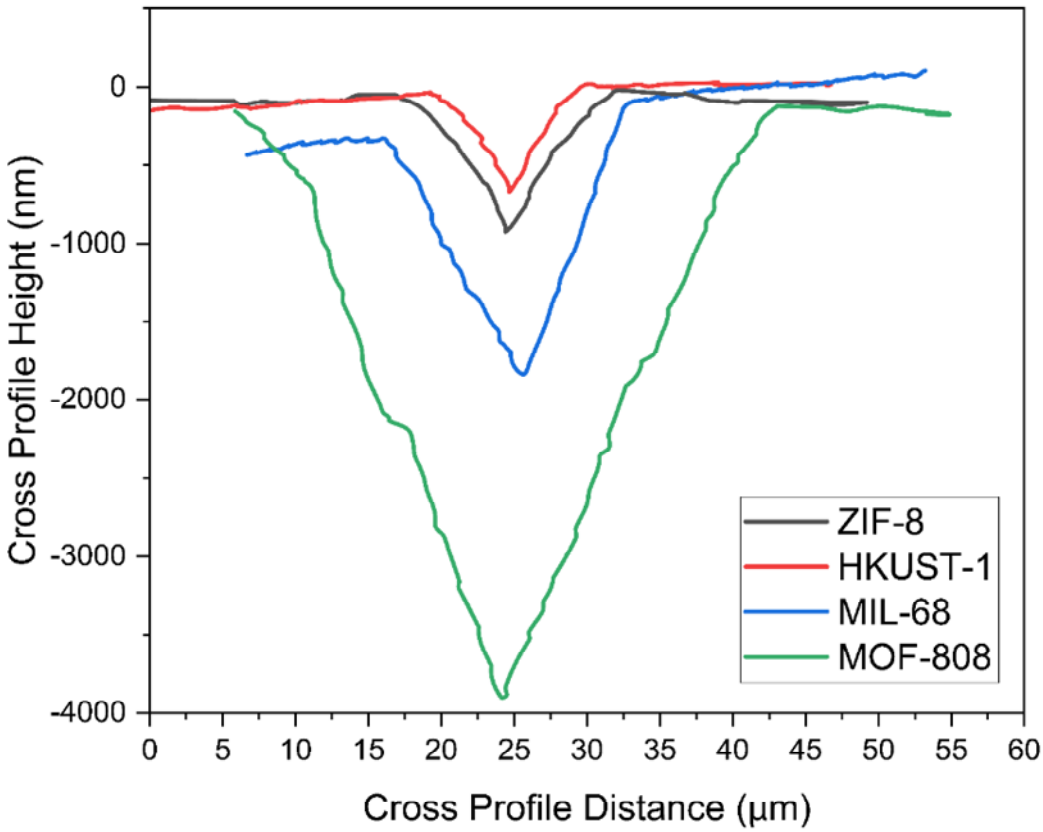

Figure 5.7 Representative mid-way cross profiles (load ~25 mN) of scratches in pushing mode on the four monoliths.

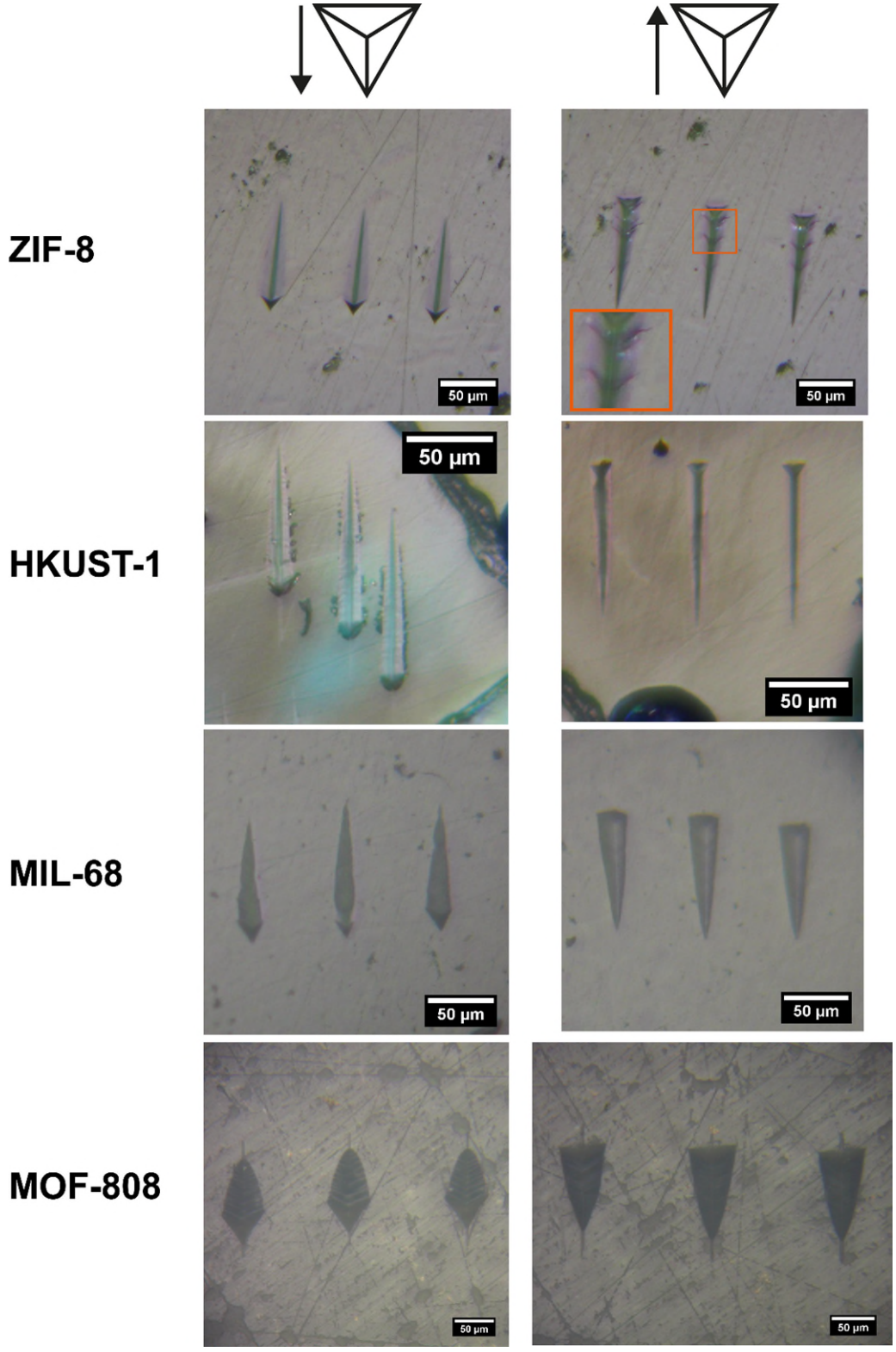

Figure 5.8 Optical micrographs of the scratches on the four monoliths in ploughing mode (left) and pushing mode (right). The inset shows a magnified view of the cracks in the ZIF-8 monolith.

5.2.3 Role of the nanostructure in crack initiation and propagation

The four monoliths are characterised by a nanogranular structure (Figure 3 in Paper II), characteristic of the sol-gel process, consistent with the findings presented in Chapter 4. However, some differences were observed: ZIF-8 and HKUST-1 nanocrystals are “nanoplates”, which aggregates by stacking onto each other, while MIL-68 and MOF-808 aggregates are “lumps” made of smaller nanograins (Figure 3 in Paper II, Figures 5.9 and 5.10). This nanostructural diversity contributes to the difference in ductility. The reduced size of MIL-68 and MOF-808 nanocrystals results in a higher grain boundaries volume fraction, which favours grain boundary sliding (GBS) and grain rotations; these mechanisms may reduce the hardness of the monoliths (and the *H/E* ratio).

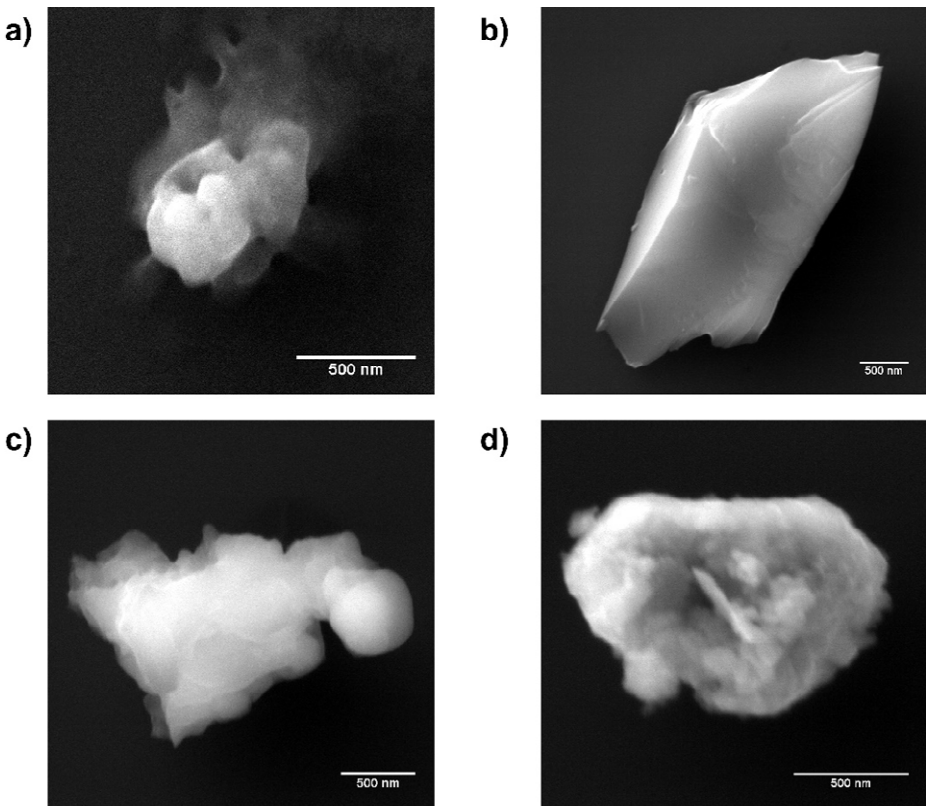

Figure 5.9 FESEM micrographs revealing the morphology and size of a) ZIF-8, b) HKUST-1, c) MIL-68, and d) MOF-808 nanocrystalline aggregates.

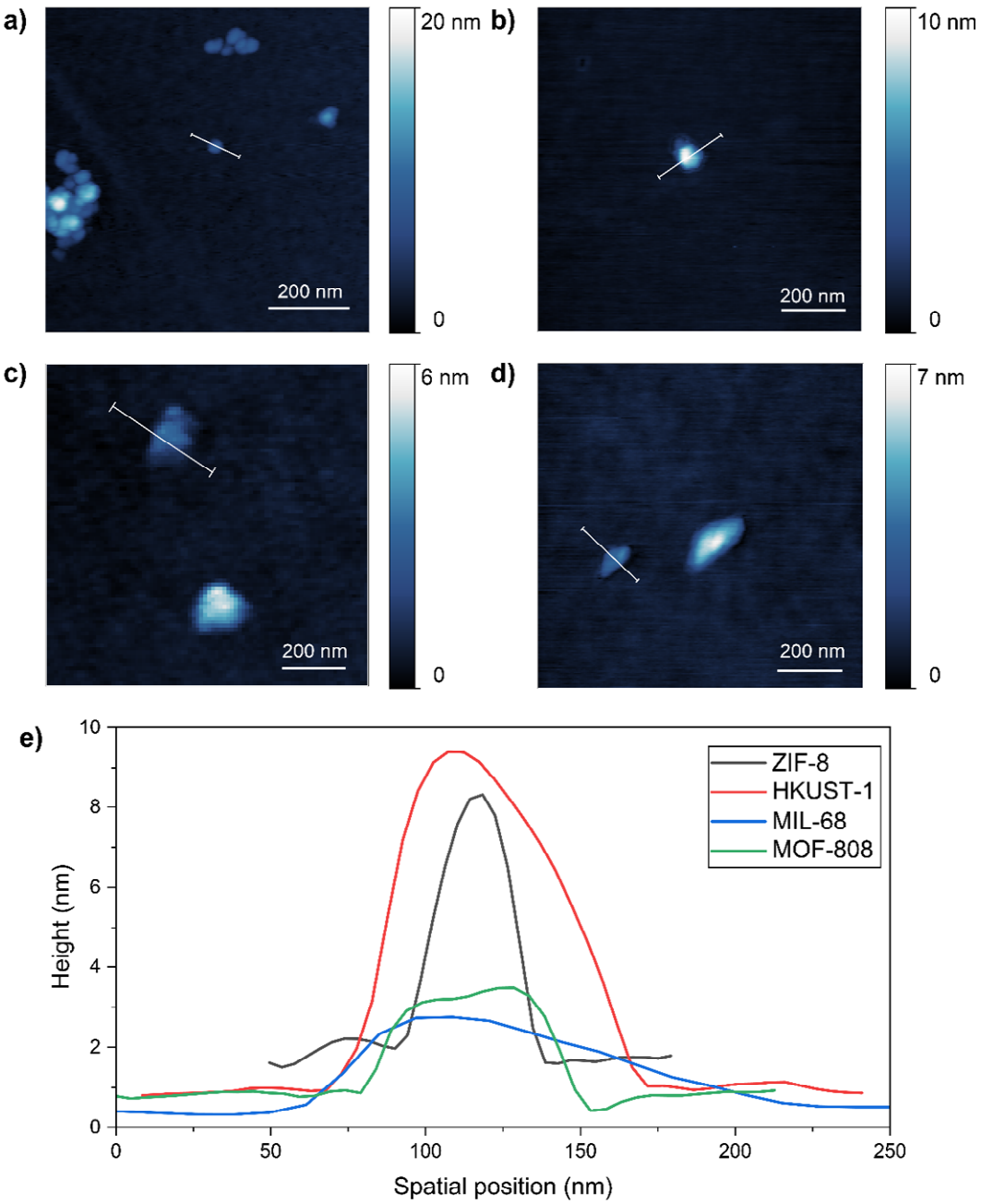

Figure 5.10 AFM height topography images revealing the nanocrystals morphology and size of a) ZIF-8, b) HKUST-1, c) MIL-68, and d) MOF-808. The corresponding line profiles are plotted in e). MIL-68 and MOF-808 nanograins are approximately 3 times smaller than the ZIF-8 and HKUST-1 counterparts.

The results of nanoscratch tests, provided insights on the nature of plastic flow in these materials. Plastic flow is usually associated with pile-up on the scratch sides, which was not observed in any of the monoliths. This observation, together

with the shear faults observed within the indentation contact area and the scratches, suggest that the material flows as a result of shear-activated microfailure along the low-energy grain boundaries. Such a localised failure mechanism is well contained within the indent and scratch areas, dissipating energy and preventing catastrophic crack propagation. This assumption was supported by local nanoFTIR spectra acquired inside the Vickers residual imprint of ZIF-8 (Figure 5 in Paper II). The material does not exhibit signs of pressure-induced structural amorphisation in the proximity of shear faults, contrary to what was observed in a cube corner residual indent in Chapter 4, hinting that failure and energy dissipation take place at the grain boundaries rather than within the framework structure.

5.3 Paper II: Nanostructure-dependent indentation fracture toughness of metal-organic framework monoliths

Online version: https://doi.org/10.1016/j.nxmate.2023.100009

Next Materials xxx (xxxx) xxx

Contents lists available at ScienceDirect

Next Materials

journal homepage: www.sciencedirect.com/journal/next-materials

Nanostructure-dependent indentation fracture toughness of metal-organic framework monoliths

Michele Tricarico, Jin-Chong Tan*

Multifunctional Materials and Composites (MMC) Laboratory, Department of Engineering Science, University of Oxford, Parks Road, Oxford OX1 3PJ, United Kingdom

ARTICLE INFO

Keywords:
Metal-organic framework monolith
Fracture
Nanoindentation
Nanoscratch
Shear faults

ABSTRACT

Monolithic metal-organic frameworks (MOFs) represent a promising solution for the industrial implementation of this emerging class of multifunctional materials, due to their structural stability. When compared to MOF powders, monoliths exhibit other intriguing properties like hierarchical porosity, that significantly improves volumetric adsorption capacity. The mechanical characterization of MOF monoliths plays a pivotal role in their industrial expansion, but so far, several key aspects remain unclear. In particular, the fracture behavior of MOF monoliths has not been explored. In this work, we studied the initiation and propagation of cracks in four prototypical MOF monoliths, namely ZIF-8, HKUST-1, MIL-68 and MOF-808. We observed that shear faults inside the contact area represent the main failure mechanism of MOF monoliths and are the source of radial cracks. MIL-68 and MOF-808 showed a remarkably high resistance to cracking, which can be ascribed to their consolidated nanostructure.

Introduction

Metal-organic frameworks (MOFs) are hybrid materials composed of metal nodes and organic linkers that self-assemble to form one-, two-, or three-dimensional lattice structures [1,2], characterized by a large internal surface area, which makes MOF suitable for a wide range of applications [3–6].

However, nowadays industrial applications are limited by the morphology of this class of materials, which are mostly available as polydisperse microcrystalline powders. A way to overcome this limitation is the realization of "monolithic" materials, which, together with bulk morphology and structural stability, offer other advantages such as reduced mass transfer resistance (for improved gas separation capabilities) and higher volumetric adsorption capacities compared to the powder counterparts [7].

One of the most frequently used techniques to synthetize MOF monoliths is the sol-gel processing route [8–12]. Sol-gel monoliths are formed by removing solvent from a gel by slow drying, generating a polycrystalline bulk solid. This method allows also to obtain different pore sizes within the same material, forming hierarchical structures which are desirable for applications [13]. By way of example, in adsorption columns, when MOF powders are used, their packing can lead to a significant pressure drop over time, caused by the gradual compaction of powders with pressure, resulting in higher mass resistance within the column. Mechanically robust monoliths could overcome this problem.

The mechanical properties of MOF monoliths (and MOFs in general [14]) have been measured mostly by nanoindentation, which allows to probe very small volume of material and yet providing accurate measurements of Young's modulus (E) and hardness (H). In our previous study [11], we explored the correlation between the nanostructure and the mechanical response of two prototypical MOF monoliths, namely ZIF-8 and ZIF-71, by employing nanoindentation, atomic force microscopy (AFM) and nearfield infrared (IR) nanospectroscopy, along with finite element simulations. We were able to identify grain boundary sliding (GBS) as the main deformation mechanism in crystalline MOF monoliths, followed by densification caused by framework collapse for higher pressures.

The aim of this work is to focus on the nanoindentation fracture behavior of MOF monoliths, that, to the best of our knowledge has never been systematically studied to reveal the underpinning mechanisms. In fact, only a few studies have explored the field of MOF fracture, but these are limited to specific single crystals [15] and glasses [16,17].

Nanoindentation techniques have been widely used to evaluate the fracture toughness of brittle materials, using sharp tip geometries such as Vickers or cube corner. These measurements rely on empirical models that correlate K_c with the length of the radial cracks originating from the corners of the indenter marks [18]. However, initiation and

* Corresponding author.
E-mail address: jin-chong.tan@eng.ox.ac.uk (J.-C. Tan).

https://doi.org/10.1016/j.nxmate.2023.100009
Received 23 November 2022; Received in revised form 7 March 2023; Accepted 7 March 2023

Please cite this article as: M. Tricarico and J.-C. Tan, Nanostructure-dependent indentation fracture toughness of metal-organic framework monoliths, Next Materials, https://doi.org/10.1016/j.nxmate.2023.100009

the propagation of such cracks is not easy to model. Furthermore, cracking can occur also underneath the contact area, i.e. median and lateral cracks [19], and other parameters have been shown to complement toughness in the fracture mechanisms, such as the hardness-to-modulus ratio (*H/E*) [20]. Although the fracture toughness values for two ZIF monoliths have been estimated in our recent study [11], the origin of the failure, particularly in connection to the nature of crack initiation and propagation has not been investigated.

In addition, nanoscratch tests were conducted for the first time on crystalline MOF monoliths. This type of test is a well-established technique to characterize the wear resistance of metals [21], ceramics [22] and polymers [23]. Nanoscratch experiments have been used to study the cohesion and adhesion properties of MOF films [24,25] and a MOF glass [26], but never in the context of the fracture of nanocrystalline MOF monoliths.

In this paper, we employed nanoindentation, microindentation, and nanoscratch on four prototypical MOF monoliths that form crystalline monoliths, namely ZIF-8, HKUST-1, MIL-68 and MOF-808. These materials were selected due to their excellent structural stability and water resistance, thereby allowing us to prepare suitable samples for a systematic nanoindentation study. These MOFs are also characterized by distinctively different open-framework structures:

- ZIF-8 ($Zn(mIm)_2$, mIm = 2-methylimidazolate) consists of the ZnN_4 tetrahedral metal centres (Zn(II)) coordinated by N atoms of the mIm linkers. An angle of 145° is formed at the Zn − mIm − Zn centre, mimicking the Si − O − Si angle in zeolites. Its sodalite architecture results in a pore size (diameter of the largest sphere that will fit into the nanocage) of 11.6 Å. Its chemical and thermal stability make this material suitable for gas adsorption and separation applications [27].
- HKUST-1 (Cu_3BTC_2, BTC = benzene-1,3,5-tricarboxylate) is a faced-centred cubic crystal, which contains an intersecting 3D system of square-shaped pores of 9 Å × 9 Å. The framework is built up of dimeric metal units (Cu(II)), which are connected by BTC ligands, forming a paddlewheel motif, also called secondary building unit (SBU) [28].
- MIL-68 is characterised by a 3D network with a Kagomé-like lattice, made of infinite trans-connected chains of octahedral units $InO_4(OH)_2$ linked to each other through terephthalate ligands, resulting in triangular and hexagonal one-dimensional channels (window diameters of 6 Å × 16 Å, respectively) [29].
- MOF-808 ($Zr_6O_4(OH)_4(BTC)_2(HCOO)_6$) is built up of zirconium oxide SBUs, consisting of six octahedrally coordinated zirconium atoms held together by eight μ_3-oxygen atoms, each connected to six BTC linkers. The coordination of SBU is completed with six non-structural ligands, providing charge compensation. This framework architecture yields tetrahedral cages (pore diameter 4.8 Å) with SBUs on the vertices and linkers on the faces (tertiary building units, TBUs). The MOF-808 framework is finally obtained by the TBUs sharing corner, in such a way that a large adamantane-shaped pore is formed (pore diameter 18.4 Å) [30].

We have observed initiation and propagation of the cracks following a sharp contact load and established a correlation between the fracture behavior and the elastic-plastic response of the materials and their underlying nanostructures and specific framework architectures.

Results

Mechanical characterization of the monoliths by nanoindentation

We measured the mechanical properties of the four monoliths by nanoindentation, as shown in Fig. 1A and Fig. S2. We used a Berkovich indenter tip to probe the indentation modulus (E^*) and hardness (H), see *Experimental Procedures* for details. The above-mentioned mechanical properties are reported in Table S1. MIL-68 and HKUST-1 show the higher elastic modulus, with the latter also exhibiting an outstanding hardness, exceeding the one already reported for this material [9]. The elastic energy was also computed on the basis of $W_{elastic}/W_{total}$ (see *Experimental Procedures*) and plotted against the H/E ratio in Fig. 1B. In this plot we distinguish three zones, corresponding to the high, intermediate, and low elastic recovery [31,32]. It can be seen that, ZIF-8 and ZIF-71 monoliths reported by a previous work of the authors [11], and ZIF-62 glass reported by Stepniewska et al. [16], all fall into the category of high elastic recovery. HKUST-1 monolith shows an intermediate recovery, while the monoliths of MIL-68 and MOF-808 show a low elastic recovery. This wide difference in elastic recovery may be explained by the distinct architectures, in terms of framework topology [33] and chemical bonding [34,35], among the four materials. The hardness of MOFs has been reported to be correlated to their internal accessible void space [33]. Hence, frameworks with large pores (low density) are softer. Since hardness is a measure of resistance to permanent deformation, hard materials would usually experience a large elastic recovery. The large pore size of MIL-68 and MOF-808 makes them more prone to deform permanently (lower H), while the high elastic recovery of ZIF-8 may be ascribed to its relatively smaller pore size and the lower coordination number of the zinc metal node (i.e., ZnN_4 tetrahedron), which governs the framework flexibility of the sodalite cage (lower E) [36].

In Table S1, we compared the residual depth at the end of the test (from the indentation load-depth curves) with the residual depth observed from AFM height topography of the residual indents (Fig. S3). We noticed a large discrepancy in residual indentation depths, which demonstrates a viscoelastic recovery of the residual imprint over time [37]. Such a time-dependent stress relaxation was relatively limited for ZIF-8 and MIL-68 (~27 % and ~34 %, respectively), while it is significant for HKUST-1 and MOF-808 (67 % and 43 %, respectively).

With the aim of inducing radial cracks, we probed the monoliths with a cube-corner indenter (Fig. S4), applying a load of 50 mN (maximum capacity of the nanoindenter load cell). Only ZIF-8 and HKUST-1 monoliths show crack propagation from the indent corners, while MIL-68 and MOF-808 monoliths are completely radial crack-free in the apparent vicinity of the residual indent. Subsequently, we estimated the indentation fracture toughness of the HKUST-1 monolith by employing Laugier's empirical formula [18], adapted for a cube-corner indenter [38] (see *Experimental Procedures*). We obtained $K_c = 0.80 \pm 0.45\ MPa\sqrt{m}$, which is the highest reported value so far for MOF materials. Notably, it is significantly higher than the monoliths of ZIF-8 ($0.074 \pm 0.023\ MPa\sqrt{m}$) and ZIF-71 ($0.145 \pm 0.050\ MPa\sqrt{m}$) reported in [11], and it is also considerably higher than previously reported ZIF-62 glass ($0.104 \pm 0.020\ MPa\sqrt{m}$) [17] and against dense hybrid frameworks single crystals ($K_c \sim 0.1 - 0.3\ MPa\sqrt{m}$) [15].

Vickers microindentation

In an attempt to crack also MIL-68 and MOF-808 monoliths, we used a microhardness Vickers indenter, which is capable of reaching much higher loads. Surprisingly, we found that none of the samples exhibited radial cracks from the indent corners, even with a load of 50 gf (~0.49 N). However, we observed the formation of layered shear faults in the contact area (Fig. 2A-D), similarly to what Stepniewska et al. [16] reported for ZIF-62 glass. The distance between two consecutive faults is different in all the materials and somehow decreases with hardness. For the sake of comparison, let us consider the distance between the outermost faults. MOF-808 (Fig. 2D), which is the softer of the materials analyzed, shows the larger distance (~4 μm), while HKUST-1 (Fig. 2B), the hardest one, shows the smallest distance (~1–1.5 μm). ZIF-8 (Fig. 2A) and MIL-68 (Fig. 2C), which exhibit an intermediate hardness, similar to each other, are characterized by an intermediate distance (~2 μm). Interestingly, HKUST-1 does not show evident faults like the other three monoliths. We believe that, given the outstanding

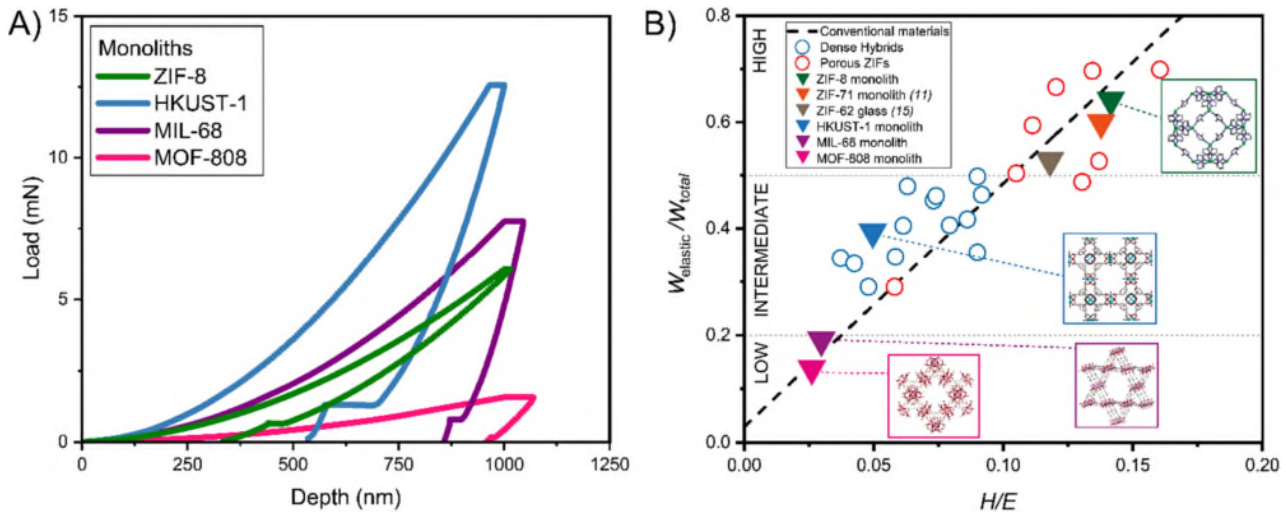

Fig. 1. Mechanical properties of the four MOF monoliths characterized by nanoindentation. A) Representative load-depth curves resulting from nanoindentation of the monolithic samples of ZIF-8, HKUST-1, MIL-68 and MOF-808, using a Berkovich indenter. The tests were performed under displacement control, with the maximum surface penetration depth set to 1000 nm. The maximum load was held for 1 s to assess creep deformation; during unloading the load was held constant at 10 % of the maximum load to quantify and correct for thermal drift (horizontal segment < 2 mN). B) Map of elastic recovery ($W_{elastic}/W_{total}$) vs the (H/E) ratio, the data for conventional materials, dense hybrid frameworks, and porous ZIFs were adapted from reference [32].

hardness of this material, the cohesive force between the nanograins is such that microcracks do not propagate as easily as in the other materials. We propose that the shear bands observed inside HKUST-1 contact area are rather "minor slip bands", from which shear faults will eventually propagate. Lawn et al. [39] proposed that when these shear defects cannot accommodate the build-up of surface displacement at the contact interface, at some catastrophic point, a major shear fault develops into the material. This model, illustrated in Fig. 2E, has been derived from several studies of indentation fracture in brittle materials [39–41].

The shear faults also resulted in a vertical displacement at the nanoscale, similarly to what Stepniewska et al. [16] observed in ZIF-62 glass. These vertical steps were quantified by AFM, as shown in Fig. 2F for ZIF-8 and Figs. S5, S6, S7 for HKUST-1, MIL-68 and MOF-808 respectively. Predictably, the monoliths characterized by a smaller elastic recovery (MIL-68 and MOF-808) showed larger vertical steps (> 100 nm), while the high-intermediate elastic springback in ZIF-8 and HKUST-1 likely allowed for a larger recovery of such a nanoscale displacement.

We observed cracks for even higher loads: 500 gf (~4.9 N) for MIL-68 and 300 gf (~2.9 N) for MOF-808, as shown in Figs. S8 and S10, respectively. However, when we repeated the test with the same parameters on MIL-68, no radial crack was observed (Fig. S9). The radial cracks observed in Figs. S8 and S10 initiate from the shear faults inside the indents and propagate in a catastrophic fashion. Upon propagation, the cracks deflect following unpredictable paths; we reasoned that this occurs along the low-energy grain boundaries present in the MIL-68 and MOF-808 monoliths. Given the catastrophic fashion in which cracking occurs and the large size of the indented areas, we believe the crack initiation event to take place in correspondence of pre-existing defects within the monolith, for instance macropores or flaws which are intrinsic to the sol-gel process. Importantly, such cracking behavior found in a polycrystalline monolith is distinct from that observed for the amorphous ZIF-62 glass (no grain boundaries) which exhibits radial cracking from all four corners of Vickers indentation [16].

Nanostructural characterization of the monoliths

According to what we have reported in our previous work on ZIF monoliths [11], we observed a nanograined structure (Fig. 3), with each nanograin being a single crystal. AFM phase images and FESEM micrographs in the insets of Fig. 3, AFM height topographies (Fig. S11), and additional FESEM images (Fig. S12) reveal the morphology and the size of these nanograins. Indeed, we can clearly distinguish two different kinds of polycrystalline aggregates. For ZIF-8 and HKUST-1, which were synthesized by leveraging the high-concentration reaction (HCR) method [42], we observe a "nanoplate" morphology of the nanocrystals, with a maximum size of approximately 100 nm. Such nanoplates form aggregates by stacking on top of each other. In contrast, the synthesis of MIL-68 and MOF-808 resulted in relatively smaller nanograins, which tend to aggregate forming polycrystalline "lumps". The AFM height topographies shown in Fig. S13 reveal that MIL-68 and MOF-808 nanograins are approximately 3 times smaller than the ZIF-8 and HKUST-1 counterparts. The above finding supports the notion that this particular nanostructural feature, which results in an increased volume fraction of grain boundaries, together with the framework structure, contributes to the outstanding ductility of MIL-68 and MOF-808 monoliths in compression; hence their correspondingly low H/E ratios (Fig. 1B).

Scratch tests

Nanoscratch experiments were performed employing a Berkovich tip. Each test consists of three sequential steps: (i) a small load is applied allowing for the tip to track the pre-scratch surface profile; (ii) the same process is repeated during the actual scratch phase, with the prescribed applied load; (iii) the post-scratch profile and a cross-section profile (at half the length of the scratch) is recorded in order to measure the residual deformation after elastic recovery. We set the maximum ramp load to 50 mN and a scratch length of 100 µm, the scratch velocity was set to 10 µm s^{-1}. The test can be performed in two distinct modes (Fig. S14), depending on which end of the tip is cutting the material: ploughing (sharp end) or pushing (flat end). We observed systematically higher scratch critical depths in pushing mode compared to those in ploughing mode (Fig. 4 and Table S2). This is due to the larger area of the flat end of the tip, with the same load, is able to remove a larger amount of material compared to the sharp counterpart. From the micrographs in Fig. S16, we notice that only the ZIF-8 monolith shows evidence of crack events (outward from the scratch direction), while the other monoliths exhibit a very good ductility under the nanoscratch test conditions. Moreover, no pile-up is observed around the scratch (Fig. S15).

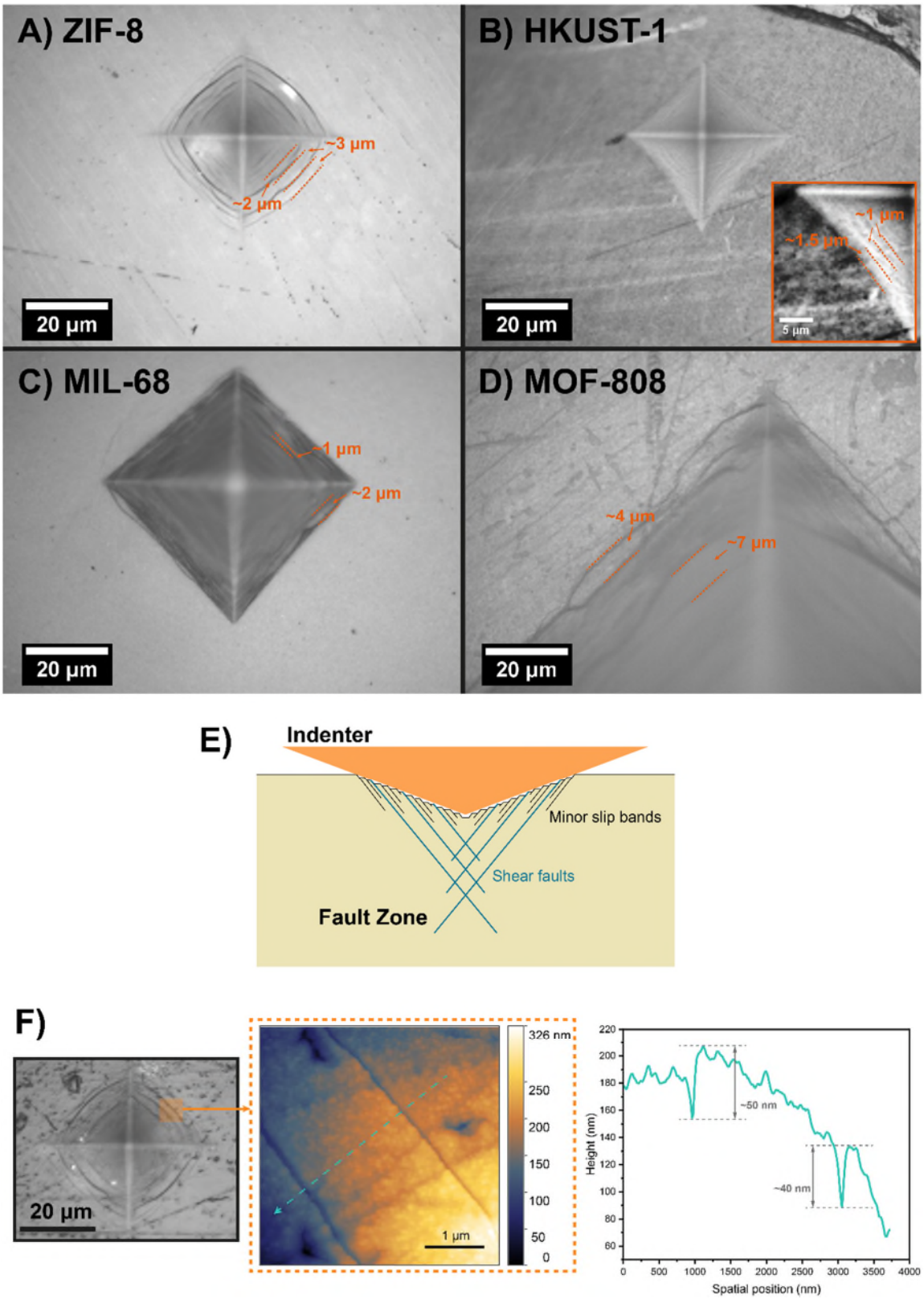

Fig. 2. Indentation shear faults. Optical micrographs of the residual indentations by Vickers microhardness, subjected to HV0.05 (50 gf ~ 0.49 N) on A) ZIF-8, B) HKUST-1, C) MIL-68 and D) MOF-808 monoliths. Shear faults inside the contact area are visible. No radial cracks are detected on the sample surface. E) Schematic of shear faults formation beneath sharp indenter, as proposed by Lawn et al. [39]. F) Detail of shear faults on a ZIF-8 monolith: overview of the Vickers residual indent HV0.05 (*left*), AFM height topography of a 4 × 4 µm scan area (*middle*) and AFM height profile along the dashed line (*right*), revealing the vertical displacement corresponding to the shear faults.

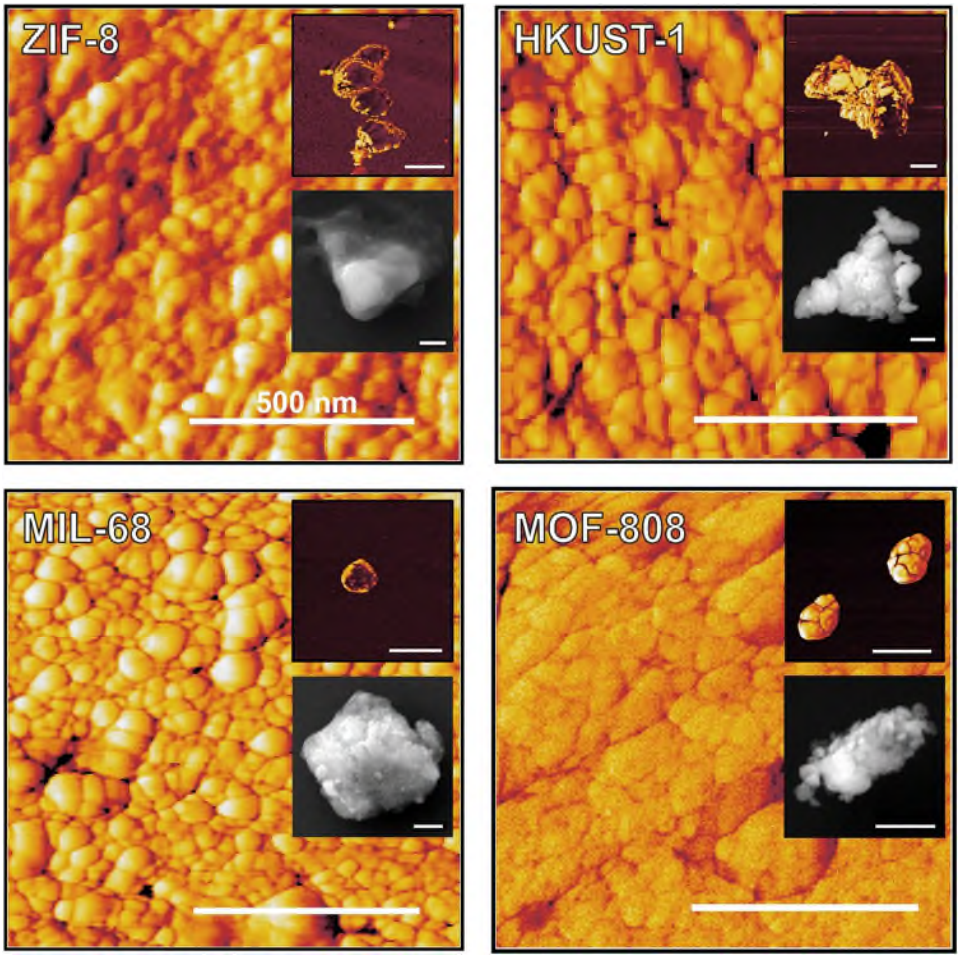

Fig. 3. Nanostructural characterization of the monoliths. AFM phase images revealing the nanograined structure of the four monoliths. The insets show the nanostructured morphology and size of the nanocrystals constituting such a monolithic material, examined by AFM phase (top) and FESEM (bottom). Two different types of aggregates can be distinguished: stack of nanoplates (ZIF-8 and HKUST-1), and lumps of nanocrystals (MIL-68 and MOF-808). Scalebar is 500 nm.

Analysis of stress-induced structural modifications of the framework by nearfield infrared nanospectroscopy

Finally, we employed nearfield infrared nanospectroscopy (nanoFTIR) to gain further insights into the pressure-induced structural modifications of the framework within the monoliths. Local-scale IR absorption spectra, with a spatial resolution of ~20 nm, were taken inside the Vickers residual indent of ZIF-8 (the only sample that the AFM tip was able to probe thanks to its large elastic recovery). The point-to-point spectra taken on and around the shear faults (Fig. 5A-B) are resembling the ones far away from the indented area, suggesting that the framework preserves its structural integrity. When we move the probe to the apex of the indent (Fig. 5C-D), where the stress is supposed to be the highest, we observed some changes in the characteristic peaks of ZIF-8. Let us consider the spectrum taken at the center of the indent (in green in Fig. 5 C): a new peak appears at 970 cm^{-1} and the intensity of the 1124 cm^{-1} band, relatively to the characteristic peak at 1145 cm^{-1}, increases. Also, the relative intensity of 1311 cm^{-1} increases. According to Möslein et al. [43] the peak at 1311 cm^{-1} can be assigned to the missing linker defect in the framework of ZIF-8. This result is in line with what the authors observed in a previous work [11] inside a Berkovich residual indent, which is characterized by an apex angle similar to the one of a Vickers indenter. The absence of defects in the vicinity of the shear faults suggests that the material fails along the grain boundaries. This process dissipates energy, relieving the stress applied to the grains, which therefore do not become amorphized.

Discussion

As illustrated in Fig. 1B, the monoliths lying in the high-intermediate elastic recovery region are the only ones exhibiting radial cracks. Interestingly, also the ZIF-62 glass reported by [16], is located in the high elastic recovery region and evidently radial cracks are observed propagating from the shear faults inside the contact area.

The correlation between elastic recovery and radial cracks can be explained with the model for indentation fracture theory proposed by Lawn et al. [44] for ceramic materials. When a sharp indenter contacts and starts penetrating the surface, a plastically deformed zone develops about the indenter and a sub-surface tensile stress field is generated immediately beneath the tip. This leads to the formation of sub-surface median cracks. Upon unloading, the median cracks would want to close up, but are prevented in doing so by the existence of a residual stress field due to an elastic-plastic mismatch existing at the border of the plastic zone, caused by the material attempting to accommodate the plastically deformed zone. The residual stress is also the cause of lateral cracks [19]. In their work on soda lime glasses, Lawn et al. [39] observed that radial cracks originate from the shear faults and then

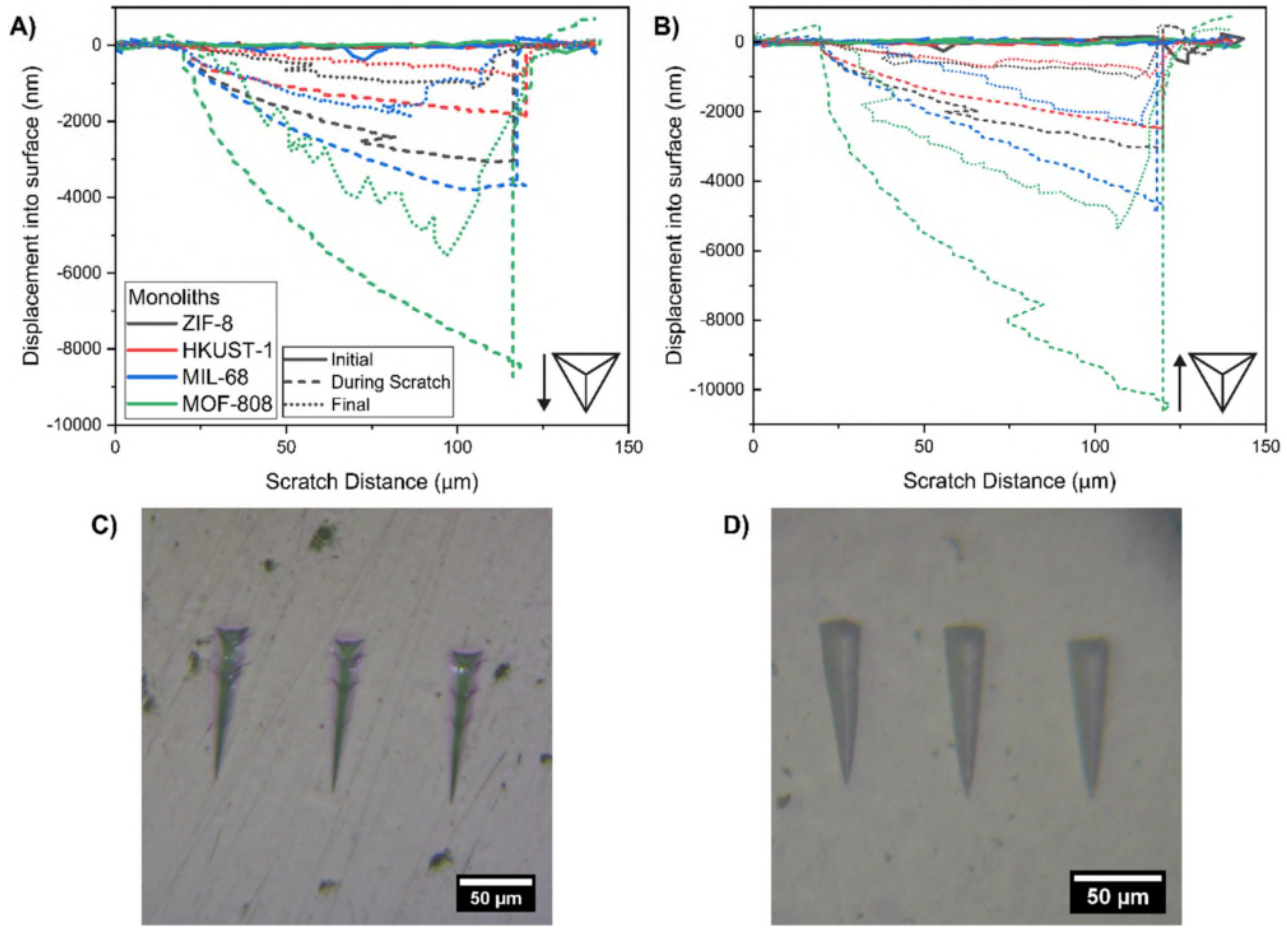

Fig. 4. Scratch tests. Nanoscratch profiles of the monoliths tested by ploughing mode (A) and pushing mode (B), with the displacement into the surface plotted as a function of the scratch distance. The normal load was linearly increased from 0 to 50 mN, over a total scratch length of 100 μm. Note that some of the profiles are affected by artifacts likely due to imperfect surface detection of the Berkovich tip. Optical micrographs of the scratches on ZIF-8 (C) and MIL-68 (D) monoliths in pushing mode reveal different responses: ZIF-8 exhibits cracks formation outward from the scratching direction, while MIL-68 is visually crack-free. A summary of the optical images of all the scratches in the four monoliths in both pushing and ploughing modes is provided in Fig. S16.

propagate upon unloading when the normal stress on such a crack is tensile. The indentation stress field can be divided into a reversible (elastic) and irreversible (residual) component [44]. During loading, only median cracks, which give rise to shear faults, are formed, driven mainly by elastic components of the stress field. Lateral and radial cracks are formed upon unloading when the driving force is represented by residual stresses.

We propose that this mechanism, observed for glasses and other brittle materials, can apply to the MOF monoliths. The high elastic recovery of ZIF-8 monolith upon unloading provides the driving force for radial crack propagations, initiating from the shear faults and propagating towards the external surface as evidenced in this work.

The extraordinary resistance to radial cracking of MIL-68 and MOF-808 monoliths, which exhibit low elastic recovery, can be ascribed to their nanostructure. The reduced size of the nanograins and the consequently higher density of grain boundaries causes the material to undergo large "plastic" deformations by means of grain boundary sliding (GBS) in the vicinity of the contact area, thereby hindering the elastic propagation of the crack from the shear faults. The sliding and rotation of grain boundaries therefore may play a crucial role in the toughening of these nanograined monolithic materials, promoting a mechanism that closely resembles the one observed in nacre [45], which is well known for its superior nanostructure-related toughness. The viscoelastic recovery of the residual imprints, a time-dependent effect, is also likely to play a role in preventing crack propagation by crack closure. Combined, these mechanisms help to enhance the toughness of the MIL-68 and MOF-808 monoliths.

From the scratch tests we observed how MIL-68 and MOF-808 monoliths are more ductile and they can undergo large plastic deformation, being able to accommodate large penetration depths (in both ploughing and pushing modes) without any sign of cracking. On the contrary, ZIF-8 is not able to sustain such a plastic deformation and dissipates energy by brittle fracture. We ascribe this behavior to the nanostructure of the monoliths: the higher volume fraction of grain boundaries in MIL-68 and MOF-808 promotes GBS and hence enabling plastic deformation. Plastic flow is usually associated with material pile-up around the indenter; however, such a phenomenon is not observed in this case (Fig. S15). We reasoned that a continuous flow of material is prevented by the stepwise shear-activated failure of the material, which, given the small size of the nanograins, it is well contained inside the scratch area and does not result in any catastrophic cracking or chipping events. This phenomenon was confirmed by local nanoFTIR spectra taken inside the Vickers residual imprint of ZIF-8 (Fig. 5). In the vicinity of the shear faults, the material does not exhibit signs of pressure-induced structural amorphization, suggesting that the material tends to fail along the grain boundaries instead, dissipating energy.

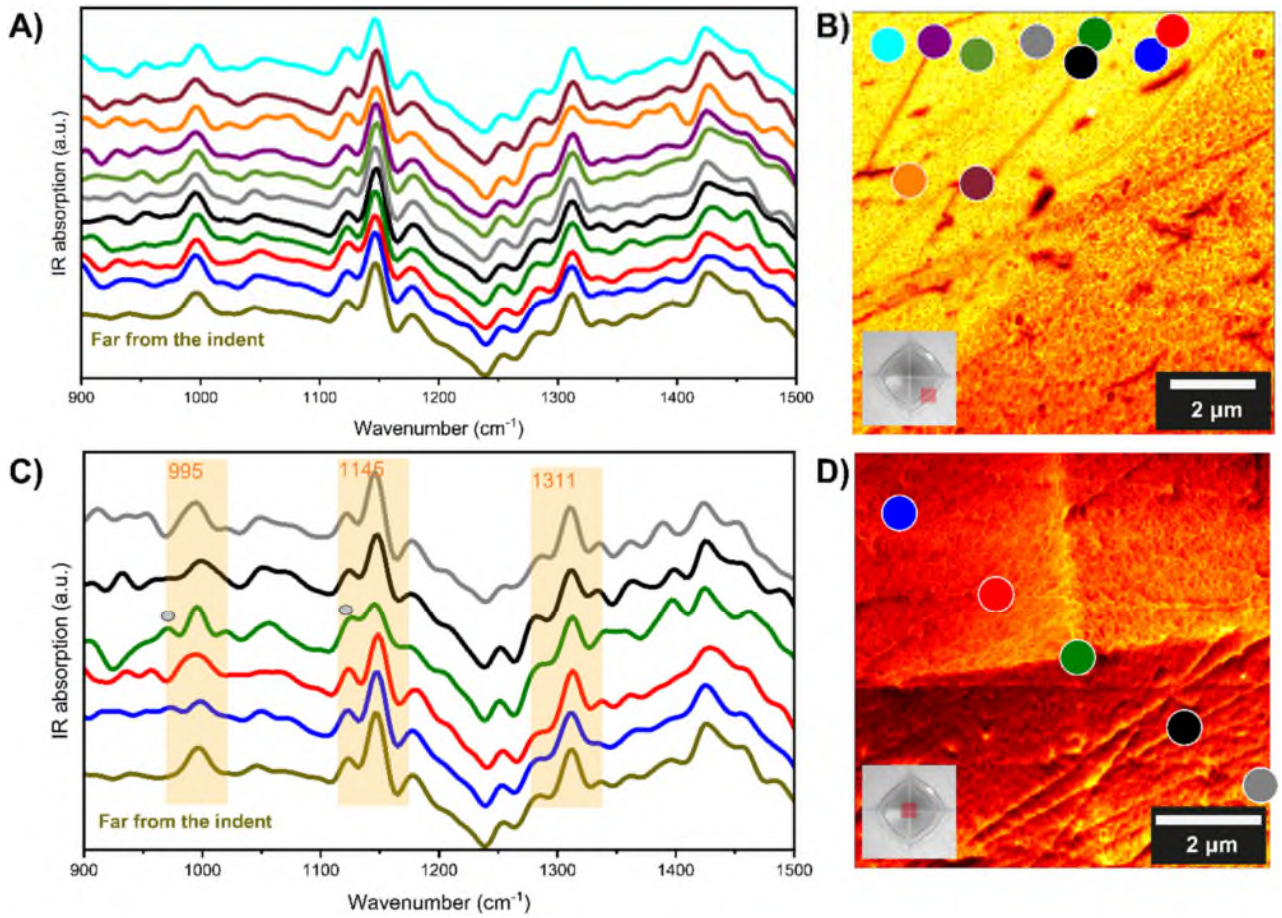

Fig. 5. Analysis of stress-induced structural modifications of the framework by nearfield infrared nanospectroscopy. Nearfield nanoFTIR absorption spectra of ZIF-8 monolith measured locally on and around the shear faults (A) and at the indent apex inside a residual Vickers indent (C), corresponding to the positions highlighted in (B) and (D), respectively. Note that the probe size of nanoFTIR was about 20 nm. The first spectrum from the bottom in (A) and (C) was taken far away from the indented area and used as a reference for the unstrained material. The infrared absorption peaks at 995 cm^{-1}, and 1145 cm^{-1} (highlighted by orange bands in C) are related to the characteristic vibrational modes of ZIF-8, namely, in-plane stretching of the mIm ring and C-H rocking of mIm, respectively.

Conclusion

In summary, we investigated the cracking behavior of monoliths under indentation and establish a correlation with their nanostructure and framework architecture. For MIL-68 and MOF-808, we observed a remarkable resistance to radial cracking and the occurrence of shear faults as the principal failure mechanism. This mechanism allows, to some extent, to contain the damage within the contact area, since the cracks follow the low-energy grain boundaries separating the aggregated nanocrystals forming the monolith.

The basic new insights derived from our research on the fracture and cracking behavior of nanocrystalline MOF monoliths will open the door to the nanostructural engineering and shaping of a class of *mechanically resilient framework solids* fit for real-world applications. For instance, the basic knowledge of the fracture toughness of porous luminescent films, sensor chips, and energy converters constructed from monolithic MOF materials will be key to the engineering of damage-tolerant devices and functional parts. In essence, if the risk of catastrophic fast fracture intrinsic to brittle MOF materials can be mitigated, this will warrant a good service life.

Experimental procedures

Resource availability

Lead contact

The lead contact is Jin-Chong Tan, jin-chong.tan@eng.ox.ac.uk.

Materials availability

This study did not generate new unique reagents.

Data and code availability

The authors declare that the data supporting the findings of this study are available in the manuscript and its supplemental information files. The authors declare that there was no code generated during the study.

Synthesis and sample preparation

ZIF-8 monoliths ZIF-8 ($Zn(mIm)_2$) monoliths were synthesized following the procedure described in [11]: 0.595 g of $Zn(NO_3)_2{\cdot}6\,H_2O$ and 0.493 g of mIm were dissolved in 9 mL of DMF each and stirred for 5 min. Then, 0.837 mL of triethylamine (NEt_3) were added to the linker solution. Subsequently, the two solutions were combined in a 50 mL vial, where a gel was promptly formed. The molar ratio of Zn $(NO_3)_2{\cdot}6\,H_2O$: mIm: DMF: NEt_3 used was 1: 3: 116: 3. The mixture was sonicated for 5 min and then washed three times, in 50 mL of solvent (DMF, MeOH and MeCN, respectively), followed by centrifugation at 8000 RPM. The collected solid was dried slowly at room temperature (RT ~25 °C) for 3 days under the fume cupboard to yield monoliths.

HKUST-1 (Cu_3BTC_2) monoliths 300 mg of benzene-1,3,5-tricarboxylate (BTC) were dissolved in 10 mL of ethanol and subsequently 0.519 mL of NEt_3 were added to the solution. 270 mg of copper nitrate were dissolved in 10 mL of EtOH and added to the linker solution. The resulting solution was stirred for 15 min and washed three times in EtOH. A gel was collected and dried at RT for 2 days, yielding millimeter-sized "glassy" monoliths.

MIL-68(In) monoliths 9 mL DMF solution of 797 mg 1,4-benzenedicarboxylate (BDC) plus NEt_3 (9.6 mmol) were dissolved together. After that, 9 mL DMF solution of 1444 mg indium nitrate was immediately added into the mixture. Then the product was washed thoroughly 4 times (2 times with DMF, 2 times with MeOH). The nanocrystals of MIL-68(In) were separated from the suspension by centrifugation at 8000 rpm for 10 mins and the excess solvent decanted. The obtained material was dried at room temperature for 3 days to yield monoliths.

MOF-808 monoliths 210 mg of benzene-1,3,5-tricarboxylate (BTC) and 970 mg of zirconyl chloride octahydrate were dissolved in a DMF/formic acid (30 mL + 30 mL), placed in a glass reagent bottle and heated at 130 °C for two days. The solution was centrifuged, and the collected material was washed four times with DMF. The resulting compound was then soaked in 100 mL of acetone for four days, with the solvent being replaced twice per day. The acetone-exchanged sample was finally evacuated at room temperature for 24 h and activated at 150 °C for 24 h to yield the monoliths.

Powder X-ray diffraction (XRD) patterns (Figs. S1) confirm the successful synthesis of the MOF structures, since all the main characteristic Bragg diffraction peaks are present in the resultant monoliths.

The as-synthetized monoliths were cold-mounted in epoxy resin (Struers Epofix), resulting in a cylindrical sample, suitable for nanoindentation. In order to get reproducible results from the indentation tests, the contact surface must be flat. Therefore, the mounted specimen surface was carefully ground with different grades of SiC papers, followed by fine polishing in diamond suspensions.

Nanoindentation tests

Indentation modulus (E^*) and hardness (H) were measured following the approach proposed by Oliver and Pharr [46]:

$$E^* = \frac{\sqrt{\pi}}{2}\frac{S}{\sqrt{A(h_{max})}} \tag{1}$$

$$H = \frac{P_{max}}{A(h_{max})} \tag{2}$$

where S is the contact stiffness (slope of the unloading curve at maximum load), $A(h)$ is the area function, and P_{max} and h_{max} are the maximum load and depth, respectively. The indentation modulus (E^*) is a function of the Young's moduli and Poisson's ratios of the sample (E_s, ν_s) and the indenter (E_i, ν_i):

$$\frac{1}{E^*} = \frac{1-\nu_s^2}{E_s} + \frac{1-\nu_i^2}{E_i} \tag{3}$$

The area function $A(h)$ is a 3rd order polynomial that relates the contact area to the contact depth, and it is determined through calibration using a fused silica sample.

From the load-depth curves, we also computed the elastic recovery, $W_{elastic}/W_{total}$, defined as the ratio between the area under the unloading and loading curves respectively:

$$\frac{W_{elastic}}{W_{total}} = \frac{\int_{h_f}^{h_{max}} P_{unloading}\,dh}{\int_0^{h_{max}} P_{loading}\,dh} \tag{4}$$

where h_{max} is the maximum indentation depth, h_f the residual depth after unloading, and $P_{unloading}$ and $P_{loading}$ are the loads applied upon loading and unloading, respectively.

We employed an iMicro nanoindenter (KLA-Tencor) equipped with a Berkovich tip. The Continuous Stiffness Measurement (CSM) method was employed to continuously measure the change in mechanical properties as a function of the indenter tip penetration depth. This technique superimposes a 2-nm oscillation on the quasi-static force, using a frequency-specific amplifier to measure the response of the indenter. The measurements were conducted by setting a maximum depth of 1000 nm and an indentation strain rate of 0.2 s^{-1}. The values for E and H were computed by averaging the CSM data between 500 and 1000 nm.

For fracture studies, a cube corner indenter (three-sided pyramid with mutually perpendicular faces) was used to induce cracking, since its sharpness produces much higher stresses and strains in the region of contact compared with a Berkovich tip. Assuming a Palmqvist crack configuration, the Laugier's empirical formula [18] was used:

$$K_{IC} = k\left(\frac{a}{l}\right)^{\frac{1}{2}}\left(\frac{E}{H}\right)^{\frac{2}{3}}\frac{P}{c^{\frac{3}{2}}} \tag{5}$$

where k is an empirical constant of the indenter shape ($k = 0.057$ for cube corner [38]), a is the distance between the center and the tip of the indent, l is the crack length starting from the corner of the indent, E and H are the Young's modulus and hardness respectively, P is the maximum indentation load, and $c = a + l$.

Vickers microindentation tests

Vickers microindentation was performed using a Duramin-40 hardness tester (Struers). The maximum load (measured in gf) was held for 10 s before unloading.

Nanoscratch tests

Nanoscratch tests were carried out on an iMicro nanoindenter (KLA-Tencor) equipped with a Berkovich tip. The maximum ramp load was set to 50 mN, the scratch length to 100 μm, and the scratch velocity to 10 μm s^{-1} for all the tests.

AFM imaging

The surface topography of the monoliths and the drop-casted aggregates were measured by atomic force microscopy (AFM) as implemented in a neaSNOM instrument (neaspec GmbH) under the tapping-mode. A Scout350 (NuNano) probe was employed, with a nominal tip radius of 5 nm and a resonant frequency of 350 kHz.

FESEM imaging

Secondary electron images of the nanocrystalline aggregates were acquired with a Tescan Lyra 3 (Tescan, Czech Republic) field-emission scanning electron microscope, operating under a voltage of 10 keV.

NanoFTIR

Nearfield Fourier transform infrared nanospectroscopy (nanoFTIR) was performed using the s-SNOM instrument (neaspec GmbH), where a platinum-coated AFM probe (Arrow-NCPt, tip radius < 25 nm, 285 kHz) under the tapping mode is illuminated by a broadband mid-infrared (IR) laser source (Toptica). Local nano-FTIR spectra of specific regions inside and away from the residual indentations were measured under a spot size of 20 nm. Each point spectrum was acquired as an average of 12 individual interferograms taken on the same spot, with 1024 pixels and an integration time of 14 ms per pixel, normalized by a reference spectrum taken on a silicon wafer.

CRediT authorship contribution statement

M.T.: Conceptualization, Methodology, Investigation, Data Curation, Writing - Original Draft, Visualization. J.-C. T.: Resources, Writing - Review & Editing, Supervision, Funding acquisition.

Declaration of Competing Interest

The authors declare the following financial interests/personal relationships which may be considered as potential competing interests: Jin-Chong Tan reports financial support was provided by University of Oxford.

Acknowledgments

We thank the ERC Consolidator Grant (PROMOFS grant agreement 771575) and EPSRC Impact Acceleration Account Award (EP/R511742/1) for funding the research. We are grateful to Dr. Igor Dyson (Oxford Engineering) for providing access to the microhardness Vickers indenter. We thank Dr. Cyril Besnard and Prof. Alexander M. Korsunsky for the FESEM images.

Appendix A. Supporting information

Supplementary data associated with this article can be found in the online version at doi:10.1016/j.nxmate.2023.100009.

References

[1] H. Furukawa, K.E. Cordova, M. O'Keeffe, O.M. Yaghi, The chemistry and applications of metal-organic frameworks, Science 341 (2013) 1230444, https://doi.org/10.1126/science.1230444

[2] R. Freund, S. Canossa, S.M. Cohen, W. Yan, H. Deng, V. Guillerm, M. Eddaoudi, D.G. Madden, D. Fairen-Jimenez, H. Lyu, et al., 25 years of reticular chemistry, Angew. Chem. Int Ed. 60 (2021) 23946–23974, https://doi.org/10.1002/anie.202101644

[3] M. Gutiérrez, Y. Zhang, J.-C. Tan, Confinement of luminescent guests in metal–organic frameworks: understanding pathways from synthesis and multimodal characterization to potential applications of LG@MOF systems, Chem. Rev. 122 (2022) 10438–10483, https://doi.org/10.1021/acs.chemrev.1c00980

[4] P. Falcaro, R. Ricco, C.M. Doherty, K. Liang, A.J. Hill, M.J. Styles, MOF positioning technology and device fabrication, Chem. Soc. Rev. 43 (2014) 5513–5560, https://doi.org/10.1039/c4cs00089g

[5] I. Stassen, N. Burtch, A. Talin, P. Falcaro, M. Allendorf, R. Ameloot, An updated roadmap for the integration of metal-organic frameworks with electronic devices and chemical sensors, Chem. Soc. Rev. 46 (2017) 3185–3241, https://doi.org/10.1039/c7cs00122c

[6] A. Bavykina, N. Kolobov, I.S. Khan, J.A. Bau, A. Ramirez, J. Gascon, Metal–organic frameworks in heterogeneous catalysis: recent progress, new trends, and future perspectives, Chem. Rev. 120 (2020) 8468–8535, https://doi.org/10.1021/acs.chemrev.9b00685

[7] J. Hou, A.F. Sapnik, T.D. Bennett, Metal–organic framework gels and monoliths, Chem. Sci. 11 (2020) 310–323, https://doi.org/10.1039/c9sc04961d

[8] T. Tian, J. Velazquez-Garcia, T.D. Bennett, D. Fairen-Jimenez, Mechanically and chemically robust ZIF-8 monoliths with high volumetric adsorption capacity, J. Mater. Chem. A 3 (2015) 2999–3005, https://doi.org/10.1039/c4ta05116e

[9] T. Tian, Z. Zeng, D. Vulpe, M.E. Casco, G. Divitini, P.A. Midgley, J. Silvestre-Albero, J.C. Tan, P.Z. Moghadam, D. Fairen-Jimenez, A sol-gel monolithic metal-organic framework with enhanced methane uptake, Nat. Mater. 17 (2018) 174–179, https://doi.org/10.1038/nmat5050

[10] B.M. Connolly, M. Aragones-Anglada, J. Gandara-Loe, N.A. Danaf, D.C. Lamb, J.P. Mehta, D. Vulpe, S. Wuttke, J. Silvestre-Albero, P.Z. Moghadam, et al., Tuning porosity in macroscopic monolithic metal-organic frameworks for exceptional natural gas storage, Nat. Commun. 10 (2019) 2345, https://doi.org/10.1038/s41467-019-10185-1

[11] M. Tricarico, J.-C. Tan, Mechanical properties and nanostructure of monolithic zeolitic imidazolate frameworks: a nanoindentation, nanospectroscopy, and finite element study, Mater. Today Nano 17 (2022) 100166, https://doi.org/10.1016/j.mtnano.2021.100166

[12] P. Küsgens, A. Zgaverdea, H.-G. Fritz, S. Siegle, S. Kaskel, Metal-organic frameworks in monolithic structures, J. Am. Ceram. Soc. 93 (2010) 2476–2479, https://doi.org/10.1111/j.1551-2916.2010.03824.x

[13] A. Feinle, M.S. Elsaesser, N. Husing, Sol-gel synthesis of monolithic materials with hierarchical porosity, Chem. Soc. Rev. 45 (2016) 3377–3399, https://doi.org/10.1039/c5cs00710k

[14] B.B. Shah, T. Kundu, D. Zhao, Mechanical properties of shaped metal–organic frameworks, Top. Curr. Chem. 377 (2019) 25, https://doi.org/10.1007/s41061-019-0250-7

[15] J.C. Tan, C.A. Merrill, J.B. Orton, A.K. Cheetham, Anisotropic mechanical properties of polymorphic hybrid inorganic–organic framework materials with different dimensionalities, Acta Mater. 57 (2009) 3481–3496, https://doi.org/10.1016/j.actamat.2009.04.004

[16] M. Stepniewska, K. Januchta, C. Zhou, A. Qiao, M.M. Smedskjaer, Y. Yue, Observation of indentation-induced shear bands in a metal−organic framework glass, Proc. Natl. Acad. Sci. U. S. A. 117 (2020) 10149–10154, https://doi.org/10.1073/pnas.2000916117

[17] T. To, S.S. Sorensen, M. Stepniewska, A. Qiao, L.R. Jensen, M. Bauchy, Y. Yue, M.M. Smedskjaer, Fracture toughness of a metal-organic framework glass, Nat. Commun. 11 (2020) 2593, https://doi.org/10.1038/s41467-020-16382-7

[18] M.T. Laugier, New formula for indentation toughness in ceramics, J. Mater. Sci. Lett. 6 (1987) 355–356, https://doi.org/10.1007/Bf01729352

[19] J. Hagan, M.V. Swain, The origin of median and lateral cracks around plastic indents in brittle materials, J. Phys. D. -Appl. Phys. 11 (1978) 2091.

[20] A.G. Evans, T.R. Wilshaw, Quasi-static solid particle damage in brittle solids—I. Observations analysis and implications, Acta Met. 24 (1976) 939–956, https://doi.org/10.1016/0001-6160(76)90042-0

[21] E. Frutos, A. Cuevas, J.L. González-Carrasco, F. Martín, Characterization of the elastic–plastic behavior of intermetallic coatings growth on medical stainless steel by instrumented ultramicroindentation, J. Mech. Behav. Biomed. Mater. 16 (2012) 1–8, https://doi.org/10.1016/j.jmbbm.2012.08.008

[22] J.L. Hay, R.L. White, B.N. Lucas, W.C. Oliver, Mechanical characterization of ultra-thin, hard-disk overcoats using scratch testing and depth-sensing indentation, MRS Online Proc. Lib. 505 (1997) 325–330, https://doi.org/10.1557/PROC-505-325

[23] F. Mammeri, E. Le Bourhis, L. Rozes, C. Sanchez, Elaboration and mechanical characterization of nanocomposites thin films: part I: determination of the mechanical properties of thin films prepared by in situ polymerisation of tetra-ethoxysilane in poly(methyl methacrylate), J. Eur. Ceram. So 26 (2006) 259–266, https://doi.org/10.1016/j.jeurceramsoc.2004.11.013

[24] B. Van de Voorde, R. Ameloot, I. Stassen, M. Everaert, D. De Vos, J.-C. Tan, Mechanical properties of electrochemically synthesised metal–organic framework thin films, J. Mater. Chem. C 1 (2013) 7716, https://doi.org/10.1039/c3tc31039f

[25] I. Buchan, M.R. Ryder, J.-C. Tan, Micromechanical behavior of polycrystalline metal–organic framework thin films synthesized by electrochemical reaction, Cryst. Growth Des. 15 (2015) 1991–1999, https://doi.org/10.1021/acs.cgd.5b00140

[26] S. Li, R. Limbach, L. Longley, A.A. Shirzadi, J.C. Walmsley, D.N. Johnstone, P.A. Midgley, L. Wondraczek, T.D. Bennett, Mechanical properties and processing techniques of bulk metal–organic framework glasses, J. Am. Chem. Soc. 141 (2019) 1027–1034, https://doi.org/10.1021/jacs.8b11357

[27] K.S. Park, Z. Ni, A.P. Côté, J.Y. Choi, R. Huang, F.J. Uribe-Romo, H.K. Chae, M. O'Keeffe, O.M. Yaghi, Exceptional chemical and thermal stability of zeolitic imidazolate frameworks, Proc. Natl. Acad. Sci. U. S. A. 103 (2006) 10186–10191, https://doi.org/10.1073/pnas.0602439103

[28] S.S. Chui, S.M. Lo, J.P. Charmant, A.G. Orpen, I.D. Williams, A chemically functionalizable nanoporous material $[Cu_3(TMA)_2(H_2O)_3]_n$, Science 283 (1999) 1148–1150, https://doi.org/10.1126/science.283.5405.1148

[29] C. Volkringer, M. Meddouri, T. Loiseau, N. Guillou, J. Marrot, G. Férey, M. Haouas, F. Taulelle, N. Audebrand, M. Latroche, The Kagomé topology of the gallium and indium metal-organic framework types with a MIL-68 structure: synthesis, XRD, solid-state NMR characterizations, and hydrogen adsorption, Inorg. Chem. 47 (2008) 11892–11901, https://doi.org/10.1021/ic801624v

[30] H. Furukawa, F. Gándara, Y.-B. Zhang, J. Jiang, W.L. Queen, M.R. Hudson, O.M. Yaghi, Water adsorption in porous metal–organic frameworks and related materials, J. Am. Chem. Soc. 136 (2014) 4369–4381, https://doi.org/10.1021/ja500330a

[31] Y.-T. Cheng, C.-M. Cheng, Relationships between hardness, elastic modulus, and the work of indentation, Appl. Phys. Lett. 73 (1998) 614–616, https://doi.org/10.1063/1.121873

[32] C.S. Coates, M.R. Ryder, J.A. Hill, J.C. Tan, A.L. Goodwin, Large elastic recovery of zinc dicyanoaurate, APL Mater. 5 (066107) (2017) 066107, https://doi.org/10.1063/1.4990549

[33] J.C. Tan, T.D. Bennett, A.K. Cheetham, Chemical structure, network topology, and porosity effects on the mechanical properties of Zeolitic Imidazolate Frameworks, Proc. Natl. Acad. Sci. USA 107 (2010) 9938–9943, https://doi.org/10.1073/pnas.1003205107

[34] S. Henke, W. Li, A.K. Cheetham, Guest-dependent mechanical anisotropy in pillared-layered soft porous crystals – a nanoindentation study, Chem. Sci. 5 (2014) 2392–2397, https://doi.org/10.1039/C4SC00497C

[35] S.M. Moosavi, P.G. Boyd, L. Sarkisov, B. Smit, Improving the mechanical stability of metal–organic frameworks using chemical caryatids, ACS Cent. Sci. 4 (2018) 832–839, https://doi.org/10.1021/acscentsci.8b00157

[36] J.C. Tan, B. Civalleri, C.C. Lin, L. Valenzano, R. Galvelis, P.F. Chen, T.D. Bennett, C. Mellot-Draznieks, C.M. Zicovich-Wilson, A.K. Cheetham, Exceptionally low shear modulus in a prototypical imidazole-based metal-organic framework, Phys. Rev. Lett. 108 (2012) 095502, https://doi.org/10.1103/PhysRevLett.108.095502

[37] Y. Sun, Y. Li, J.C. Tan, Framework flexibility of ZIF-8 under liquid intrusion: discovering time-dependent mechanical response and structural relaxation, Phys. Chem. Chem. Phys. 20 (2018) 10108–10113, https://doi.org/10.1039/c8cp00447a

[38] N. Cuadrado, D. Casellas, M. Anglada, E. Jiménez-Piqué, Evaluation of fracture toughness of small volumes by means of cube-corner nanoindentation, Scr. Mater. 66 (2012) 670–673, https://doi.org/10.1016/j.scriptamat.2012.01.033

[39] B.R. Lawn, T.P. Dabbs, C.J. Fairbanks, Kinetics of shear-activated indentation crack initiation in soda-lime glass, J. Mater. Sci. 18 (1983) 2785–2797, https://doi.org/10.1007/BF00547596

[40] B.R. Lawn, Fracture and deformation in brittle solids: a perspective on the issue of scale, J. Mater. Res 19 (2004) 2, https://doi.org/10.1557/jmr.2004.19.1.22

[41] J.T. Hagan, Shear deformation under pyramidal indentations in soda-lime glass, J. Mater. Sci. 15 (1980) 1417–1424, https://doi.org/10.1007/Bf00752121

[42] A.K. Chaudhari, H.J. Kim, I. Han, J.C. Tan, Optochemically responsive 2D nanosheets of a 3D metal-organic framework material, Adv. Mater. 29 (2017) 8491–8626, https://doi.org/10.1002/adma.201701463

[43] A.F. Möslein, L. Donà, B. Civalleri, J.-C. Tan, Defect engineering in metal–organic framework nanocrystals: implications for mechanical properties and performance, ACS Appl. Nano Mater. 5 (2022) 6398–6409, https://doi.org/10.1021/acsanm.2c00493

[44] B.R. Lawn, A.G. Evans, D. Marshall, Elastic/plastic indentation damage in ceramics: the median/radial crack system, J. Am. Ceram. Soc. 63 (1980) 574–581.

[45] X. Li, Z.-H. Xu, R. Wang, In situ observation of nanograin rotation and deformation in nacre, Nano Lett. 6 (2006) 2301–2304, https://doi.org/10.1021/nl061775u

[46] W.C. Oliver, G.M. Pharr, An improved technique for determining hardness and elastic modulus using load and displacement sensing indentation experiments, J. Mater. Res. 7 (1992) 1564–1583, https://doi.org/10.1557/jmr.1992.1564

6 Stress-Strain Relationships and Yielding Behaviour of MOF Monoliths

6.1 Background and motivations

As widely discussed in this thesis, the design of MOF-based devices cannot be separated from the mechanical characterisation. The most effective way for evaluating the mechanical response of materials in this sense is arguably through stress-strain relations. However, these relations are not easy to estimate experimentally for nanomaterials due to practical limitations that make it challenging to manufacture samples suitable for conventional mechanical testing by means of tensile tests, bending tests, etc.

Nanoindentation and micropillar compression are amongst the most used techniques to characterise this type of materials. The first, has been widely employed in this thesis and in the field of MOF mechanics in general, but the complex stress field generated under the indenter does not allow an easy extrapolation of traditional uniaxial stress-strain curves (151-155). Micropillar compression, on the other hand, allows to reproduce a uniaxial stress field (or at least, in good approximation) and determine the stress-strain relations at different length scales (156, 157). Nevertheless, microfabrication of micron-sized pillars is not always straightforward. Focused ion beam (FIB) milling is the most common micro-machining technique, that permits to perform milling at the micron and sub-micron scale. There are numerous ion-solid interactions that occur when

an ion beam is used to shape a material, and these interactions may often result in undesirable artefacts and defects. These include channelling, curtaining, beam tails, heat damage, amorphisation, ion implantation and phase transformation (158-160). Particularly, FIB milling of nanoparticle self-assembled structures, if not controlled, can result in unwanted increases in porosity (161).

This chapter aims to describe the yielding and the stress-strain relationships of two prototypical MOF monoliths, ZIF-8 and MIL-68, characterised by different architectures and nanostructures that were already found to strongly affect the fracture behaviour (Chapter 5). Flat punch indentation and micropillar compression were employed and the results compared to each other. Notably, this is, to the best of my knowledge, the first attempt of micropillar compression of MOF monoliths. Recent reports concerning MOF glasses (162) and single crystals (104) have been published, although research of this kind are still rather scarce because of the high susceptibility to FIB damage of the materials.

6.2 Summary of paper III

6.2.1 Microscopic measurements of stress-strain relations by flat punch indentation

A patented technique developed by KLA (163) was employed for estimating the stress-strain behaviour from flat punch (diameter 10.64 μm) nanoindentation tests.

The uniaxial strain (ε) and stress (σ) are defined as follows:

$$\varepsilon = \left(\frac{2}{\pi}\right)\left(\frac{h}{a}\right) \tag{6.1}$$

$$\sigma = \zeta p_m \tag{6.2}$$

Where h is the indentation depth, a is the contact radius, ζ a scaling factor and p_m the mean pressure.

The definition of strain in equation 6.1 is derived from Sneddon's solution for the elastic indentation with a flat punch (79), according to which the relationship between load (P) and indentation depth is given by:

$$P = 2E_r ah \tag{6.3}$$

where E_r is the contact modulus.

By dividing the load by the contact area, an expression for the mean pressure can be obtained:

$$p_m = \frac{P}{\pi a^2} = \frac{2}{\pi} E_r \frac{h}{a} \tag{6.4}$$

If the stress-strain relationship $p_m = E_r \varepsilon$ is introduced, equation 6.1 is derived.

The scaling factor ζ depends on the extent of plasticity caused by the contact, which is quantified by the parameter S^*, defined as:

$$S^* = \frac{S_L}{S} \tag{6.5}$$

where S_L is the instantaneous slope of the loading curve (calculated by continuous stiffness method, CSM) and S the elastic contact stiffness (slope of unloading curve at the maximum load). S^* is equal to zero when the contact is fully plastic, while it is 1 for a fully elastic indentation and its relationship. The scaling factor was found by hundreds of FEM simulations on a wide variety of materials:

$$\zeta = 0.39690\ (S^*)\ + 0.32180 \tag{6.6}$$

Figure 6.1 depicts the method's concept. During loading, the parameter S^* is calculated for each data point and transformed into uniaxial stress using equation 6.2. However, only the data points that met the requirement of full contact ($S > 2E_r a$) were

included. Hollomon's constitutive law for plasticity (power law hardening) was then fitted to these points:

$$\sigma = K\varepsilon^n \tag{6.7}$$

where K is the strength coefficient and n the strain hardening exponent.

Finally, a straight line with a slope equal to the Young's modulus, as determined by conventional Berkovich nanoindentation, was used to describe the elastic behaviour. The intersection of the elastic line and Hollomon's law fit was identified as the yield point.

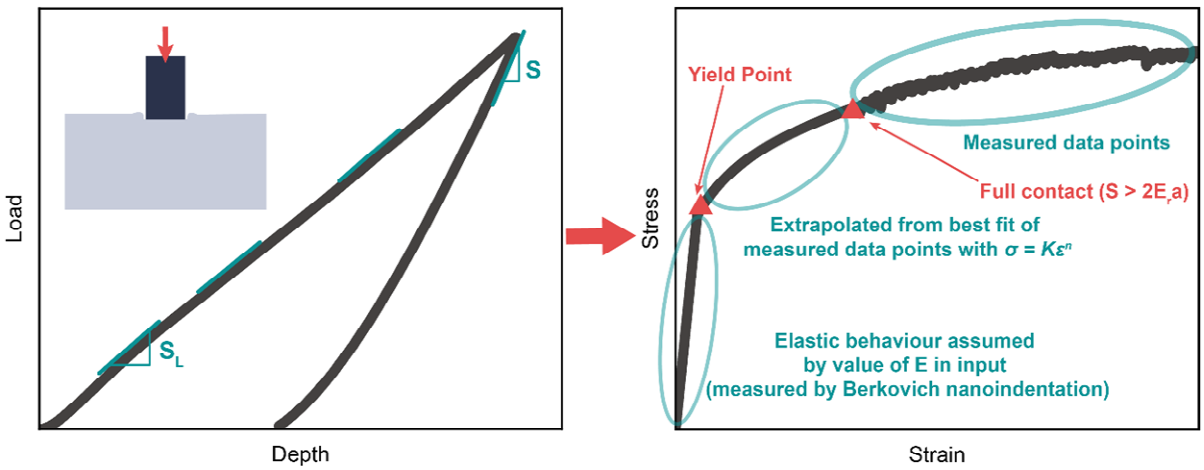

Figure 6.1 Illustration of the procedure for estimating the stress-strain behaviour (right) using flat punch nanoindentation testing (left).

The method was applied to ZIF-8 and MIL-68 monoliths. The results are illustrated in Figure 2 of Paper 3. Both materials tested exhibit a relatively low strain hardening, with a similar yield stress and flow stress to $H/3$, in accordance with Tabor's theory of elastic-plastic contact (164). SEM images of the residual indents revealed ring-shaped cracks around the indents. This, together with the absence of "pop-ins" in the load-depth curves, suggests that the "pseudo-plastic" behaviour of the two monoliths is promoted by stepwise microcracking, most likely initiating at the grain boundaries between nanocrystals.

6.2.2 Residual strain analysis by spectroscopy techniques

The local Raman scattering spectra of the residual flat punch indents were measured using confocal Raman microscopy. Raman scattering, which is sensitive to mechanical strain, was used to identify changes caused by stress in the two frameworks. Shifts of some characteristic bands were observed inside the indent for ZIF-8 (Figure 3 of paper 3 and Figure 6.2), while the positions of all the MIL-68 (Figure 4 of paper 3) bands were unchanged. These results indicate that ZIF-8 framework undergoes structural modifications under stress, likely caused by shear deformation, in accordance with the nanoFTIR result of Chapter 4, while MIL-68 framework retains its morphology, and the deformation of the monolith is only due to GBS.

To corroborate this finding, the effect of mechanical pressure on ZIF-8 and MIL-68 pellets was studied. Pellets can be analysed by bulk characterisation techniques, since the pressure is applied to the whole sample, rather than locally as in the indents. ATR-FTIR, XRD and Raman spectroscopy measurements were performed on ZIF-8 and MIL-68 pellets, obtained by compressing the as-synthesised materials with pressure when confined in a pelleting die comparable to the stresses generated under the indenter (namely 0.075, 0.175 and 0.375 GPa).

ATR-FTIR did not reveal any major changes of the vibrational bands after pelletisation, for both ZIF-8 (Figure 6.3) and MIL-68 (Figure 6.4). However, it was possible to clarify the behaviour of residual solvent trapped into the nanopores. For ZIF-8, the intensity of the 1088 cm^{-1} and 1255 cm^{-1} peaks, corresponding to N-CH_3 vibrations in DMF molecules, dropped with pressure, suggesting that the residual solvent was squeezed out of the pores upon compression. On the other hand, for MIL-68, the intensity of the band relative to C=O stretching in DMF (~1673 cm^{-1}) is not significantly reduced

with the increasing pressure, as opposed to ZIF-8, indicating that the solvent might still be trapped inside the framework channels.

XRD patterns of both ZIF-8 (Figure 6.5) and MIL-68 (Figure 6.6) did not exhibit any major changes, implying that the crystal structure is preserved after a compression of 0.375 GPa.

From Raman spectroscopy of ZIF-8 pellets (Figure 6.7 and Table 6.1), shifts of characteristic bands due to mechanical strain were observed, even though the direction of the shift was inverted compared to the flat punch indents. MIL-68 Raman spectra were again unchanged (Figure 6.8).

The insights from XRD and Raman analysis of ZIF-8 pellets seem to be inconsistent with the microRaman analysis of the residual indents. This discrepancy can be attributed to the distinct stress fields produced by hydrostatic compression and flat punch indentation, with the first distinguished by the lack of a shear component, which represent a key factor in ZIF-8 sodalite cage deformation (13, 75, 165).

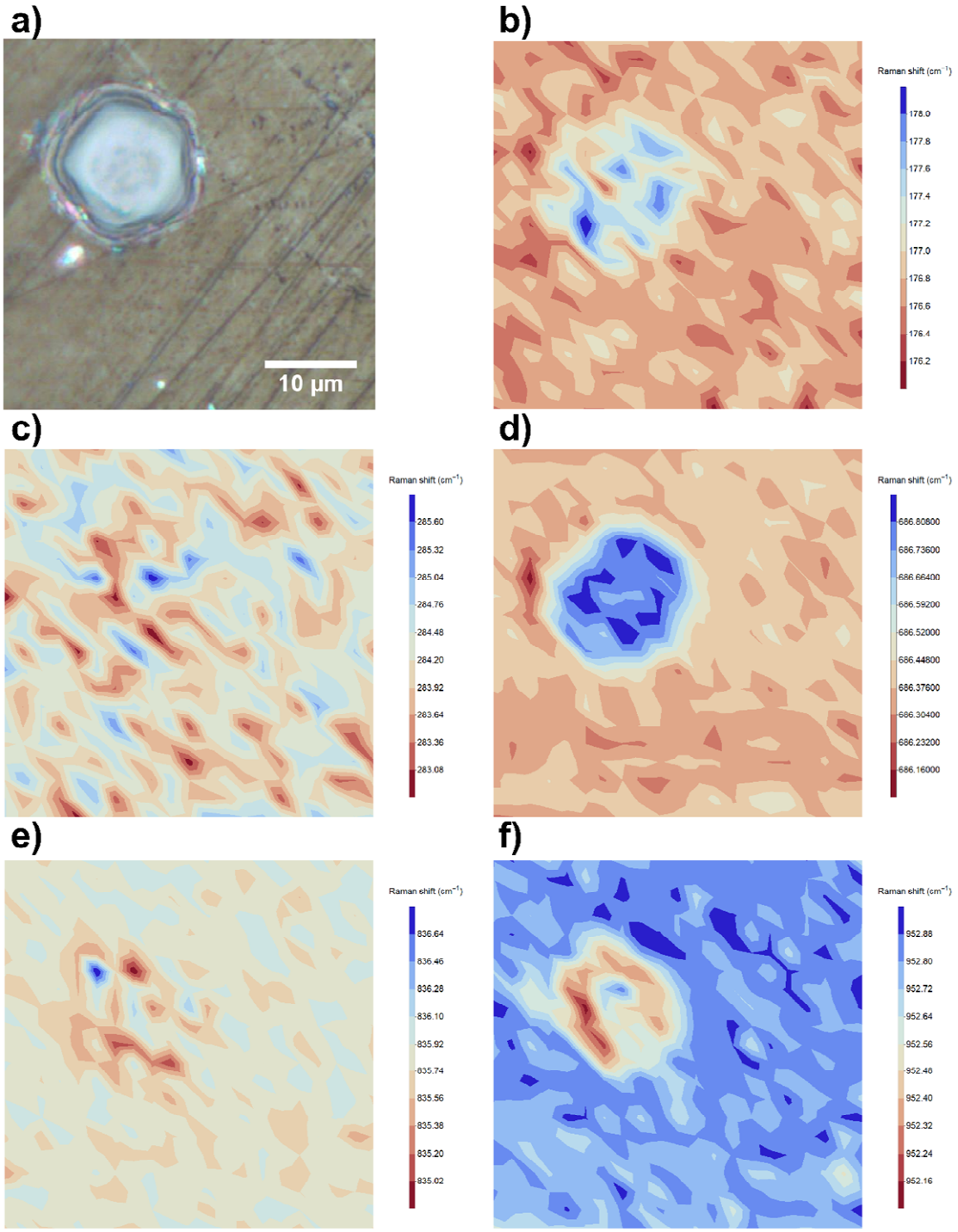

Figure 6.2 continue

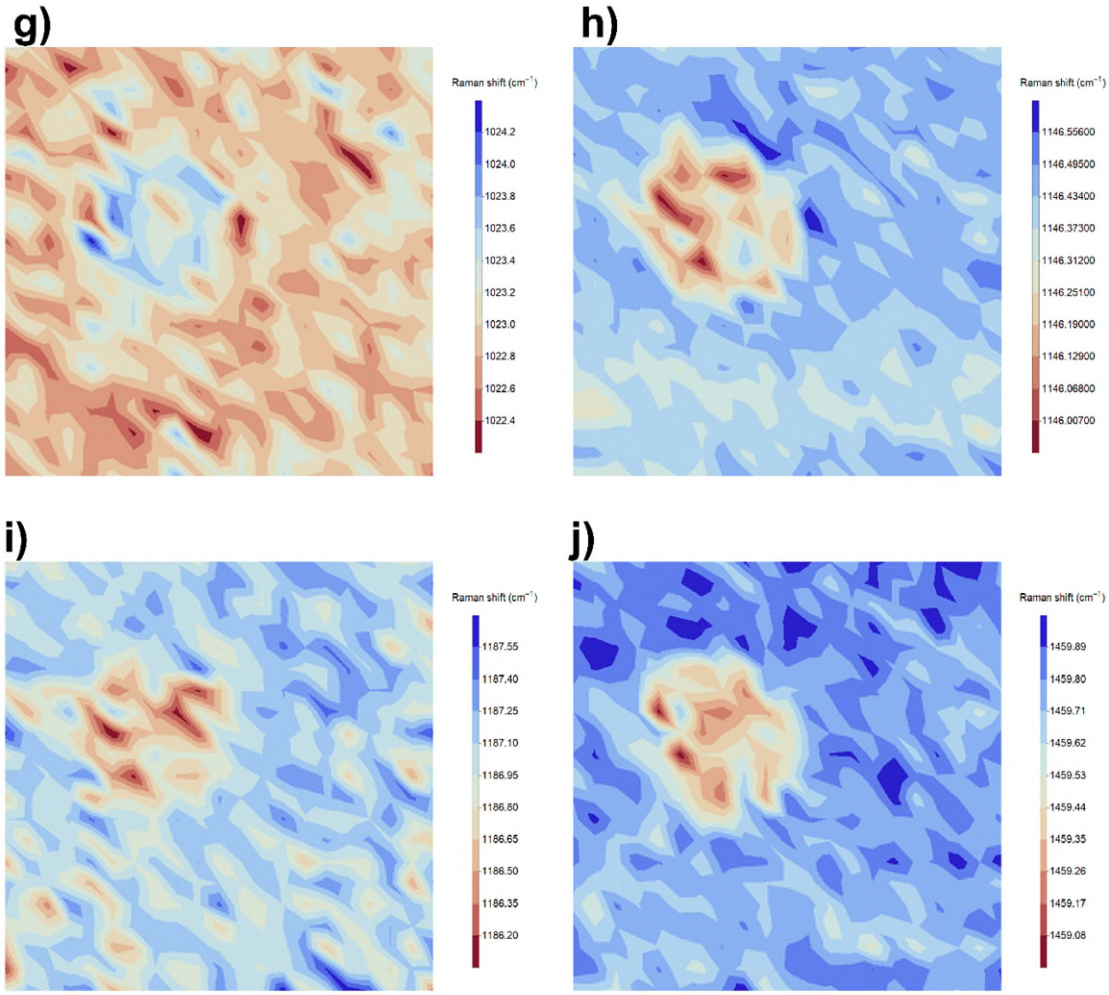

Figure 6.2 continue

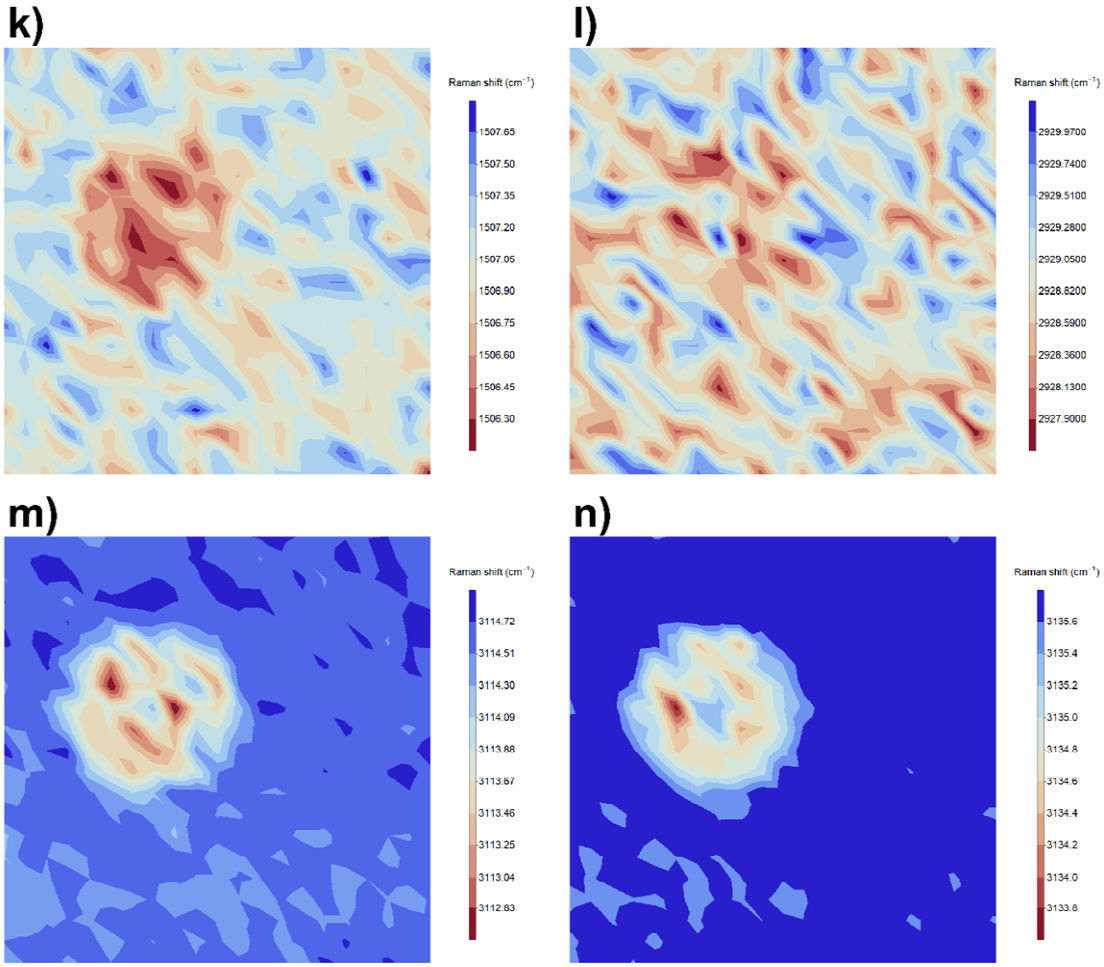

Figure 6.2 Confocal Raman microscopy of a residual flat punch indent on a ZIF-8 monolith. a) Micrograph of the indent, (b-m) maps indicating the spectral position of the charactersistic vibrational bands of ZIF-8: b) 176 cm^{-1}, c) 284 cm^{-1}, d) 686 cm^{-1}, e) 836 cm^{-1}, f) 953 cm^{-1}, g) 1024 cm^{-1}, h) 1146 cm^{-1}, i) 1185 cm^{-1}, j) 1461 cm^{-1}, k) 1510 cm^{-1}, l) 2930 cm^{-1}, m) 3114 cm^{-1}, n) 3135 cm^{-1}.

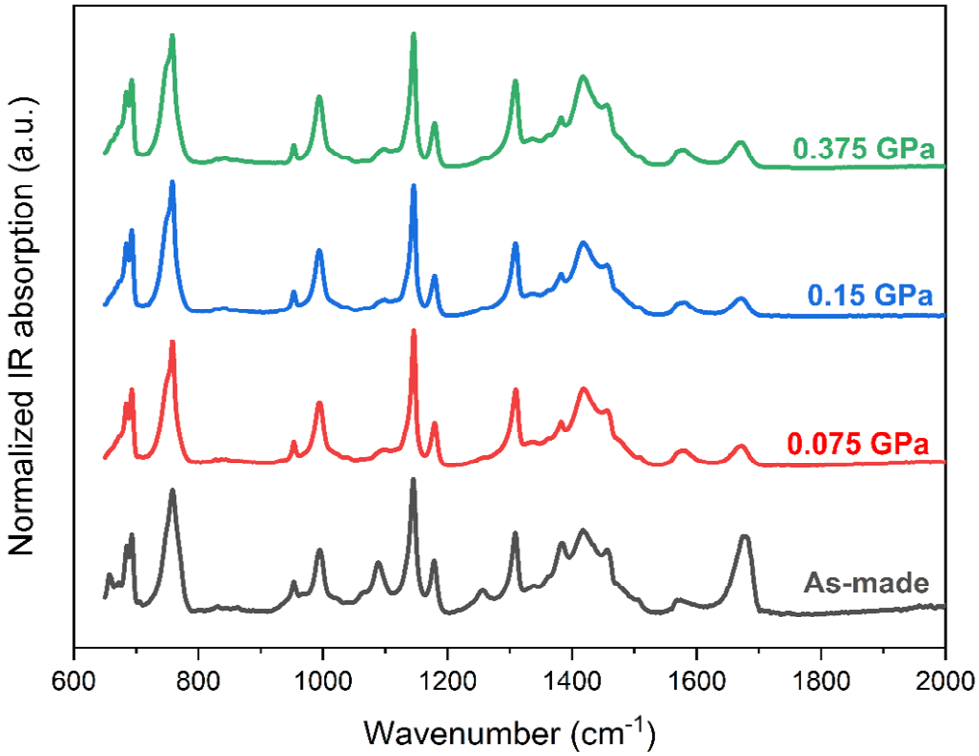

Figure 6.3 ATR-FTIR spectra of ZIF-8 pellets prepared with different compaction pressures under a pellet press.

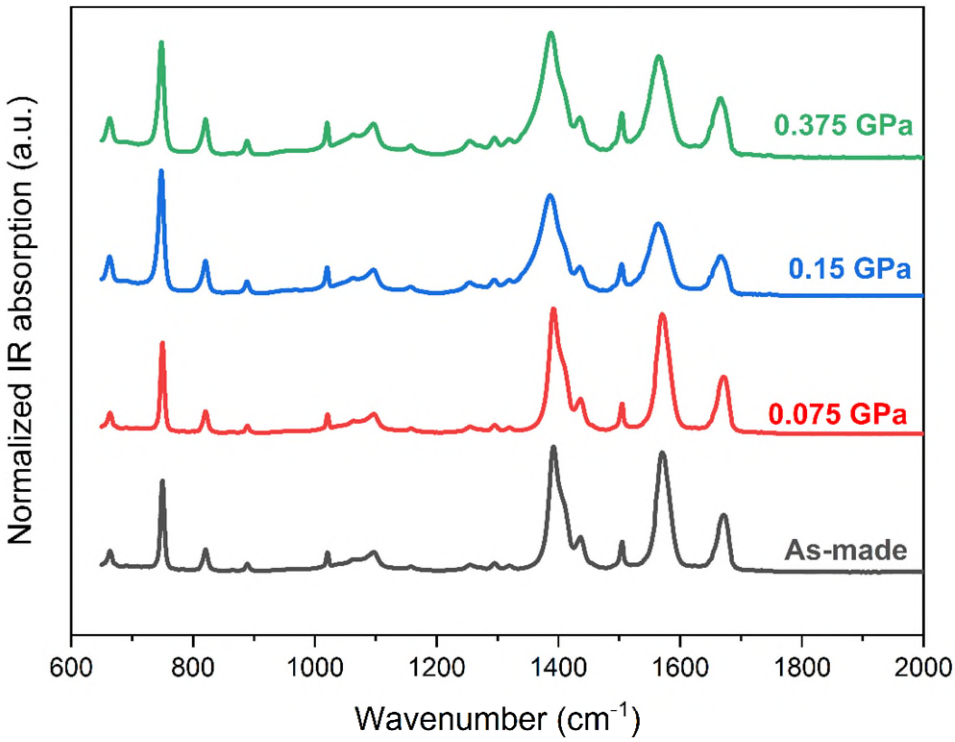

Figure 6.4 ATR-FTIR spectra of MIL-68 pellets prepared with different compaction pressures.

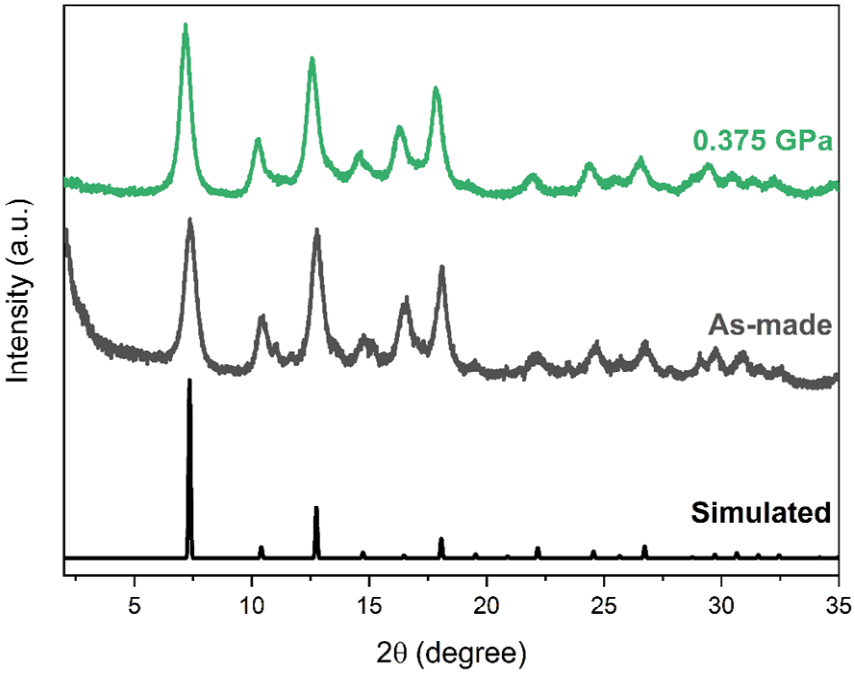

Figure 6.5 XRD patterns of as-synthesised ZIF-8 monolith and 0.375 GPa pellet in comparison with the simulated pattern from the Cambridge Structural Database (CCDC code: TUDKEJ).

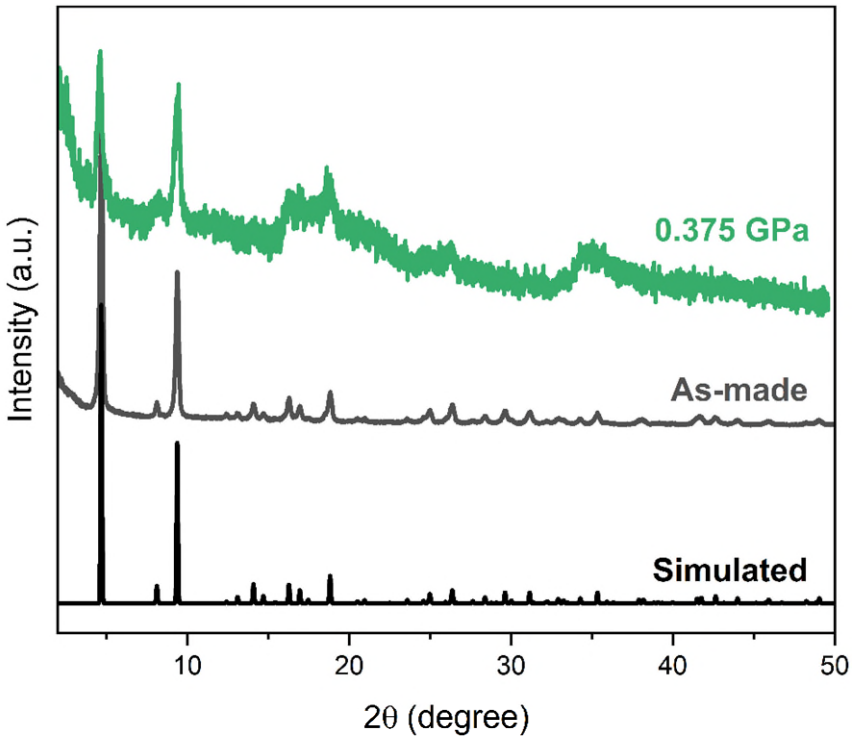

Figure 6.6 XRD patterns of as-synthesised MIL-68 monolith and 0.375 GPa pellet in comparison with the simulated pattern from the Cambridge Structural Database (CCDC code: LOQLEJ).

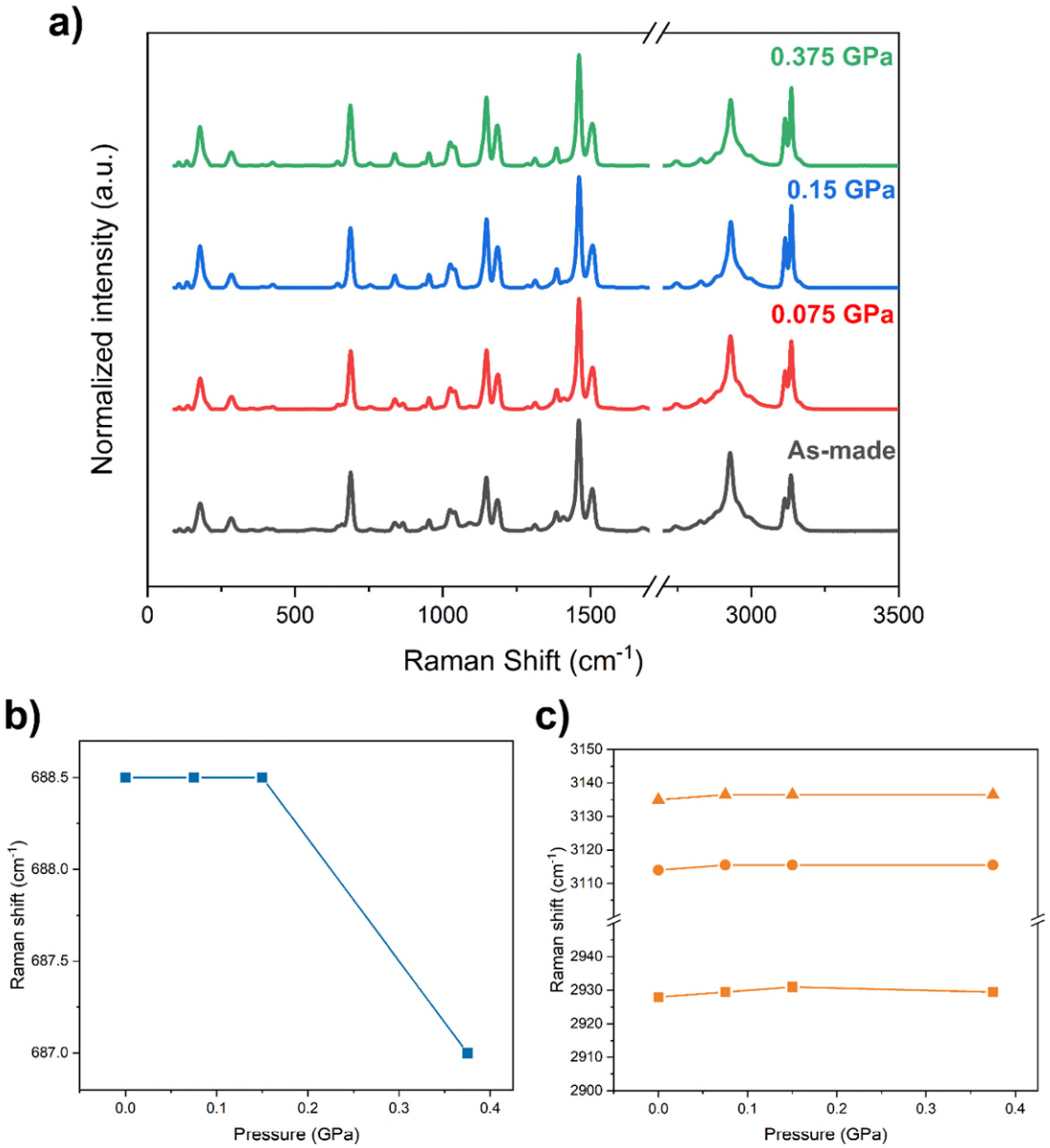

Figure 6.7. a) Raman spectra of ZIF-8 pellets prepared with different compaction pressures. b, c) Evolution of some characteristic peak shifts within the pressure range analysed (imidazolate ring puckering and C-H stretching, respectively).

Pelleting pressure (GPa)	**Raman shift (cm^{-1})**								
0	178.5	688.5	1147.5	1185	1461	1506	2928	3114	3135
0.075	178.5	688.5	1147.5	1186.5	1461	1507.5	2929.5	3115.5	3136.5
0.15	177	688.5	1147.5	1185	1461	1507.5	2931	3115.5	3136.5
0.375	177	687	1147.5	1185	1461	1506	2929.5	3115.5	3136.5

Table 6.1 Evolution of the characteristic Raman peaks of ZIF-8 within the pressure range analysed.

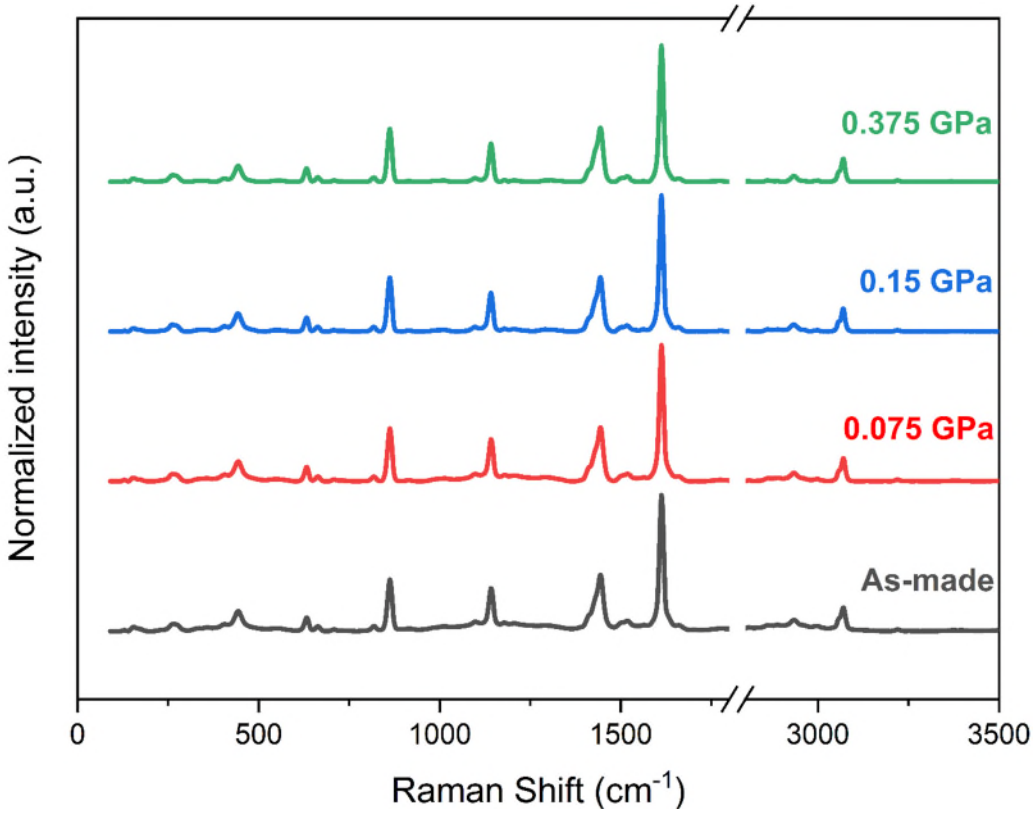

Figure 6.8 Raman spectra of MIL-68 pellets prepared with different compaction pressures.

6.3 Micropillar compression

The stress-strain relationships of ZIF-8 and MIL-68 monoliths were also estimated by micropillar compression (Figure 5 of Paper 3).

Two sets of micropillars per sample were fabricated by focused ion beam (FIB) milling, as illustrated in Figure 6.9, using the settings listed in Table 6.2. The voltage was set to 30 keV. Figures 6.10 to 6.13 and 6.14 to 6.17 show SEM pictures of the micropillars for ZIF-8 and MIL-68 respectively, before and after the uniaxial compression test performed in the instrumented nanoindenter. Figures 6.18 and 6.19 display the load displacement curves obtained from each test, for ZIF-8 and MIL-68, respectively, from which the stress-strain curves were derived.

The two monoliths exhibited two different stress-strain behaviours. ZIF-8 micropillars failed by brittle fracture, due to elastic crack propagation, as revealed by the presence of "pop-ins" (sudden displacement bursts at a constant load) in the load-displacement and stress-strain curves. Splitting along the pillar axis direction was observed to be the failing mechanism (Figure 6.20). On the other hand, MIL-68 displayed a substantial plastic deformation, and no pop-in was detected. In contrast to ZIF-8, SEM images of the collapsed micropillars show no sign of longitudinal cracking (Figure 6.21).

Material	Set #	Pillar #	FIB beam current (mA)	Height (µm)		Diameter (µm)	
				input	measured	input	measured
ZIF-8	1	1	1.234	10	11	7	6
		2	1.232	7	10	7	7
		3	1.234	7	10	7	7
	2	1	1.557	7	8.4	7	7
		2	1.571	7	8.7	7	7
		3	1.58	7	8.5	7	7
		4	1.583	7	8.5	7	7
MIL-68	1	1	1.418	7	18	7	7
		2	1.422	3.5	7	9	8
		3	1.43	5	8	9	7.5
	2	1	1.418	5.5	8.7	7	6.7
		2	1.432	4	7.2	7	6.4
		3	1.44	4.4	7.6	9	8.8

Table 6.2. Beam current used for FIB milling and dimensions (height and diameter) of the micropillars manufactured from MOF monoliths.

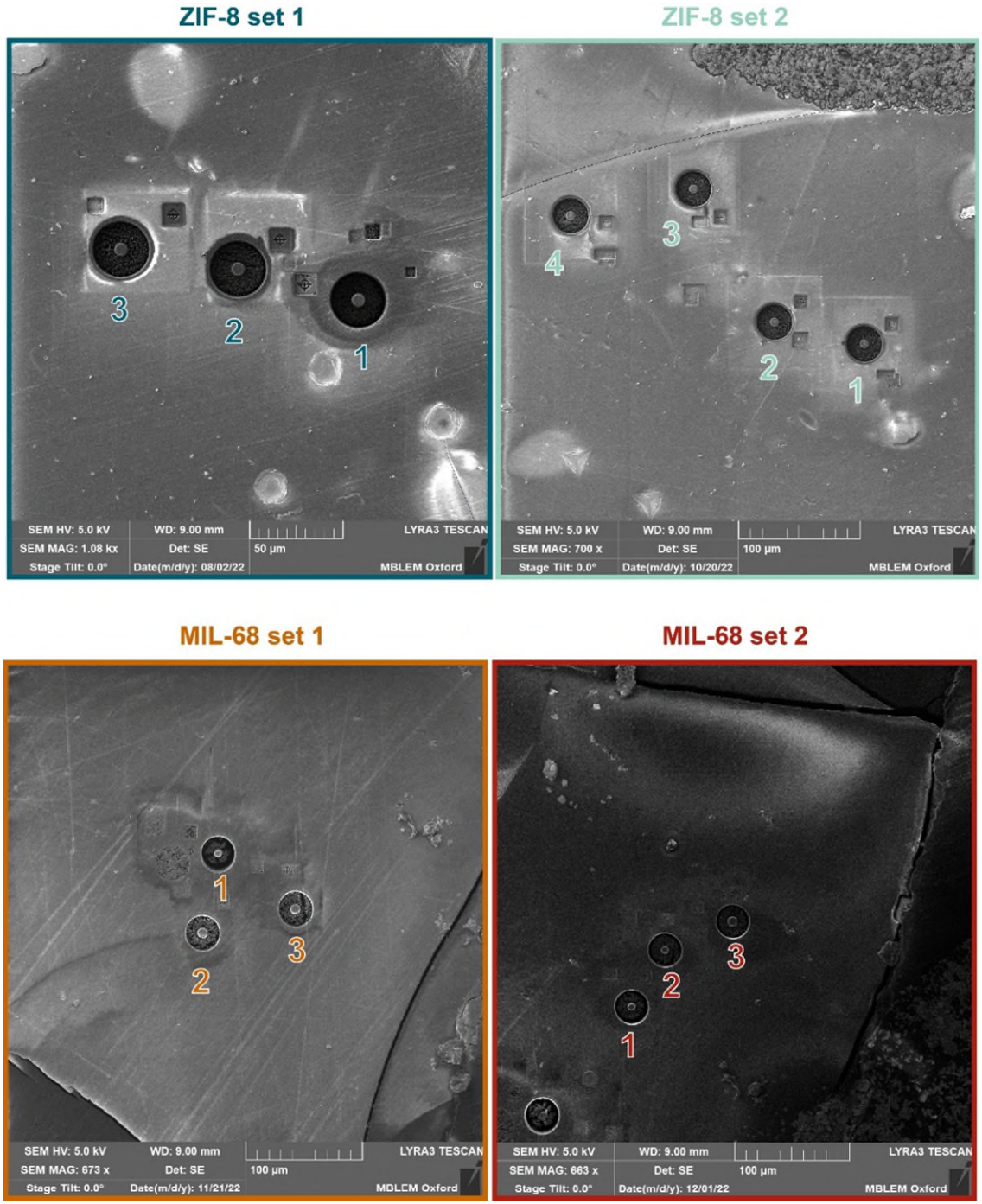

Figure 6.9. Overview of the micropillars set fabricated on the ZIF-8 and MIL-68 monolithic samples.

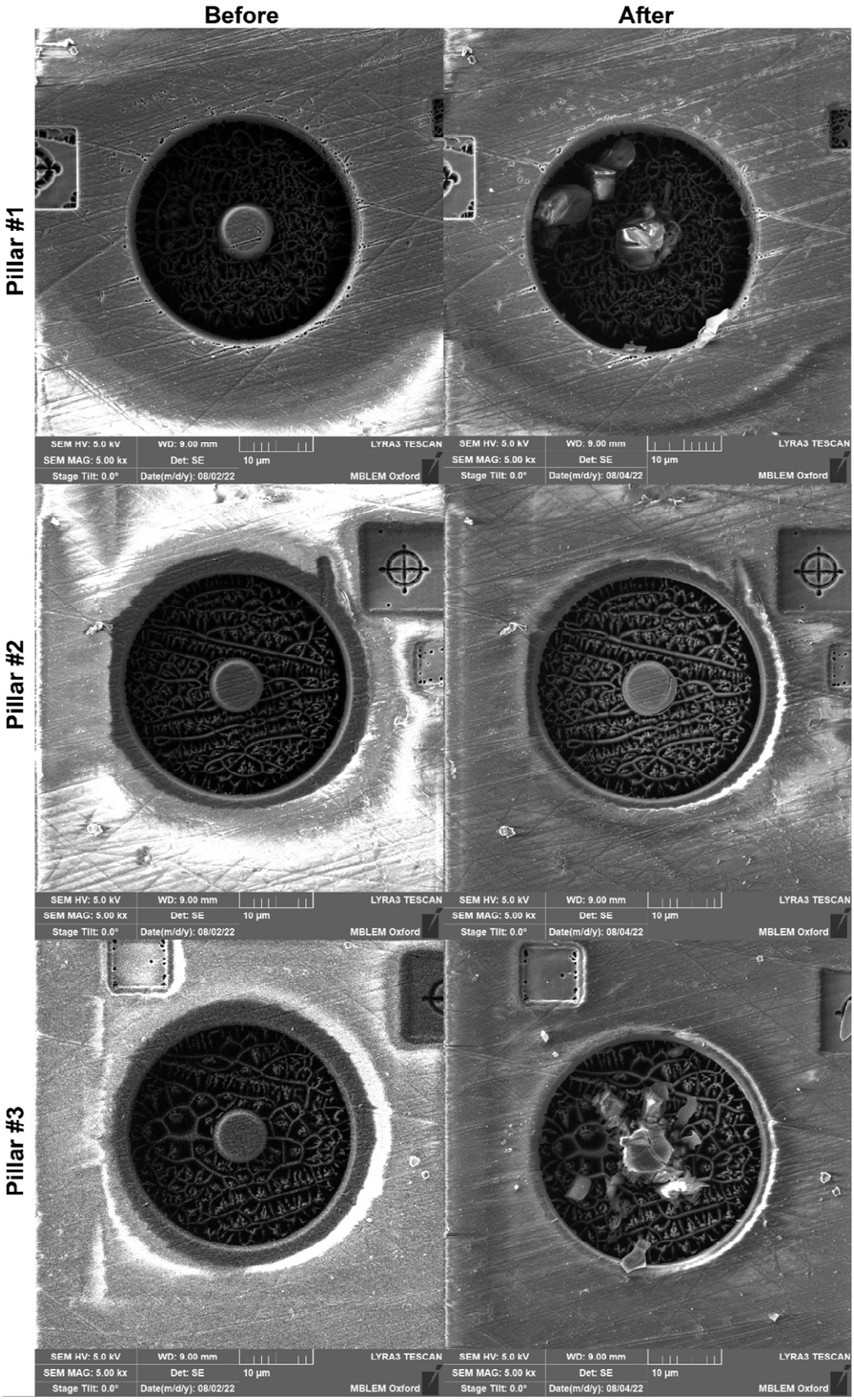

Figure 6.10. Top view of the set #1 of micropillars made on a ZIF-8 monolith, before and after the compression test.

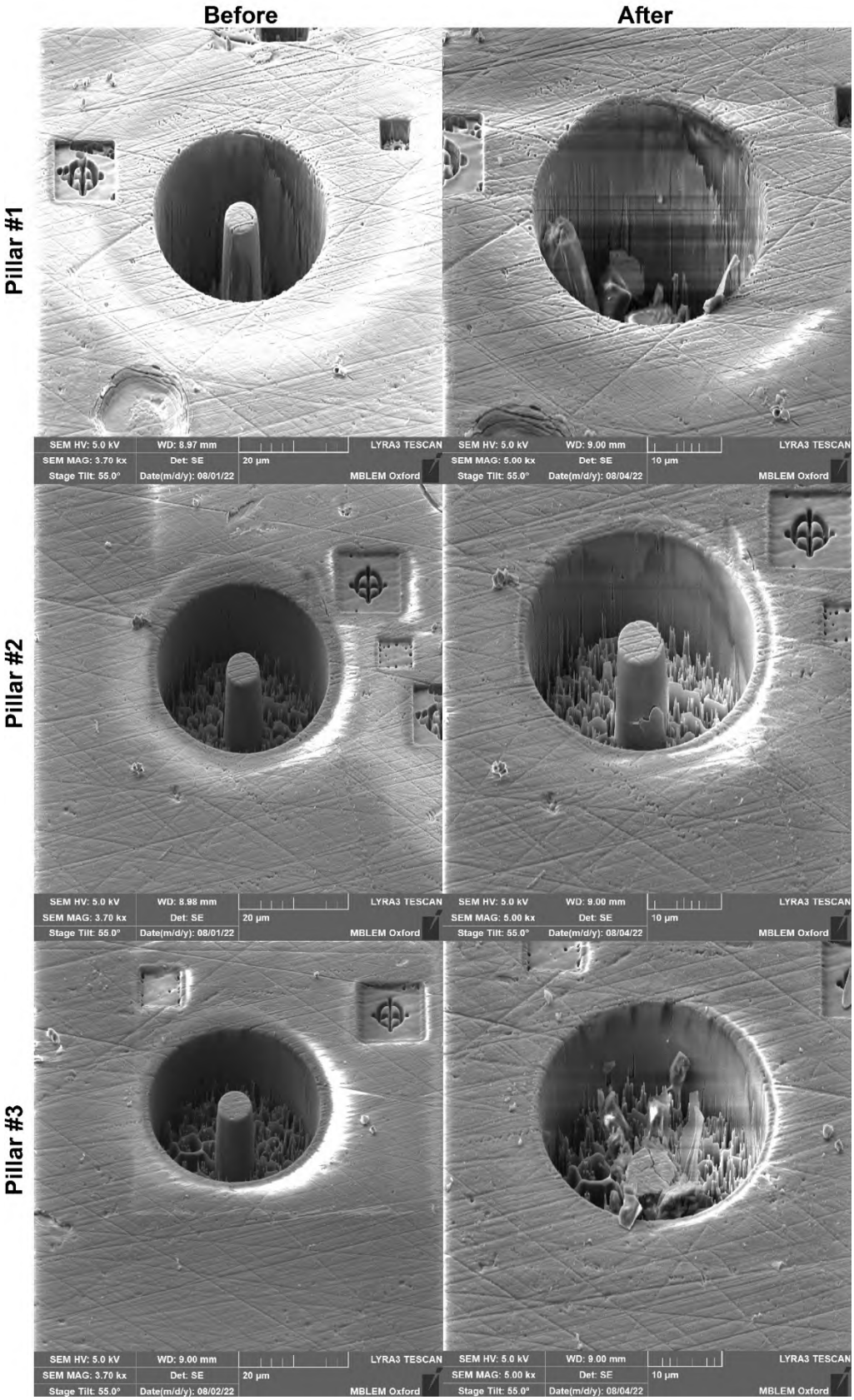

Figure 6.11. Tilted view (55°) of the set #1 of micropillars made on a ZIF-8 monolith, before and after the compression test.

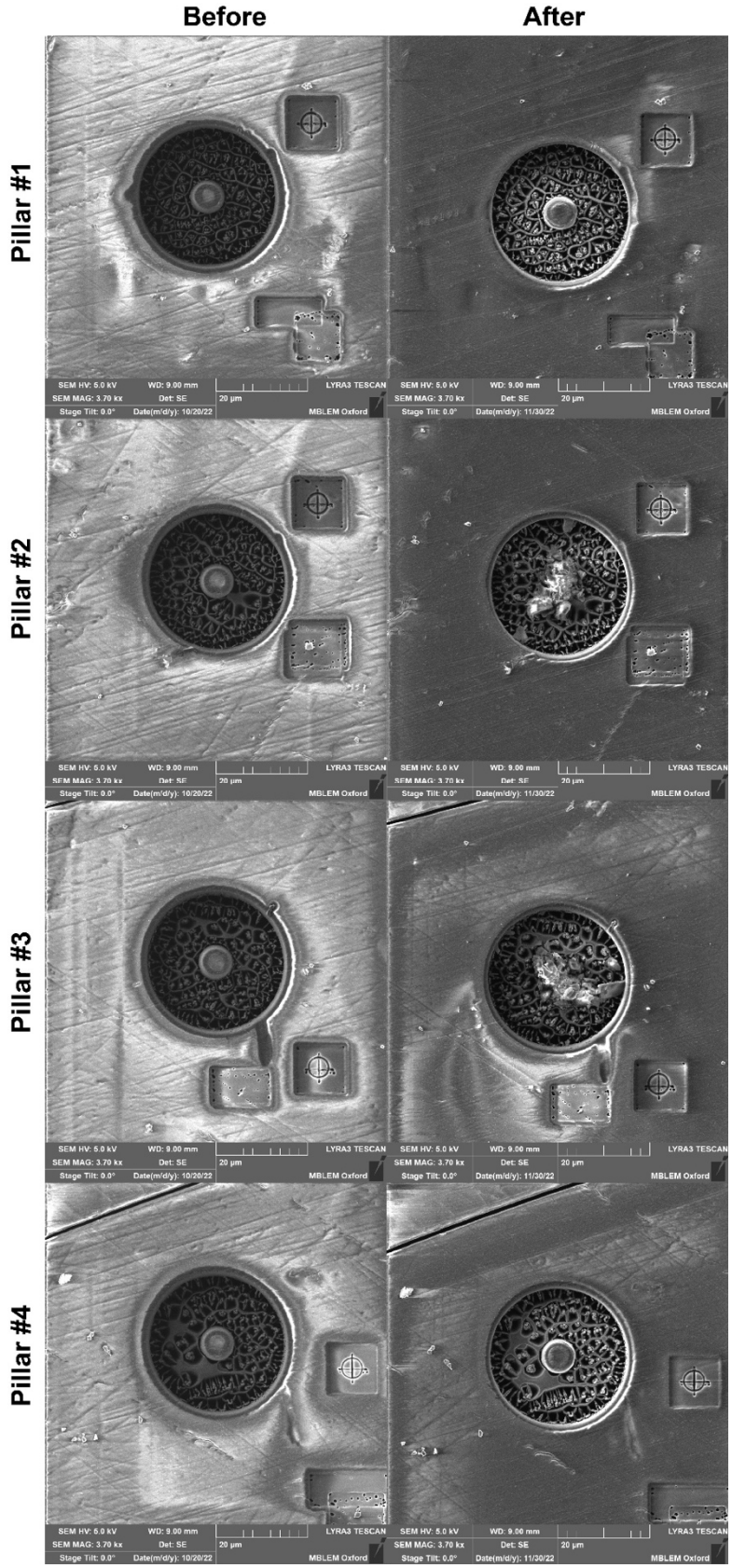

Figure 6.12. Top view of the set #2 of micropillars made on a ZIF-8 monolith, before and after the compression test.

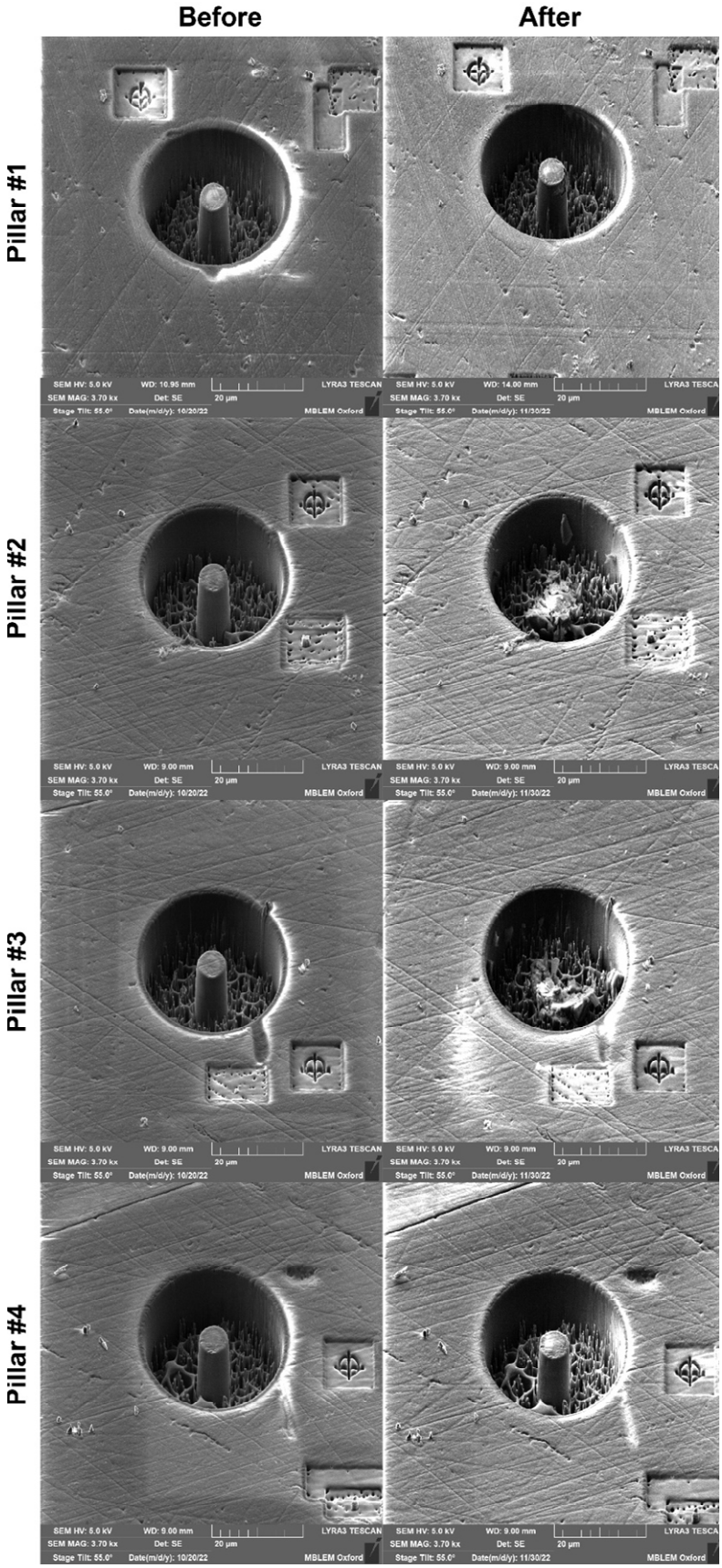

Figure 6.13. Tilted view (55°) of the set #1 of micropillars made on a ZIF-8 monolith, before and after the compression test.

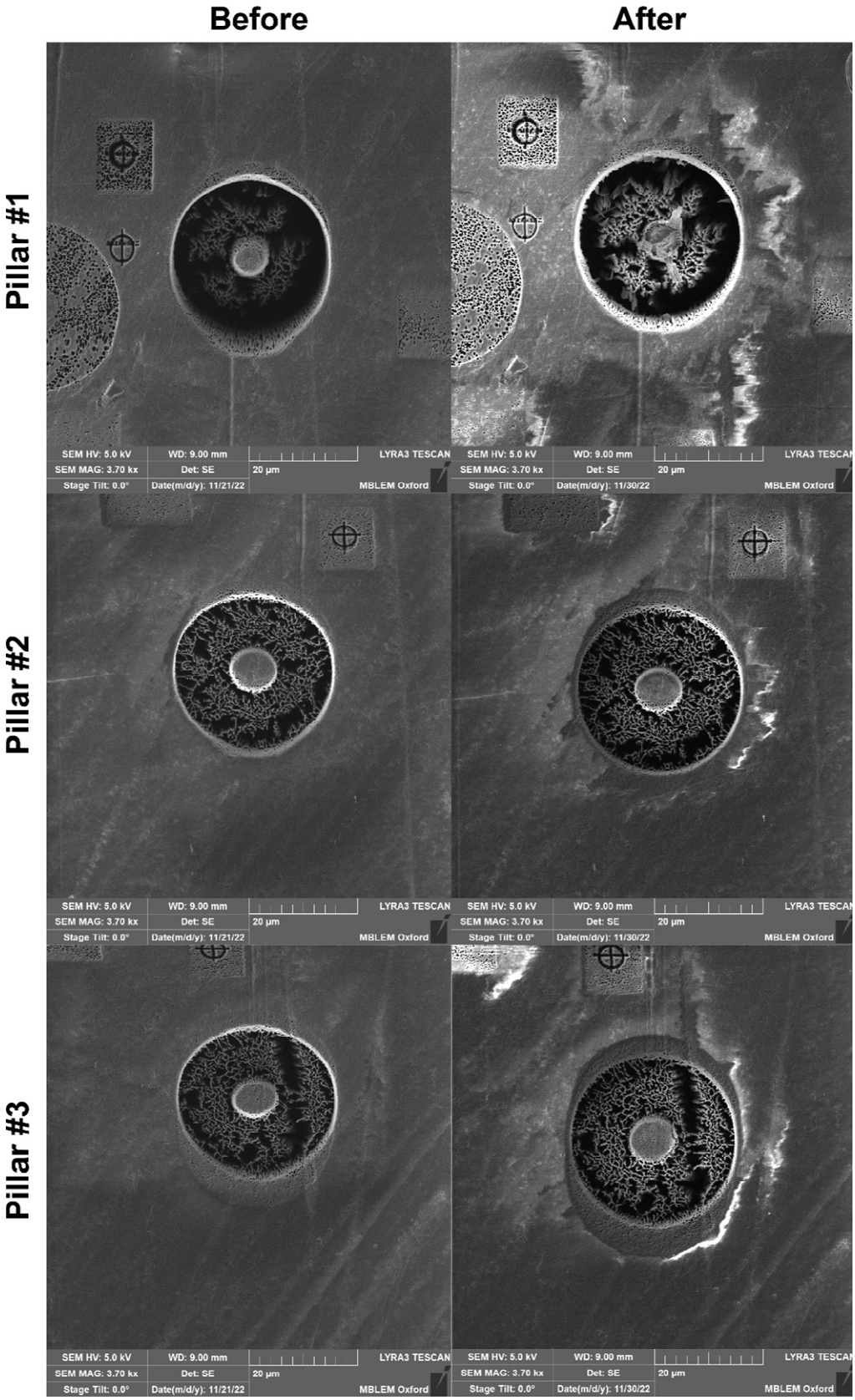

Figure 6.14. Top view of the set #1 of micropillars made on a MIL-68 monolith, before and after the compression test.

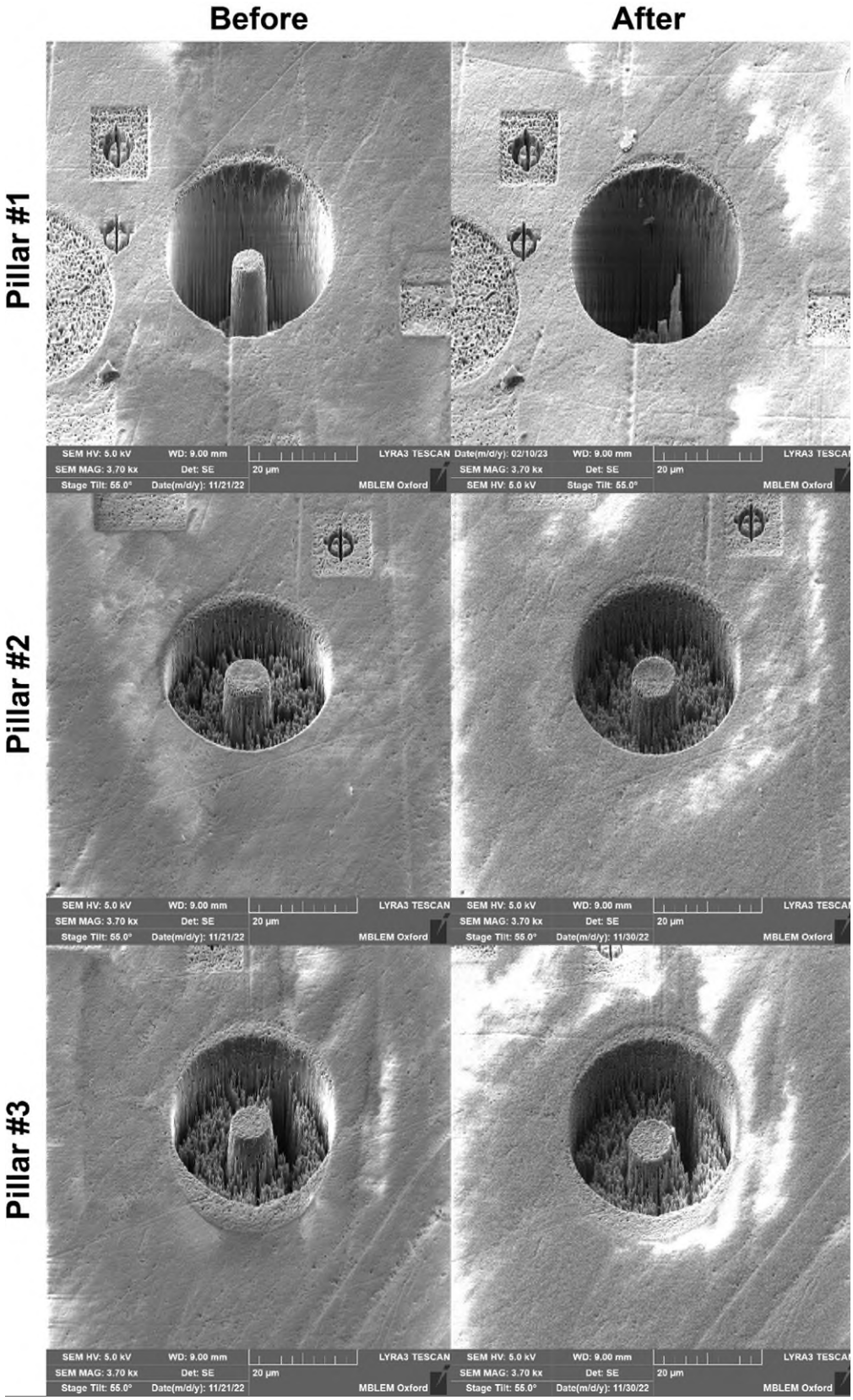

Figure 6.15. Tilted view (55°) of the set #1 of micropillars made on a MIL-68 monolith, before and after the compression test.

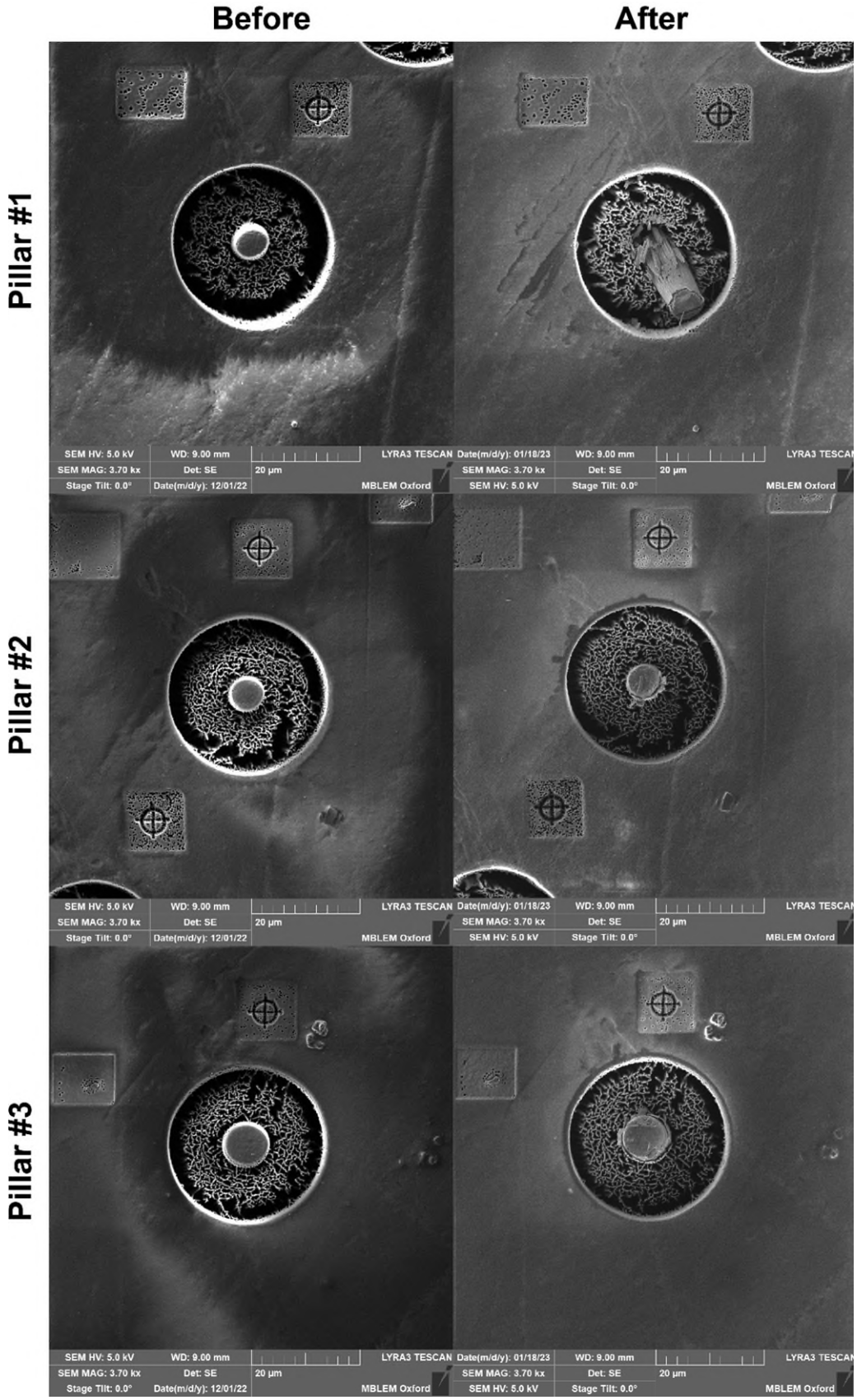

Figure 6.16. Top view of the set #2 of micropillars made on a MIL-68 monolith, before and after the compression test.

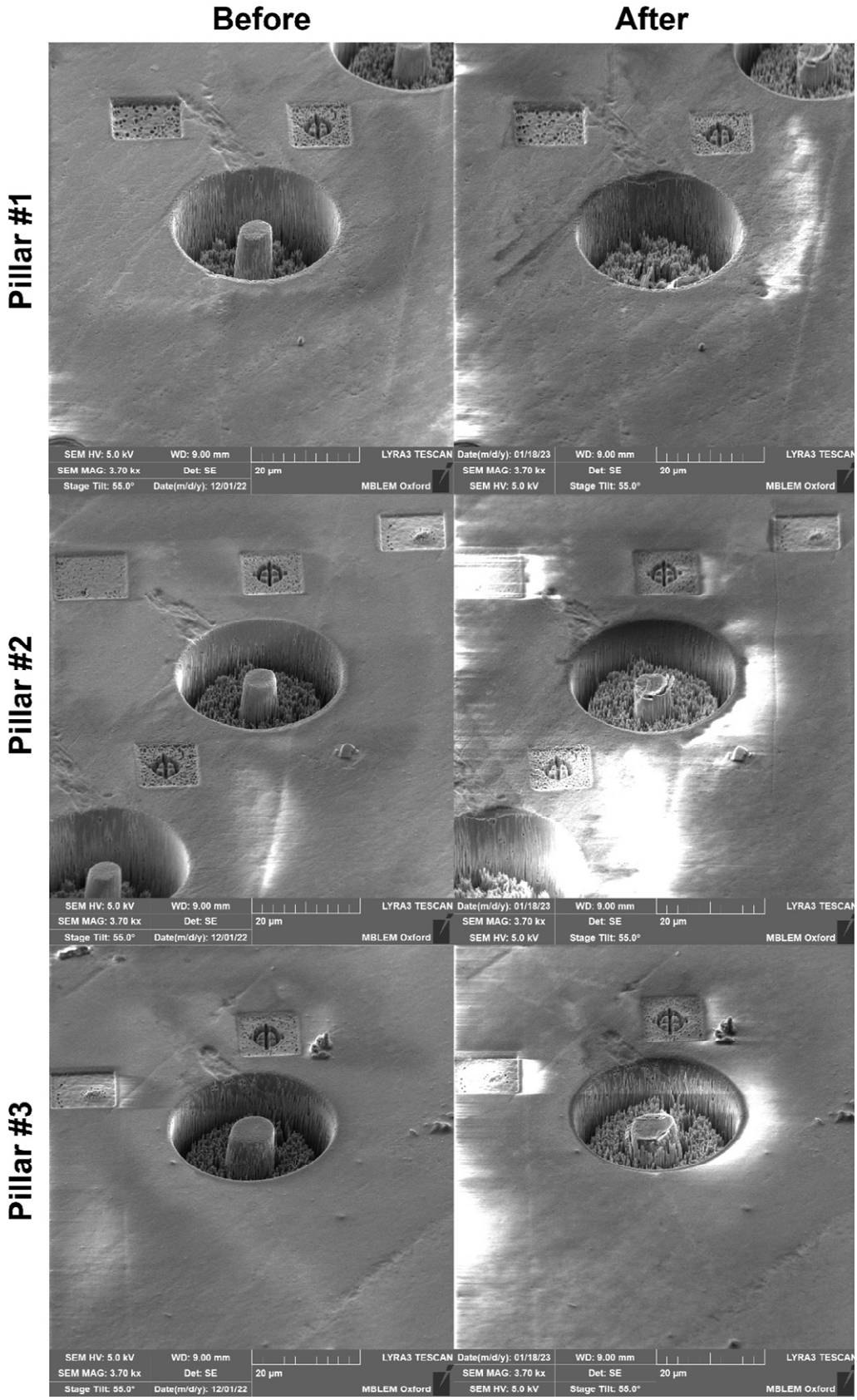

Figure 6.17. Tilted view (55°) of the set #2 of micropillars made on a MIL-68 monolith, before and after the compression test.

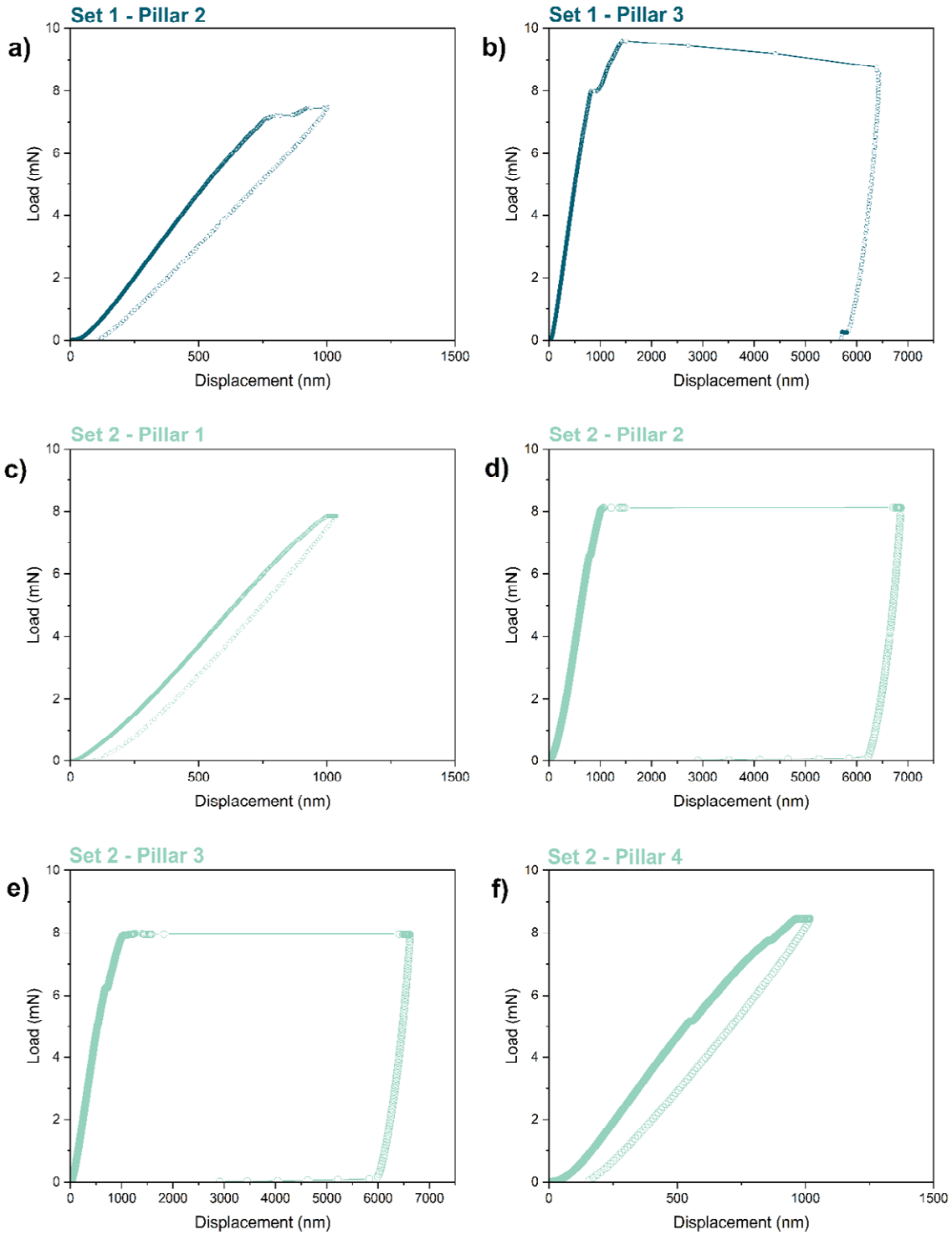

Figure 6.18 Load-displacement curves measured from the uniaxial compression of ZIF-8 micropillars.

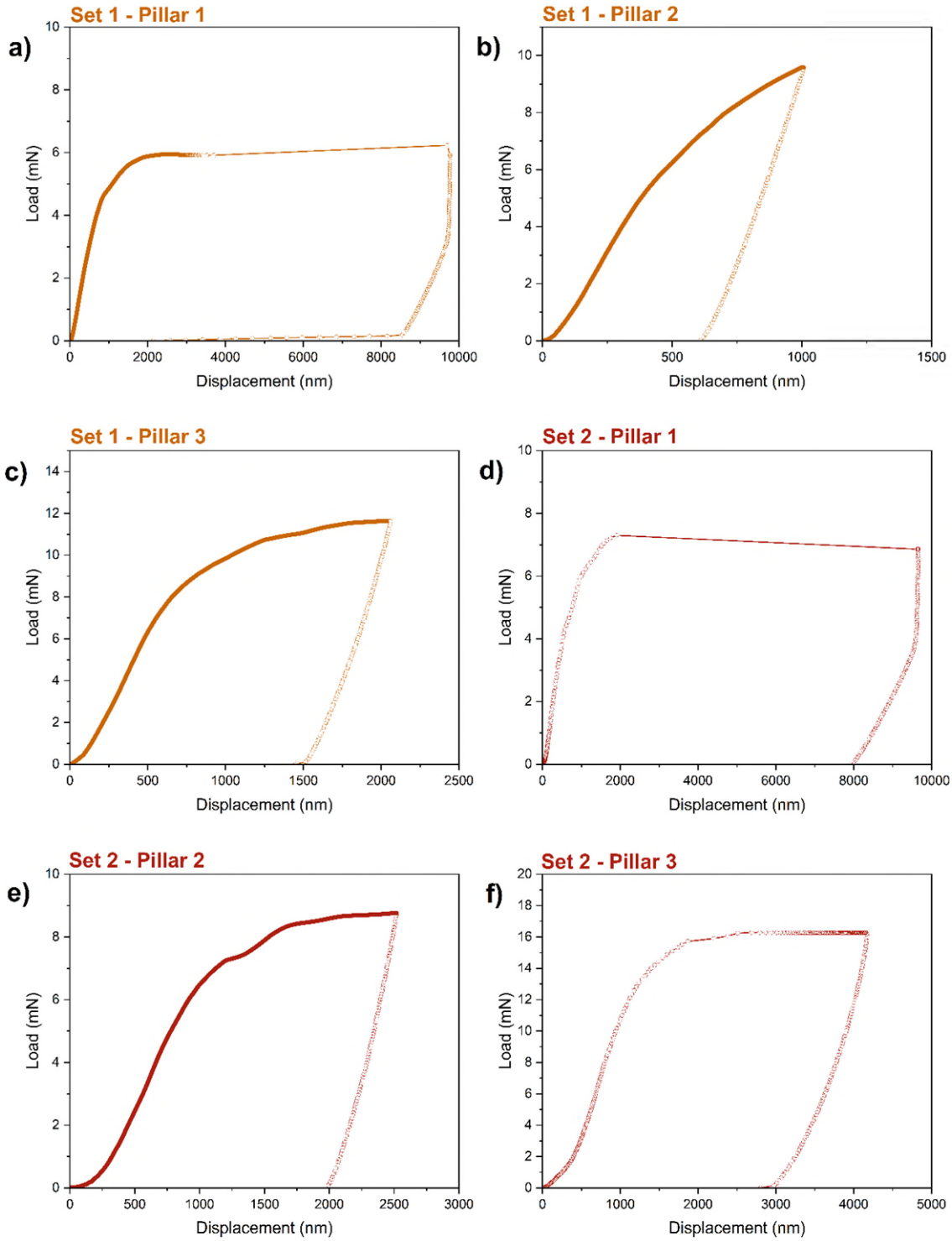

Figure 6.19 Load-displacement curves measured from the uniaxial compression of MIL-68 micropillars.

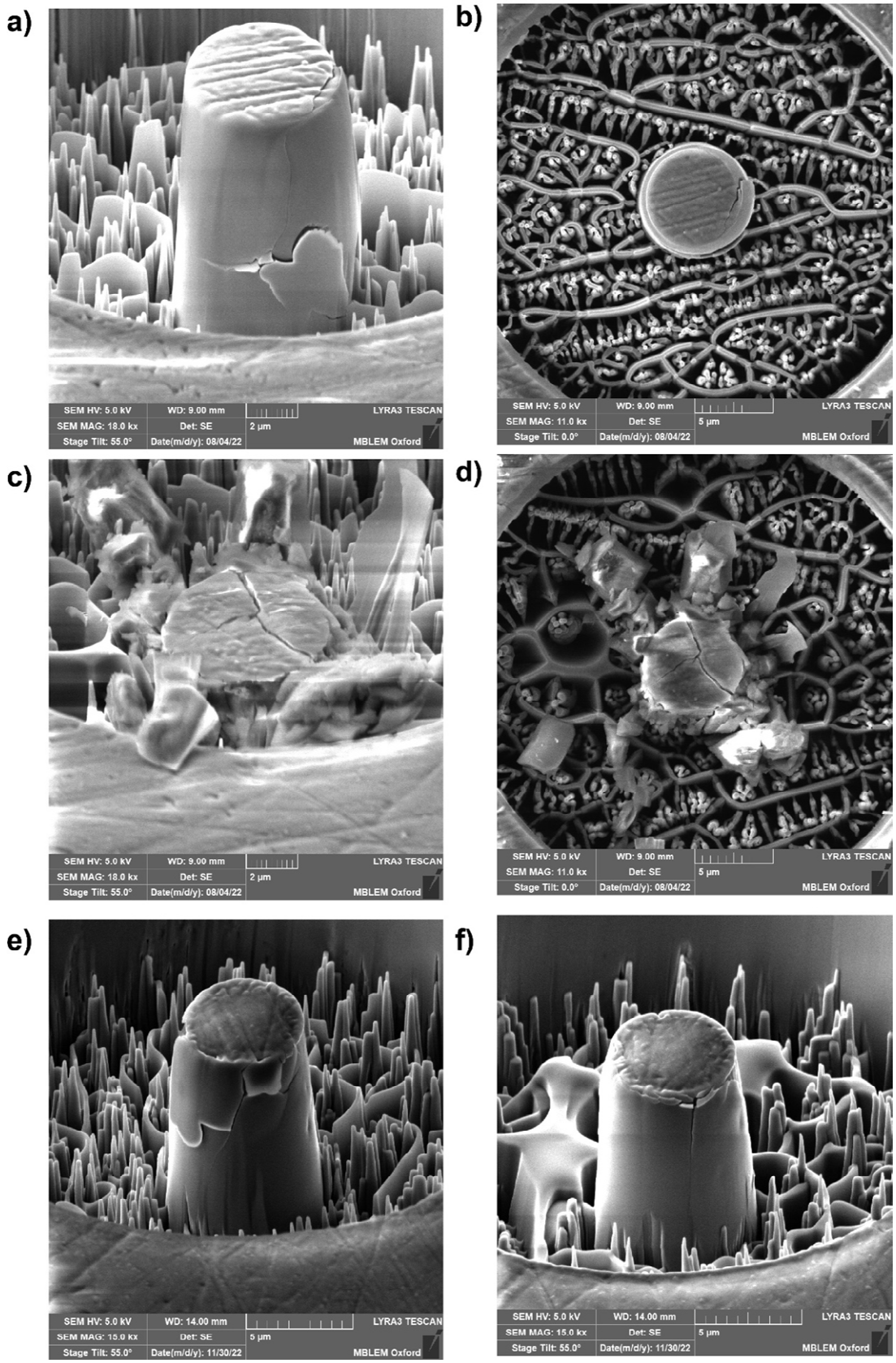

Figure 6.20 Details of post-compression of ZIF-8 micropillars: a-b) tilted and top views of pillar #2 of set #1; c-d) tilted and top views of pillar #3 of set #1; e) pillar #1 of set #2; f) pillar #4 of set #2.

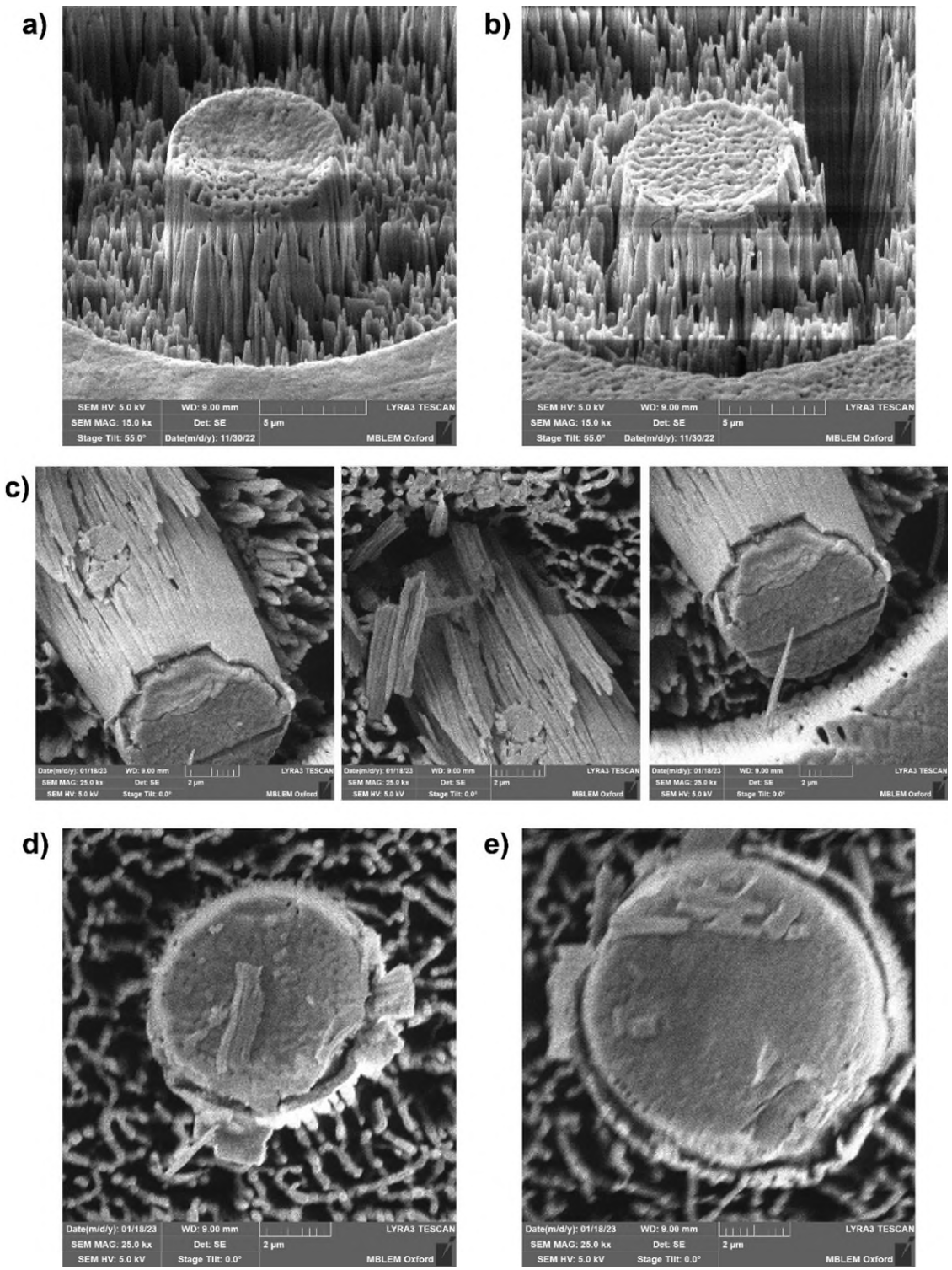

Figure 6.21 Details of post-compression of MIL-68 micropillars: a) pillar#2 of set#1; b) pillar#3 of set#1; c) pillar#1 of set#2; d) pillar#2 of set#2; e) pillar#3 of set#2;

6.4 Paper III: Stress-strain relationships and yielding of MOF monoliths

(Manuscript draft)

Stress-strain relationships and yielding of MOF monoliths

*Michele Tricarico[a], Cyril Besnard[b], Gianfelice Cinque[c], Alexander M. Korsunsky[b] and Jin-Chong Tan[a]**

[a] *Multifunctional Materials and Composites (MMC) Laboratory, Department of Engineering Science, University of Oxford, Parks Road, Oxford, OX1 3PJ, United Kingdom*

[b] *MBLEM, Department of Engineering Science, University of Oxford, Parks Road, Oxford, OX1 3PJ, United Kingdom*

[c] *Diamond Light Source, Harwell Campus, Chilton, Oxford OX11 0DE, United Kingdom*

**E-mail: jin-chong.tan@eng.ox.ac.uk*

Abstract

Metal-organic frameworks (MOFs) have emerged as a versatile material platform for a wide range of applications, including chemical sensing, separation, gas adsorption and energy storage. However, the development of practical devices is constrained by their inherently low mechanical stability. The synthesis of MOFs in a monolithic morphology represents a viable way for the transition of these materials from laboratory research to real-word applications. The design of MOF-based devices cannot overlook the mechanical characterisation of such materials. In this regard, stress-strain relations represent the most valuable tool for assessing the mechanical response of materials. Here we performed flat punch nanoindentation and micropillar compression on ZIF-8 and MIL-68 monoliths, to estimate, for the first time, the stress-strain behaviour of this class of MOF materials. We employed Raman spectroscopy to pinpoint residual strain locally, at the framework length scale. A “pseudo-plastic” flow was observed under indentation, where the confining pressure prevents unstable crack propagation. Material flow is accommodated by grain boundary sliding, with occasional stepwise cracking to accommodate excessive stress building-up. Permanent distortions at the framework level take place when the stiffness of the MOF cage is close to the intergranular cohesion (high *H/E*), as in the case of ZIF-8. Micropillar compression revealed a brittle failure of ZIF-8, due to elastic propagation of cracks, while plastic flow was observed for MIL-68.

1. Introduction

Metal-organic frameworks (MOFs) represent a relatively new class of hybrid nanoporous materials, made up of organic ligands and metal clusters that self-assemble into a lattice framework with a significant internal surface area. Several different framework-type

compounds with high chemical stability, adjustable physical properties, organic functionality, and porosity have been developed over the past 25 years of research [1], opening up a wide range of potential technological applications [2-6].

Yet, there is not much of a crossover between academic research and industrial practical uses. A poor understanding of the mechanical properties is one of the causes of this shortcoming. The topic of MOF mechanics [7-10] is still in its infancy despite the extensive research put into the chemical synthesis of new framework structures and the characterisation of their functional properties. The primary reason for this is the morphological limitations of this class of materials, which are frequently synthesised as polydisperse microcrystalline powders and challenging to characterise using traditional mechanical testing. A way to overcome this limitation is represented by the sol-gel synthesis route, which enables the fabrication of sturdy and bulk monolithic morphologies [11]. Several types of nanoporous sol-gel monoliths have already been reported, including MOFs such as ZIFs [12-14], HKUST-1 [15] and UiO-66 [16, 17] and COFs (covalent organic frameworks) [18]. This method produces a hierarchical pore distribution, which enhances gas absorption capabilities [19].

Most of the mechanical characterisation of MOFs to date is based on nanoindentation-based measurements, particularly of Young's modulus and hardness, by using the method developed by Oliver and Pharr [20]. One of the first studies reporting the mechanical properties of a MOF material were carried out by Bahr *et al.* [21], who characterised MOF-5, a zinc-based framework, and determined a Young's modulus of 7.9 *GPa* for the (100)-oriented face. Tan *et al.* [22] performed nanoindentation measurements on different types of zeolitic imidazolate frameworks (ZIFs) and were able to correlate the mechanical responses with the different ZIF structures (given by the different combinations of organic

and inorganic building blocks). Their findings revealed that crystals porosity and linker morphology strongly affect the mechanical properties of the framework. Particularly, crystals with a higher porosity can sustain lower loads and show a smaller elastic recovery, compared to the structure characterised by smaller pore sizes. When frameworks of the same topology are considered, the ones incorporating bulky imidazole ligands will exhibit a greater stiffness. The aromatic linkers tend to fill up the pores, inducing steric hindrance and additional short-range dispersion interactions resulting in the stiffening of the structure. Furthermore, it was demonstrated that the metal sites serve only as compliant nodes for connecting linkages [23]. The effect of linkers on the elastic properties was explored also by Bennett *et al.* [24], who observed that the Young's modulus of ZIF-zni is three times greater than that of its Boron Imidazolate Framework (BIF) isostructural analogue (alternate Zn cations are replaced by Li and B respectively), $LiB(Im)_4$, due to the superior stiffness of Zn-Im-Zn linkages compared to their Li-Im-Li counterparts.

Mechanical properties of MOF thin films and coatings have been explored either by nanoindentation [25] or nanoscratch tests [26].

The literature regarding MOF monoliths mechanics has started to grow in the last few years. Tian *et al.* [15] performed nanoindentation on a HKUST-1 sol-gel monolith, and measured a Young's modulus of 9.3 ± 0.3 GPa, which resembles the stiffness value predicted by theoretical calculations (E = 8.1 GPa, [27]). The monolith hardness (H = 460 MPa) is about 130% greater than the HKUST-1 epitaxial film (H = 200 MPa) reported by [25]. Their findings suggest that the high bulk density of the HKUST-1 monolith not only improves the volumetric adsorption capability but also the mechanical resilience. Connolly *et al.* [16] reported the mechanical properties of UiO-66 monoliths,

which were found to vary significantly with drying conditions and washing procedures. In our recent study [13], the mechanical response of two ZIF sol-gel monoliths, namely ZIF-8 and ZIF-71, was analysed by a combination of nanoindentation, nanoscale Fourier transform infrared spectroscopy (nanoFTIR), tip force microscopy (TFM) and finite element method (FEM) simulations. In a nutshell, we were able to pinpoint the mechanical deformation mechanisms in monolithic ZIF materials. Grain boundary sliding predominates at low stresses, followed by the collapse of chemical bonds and a partial failure of the framework due to shear stress, which eventually leads to densification of the porous framework at the contact area. In a follow-up study [28] we explored the fracture behaviour of MOF monoliths, by analysing the nanoindentation-induced crack initiation and propagation of four prototypical MOF monoliths (ZIF-8, HKUST-1, MIL-68 and MOF-808), characterised by different framework architectures. We observed a clear correlation between elastic recovery and crack resistance, with the monoliths exhibiting low elastic recovery being remarkably tough (i.e., MIL-68 and MOF-808). This outstanding ductility was ascribed to a combination of nanostructure (size and shape of nanogranular aggregates) and framework architecture. These factors result in the occurrence of shear faults, most likely in correspondence of the grain boundaries, well contained within the contact area. This localised micro-failure mechanism dissipates energy, hence preventing the initiation of cracks form the indent's corners.

In the present work, we have studied two monoliths, ZIF-8 and MIL-68, prepared by sol-gel processing, leveraging the high concentration reaction (HCR) method [29], as illustrated in Figure 1. These two materials are characterised by different fracture behaviours under sharp indentation [28]. For the first time, we estimated the stress-strain ($\sigma - \varepsilon$) relationships of the two systems by two different approaches, flat punch

indentation and micropillars compression, with the aim of elucidating the yielding and plastic behaviour of this class of materials. Our findings reveal different plastic responses, which can be ascribed to the nanogranular structure and the framework architecture. Moreover, we used confocal Raman spectroscopy to shed light on the contribution of the framework to the residual strains induced by flat punch indentation. To the best of our knowledge, this is the first attempt to evaluate stress-strain relations of MOF monoliths. Micropillar compression of MOF glasses [30] and single crystals [31] have been reported recently, but studies of this type are still quite limited due to the great susceptibility of this materials to focused ion beam (FIB) damage.

2. Experimental methods

2.1 Materials synthesis

Zinc nitrate hexahydrate ($Zn(NO_3)_2 \cdot 6H_2O$), 2-methylimidazole (mImH), indium nitrate, 1,4-benzenedicarboxylate (BDC), triethylamine (NEt_3), dimethylformamide (DMF), methanol (MeOH), and acetonitrile (MeCN) were purchased from Fisher Scientific and used as received.

ZIF-8 monoliths were synthesised following the procedure described in [13]: 0.595 g of $Zn(NO_3)_2 \cdot 6H_2O$ and 0.493 g of mImH were dissolved in 9 mL of DMF each and stirred for 5 minutes. Then, 0.837 mL of triethylamine (NEt_3) was added to the linker solution. Subsequently, the two solutions were combined in a 50 mL vial, where a gel was promptly formed. The mixture was sonicated for 5 minutes and then washed three times, in 50 mL of solvent (DMF, MeOH and MeCN, respectively), followed by centrifugation at 8,000 RPM. The collected solid was dried slowly at room temperature (RT ~25 °C) for 3 days under the fume cupboard to yield monoliths.

MIL-68(In) monoliths 9 mL DMF solution of 797 mg 1,4-benzenedicarboxylate (BDC) plus NEt_3 (9.6 mmol) were dissolved together. Subsequently, 9 mL DMF solution of 1444 mg indium nitrate was added into the mixture. Then the product was washed thoroughly 4 times (2 times with DMF, 2 times with MeOH). The nanocrystals of MIL-68(In) were separated from the suspension by centrifugation at 8,000 rpm for 10 mins and the excess solvent decanted. The obtained material was dried at room temperature for 3 days to yield monoliths.

2.2 Nanoindentation

Nanoindentation tests were carried out using an iMicro nanoindenter (KLA-Tencor), equipped with a 1N load cell. The as-synthesised monoliths were cold mounted in epoxy resin (Struers Epofix), resulting in cylindrical samples. The specimens were thoroughly polished with sandpapers and diamond suspensions, in order to minimize roughness and obtain a flat surface, suitable for nanoindentation.

We employed a flat punch indenter (diameter 10.64 μm) and the method described in [32] to estimate stress-strain relations. The flat punch indenter was pressed into the surface at a constant strain rate (0.005 s^{-1}) to a maximum depth of 5000 *nm*. More details of the method are given in the Supporting Information, section S1.

2.3 Pellet preparation

ZIF-8 and MIL-68 pellets were produced by using a hydraulic press. 100 mg of material per pellet were compressed under pressures of 0.075, 0.15 and 0.375 GPa.

2.4 Confocal Raman microscopy (microRaman)

Raman spectroscopy measurements were performed at beamline B22, Diamond Light Source (DLS), Didcot (UK), using a confocal Bruker Senterra Raman microscope. The maps of the residual flat punch indents were collected by setting the following

measurements conditions: objective 50x, laser 532 nm with grating 1200, resolution 3-5 cm^{-1}, laser power 12 mW, integration time 5000 ms, scan area 40 μm x 40 μm, 21 x 21 points.

Averaged Raman spectra of the pellets were obtained by collecting 20 spectra per sample, in different areas. In this case a 20x objective was employed and a 5 s bleaching step was necessary for baseline corrections. All the other parameters were kept constant.

2.5 XRD

X-Ray diffraction (XRD) patterns were recorded using a Rigaku MiniFlex with a Cu Kα source (1.541 Å).

2.6 ATR-FTIR

Attenuated total reflection Fourier Transform Infrared (ATR−FTIR) spectra were recorded using a Nicolet iS10 FTIR spectrometer.

2.7 SEM and FIB

SEM images of the nanocrystalline aggregates were acquired with a Tescan Lyra 3 (Tescan, Czech Republic) field-emission scanning electron microscope, operating under a voltage of 10 keV. A focused ion beam (FIB) setup, equipped to the SEM instrument, was used to fabricate the micropillars for compression test. The voltage was set to 30 kV, the values of beam current are listed in Table S2.

2.8 Micropillar compression

Compression tests of the micropillars were performed by a flat punch indenter (diameter 10.64 μm), using an iMicro nanoindenter (KLA-Tencor), equipped with a 50 mN load cell.

3. Results

3.1 Stress-strain relations by flat punch nanoindentation tests

The resulting load-depth and stress-strain ($\sigma - \varepsilon$) curves are shown in Figure 2. The elastic recovery, which is more prominent for ZIF-8, is the key difference when examining the load depth curves (Figure 2a). For both monoliths, a moderate strain hardening was observed in the $\sigma - \varepsilon$ curves (Figure 2b), particularly for ZIF-8. The results are listed in Table 1. It should be noted that since these values were calculated using a model conceived for metals (Hollomon's power law), they cannot be regarded as absolute material properties. However, these numbers can be used to contrast the two monoliths' plastic behaviour. Similar yield stresses exist for the two materials (88.2 and 90 MPa for ZIF-8 and MIL-68 respectively). Given its higher hardness, ZIF-8 has a slightly higher strength coefficient (K). ZIF-8's strain hardening exponent (n) is about twice as large as MIL-68's. This can be attributed to the ZIF-8 framework's better flexibility, which makes it more likely to densify (and ultimately collapse) [13], increasing the monolith's strength. MIL-68, on the other hand, has a stiffer framework and smaller particle size, which leads to improved ductility [28]. Notably, the flow stress of the monoliths in their fully plastic regime (plateau in $\sigma - \varepsilon$ curves) is 1/3 of the hardness, in accordance with Tabor theory of elastic-plastic contact [33]. The data points in such a regime are actual experimental data (as opposed to the elastic and initial yielding regime, extrapolated from Hollomon's power law), which confirms the results of our previous work [13], where we suggested that the behaviour of MOF monoliths can be well approximated by a simple elastic-perfectly plastic mechanical model.

Another difference between the load-depth curves of the two monoliths can be observed in the very first part of the loading curve (indentation depth < 200 nm). Figure 2c

illustrates a detailed view of the loading curve in such a range and its first derivative: MIL-68 exhibits a stiff response in this range, followed by an evident softening for depths > 200 nm. This is not the case for ZIF-8, which exhibits a softer response, without any slope changes. We reasoned that this may be due to the higher elastic modulus of the MIL-68 framework, that provides a stiff response prior to grain boundary sliding taking place.

The residual imprints left by the flat punch on the two monoliths surface are shown in Figures 2d-e. Concentrical ring-shaped cracks are evident in both cases, which resemble the shear faults observed in Vickers residual indents in our previous work [28]. This suggests that the yielding of these MOF monoliths consists of stepwise microcracking - accommodating excessive build-up of stress - likely taking place at the grain boundaries between the nanocrystals. Such a localised failure mechanism is well contained in the vicinity of the residual imprints and does not lead to critical crack propagation. This is supported by the absence of “pop-ins” (i.e., sudden displacement bursts) in the load-depth curves, which are typically associated with indentation cracking.

3.2 Spectroscopy analysis of residual strains

3.2.1 microRaman of residual flat punch imprints

The two materials, characterised by different framework architectures (Figure 1b-c), exhibited a different behaviour: we noticed shifts of some characteristic Raman bands in ZIF-8 moving from outside to inside the indent, while the position of all the MIL-68 bands was not affected.

Let us analyse in detail the ZIF-8 Raman spectrum. As reported by Chen *et al.* [34] in their *in-situ* study of the effect of high-pressure on ZIF-8 crystalline powders, the majority

of the bands are due to methyl group and imidazolate ring vibrations. The low-frequency bands (176, 284 and 422 cm^{-1}) are ascribed to the ZnN_4 tetrahedra vibrations. The other bands are assigned as follows:

- 686 cm^{-1} and 694 cm^{-1} (shoulder): imidazolate ring puckering;
- 836 cm^{-1}, 953 cm^{-1} and 1024 cm^{-1}: C-H out-of-plane bending vibration in the Im ring;
- 1146 cm^{-1} and 1185 cm^{-1}: C-N stretching vibration in the Im ring;
- 1461 cm^{-1}: C-H wag in the methyl group;
- 1500 cm^{-1}: C=C stretching in the Im ring;
- 2930 cm^{-1}: C-H stretching in the methyl group;
- 3114 cm^{-1} and 3135 cm^{-1}: C-H stretching in the Im ring (aromatic group).

We can compare our results (Figure 3) with those obtained by Chen *et al.* [34], whom observed the evolution of Raman bands with *in-situ* high pressure, up to 19.9 GPa. In our case the maximum pressure applied by the punch is much smaller (in the order of 0.1-0.2 GPa) and the material underwent elastic recovery before the measurement. Despite these differences, some similarities can still be observed. First, a broadening of all the bands was observed inside the indent due to compression, as expected. As shown in Figure 3 and Figure S2, blue shifts, caused by bond compression, were observed for Zn-N vibrations (176 cm^{-1}), Im ring puckering (686 cm-1) and out-of-plane bending (1024 cm^{-1}). Interestingly, red shifts – usually related to a state of tension of the bonds – were observed for two of the bands relative to C-H out-of-plane bending vibrations in the Im ring (836 cm^{-1} and 953 cm^{-1}), C-N stretching vibration in the Im ring (1146 cm^{-1} and 1185 cm^{-1}), C-H wag in the methyl group (1461 cm^{-1}), C=C stretching in the Im ring (1500 cm^{-1}) and C-H stretching in the Im ring (3114 cm^{-1} and 3135 cm^{-1}). The red shifts

mostly correspond to stretching vibrations in the linker (Im ring): this is due to the peculiar mechanical instability of the ZIF-8 framework, that is characterised by an extremely low shear modulus [23] and undergoes shear-mode softening under compression [35]. We reasoned that the shear-induced deformation of the framework induces a state of tension in the linker.

It is worth noting that the indentation does not induce any residual strain of the crystal structure outside the contact area, suggesting that the plastic flow consist of shear-driven grain boundary sliding and rearrangement of the nanograins to accommodate the applied shear strain [13].

On the other hand, the Raman spectra of MIL-68 inside and outside the indent are identical, except for some amount of band broadening (Figure 4). To the best of our knowledge, no Raman studies of the structural stability of MIL-68 are available so far. Hu *et al.* [36] analysed the behaviour of MIL-68 under high pressure by FTIR spectroscopy. They observed a full recovery of the structure upon releasing of the pressure for the as-made sample (i.e., prior to activation, with some DMF still trapped in the channels), while the spectrum of activated MIL-68 was irreversibly modified, especially the OH stretching mode, which is more sensitive to compression. The peaks relative to OH stretching were strongly broadened and their intensity decreased already with a small pressure (namely 0.12 GPa, comparable to the one applied by our nanoindentation test). This suggests a significant guest-host interaction in the framework upon compression. The absence of major changes in the Raman spectrum in our case suggests a complete recovery of the framework structure, facilitated by the presence of some residual DMF molecules in the channels, demonstrated by the (weak) band at ~1664cm^{-1} (C=O stretching in DMF), as highlighted in Figure 4.

3.2.2 Effect of mechanical pressure on ZIF-8 and MIL-68 pellets

We wanted to investigate the effect of pressure on the monoliths by bulk spectroscopy measurements and compare it to the results obtained for the flat punch indents. We prepared pellets by applying pressures of the same order of magnitude of the one generated under the punch during nanoindentation (see *Experimental Methods*). The resulting pellets were characterised by means of bulk ATR-FTIR, Raman spectroscopy and XRD.

The FTIR spectra of the ZIF-8 pellets (Figure S3) suggest that the framework structure is preserved in the examined pressure range. This hypothesis was confirmed by XRD diffraction (Figure S4), which indicates that the crystal structure is preserved after a compression to 0.375 GPa. Our results are in agreement with the IR *in-situ* study by Hu *et al.* [37], that observed a reversibility of the pressure-induced structural modifications in ZIF-8 microcrystals upon compression to 1.6 GPa followed by decompression. The only change detected was a slight splitting of the out-of-plane bending mode of the linker (~760 cm^{-1}). We observed the appearance of a shoulder on the low frequency side of the peak rather than a split, due to the low intensity of the pressure applied. In the IR spectrum of the as-made monolith we noticed two extra peaks (~1088 cm^{-1} and ~1255 cm^{-1}), corresponding to N-CH_3 vibrations modes in DMF molecules, which suggest the presence of residual solvent. The intensity of these peaks is severely reduced after pelletisation, indicating that solvent squeezes out upon compression. Raman spectroscopy (Figure S5) revealed shifts of the framework characteristic bands, similarly to what was observed inside the flat punch indents. However, some peaks shifted in a direction opposite to the residual indent, as reported in Table S1. For example, the imidazolate ring puckering (688 cm^{-1}) and the C-H stretching bands (3114 cm^{-1} and 3135 cm^{-1}) exhibited red and

blue shifts respectively (Figures S5b and c). This difference can be ascribed to the different stress fields generated by flat punch indentation and hydrostatic compression, with the latter being characterised by the absence of a shear component.

Let us now consider MIL-68 pellets. Also in this case we did not observe any significant changes in the FTIR spectra after decompression (Figure S6), proving again that the framework structure can be easily recovered in the pressure range examined. Moreover, the intensity of the band relative to C=O stretching in DMF (~1673 cm^{-1}) is not significantly reduced with the increasing pressure, as opposed to ZIF-8. This might indicate that the solvent is trapped inside the MIL-68 framework channels. XRD patterns (Figure S7) proved once again that the crystal structure was not modified upon compression to 0.375 GPa. Again, no peak shifts were seen when Raman spectra were examined (Figure S8).

3.3 Micropillar compression

Two sets of micropillars were fabricated on each sample (Figure S9). SEM images of the micropillars before and after the tests were taken for each ZIF-8 (Figures S10 to S13) and MIL-68 (Figures S14 to S17). The load-displacement curves resulting from each test are shown in Figure S20 and Figure S21 for ZIF-8 and MIL-68 respectively. These curves were converted into classical stress-strain (σ - ε) curves, using the following relations:

$$\sigma = \frac{P}{\pi \frac{d^2}{4}} \tag{1}$$

$$\varepsilon = \frac{h}{l} \tag{2}$$

Where P is the load, d the pillar diameter, h the vertical displacement and l the pillar height. The resulting $\sigma - \varepsilon$ curves (Figure 5a and 5b for ZIF-8 and MIL-68 respectively) showed good reproducibility, particularly the elastic behaviour.

ZIF-8 exhibited a brittle behaviour (Figure 5a): "pop-in" events that are visible during elastic loading and may have been caused by the propagation of cracks, are followed by a second, less steep, linear (elastic) segment, indicating that the material response is still elastic but that a smaller cross-sectional area is now bearing the applied load. As we can observe in Figure 5d and Figure S18, the cracks propagate along the longitudinal direction of the pillars, essentially splitting it in two, hence reducing the cross-sectional area bearing the load. The pillars that were brought to failure (see Table 2) were all broken at ~17% strain. The strain rate was found to influence the yield stress (in this case defined as the stress at which the first “pop-in” appears), which decreased of ~30% (from ~200 to ~135 MPa) when the strain rate was reduced from 0.2 to 0.001 s^{-1}. The Young’s modulus (measured as the slope of the linear segments, before pop-ins) was 2.45 ± 0.37 GPa, slightly lower than the one measured by nanoindentation for the same material (3.18 GPa) [13].

The stress-strain behaviour of MIL-68 was very different from that of ZIF-8. As shown in Figure 5b, there is a significant plastic deformation (large strains lying within the 20-50% range) and no “pop-ins” are observed. There is no evidence of longitudinal cracks (Figure 5e and Figure S19), as opposed to ZIF-8. Two pillars failed (set #1 - pillar #1 and set #2 - pillar #1) and their fracture surfaces (Figure S14 and Figure S16, respectively) suggest that the pillars cracked in the direction perpendicular to their axis, contrary to what was observed for ZIF-8 (Figure S18c-d), with the pillar failing after longitudinal splitting. Particularly noteworthy is the case of pillar #1 of set #2 (Figure S19c), that was

not crushed like the others, but rather "cut" at its base. This outcome may suggest a buckling failure, given the greater slenderness of this pillar (h/l = 2.6, against ~1 of the others). The average Young's modulus was 2.28 ± 0.40 GPa, which is considerably lower than the indentation modulus of 13.24 ± 0.52 reported in [28].

4. Discussion

The stress-strain behaviour of ZIF-8 and MIL-68 was studied by flat punch nanoindentation and micropillar compression. In the first case, both monoliths showed a relatively ductile behaviour, with a small amount of strain hardening, and their flow stress is extremely close to $H/3$, as predicted by Tabor [33] for elastic-perfectly plastic materials in the fully plastic regime. However, ring-shaped cracks were observed around the residual imprints, but no pop-ins events were detected in the load-depth curves. These results suggest that the yielding of the monoliths is triggered by localised stepwise micro-failure, most likely taking place at the grain boundaries, rather than plastic flow driven by dislocations motion, as is the case for metals. This "pseudo-ductility" is promoted by the fine granular nanostructure of these materials, in accordance to the findings of our previous works [13, 28]. Confocal Raman microscopy of the residual indents revealed that ZIF-8 framework is distorted in the contact area, presumably by shear, while MIL-68 framework remains stable, with the whole load absorbed by grain boundary sliding. The densification associated to framework distortion in ZIF-8, may be the reason of its slightly higher strain hardening exponent (n).

Nevertheless, the $\sigma - \varepsilon$ curves of ZIF-8 obtained by micropillar compression indicate a brittle behaviour. This is due to the different stress states generated by the two tests: uniaxial for micropillar compression and triaxial for nanoindentation. The latter results in

a confining pressure that compacts the nanocrystals, improving the overall toughness. The failure of ZIF-8 micropillars was caused by elastic crack propagation: longitudinal cracks generated during compression propagate leading to pillar splitting. On the other hand, MIL-68 does undergo significantly larger plastic deformations, associated to material flow. These results are in good agreement with what was reported in [28] concerning the indentation fracture toughness of these two monoliths. ZIF-8 was found to be more prone to sharp indentation cracking than MIL-68. The different fracture behaviour was ascribed to the different framework architectures and nanostructures, resulting in distinct elastic-plastic behaviours: ZIF-8 is characterised by large elastic recovery and high *H/E*, distinctive features of brittle materials, contrary to MIL-68 (low elastic recovery and low *H/E*), which exhibits an extraordinary resistance to indentation cracking. The ductility of MIL-68 stems from the small size of the nanoparticles building blocks and the stiff and robust nature of the framework: this combination promotes the grain boundary sliding (GBS) as principal deformation mechanism. This dramatically reduces the share of load transferred to the framework, avoiding its distortion and eventual collapse, as confirmed by the microRaman results, where no stress-induced spectral modifications were observed.

The effect of strain rate on the yield stress of ZIF-8 might be explained with an inertial effect, similarly to what is widely observed in rock-like materials (i.e., solid aggregates of minerals) [38]. Inertia initially inhibits crack growth, meaning that the cracks will have less time to nucleate at higher strain rate, hence starting to propagate at higher stresses.

The Young's modulus values measured by $\sigma - \varepsilon$ curves obtained from micropillar compression are lower than the results for ZIF-8 and MIL-68 monoliths based on traditional nanoindentation [13, 28], particularly for MIL-68, for which it is only 20% of

the counterpart measured by nanoindentation. Numerous studies have found that the modulus values for micropillars compression are significantly lower than those for nanoindentation [39-42]. One explanation for this discrepancy could be the basic differences between the two methods. Micropillar compression produces a uniaxial stress state, whereas nanoindentation creates a complicated triaxial stress state close to the indenter. Additionally, in nanoindentation experiments [20] elastic modulus is estimated from unloading slope, which is supposed to be entirely elastic. Moreover, a system misalignment due to imperfect initial contact between the pillar and indenter may cause an underestimate of the elastic modulus. Another reason may be the inaccurate computation of stresses and strains (equations 1 and 2), which only rely on geometrical features of the pillars (i.e., height and diameters) measured from SEM images. For instance, the nature of FIB milling results in the fabrication of slightly tapered pillars, which are approximated to perfect cylinders to calculate the uniaxial stress. Moreover, in the case of self-assembled nanoparticles-based materials, like the monoliths analysed in this work, FIB milling induces the formation of highly porous network, caused by the nanoparticles migration and melting upon ion beam exposure [43]. This phenomenon was observed in both ZIF-8 and MIL-68 samples, as porous networks are visible inside the trenches surrounding the pillars (Figures S10-17). The presence of this features may affect the computation of strain since the actual height of the pillars may be higher than the measured one. Finally, there may be some experimental aspects that are material specific. The extremely high vacuum pumping in FIB might damage the porous monoliths containing entrapped solvent. This could lead to further loss of stiffness. The mechanical properties could also be impacted by FIB-induced damage due to Ga+ ion implantation.

5. Conclusions

The stress-strain relations of two prototypical MOF monoliths, ZIF-8 and MIL-68, obtained by sol-gel synthesis route, were evaluated by flat punch indentation and micropillar compression. Under indentation, when a confining pressure is present and crack propagation is constrained, both the materials display a similar plastic behaviour, characterised by a minimal amount of strain hardening. As reported in previous works, this behaviour is promoted by the peculiar nanostrucuture of the sol-gel monoliths, which favours grain boundary sliding as the main deformation mechanism. When the framework itself is compliant enough, it can permanently deform, absorbing part of the applied load. This phenomenon was observed in ZIF-8 monolith, as demonstrated by the microRaman analysis of the residual flat punch indent, which evidenced the presence of residual strains at the framework level. Micropillar compression resulted in two different yielding behaviours: ZIF-8 fails by elastic crack propagation, while MIL-68 exhibits a certain amount of plastic flow prior to failure.

The results of this work will broaden the current understating of the mechanical behaviour of MOF monoliths and nanocrystalline porous materials in general, which are currently still at an early stage, but are essential for moving this class of materials from academic interest to real-world use.

Sample	Number of tests	Yield stress (MPa)	Yield strain (-)	K (MPa)	n (-)	Average flow stress (MPa)	Hardness (MPa)
ZIF-8	18	88.2 ± 16.4	0.0238 ± 0.0033	184.1 ± 9.5	0.1976 ± 0.0405	140 ± 10	452 ± 20 [13]
MIL-68	16	90.0 ± 10.5	0.0072 ± 0.0008	154.0 ± 6.6	0.1093 ± 0.029	150 ± 16	402 ± 13 [28]

Table 1. Mechanical properties of ZIF-8 and MIL-68 monoliths extrapolated from the stress-strain curves obtained by flat punch nanoindentation. The values of hardness were computed by Berkovich nanoindentation in previous works.

Material	Set	Pillar	Max depth (nm)	Sample failed? (Y/N)	Strain rate (s^{-1})	Young's modulus (GPa)	Yield stress (MPa)	Stress at failure (MPa)	Strain at failure (-)
ZIF-8	1	1	- (*)	Y	0.2	- (*)	- (*)	- (*)	- (*)
		2	1000	N	0.2	2.9	185	-	-
		3	3000	Y	0.2	2.8	207	250	0.151
	2	1	1000	N	0.2	1.9	206	-	-
		2	1300	Y	0.2	2.2	173	214	0.170
		3	1500	Y	0.001	2.4	133	209	0.187
		4	1000	N	0.001	2.5	136	-	-
Average						2.45 ± 0.34	173 ± 30	224 ± 18	0.169 ± 0.015
MIL-68	1	1	3000	Y	0.001	2.9	120	153	0.208
		2	1000	N	0.001	2.1	115	-	-
		3	2000	N	0.001	2.6	157	-	-
	2	1	2500	Y	0.2	2.3	125	207	0.222
		2	2500	N	0.001	1.9	200	-	-
		3	2500	N	0.2	1.9	210	-	-
Average						2.28 ± 0.37	154 ± 38	180 ± 27	0.215 ± 0.007

Table 2. Test inputs and material properties of the two monoliths resulting from micropillar compression tests. (* Test failed)

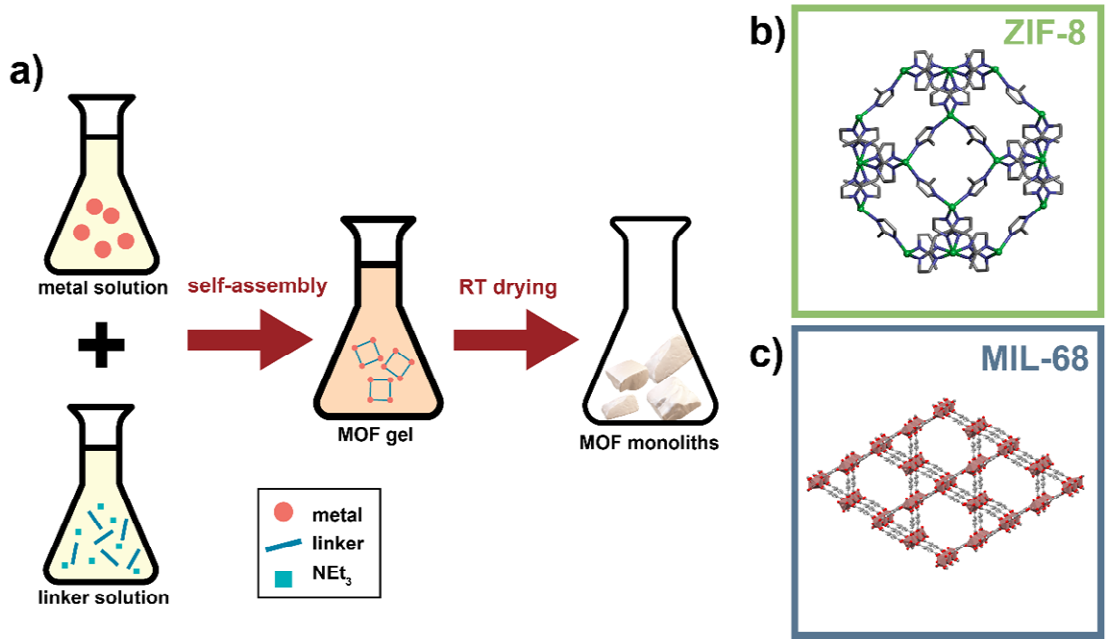

Figure 1. a) Schematic of the synthesis of sol-gel MOF monoliths, obtained by leveraging the high concentration reaction (HCR) route. b) ZIF-8 framework cage-like architecture (unit cell). c) MIL-68 framework channel-like architecture.

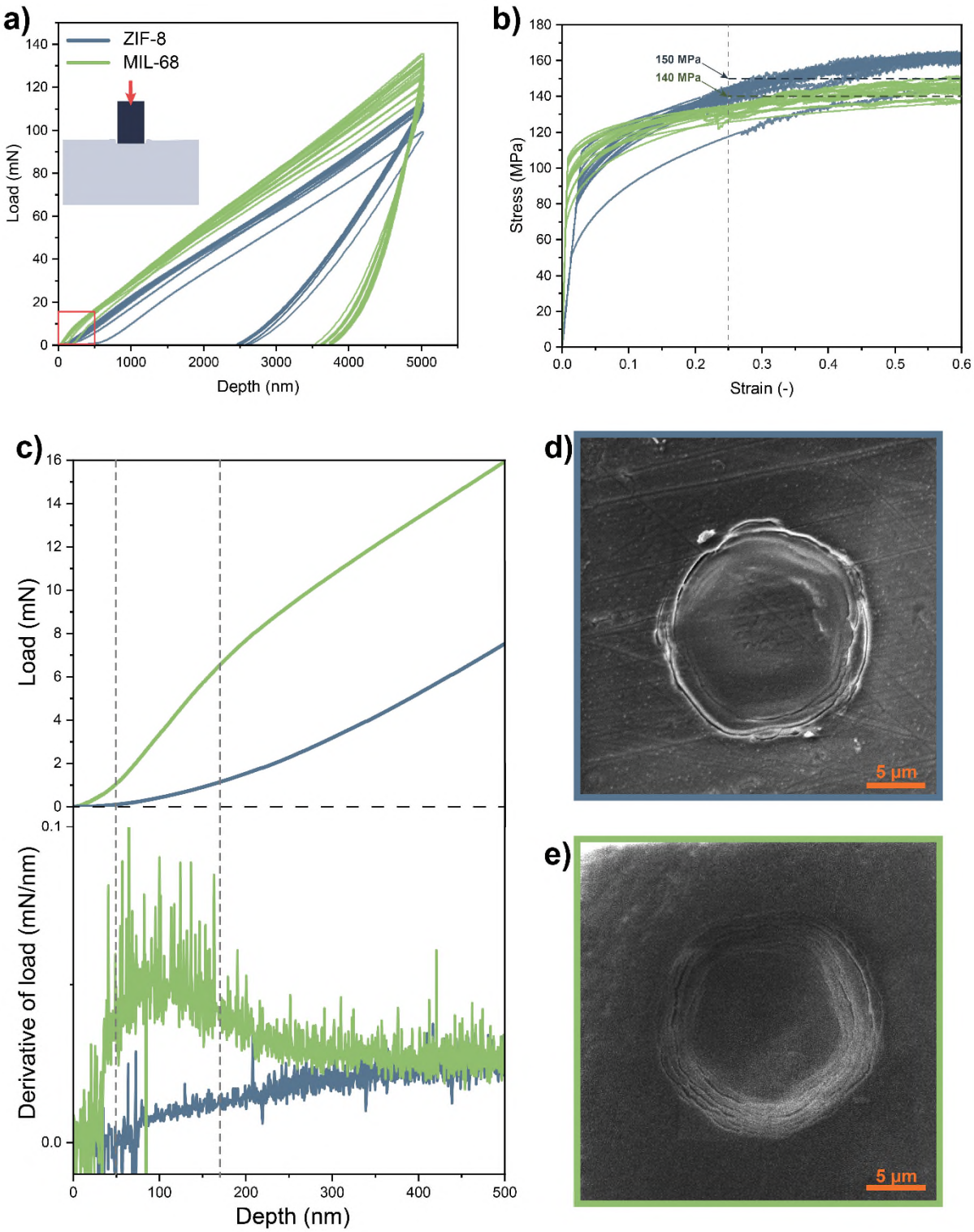

Figure 2. Flat punch nanoindentation tests. a) Load-depth and b) stress-strain curves resulting from nanoindentation tests of ZIF-8 and MIL-68 monoliths using a flat punch (diameter 10.64 µm). c) Magnification of two representative load-depth curves in the range 0-500 nm (top) and their first derivative (bottom). SEM images of some representative residual flat punch imprints on d) ZIF-8 and e) MIL-68.

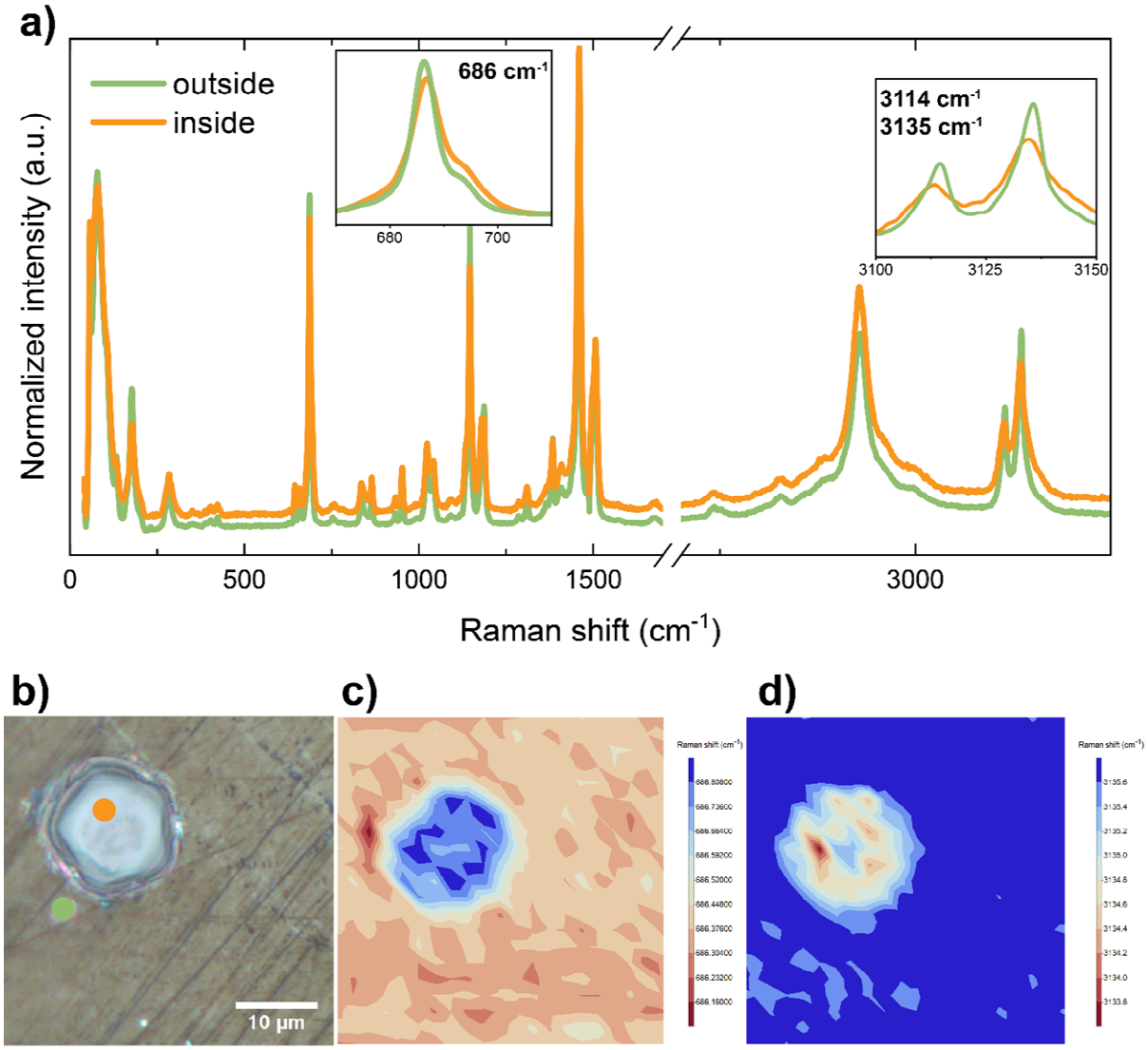

Figure 3. Confocal Raman microscopy of a flat punch residual imprint on ZIF-8. a) Representative Raman spectra taken outside and inside the residual indent. The insets show details of the stress-induced blue-shift of the 686 cm^{-1} band (Im ring puckering) and red-shift of the 3114 cm^{-1} and 3135 cm^{-1} bands (C-H stretching in the Im ring). b) Micrograph of the indent. c-d) Maps indicating the spectral position of some of the characteristic phonon bands of ZIF-8, 686 cm^{-1} and 3135 cm^{-1} respectively.

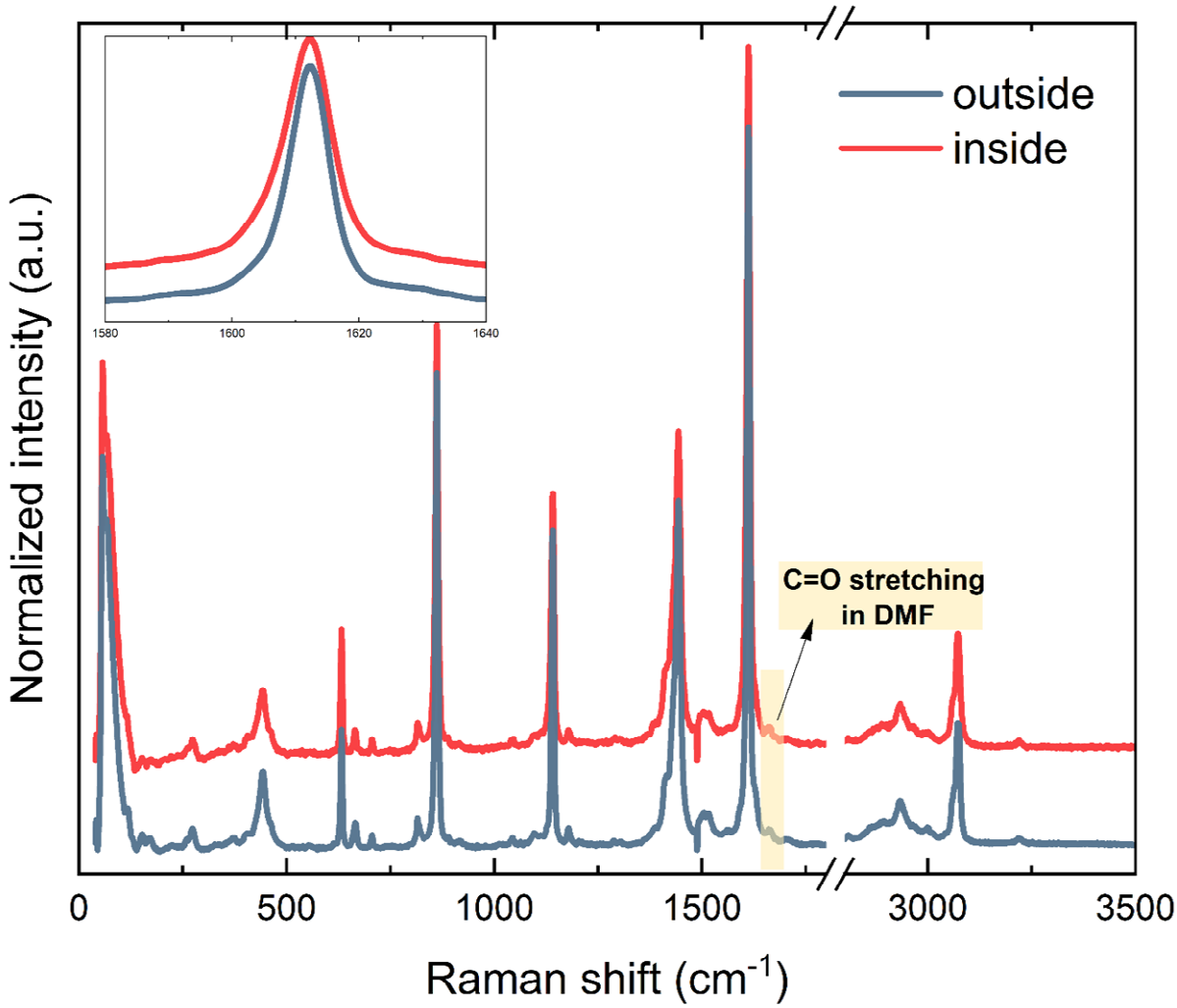

Figure 4. Representative Raman spectra of a MIL-68 monolith taken outside and inside a residual flat punch imprint. The inset shows a magnified view of the 1611 cm^{-1} band, clarifying the absence of stress-induced shifts.

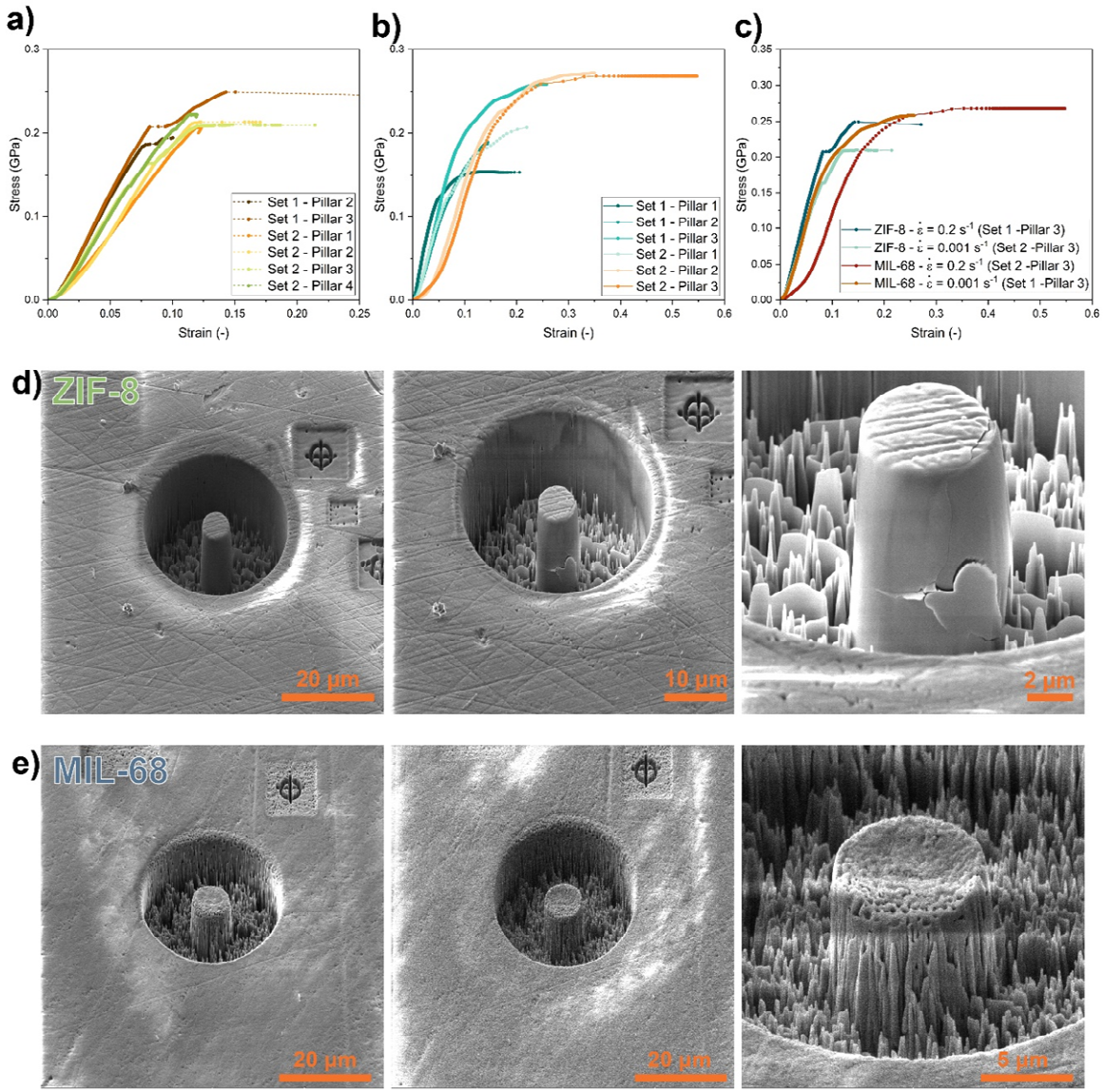

Figure 5. Micropillars compression tests. a-b) Stress-strain curves relative to ZIF-8 and MIL-68 micropillars compression, respectively. c) Comparison of some representative ZIF-8 and MIL-68 stress-strain curves, obtained by compression at different strain rates. d-e) Representative pillars before test (left), after test (middle) and detailed view after the test (right) of ZIF-8 and MIL-68 monoliths.

References

[1] R. Freund, S. Canossa, S.M. Cohen, W. Yan, H. Deng, V. Guillerm, M. Eddaoudi, D.G. Madden, D. Fairen-Jimenez, H. Lyu, L.K. Macreadie, Z. Ji, Y. Zhang, B. Wang, F. Haase, C. Woll, O. Zaremba, J. Andreo, S. Wuttke, C.S. Diercks, 25 Years of Reticular Chemistry, Angew Chem Int Ed 60(45) (2021) 23946-23974.

[2] P. Falcaro, R. Ricco, C.M. Doherty, K. Liang, A.J. Hill, M.J. Styles, MOF positioning technology and device fabrication, Chem Soc Rev 43(16) (2014) 5513-60.

[3] I. Stassen, N. Burtch, A. Talin, P. Falcaro, M. Allendorf, R. Ameloot, An updated roadmap for the integration of metal-organic frameworks with electronic devices and chemical sensors, Chem Soc Rev 46(11) (2017) 3185-3241.

[4] M.R. Ryder, J.-C. Tan, Nanoporous metal organic framework materials for smart applications, Mater Sci Tech 30(13a) (2014) 1598-1612.

[5] A. Bavykina, N. Kolobov, I.S. Khan, J.A. Bau, A. Ramirez, J. Gascon, Metal–organic frameworks in heterogeneous catalysis: recent progress, new trends, and future perspectives, Chem Rev 120(16) (2020) 8468-8535.

[6] M. Gutiérrez, Y. Zhang, J.-C. Tan, Confinement of Luminescent Guests in Metal–Organic Frameworks: Understanding Pathways from Synthesis and Multimodal Characterization to Potential Applications of LG@MOF Systems, Chem Rev 122(11) (2022) 10438-10483.

[7] J.-C. Tan, Mechanical Behaviour of Metal–Organic Framework Materials, Royal Society of Chemistry2023.

[8] J.C. Tan, A.K. Cheetham, Mechanical properties of hybrid inorganic-organic framework materials: establishing fundamental structure-property relationships, Chem Soc Rev 40(2) (2011) 1059-80.

[9] N.C. Burtch, J. Heinen, T.D. Bennett, D. Dubbeldam, M.D. Allendorf, Mechanical Properties in Metal-Organic Frameworks: Emerging Opportunities and Challenges for Device Functionality and Technological Applications, Adv Mater 30(37) (2018) 1704124.

[10] L.R. Redfern, O.K. Farha, Mechanical properties of metal–organic frameworks, Chem Sci 10(46) (2019) 10666-10679.

[11] J. Hou, A.F. Sapnik, T.D. Bennett, Metal–organic framework gels and monoliths, Chem Sci 11(2) (2020) 310-323.

[12] T. Tian, J. Velazquez-Garcia, T.D. Bennett, D. Fairen-Jimenez, Mechanically and chemically robust ZIF-8 monoliths with high volumetric adsorption capacity, J Mater Chem A 3(6) (2015) 2999-3005.

[13] M. Tricarico, J.-C. Tan, Mechanical properties and nanostructure of monolithic zeolitic imidazolate frameworks: a nanoindentation, nanospectroscopy, and finite element study, Mater Today Nano 17 (2022) 100166.

[14] J.P. Mehta, T. Tian, Z. Zeng, G. Divitini, B.M. Connolly, P.A. Midgley, J.-C. Tan, D. Fairen-Jimenez, A.E.H. Wheatley, Sol-Gel Synthesis of Robust Metal-Organic Frameworks for Nanoparticle Encapsulation, Adv Funct Mater 28(8) (2018).

[15] T. Tian, Z. Zeng, D. Vulpe, M.E. Casco, G. Divitini, P.A. Midgley, J. Silvestre-Albero, J.C. Tan, P.Z. Moghadam, D. Fairen-Jimenez, A sol-gel monolithic metal-organic framework with enhanced methane uptake, Nat Mater 17(2) (2018) 174-179.

[16] B.M. Connolly, M. Aragones-Anglada, J. Gandara-Loe, N.A. Danaf, D.C. Lamb, J.P. Mehta, D. Vulpe, S. Wuttke, J. Silvestre-Albero, P.Z. Moghadam, A.E.H. Wheatley, D. Fairen-Jimenez, Tuning porosity in macroscopic monolithic metal-organic frameworks for exceptional natural gas storage, Nat Commun 10(1) (2019) 2345.

[17] B. Bueken, N. Van Velthoven, T. Willhammar, T. Stassin, I. Stassen, D.A. Keen, G.V. Baron, J.F.M. Denayer, R. Ameloot, S. Bals, D. De Vos, T.D. Bennett, Gel-based morphological design of zirconium metal-organic frameworks, Chem Sci 8(5) (2017) 3939-3948.

[18] M.E. Carrington, N. Rampal, D.G. Madden, D. O'Nolan, N.P.M. Casati, G. Divitini, J.Á. Martín-Illán, M. Tricarico, R. Cepitis, C. Çamur, T. Curtin, J. Silvestre-Albero, J.-C. Tan, F. Zamora, S. Taraskin, K.W. Chapman, D. Fairen-Jimenez, Sol-gel processing of a covalent organic framework for the generation of hierarchically porous monolithic adsorbents, Chem 8(11) (2022) 2961-2977.

[19] B.M. Connolly, D.G. Madden, A.E.H. Wheatley, D. Fairen-Jimenez, Shaping the Future of Fuel: Monolithic Metal-Organic Frameworks for High-Density Gas Storage, J Am Chem Soc 142(19) (2020) 8541-8549.

[20] W.C. Oliver, G.M. Pharr, An improved technique for determining hardness and elastic modulus using load and displacement sensing indentation experiments, J Mater Res 7(6) (1992) 1564-1583.

[21] D.F. Bahr, J.A. Reid, W.M. Mook, C.A. Bauer, R. Stumpf, A.J. Skulan, N.R. Moody, B.A. Simmons, M.M. Shindel, M.D. Allendorf, Mechanical properties of cubic zinc carboxylate IRMOF-1 metal-organic framework crystals, Phys Rev B 76(18) (2007).

[22] J.C. Tan, T.D. Bennett, A.K. Cheetham, Chemical structure, network topology, and porosity effects on the mechanical properties of Zeolitic Imidazolate Frameworks, Proc Natl Acad Sci USA 107(22) (2010) 9938-43.

[23] J.C. Tan, B. Civalleri, C.C. Lin, L. Valenzano, R. Galvelis, P.F. Chen, T.D. Bennett, C. Mellot-Draznieks, C.M. Zicovich-Wilson, A.K. Cheetham, Exceptionally low shear modulus in a prototypical imidazole-based metal-organic framework, Phys Rev Lett 108(9) (2012) 095502.

[24] T.D. Bennett, J.C. Tan, S.A. Moggach, R. Galvelis, C. Mellot-Draznieks, B.A. Reisner, A. Thirumurugan, D.R. Allan, A.K. Cheetham, Mechanical properties of dense zeolitic imidazolate frameworks (ZIFs): a high-pressure X-ray diffraction, nanoindentation and computational study of the zinc framework Zn(Im)2, and its lithium-boron analogue, LiB(Im)4, Chem 16(35) (2010) 10684-90.

[25] S. Bundschuh, O. Kraft, H.K. Arslan, H. Gliemann, P.G. Weidler, C. Wöll, Mechanical properties of metal-organic frameworks: An indentation study on epitaxial thin films, Appl Phys Lett 101(10) (2012) 101910.

[26] B. Van de Voorde, R. Ameloot, I. Stassen, M. Everaert, D. De Vos, J.-C. Tan, Mechanical properties of electrochemically synthesised metal–organic framework thin films, J Mater Chem C 1(46) (2013) 7716.

[27] M.R. Ryder, B. Civalleri, G. Cinque, J.-C. Tan, Discovering connections between terahertz vibrations and elasticity underpinning the collective dynamics of the HKUST-1 metal–organic framework, CrystEngComm 18(23) (2016) 4303-4312.

[28] M. Tricarico, J.-C. Tan, Fracture behavior of MOF monoliths revealed by nanoindentation and nanoscratch, 2022, p. arXiv:2210.03219.

[29] A.K. Chaudhari, I. Han, J.C. Tan, Multifunctional Supramolecular Hybrid Materials Constructed from Hierarchical Self-Ordering of In Situ Generated Metal-Organic Framework (MOF) Nanoparticles, Adv Mater 27(30) (2015) 4438-4446.

[30] R.N. Widmer, A.M. Bumstead, M. Jain, T.D. Bennett, J. Michler, Plasticity of Metal–Organic Framework Glasses, J Am Chem Soc 143(49) (2021) 20717-20724.

[31] Y.X. Zhixin Zeng, Jeffrey M. Wheeler, Jin-Chong Tan, In situ micropillar compression of an anisotropic metal-organic framework single crystal, 2022.
[32] J. Hay, Instrumented indentation apparatus having indenter punch with flat end surface and instrumented indentation method using the same, Google Patents, 2019.
[33] D. Tabor, Indentation hardness: Fifty years on a personal view, Philos Mag A 74(5) (1996) 1207-1212.
[34] S. Chen, X. Li, E. Dong, H. Lv, X. Yang, R. Liu, B. Liu, Intrinsic and Extrinsic Responses of ZIF-8 under High Pressure: A Combined Raman and X-ray Diffraction Investigation, J Phys Chem C 123(49) (2019) 29693-29707.
[35] A.U. Ortiz, A. Boutin, A.H. Fuchs, F.X. Coudert, Investigating the Pressure-Induced Amorphization of Zeolitic Imidazolate Framework ZIF-8: Mechanical Instability Due to Shear Mode Softening, J Phys Chem Lett 4(11) (2013) 1861-5.
[36] Y. Hu, B. Lin, P. He, Y. Li, Y. Huang, Y. Song, Probing the Structural Stability of and Enhanced CO2 Storage in MOF MIL-68 (In) under High Pressures by FTIR Spectroscopy, Chemistry–A European Journal 21(51) (2015) 18739-18748.
[37] Y. Hu, H. Kazemian, S. Rohani, Y. Huang, Y. Song, In situ high pressure study of ZIF-8 by FTIR spectroscopy, Chem Commun (Camb) 47(47) (2011) 12694-6.
[38] C. Qi, M. Wang, J. Bai, X. Wei, H. Wang, Investigation into size and strain rate effects on the strength of rock-like materials, International Journal of Rock Mechanics and Mining Sciences 86 (2016) 132-140.
[39] R. Shahrin, C.P. Bobko, Characterizing Strength and Failure of Calcium Silicate Hydrate Aggregates in Cement Paste under Micropillar Compression, Journal of Nanomechanics and Micromechanics 7(4) (2017) 06017002.
[40] E.D. Yilmaz, H. Jelitto, G.A. Schneider, Uniaxial compressive behavior of micro-pillars of dental enamel characterized in multiple directions, Acta Biomater 16 (2015) 187-95.
[41] B. An, R. Wang, D. Arola, D. Zhang, Damage mechanisms in uniaxial compression of single enamel rods, J Mech Behav Biomed Mater 42 (2015) 1-9.
[42] H.D. Espinosa, A. Zaheri, H. Nguyen, D. Restrepo, M. Daly, M. Frank, J. McKittrick, In situ Wear Study Reveals Role of Microstructure on Self-Sharpening Mechanism in Sea Urchin Teeth, Matter 1(5) (2019) 1246-1261.

[43] V. Håkonsen, G. Singh, J. He, Z. Zhang, Focused ion beam milling of self-assembled magnetic superstructures: an approach to fabricate nanoporous materials with tunable porosity, Materials Horizons 5(6) (2018) 1211-1218.

Statement of Authorship for joint/multi-authored papers for PGR thesis

To appear at the end of each thesis chapter submitted as an article/paper

The statement shall describe the candidate's and co-authors' independent research contributions in the thesis publications. For each publication there should exist a complete statement that is to be filled out and signed by the candidate and supervisor **(only required where there isn't already a statement of contribution within the paper itself).**

Title of Paper	Stress-strain relationships and yielding of MOF monoliths (Chapter 6)
Publication Status	□Published □ Accepted for Publication □Submitted for Publication **x** Unpublished and unsubmitted work written in a manuscript style
Publication Details	Tricarico, M., Besnard, C., Cinque G., Korsunsky, A., Tan, J.-C., Stress-strain relationships and yielding of MOF monoliths, under preparation, 2023.

Student Confirmation

Student Name:	Michele Tricarico		
Contribution to the Paper	Conceptualization: M.T. Synthesis: M.T. Sample preparation: M.T. SEM imaging and FIB: C.B. Mechanical characterisation: M.T.Micro Raman measurements: M.T. and G.C. Data analysis: M.T. Writing of the original draft: M.T.Writing, editing, and reviewing: all authors Supervision: A.K., J.C.T.Funding acquisition: A.K., J.C.T.		
Signature 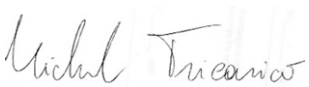		Date	09/02/2023

Supervisor Confirmation

By signing the Statement of Authorship, you are certifying that the candidate made a substantial contribution to the publication, and that the description described above is accurate.

Supervisor name and title: Professor Jin-Chong Tan		
Supervisor comments I approve this application. The information submitted is accurate.		
Signature. 	Date	9 Feb 2023

This completed form should be included in the thesis, at the end of the relevant chapter.

7 Conclusions and Perspectives

This thesis aimed to provide a detailed description of the mechanical behaviour of MOF monoliths. Some prototypical MOF systems were successfully fabricated in a monolithic morphology (a few millimetres to a centimetre in size), leveraging a sol-gel synthesis route, a low-cost process that does not require the application of a compacting pressure nor the use of support materials, such as templates and binders. These materials were systematically studied by means of nanoindentation, spectroscopy and finite element simulations, in order to investigate the mechanisms underpinning their mechanical behaviour.

Different facets of the mechanical performances were investigated, including constitutive behaviour and plasticity (Chapter 4), fracture toughness (Chapter 5), yielding and stress-strain relationships (Chapter 6).

In Chapter 4, the mechanical properties of two zeolitic MOF monoliths (ZIF-8 and ZIF-71) were investigated *via* Berkovich, cube corner, and spherical nanoindentation, AFM, and TFM imaging, along with FE simulations, conducted to gain insights into the experimental observations. A simple elastic-perfectly plastic constitutive model was found to closely simulate the mechanical behaviour of the two materials, exhibiting a good ductility in compression. This observation,

in addition to the fine-grained nanostructure revealed by TFM, suggested GBS as the initial deformation mechanism of the monoliths. However, this model slightly underestimated the load in the case of cube corner indentation. The effect of densification can provide an explanation for this discrepancy. It consists of a reduction of the volume of material in the area immediately beneath the indenter, driven by hydrostatic pressure. It was established that this impact is only relevant in the case of cube corner indentation, characterised by a larger hydrostatic pressure generated under the indenter. Thereafter, nanoFTIR measurements of the local vibrational spectra proved that some densification occurs when the stress rises as a result of framework distortion in the contact area, which is most likely caused by a shear-induced deformation.

Chapter 5 is focused on the cracking behaviour under sharp indentation of four monoliths, namely ZIF-8, HKUST-1, MIL-68 and MOF-808, each characterised by distinctively different open-framework structures. Nanoindentation (employing Berkovich and cube corner tips), microindentation (Vickers) and nanoscratch tests were carried out. Shear faults were observed inside the contact area in each sample and indicated as the principal fracture mechanism. Moreover, a relationship between the fracture toughness and the nanostructure and framework architecture was observed. Specifically, the monoliths exhibiting an intermediate to high elastic recovery (i.e., ZIF-8 and HKUST-1) were the only ones in which the propagation of radial cracks took place, indicating that this phenomenon is driven by residual stresses upon unloading, as observed in previous indentation studies on brittle materials (i.e., soda-lime glass). In contrast, this was not the case for MIL-68 and

MOF-808, both characterised by a low elastic recovery, which displayed a higher ductility, resulting from their specific framework architecture and smaller size of nanograins, which favours the deformation by GBS. This mechanism enables, to some extent, to limit the damage to the contact region since the cracks will follow the low-energy grain boundaries separating the aggregated nanocrystals making up the monolith. Local nanoFTIR spectra collected inside the Vickers residual impression of ZIF-8 corroborated this hypothesis: the absence of stress-induced structural modifications in the vicinity of the shear faults indicates that the material likely fractures at the grain boundaries, dissipating energy. Nanoscratch tests further confirmed these speculations. MIL-68 and MOF-808 monoliths in fact underwent larger plastic deformation and accommodated larger penetration depths with no sign of cracking. On the other hand, ZIF-8 dissipated energy by brittle fracture, being unable to sustain such a plastic deformation. The absence of pile-up along the scratch direction, usually associated with plastic flow, suggests that a continuous flow of material is prevented by the stepwise shear-activated failure of the material, well contained inside the scratch area, and not resulting in any catastrophic cracking or chipping events.

Building upon the findings of the previous chapters, Chapter 6 described the yielding behaviour and the stress-strain relationships of the ZIF-8 and MIL-68 monoliths, determined by means of flat punch indentation and micropillar compression experiments. These two materials were specifically chosen due to their different fracture behaviour under sharp indentation (Chapter 5). They both exhibit a similar plastic response to flat punch indentation, when a confining pressure exists

and crack propagation is inhibited, with limited strain hardening. This behaviour can again be ascribed to the nanostructure of the sol-gel monoliths, promoting GBS as the principal deformation mechanism. The microRaman study of the residual flat punch indent, revealed the presence of residual strains at the framework level in the case of ZIF-8, resulting from the exceptional compliance of its sodalite cage architecture. Conversely, the MIL-68 framework was not modified by the applied stress, suggesting that the deformation of the monolith was only related to GBS.

Micropillar compression revealed two kinds of yielding behaviour: ZIF-8 failed by elastic crack propagation, evidenced by the occurrence of pop-ins in the stress-strain curves, while MIL-68 exhibited more significant plastic flow prior to failure.

The results of this research on the mechanical behaviour of nanocrystalline sol-gel monoliths has produced significant new insights that will pave the way for the nanostructural engineering and shaping of a class of mechanically robust and resilient framework solids suitable for practical applications.

The fabrication of monolithic MOF materials and composites, as well as the mechanical behaviour of MOFs in general are rapidly expanding research areas, however they are still in their infancy. This implies that a number of distinct research paths can be pursued with the aim of manufacturing mechanically robust and resilient devices and sensors. I believe that the following aspects should be explored for future work.

- FEM simulations can be further utilised to model the behaviour of MOF monoliths, by employing more elaborate constitutive models. The

continuum elastic-plastic material behaviour employed to model ZIF monoliths in Chapter 4 represents a first attempt in this sense, but it is not totally comprehensive. I envision that some aspects of compressible solids such as soil mechanics can be borrowed and adapted to this problem, given the consolidated granular nature of MOF monoliths. They can be modelled as an aggregate of nanocrystals with a certain size distribution, intergranular cohesion, and porosity. In this context, X-ray tomography scans may give useful insights on the porous microstructure of this class of materials.

- Throughout this thesis, local spectroscopy techniques (i.e., nanoFTIR and microRaman) have been employed to pinpoint the effect of indentation stress on the frameworks, in order to decouple the intragranular and the intergranular deformations. Advances in the field of local X-ray diffraction techniques may further shed light on this aspect, clarifying how crystallinity is affected by the local stress field. At the moment this is still challenging due to some practical limitations. Firstly, in order to achieve nanometric resolution, high laser powers are necessary, which would result in thermal degradation of many MOFs. Secondly, techniques like SAXS (small-angle X-ray scattering) require a strict sample preparation that would make it impossible to examine indented monoliths. For instance, it is frequently necessary to use small samples like TEM lamellae or micropillars.
- Drying shrinkage cracks represents an important drawback of the sol-gel process, severely limiting its scale-up capability. Shrinkage could be mitigated by considering alternative drying processes, such as supercritical

drying and freeze drying, which are well-established for other materials, which will however significantly increase the manufacturing costs. Another possibility is through the use of suitable binders, but this would probably come with the cost of a decreased "purity" of the monoliths. The inclusion of binders could introduce impurities in the system that may affect the functional properties of the framework.

- The fabrication and mechanical characterisation of MOF-polymer composites, with the aim of improving the fracture toughness of these materials, without sacrificing the functional properties of the frameworks, would represent a ground-breaking accomplishment in the field. Observing nature can help to achieve this objective: seashells and nacre are an outstanding example of extremely tough composites, consisting of highly concentrated hard nanoparticles (typically ~95 wt%) in an organic matrix (~5 wt% or less). The current limitations of MOF-polymer composites include the difficulty of achieving high effective loadings due to reduced colloidal stabilities of MOF crystals during the fabrication process (aggregates and sediments of MOF powders will form as the loading increases) and reduced accessibility of nanopores (the polymer matrix can block the internal porosity). At present, a high MOF filler loading exceeding ~20-30 wt% leads to embrittlement of the resultant MOF-polymer composites in the form of mixed-matrix membranes. Further research is needed to address the embrittlement issue.

- Luminescent sensors represent a promising and rapidly growing area in MOF engineering. They often exploit the guest@MOF principle, consisting of the encapsulation of luminescent “guest” molecules in the pores of a “host” MOF framework. Several combinations of guest and hosts, resulting in a wide range of optical properties, have been reported to date. However, to the best of my knowledge, they are mostly produced in the form of polydisperse powder and MOF-polymer composites. The idea of luminescent MOF monoliths has not been explored thus far. I believe that this solution would allow to overcome some intrinsic limitation of both powders and polymer composites. With respect to the powders, they would provide a certain robustness and resilience, resulting in much easier handling. When compared to polymer composites, they would not pose issues such as the quenching of the guest@MOF luminescence induced by the polymer or the luminescent properties of the polymer itself that in some cases (i.e., acrylate photosensitive polymers employed for 3D printing) may cancel out the luminescence of the sensing material.

References

1. Q. Xu, *Nanoporous materials: synthesis and applications* (CRC press, 2013).
2. G. M. Lu, X. S. Zhao, *Nanoporous materials: science and engineering* (World Scientific, 2004), vol. 4.
3. S. P. Adiga *et al.*, Nanoporous materials for biomedical devices. *JOM* **60**, 26-32 (2008).
4. G. Sneddon, A. Greenaway, H. H. Yiu, The potential applications of nanoporous materials for the adsorption, separation, and catalytic conversion of carbon dioxide. *Adv. Energy Mater.* **4**, 1301873 (2014).
5. R. E. Morris, P. S. Wheatley, Gas storage in nanoporous materials. *Angew. Chem. Int. Ed.* **47**, 4966-4981 (2008).
6. H. Furukawa, K. E. Cordova, M. O'Keeffe, O. M. Yaghi, The chemistry and applications of metal-organic frameworks. *Science* **341**, 1230444 (2013).
7. R. Aniruddha, I. Sreedhar, B. M. Reddy, MOFs in carbon capture-past, present and future. *J. CO2 Util.* **42**, 101297 (2020).
8. B. M. Jun *et al.*, Applications of metal-organic framework based membranes in water purification: A review. *Sep. Purif. Technol.* **247**, 116947 (2020).
9. Y. J. Zhao, Y. Cui, X. R. Meng, J. Ding, H. W. Hou, Metal organic framework composites as adsorbents: Synergistic effect for water purification. *Coord. Chem. Rev.* **473**, 214815 (2022).
10. A. Bavykina *et al.*, Metal–organic frameworks in heterogeneous catalysis: recent progress, new trends, and future perspectives. *Chem. Rev.* **120**, 8468-8535 (2020).
11. H. Li *et al.*, Porous metal-organic frameworks for gas storage and separation: Status and challenges. *Energychem* **1**, 100006 (2019).
12. T. Jia, Y. F. Gu, F. T. Li, Progress and potential of metal-organic frameworks (MOFs) for gas storage and separation: A review. *J. Environ. Chem. Eng.* **10**, 108300 (2022).
13. M. Tricarico, J.-C. Tan, Mechanical properties and nanostructure of monolithic zeolitic imidazolate frameworks: a nanoindentation, nanospectroscopy, and finite element study. *Mater. Today Nano* **17**, 100166 (2022).
14. R. Freund *et al.*, 25 Years of Reticular Chemistry. *Angew. Chem. Int. Ed.* **60**, 23946-23974 (2021).
15. T. D. Bennett, A. K. Cheetham, Amorphous metal-organic frameworks. *Acc. Chem. Res.* **47**, 1555-1562 (2014).
16. O. M. Yaghi *et al.*, Reticular synthesis and the design of new materials. *Nature* **423**, 705-714 (2003).

17. J. Hou, A. F. Sapnik, T. D. Bennett, Metal–organic framework gels and monoliths. *Chem. Sci.* **11**, 310-323 (2020).
18. P. Falcaro *et al.*, MOF positioning technology and device fabrication. *Chem. Soc. Rev.* **43**, 5513-5560 (2014).
19. R. J. Kuppler *et al.*, Potential applications of metal-organic frameworks. *Coord. Chem. Rev.* **253**, 3042-3066 (2009).
20. I. Stassen *et al.*, An updated roadmap for the integration of metal-organic frameworks with electronic devices and chemical sensors. *Chem. Soc. Rev.* **46**, 3185-3241 (2017).
21. H. Uehara *et al.*, Porous Coordination Polymer Hybrid Device with Quartz Oscillator: Effect of Crystal Size on Sorption Kinetics. *J. Am. Chem. Soc.* **133**, 11932-11935 (2011).
22. I. Ellern *et al.*, HKUST-1 coated piezoresistive microcantilever array for volatile organic compound sensing. *Micro & Nano Letters* **8**, 766-769 (2013).
23. A. S. Babal *et al.*, Parts-per-billion (ppb) selective iodine sensors leveraging metal–organic framework nanoenvironment. *Mater. Today* **58**, 91-99 (2022).
24. A. F. Möslein *et al.*, A Multimodal Study on the Unique Sensing Behavior of a Guest@Metal-Organic Framework Material for the Detection of Volatile Acetone. *Adv. Mater. Interfaces* **10**, 2201401 (2022).
25. S. Mallakpour, E. Nikkhoo, C. M. Hussain, Application of MOF materials as drug delivery systems for cancer therapy and dermal treatment. *Coord. Chem. Rev.* **451**, 214262 (2022).
26. J. Gandara-Loe *et al.*, MOF-Based Polymeric Nanocomposite Films as Potential Materials for Drug Delivery Devices in Ocular Therapeutics. *ACS Appl. Mater. Interfaces* **12**, 30189-30197 (2020).
27. M. Ding, R. W. Flaig, H.-L. Jiang, O. M. Yaghi, Carbon capture and conversion using metal–organic frameworks and MOF-based materials. *Chem. Soc. Rev.* **48**, 2783-2828 (2019).
28. A. Phan *et al.*, Synthesis, structure, and carbon dioxide capture properties of zeolitic imidazolate frameworks. *Acc. Chem. Res.* **43**, 58-67 (2010).
29. D. Qian, C. Lei, G. P. Hao, W. C. Li, A. H. Lu, Synthesis of hierarchical porous carbon monoliths with incorporated metal-organic frameworks for enhancing volumetric based CO(2) capture capability. *ACS Appl. Mater. Interfaces* **4**, 6125-6132 (2012).
30. A. Bétard *et al.*, Fabrication of a CO2-selective membrane by stepwise liquid-phase deposition of an alkylether functionalized pillared-layered metal-organic framework [Cu2L2P]n on a macroporous support. *Microporous Mesoporous Mat.* **150**, 76-82 (2012).
31. D.-J. Lee, Q. Li, H. Kim, K. Lee, Preparation of Ni-MOF-74 membrane for CO2 separation by layer-by-layer seeding technique. *Microporous Mesoporous Mat.* **163**, 169-177 (2012).
32. A. Comotti, S. Bracco, T. Ben, S. Qiu, P. Sozzani, Molecular Rotors in Porous Organic Frameworks. *Angew. Chem. Int. Ed.* **53**, 1043-1047 (2014).

33. A. S. Babal, A. K. Chaudhari, H. H.-M. Yeung, J.-C. Tan, Guest-Tunable Dielectric Sensing Using a Single Crystal of HKUST-1. *Adv. Mater. Interfaces* **7**, 2000408 (2020).
34. M. Gutiérrez, C. Martín, M. Van der Auweraer, J. Hofkens, J. C. Tan, Electroluminescent Guest@MOF Nanoparticles for Thin Film Optoelectronics and Solid-State Lighting. *Adv. Opt. Mater.* **8** (2020).
35. M. Gutiérrez, Y. Zhang, J.-C. Tan, Confinement of Luminescent Guests in Metal–Organic Frameworks: Understanding Pathways from Synthesis and Multimodal Characterization to Potential Applications of LG@MOF Systems. *Chem. Rev.* **122**, 10438-10483 (2022).
36. D. Li, H.-Q. Xu, L. Jiao, H.-L. Jiang, Metal-organic frameworks for catalysis: State of the art, challenges, and opportunities. *EnergyChem* **1**, 100005 (2019).
37. M. D. Allendorf *et al.*, Guest-Induced Emergent Properties in Metal-Organic Frameworks. *J. Phys. Chem. Lett.* **6**, 1182-1195 (2015).
38. X. T. Liu *et al.*, Recent progress in host–guest metal–organic frameworks: Construction and emergent properties. *Coord. Chem. Rev.* **476**, 214921 (2023).
39. J. Ren, H. W. Langmi, B. C. North, M. Mathe, Review on processing of metal–organic framework (MOF) materials towards system integration for hydrogen storage. *Int. J. Energy Res.* **39**, 607-620 (2015).
40. A. Ahmed, M. Forster, R. Clowes, P. Myers, H. Zhang, Hierarchical porous metal-organic framework monoliths. *Chem. Commun.* **50**, 14314-14316 (2014).
41. M. Kalaj *et al.*, MOF-Polymer Hybrid Materials: From Simple Composites to Tailored Architectures. *Chem. Rev.* **120**, 8267-8302 (2020).
42. A. Sachse *et al.*, In situ synthesis of Cu-BTC (HKUST-1) in macro-/mesoporous silica monoliths for continuous flow catalysis. *Chem. Commun.* **48**, 4749-4751 (2012).
43. P. Küsgens, A. Zgaverdea, H.-G. Fritz, S. Siegle, S. Kaskel, Metal-Organic Frameworks in Monolithic Structures. *J. Am. Ceram. Soc.* **93**, 2476-2479 (2010).
44. H. Thakkar, S. Eastman, Q. Al-Naddaf, A. A. Rownaghi, F. Rezaei, 3D-Printed Metal-Organic Framework Monoliths for Gas Adsorption Processes. *ACS Appl. Mater. Interfaces* **9**, 35908-35916 (2017).
45. A. K. Chaudhari, J. C. Tan, Dual-Guest Functionalized Zeolitic Imidazolate Framework-8 for 3D Printing White Light-Emitting Composites. *Adv. Opt. Mater.* **8**, 1901912 (2020).
46. J. Dhainaut *et al.*, Systematic study of the impact of MOF densification into tablets on textural and mechanical properties. *CrystEngComm* **19**, 4211-4218 (2017).
47. R. N. Widmer *et al.*, Manufacturing Macroporous Monoliths of Microporous Metal–Organic Frameworks. *ACS Appl. Nano Mater.* **1**, 497-500 (2018).

48. N. Moitra *et al.*, Mechanically stable, hierarchically porous $Cu_3(btc)_2$ (HKUST-1) monoliths via direct conversion of copper(II) hydroxide-based monoliths. *Chem. Commun.* **51**, 3511-3514 (2015).
49. X. Hou *et al.*, Emerging Synthetic Methods and Applications of MOF-Based Gels in Supercapacitors, Water Treatment, Catalysis, Adsorption, and Energy Storage. *Macromol. Mater. Eng.*, 2200469 (2022).
50. T. Tian *et al.*, A sol-gel monolithic metal-organic framework with enhanced methane uptake. *Nat. Mater.* **17**, 174-179 (2018).
51. M. Tricarico, J.-C. Tan, Nanostructure-dependent indentation fracture toughness of metal-organic framework monoliths. *Next Materials* **1**, 100009 (2023).
52. T. Tian, J. Velazquez-Garcia, T. D. Bennett, D. Fairen-Jimenez, Mechanically and chemically robust ZIF-8 monoliths with high volumetric adsorption capacity. *J. Mater. Chem. A* **3**, 2999-3005 (2015).
53. E. Hunter-Sellars *et al.*, Sol–Gel Synthesis of High-Density Zeolitic Imidazolate Framework Monoliths via Ligand Assisted Methods: Exceptional Porosity, Hydrophobicity, and Applications in Vapor Adsorption. *Adv. Funct. Mater.* **31**, 2008357 (2020).
54. B. M. Connolly *et al.*, Tuning porosity in macroscopic monolithic metal-organic frameworks for exceptional natural gas storage. *Nat. Commun.* **10**, 2345 (2019).
55. B. M. Connolly, D. G. Madden, A. E. H. Wheatley, D. Fairen-Jimenez, Shaping the Future of Fuel: Monolithic Metal-Organic Frameworks for High-Density Gas Storage. *J. Am. Chem. Soc.* **142**, 8541-8549 (2020).
56. J. Cravillon *et al.*, Controlling Zeolitic Imidazolate Framework Nano- and Microcrystal Formation: Insight into Crystal Growth by Time-Resolved In Situ Static Light Scattering. *Chem. Mater.* **23**, 2130-2141 (2011).
57. J. Cravillon *et al.*, Fast nucleation and growth of ZIF-8 nanocrystals monitored by time-resolved in situ small-angle and wide-angle X-ray scattering. *Angew. Chem. Int. Ed.* **50**, 8067-8071 (2011).
58. B. Bueken *et al.*, Gel-based morphological design of zirconium metal-organic frameworks. *Chem. Sci.* **8**, 3939-3948 (2017).
59. P. Liao *et al.*, Transforming HKUST-1 Metal-Organic Frameworks into Gels - Stimuli-Responsiveness and Morphology Evolution. *Eur. J. Inorg. Chem.* **2017**, 2580-2584 (2017).
60. A. K. Chaudhari, I. Han, J. C. Tan, Multifunctional Supramolecular Hybrid Materials Constructed from Hierarchical Self-Ordering of In Situ Generated Metal-Organic Framework (MOF) Nanoparticles. *Adv. Mater.* **27**, 4438-4446 (2015).
61. A. K. Chaudhari, J. C. Tan, A mechano-responsive supramolecular metal-organic framework (supraMOF) gel material rich in ZIF-8 nanoplates. *Chem. Commun.* **53**, 8502-8505 (2017).
62. Y. Zhang *et al.*, Turn-On Fluorescence Chemical Sensing through Transformation of Self-Trapped Exciton States at Room Temperature. *ACS Sensors* **7**, 2338-2344 (2022).

63. A. K. Chaudhari, H. J. Kim, I. Han, J. C. Tan, Optochemically Responsive 2D Nanosheets of a 3D Metal-Organic Framework Material. *Adv. Mater.* **29**, 8491–8626 (2017).
64. A. Feinle, M. S. Elsaesser, N. Husing, Sol-gel synthesis of monolithic materials with hierarchical porosity. *Chem. Soc. Rev.* **45**, 3377-3399 (2016).
65. M. R. Lohe, M. Rose, S. Kaskel, Metal-organic framework (MOF) aerogels with high micro- and macroporosity. *Chem. Commun.* 10.1039/b910175f, 6056-6058 (2009).
66. L. Li *et al.*, A synthetic route to ultralight hierarchically micro/mesoporous Al (III)-carboxylate metal-organic aerogels. *Nat. Commun.* **4**, 1-9 (2013).
67. W. Liang *et al.*, 3D, eco-friendly metal-organic frameworks@carbon nanotube aerogels composite materials for removal of pesticides in water. *J. Hazard. Mater.* **401**, 123718 (2021).
68. Y. Su *et al.*, Ni/carbon aerogels derived from water induced self-assembly of Ni-MOF for adsorption and catalytic conversion of oily wastewater. *Chem. Eng. J.* **402**, 126205 (2020).
69. J. C. Tan, A. K. Cheetham, Mechanical properties of hybrid inorganic-organic framework materials: establishing fundamental structure-property relationships. *Chem. Soc. Rev.* **40**, 1059-1080 (2011).
70. N. C. Burtch, J. Heinen, T. D. Bennett, D. Dubbeldam, M. D. Allendorf, Mechanical Properties in Metal-Organic Frameworks: Emerging Opportunities and Challenges for Device Functionality and Technological Applications. *Adv. Mater.* **30**, 1704124 (2018).
71. L. R. Redfern, O. K. Farha, Mechanical properties of metal–organic frameworks. *Chem. Sci.* **10**, 10666-10679 (2019).
72. J.-C. Tan, *Mechanical Behaviour of Metal – Organic Framework Materials*. J.-C. Tan, Ed. (Royal Society of Chemistry, 2023), 10.1039/9781839166594.
73. J. C. Tan, C. A. Merrill, J. B. Orton, A. K. Cheetham, Anisotropic mechanical properties of polymorphic hybrid inorganic–organic framework materials with different dimensionalities. *Acta. Mater.* **57**, 3481-3496 (2009).
74. J. C. Tan, T. D. Bennett, A. K. Cheetham, Chemical structure, network topology, and porosity effects on the mechanical properties of Zeolitic Imidazolate Frameworks. *Proc. Natl. Acad. Sci. USA* **107**, 9938-9943 (2010).
75. J. C. Tan *et al.*, Exceptionally low shear modulus in a prototypical imidazole-based metal-organic framework. *Phys. Rev. Lett.* **108**, 095502 (2012).
76. C. S. Coates, M. R. Ryder, J. A. Hill, J. C. Tan, A. L. Goodwin, Large elastic recovery of zinc dicyanoaurate. *APL Mater.* **5**, 066107 (2017).
77. S. Bundschuh *et al.*, Mechanical properties of metal-organic frameworks: An indentation study on epitaxial thin films. *Appl. Phys. Lett.* **101**, 101910 (2012).
78. M. F. Doerner, W. D. Nix, A method for interpreting the data from depth-sensing indentation instruments. *J. Mater. Res.* **1**, 601-609 (2011).

79. I. N. Sneddon, The relation between load and penetration in the axisymmetric Boussinesq problem for a punch of arbitrary profile. *Int. J. Eng. Sci.* **3**, 47-57 (1965).
80. A. C. Fischer-Cripps, *Nanoindentation*, Mechanical Engineering Series (Springer New York, NY, 2004), 10.1007/978-1-4757-5943-3.
81. J. Hay, Introduction to Instrumented Indentation Testing. *Exp. Techniques* **33**, 66-72 (2009).
82. W. C. Oliver, G. M. Pharr, An improved technique for determining hardness and elastic modulus using load and displacement sensing indentation experiments. *J. Mater. Res.* **7**, 1564-1583 (1992).
83. J. Hay, P. Agee, E. Herbert, Continuous Stiffness Measurement during Instrumented Indentation Testing. *Exp. Techniques* **34**, 86-94 (2010).
84. J. C. Hay, A. Bolshakov, G. M. Pharr, A critical examination of the fundamental relations used in the analysis of nanoindentation data. *J. Mater. Res.* **14**, 2296-2305 (2011).
85. R. B. King, Elastic analysis of some punch problems for a layered medium. *Int. J. Solids. Struct.* **23**, 1657-1664 (1987).
86. M. Troyon, L. Huang, Correction factor for contact area in nanoindentation measurements. *J. Mater. Res.* **20**, 610-617 (2005).
87. A. Bolshakov, G. M. Pharr, Influences of pileup on the measurement of mechanical properties by load and depth sensing indentation techniques. *J. Mater. Res.* **13**, 1049-1058 (2011).
88. H. Hertz, Ueber die Berührung fester elastischer Körper. (1882).
89. K. L. Johnson, K. L. Johnson, *Contact mechanics* (Cambridge university press, 1987).
90. D. Tabor (1951) The hardness of metals. Chapter 2, Clarendon. (Oxford).
91. J. J. Vlassak, W. D. Nix, Measuring the elastic properties of anisotropic materials by means of indentation experiments. *J. Mech. Phys. Solids* **42**, 1223-1245 (1994).
92. J. J. Vlassak, W. D. Nix, Indentation modulus of elastically anisotropic half spaces. *Philos. Mag. A* **67**, 1045-1056 (1993).
93. J. G. Swadener, G. M. Pharr, Indentation of elastically anisotropic half-spaces by cones and parabolae of revolution. *Philos. Mag. A* **81**, 447-466 (2001).
94. J. J. Vlassak, M. Ciavarella, J. R. Barber, X. Wang, The indentation modulus of elastically anisotropic materials for indenters of arbitrary shape. *J. Mech. Phys. Solids* **51**, 1701-1721 (2003).
95. S. Li *et al.*, Mechanical Properties and Processing Techniques of Bulk Metal–Organic Framework Glasses. *J. Am. Chem. Soc.* **141**, 1027-1034 (2019).
96. T. D. Bennett *et al.*, Structure and properties of an amorphous metal-organic framework. *Phys. Rev. Lett.* **104**, 115503 (2010).
97. Z. Zeng (2018) Quantitative studies of the nanoscale mechanical properties of metal-organic framework materials. (University of Oxford).
98. D. F. Bahr *et al.*, Mechanical properties of cubic zinc carboxylate IRMOF-1 metal-organic framework crystals. *Phys. Rev. B* **76**, 184106 (2007).

99. T. D. Bennett *et al.*, Mechanical properties of dense zeolitic imidazolate frameworks (ZIFs): a high-pressure X-ray diffraction, nanoindentation and computational study of the zinc framework Zn(Im)2, and its lithium-boron analogue, LiB(Im)4. *Chem.* **16**, 10684-10690 (2010).
100. M. R. Ryder, B. Civalleri, G. Cinque, J.-C. Tan, Discovering connections between terahertz vibrations and elasticity underpinning the collective dynamics of the HKUST-1 metal–organic framework. *CrystEngComm* **18**, 4303-4312 (2016).
101. J. P. Mehta *et al.*, Sol-Gel Synthesis of Robust Metal-Organic Frameworks for Nanoparticle Encapsulation. *Adv. Funct. Mater.* **28**, 1705588 (2018).
102. T. To *et al.*, Fracture toughness of a metal-organic framework glass. *Nat. Commun.* **11**, 2593 (2020).
103. M. Stepniewska *et al.*, Observation of indentation-induced shear bands in a metal−organic framework glass. *Proc. Natl. Acad. Sci. U.S.A.* **117**, 10149-10154 (2020).
104. Y. X. Zhixin Zeng, Jeffrey M. Wheeler, Jin-Chong Tan (2022) In situ micropillar compression of an anisotropic metal-organic framework single crystal.
105. F. Birch, Elasticity and constitution of the Earth's interior. *J. Geophys. Res.* **57**, 227-286 (1952).
106. E. C. Spencer, R. J. Angel, N. L. Ross, B. E. Hanson, J. A. Howard, Pressure-induced cooperative bond rearrangement in a zinc imidazolate framework: a high-pressure single-crystal X-ray diffraction study. *J. Am. Chem. Soc.* **131**, 4022-4026 (2009).
107. K. W. Chapman, G. J. Halder, P. J. Chupas, Pressure-Induced Amorphization and Porosity Modification in a Metal−Organic Framework. *J. Am. Chem. Soc.* **131**, 17546-17547 (2009).
108. R. Vacher, L. Boyer, Brillouin Scattering: A Tool for the Measurement of Elastic and Photoelastic Constants. *Phys. Rev. B* **6**, 639-673 (1972).
109. Y. Sun, Z. Hu, D. Zhao, K. Zeng, Mechanical Properties of Microcrystalline Metal-Organic Frameworks (MOFs) Measured by Bimodal Amplitude Modulated-Frequency Modulated Atomic Force Microscopy. *ACS Appl. Mater. Interfaces* **9**, 32202-32210 (2017).
110. Z. Zeng, I. S. Flyagina, J.-C. Tan, Nanomechanical behavior and interfacial deformation beyond the elastic limit in 2D metal–organic framework nanosheets. *Nanoscale Adv.* 10.1039/d0na00475h (2020).
111. Z. Zeng, J. C. Tan, AFM Nanoindentation To Quantify Mechanical Properties of Nano- and Micron-Sized Crystals of a Metal-Organic Framework Material. *ACS Appl. Mater. Interfaces* **9**, 39839-39854 (2017).
112. B. Van de Voorde *et al.*, Mechanical properties of electrochemically synthesised metal–organic framework thin films. *J. Mater. Chem. B* **1**, 7716 (2013).
113. I. Buchan, M. R. Ryder, J.-C. Tan, Micromechanical Behavior of Polycrystalline Metal–Organic Framework Thin Films Synthesized by Electrochemical Reaction. *Cryst. Growth Des.* **15**, 1991-1999 (2015).

114. A. K. Bhattacharya, W. D. Nix, Finite element simulation of indentation experiments. *Int. J. Solids. Struct.* **24**, 881-891 (1988).
115. Y. J. Park, G. M. Pharr, Nanoindentation with spherical indenters: finite element studies of deformation in the elastic–plastic transition regime. *Thin Solid Films* **447-448**, 246-250 (2004).
116. M. Lichinchi, C. Lenardi, J. Haupt, R. Vitali, Simulation of Berkovich nanoindentation experiments on thin films using finite element method. *Thin Solid Films* **312**, 240-248 (1998).
117. J. A. Knapp, D. M. Follstaedt, S. M. Myers, J. C. Barbour, T. A. Friedmann, Finite-element modeling of nanoindentation. *J. Appl. Phys.* **85**, 1460-1474 (1999).
118. Q. Yang, D. Liu, C. Zhong, J. R. Li, Development of computational methodologies for metal-organic frameworks and their application in gas separations. *Chem. Rev.* **113**, 8261-8323 (2013).
119. J. D. Evans *et al.*, Computational Chemistry Methods for Nanoporous Materials. *Chem. Mater.* **29**, 199-212 (2016).
120. K. Banlusan, E. Antillon, A. Strachan, Mechanisms of Plastic Deformation of Metal–Organic Framework-5. *J. Phys. Chem. C* **119**, 25845-25852 (2015).
121. A. U. Ortiz, A. Boutin, A. H. Fuchs, F.-X. Coudert, Anisotropic Elastic Properties of Flexible Metal-Organic Frameworks: How Soft are Soft Porous Crystals? *Phys. Rev. Lett.* **109**, 195502 (2012).
122. K. Banlusan, V. Amornkitbamrung, Effects of Free Volume on Shock-Wave Energy Absorption in A Metal–Organic Framework: A Molecular Dynamics Investigation. *J. Phys. Chem. C* **124**, 17027-17038 (2020).
123. A. F. Möslein, L. Donà, B. Civalleri, J.-C. Tan, Defect Engineering in Metal–Organic Framework Nanocrystals: Implications for Mechanical Properties and Performance. *ACS Appl. Nano Mater.* **5**, 6398-6409 (2022).
124. A. W. Thornton, R. Babarao, A. Jain, F. Trousselet, F. X. Coudert, Defects in metal–organic frameworks: a compromise between adsorption and stability? *Dalton Trans.* **45**, 4352-4359 (2016).
125. C. F. Holder, R. E. Schaak, Tutorial on Powder X-ray Diffraction for Characterizing Nanoscale Materials. *ACS Nano* **13**, 7359-7365 (2019).
126. D. G. Lamas, M. de Oliveira Neto, G. Kellermann, A. F. Craievich, "X-Ray Diffraction and Scattering by Nanomaterials" in Nanocharacterization Techniques, A. L. Da Róz, M. Ferreira, F. de Lima Leite, O. N. Oliveira, Eds. (William Andrew Publishing, 2017), 10.1016/b978-0-323-49778-7.00005-9, pp. 111-182.
127. A. Rosa-Zeiser, E. Weilandt, S. Hild, O. Marti, The simultaneous measurement of elastic, electrostatic and adhesive properties by scanning force microscopy: pulsed-force mode operation. *Meas. Sci. Technol.* **8**, 1333-1338 (1997).
128. H. U. Krotil *et al.*, Pulsed force mode: a new method for the investigation of surface properties. *Surf. Interface Anal.* **27**, 336-340 (1999).

129. K. Xu *et al.*, Recent development of PeakForce Tapping mode atomic force microscopy and its applications on nanoscience. *Nanotechnol. Rev.* **7**, 605-621 (2018).
130. B. Knoll, F. Keilmann, Near-field probing of vibrational absorption for chemical microscopy. *Nature* **399**, 134-137 (1999).
131. B. D. Beake, A. J. Harris, T. W. Liskiewicz, Review of recent progress in nanoscratch testing. *Tribol. - Mater. Surf. Interfaces* **7**, 87-96 (2013).
132. L. Charleux, L. Bizet, vkeryvin, mousta (2015) Abapy v1.0. (Zenodo).
133. X. Huang, J. Zhang, X. Chen, [Zn (bim) 2]·(H2O) 1.67: A metal-organic open-framework with sodalite topology. *Sci. Bull.* **48**, 1531-1534 (2003).
134. K. Tai, F.-J. Ulm, C. Ortiz, Nanogranular Origins of the Strength of Bone. *Nano Lett.* **6**, 2520-2525 (2006).
135. M. T. Laugier, New formula for indentation toughness in ceramics. *J. Mater. Sci. Lett.* **6**, 355-356 (1987).
136. N. Cuadrado, D. Casellas, M. Anglada, E. Jiménez-Piqué, Evaluation of fracture toughness of small volumes by means of cube-corner nanoindentation. *Scripta Mater.* **66**, 670-673 (2012).
137. G. R. Anstis, P. Chantikul, B. R. Lawn, D. B. Marshall, A Critical Evaluation of Indentation Techniques for Measuring Fracture Toughness: I, Direct Crack Measurements. *J. Am. Ceram. Soc.* **64**, 533-538 (1981).
138. R. D. Dukino, M. V. Swain, Comparative Measurement of Indentation Fracture Toughness with Berkovich and Vickers Indenters. *J. Am. Ceram. Soc.* **75**, 3299-3304 (1992).
139. A. A. Griffith, G. I. Taylor, VI. The phenomena of rupture and flow in solids. *Philos. Trans. Royal Soc. A* **221**, 163-198 (1997).
140. G. R. Irwin, Analysis of Stresses and Strains Near the End of a Crack Traversing a Plate. *J. Appl. Mech.* **24**, 361-364 (1957).
141. J. Ast *et al.*, A review of experimental approaches to fracture toughness evaluation at the micro-scale. *Mater. Des.* **173**, 107762 (2019).
142. M. Sebastiani, K. E. Johanns, E. G. Herbert, G. M. Pharr, Measurement of fracture toughness by nanoindentation methods: Recent advances and future challenges. *Current Opinion in Solid State and Materials Science* **19**, 324-333 (2015).
143. A. G. Evans, E. A. Charles, Fracture Toughness Determinations by Indentation. *J. Am. Ceram. Soc.* **59**, 371-372 (1976).
144. B. Lawn, R. Wilshaw, Indentation Fracture - Principles and Applications. *J. Mater. Sci.* **10**, 1049-1081 (1975).
145. M. Sakai, R. C. Bradt, Fracture-Toughness Testing of Brittle Materials. *Int. Mater. Rev.* **38**, 53-78 (1993).
146. P. Ostojic, R. McPherson, A review of indentation fracture theory: its development, principles and limitations. *Int. J. Fract.* **33**, 297-312 (1987).
147. B. R. Lawn, A. G. Evans, D. Marshall, Elastic/plastic indentation damage in ceramics: the median/radial crack system. *J. Am. Ceram. Soc.* **63**, 574-581 (1980).

148. K. I. Schiffmann, Determination of fracture toughness of bulk materials and thin films by nanoindentation: comparison of different models. *Philos. Mag.* **91**, 1163-1178 (2011).
149. J. H. Lee, Y. F. Gao, K. E. Johanns, G. M. Pharr, Cohesive interface simulations of indentation cracking as a fracture toughness measurement method for brittle materials. *Acta. Mater.* **60**, 5448-5467 (2012).
150. B. R. Lawn, T. P. Dabbs, C. J. Fairbanks, Kinetics of shear-activated indentation crack initiation in soda-lime glass. *J. Mater. Sci.* **18**, 2785-2797 (1983).
151. Z. Hu, K. Lynne, F. Delfanian, Characterization of materials' elasticity and yield strength through micro-/nano-indentation testing with a cylindrical flat-tip indenter. *J. Mater. Res.* **30**, 578-591 (2015).
152. J. Alkorta, J. M. Martínez-Esnaola, J. G. Sevillano, Absence of one-to-one correspondence between elastoplastic properties and sharp-indentation load–penetration data. *J. Mater. Res.* **20**, 432-437 (2005).
153. S. Basu, A. Moseson, M. W. Barsoum, On the determination of spherical nanoindentation stress-strain curves. *J. Mater. Res.* **21**, 2628-2637 (2006).
154. J. Dean, J. M. Wheeler, T. W. Clyne, Use of quasi-static nanoindentation data to obtain stress strain characteristics for metallic materials. *Acta. Mater.* **58**, 3613-3623 (2010).
155. S. Pathak, S. R. Kalidindi, Spherical nanoindentation stress-strain curves. *Mater. Sci. Eng. R Rep.* **91**, 1-36 (2015).
156. J. Y. Zhang *et al.*, Length scale-dependent deformation behavior of nanolayered Cu/Zr micropillars. *Acta. Mater.* **60**, 1610-1622 (2012).
157. Q. Sun *et al.*, Size effects in strength and plasticity of single-crystalline titanium micropillars with prismatic slip orientation. *Scripta Mater.* **65**, 473-476 (2011).
158. S. Rubanov, P. R. Munroe, FIB-induced damage in silicon. *J. Microsc.* **214**, 213-221 (2004).
159. J. Mayer, L. A. Giannuzzi, T. Kamino, J. Michael, TEM sample preparation and FIB-induced damage. *MRS Bull.* **32**, 400-407 (2007).
160. D. Kiener, C. Motz, M. Rester, M. Jenko, G. Dehm, FIB damage of Cu and possible consequences for miniaturized mechanical tests. *Mater. Sci. Eng. A* **459**, 262-272 (2007).
161. V. Håkonsen, G. Singh, J. He, Z. Zhang, Focused ion beam milling of self-assembled magnetic superstructures: an approach to fabricate nanoporous materials with tunable porosity. *Mater. Horiz.* **5**, 1211-1218 (2018).
162. R. N. Widmer, A. M. Bumstead, M. Jain, T. D. Bennett, J. Michler, Plasticity of Metal–Organic Framework Glasses. *J. Am. Chem. Soc.* **143**, 20717-20724 (2021).
163. J. Hay (2019) Instrumented indentation apparatus having indenter punch with flat end surface and instrumented indentation method using the same. (Google Patents, U.S.).
164. D. Tabor, Indentation hardness: Fifty years on a personal view. *Philos. Mag. A* **74**, 1207-1212 (1996).

165. A. U. Ortiz, A. Boutin, A. H. Fuchs, F. X. Coudert, Investigating the Pressure-Induced Amorphization of Zeolitic Imidazolate Framework ZIF-8: Mechanical Instability Due to Shear Mode Softening. *J. Phys. Chem. Lett.* **4**, 1861-1865 (2013).